EXPLORATION OF NEW BISMUTH AND LEAD-BASED METAL- ORGANIC FRAMEWORKS FEATURING FREE O AND N DONORS: SYNTHESIS, STRUCTURES AND PROPERTIES

MESOUN A. A. AL-NUBI AL-SUDANI

FACULTY OF SCIENCE
UNIVERSITI MALAYA
KUALA LUMPUR

2021

EXPLORATION OF NEW BISMUTH AND LEAD-BASED METAL-ORGANIC FRAMEWORKS FEATURING FREE O AND N DONORS: SYNTHESIS, STRUCTURES AND PROPERTIES

MESOUN A. A. AL-NUBI AL-SUDANI

THESIS SUBMITTED IN FULFILMENT OF THE
REQUIREMENTS FOR THE DEGREE OF
DOCTOR OF PHILOSOPHY

DEPARTMENT OF CHEMISTRY
FACULTY OF SCIENCE
UNIVERSITI MALAYA
KUALA LUMPUR

2021

UNIVERSITI MALAYA
ORIGINAL LITERARY WORK DECLARATION

Name of Candidate: **MESOUN A. A. AL-NUBI AL-SUDANI**

Matric No: **SHC 160056**

Name of Degree: **DOCTOR OF PHILOSOPHY**

Title of Thesis:

EXPLORATION OF NEW BISMUTH AND LEAD-BASED METAL-ORGANIC FRAMEWORKS FEATURING FREE O AND N DONORS: SYNTHESIS, STRUCTURES AND PROPERTIES

Field of Study:

SOLID-STATE INORGANIC CHEMISTRY

I do solemnly and sincerely declare that:

(1) I am the sole author/writer of this Work;
(2) This Work is original;
(3) Any use of any work in which copyright exists was done by way of fair dealing and for permitted purposes and any excerpt or extract from, or reference to or reproduction of any copyright work has been disclosed expressly and sufficiently and the title of the Work and its authorship have been acknowledged in this Work;
(4) I do not have any actual knowledge nor do I ought reasonably to know that the making of this work constitutes an infringement of any copyright work;
(5) I hereby assign all and every rights in the copyright to this Work to the University of Malaya ("UM"), who henceforth shall be owner of the copyright in this Work and that any reproduction or use in any form or by any means whatsoever is prohibited without the written consent of UM having been first had and obtained;
(6) I am fully aware that if in the course of making this Work I have infringed any copyright whether intentionally or otherwise, I may be subject to legal action or any other action as may be determined by UM.

Candidate's Signature Date: 05-06-2021

Subscribed and solemnly declared before,

Witness's Signature: Date: 05-06-2021

Name:

Designation:

EXPLORATION OF NEW BISMUTH AND LEAD – BASED METAL-ORGANIC FRAMEWORKS FEATURING FREE O AND N DONORS: SYNTHESIS, STRUCTURES AND PROPERTIES

ABSTRACT

This work describes the syntheses, characterizations and the properties of two new metal organic frameworks (MOFs) based on bismuth and lead cations with two different ligand linkers: 2,3-pyrazine dicarboxylic acid (H_2Pzdc) and benzene 1,3,5-tricarboxylic acid (H_3BTC). Bi-Pzdc MOFs have been synthesized by employing simple dissolution-slow evaporation method using mixture of water/DMF with different stoichiometric molar ratios and recruiting imidazole (Im) or imidazolium iodide (ImZm) as modulator agents. Pb-BTC MOFs synthesis have been conducted by employing simple and optimized solution layering approach using different mixture of water/1,4-Dioxane; water/DMF; and water/MeOH using same stoichiometric molar ratios and adopting Aniline (Ani) or Im as auxiliary ligands. The physical and chemical features of these MOFs have been characterized by using optical microscope, UV light black box, Scanning Electron Microscope coupled with Energy Dispersive X-Ray Spectroscopy SEM/EDX, Single Crystal and Powder X-ray diffraction (SC-XRD and PXRD), Thermo-gravimetric Analysis (TGA), elemental analysis (CHN), solid state Nuclear Magnetic Resonance (SS-NMR), Fourier Transform Infrared Spectrometry (FTIR), Ultra Violet-Visible (UV-Vis) spectrophotometry (solid and liquid state), solid state photoluminescence (PL), BET surface area analysis and proton conductivity measurements. SCXRD and PXRD measurements reveal that the new, water stable Bi-MOFs: (compounds **1** to **12**), which all exhibit same structure; Bi(Pzdc)(HPzdc)(H_2O); (H_2pzdc= $C_6H_3N_2O_4$), crystallize in $P2_1/n$ space group (a =14.1738(7) Å, b =21.682(1) Å, c =14.7988(8) Å, β =109.2103(8)°) and built from 2D slabs interlinked by Pzdc ligands into 3D MOF with 10.5 Å× 8.9 Å aperture size. A presence of hydrogen-bonded along the crystallographic *c*-direction, within the 2D slabs, possibly lead to the observed proton conductivity. Interestingly, its visible and photoluminescence colors depend on water content. Three new, closely resembled Pb-based organic frameworks are also reported in here along with their structural characterizations, photoluminescence, and dyes adsorption properties. Their SCXRD and PXRD measurements confirmed that Compounds **13** and **14** offered same formula, $Pb(HBTC)(1,4\text{-dioxane})_{0.5}$, and crystallize in the *C2/c* space group (a =17.239(2) Å, b =7.0225(8) Å, c =19.911(2) Å, β =104.74(1)°); Compounds **15** and **17** display same formula as well, $Pb_2(HBTC)_2(H_2O)_5$, and crystallize in the *P*-1 space group (a = 7.3989(4) Å, b =8.2196(4) Å, c =10.1437(5) Å, α =94.336(4)°, β =104.943(4)°, γ =108.270(3)°); while Compound **18** with the formula, Pb(HBTC)(DMF), crystallizes in the $P2_1/n$ space group (a = 10.5004 (3) Å, b = 7.1398 (3) Å, c = 17.1285 (5) Å, β =102.160(2)°); (H_3BTC= $C_9H_6O_6$). All three lead compounds are built from slightly different 1D structures interconnected into 3D MOFs by BTC ligands forming different pore sizes which are governed by the solvent used during synthesis. Among them, only compound **17** showcases an interesting, near white-light emission, single-component phosphor with CIE coordinate of (0.33, 0.36), while compound **14** adsorbs methylene blue and methyl red dyes.

Keywords: Porous Coordination polymers, p-block metals, proton conductivity, photoluminescence, dyes adsorbent.

PENEROKAAN KERANGKA LOGAM-ORGANIK BARU BERASASKAN BISMUT DAN PLUMBUM YANG BEBAS PENDERMA O DAN N: SINTESIS, STRUKTUR DAN SIFAT

ABSTRAK

Kajian ini menerangkan tentang sintesis, pencirian dan aplikasi oleh dua rangka organik-besi (MOFs) berdasarkan kation bismut dan plumbum dengan dua ligan penghubung yang berbeza iaitu: asid 2,3-pirazin dikarbosilik (Pzdc) dan asid 1,3,5-trikarbosilik (BTC). Bi-Pzdc MOFs telah disintesis dengan menggunakan teknik penyerapan-penyejatan perlahan mudah diantara campuran air/DMF dengan nisbah molar stokiometrik yang berbeza dan imidazol (Im) atau imidazolium ioda (ImZm) sebagai ligan pembantu, manakala sintesis Pb-BTC MOFs telah berjaya dilakukan dengan mudah dan nisbah molar stokiometrik berbeza telah dioptimumkan diantara campuran air/1,4-dioxan; air/DMF; dan air/metanol sebagai bahan pelarut serta diadaptasi oleh Anilina (Ani) atau Im sebagai ligan pembantu. Fizikal dan kimia MOFs ini telah dicirikan oleh mikroskop optikal, kotak hitam cahaya UV, Pengimbas Mikroskop Elekton berserta Analisa Tenaga Cambahan X-Ray Spektroskopi SEM/EDX, Kristal tunggal, dan serbuk pembelahan X-ray (SC-XRD dan PXRD), Analisis Termogravimetrik (TGA), Analisis elemen (CHN), bentuk pepejal Resonan Magnetik Nuklear (SS-NMR), Spekroskopi Inframerah (FT-IR), dan Ultra-Violet spektroskopi (UV-Vis) (cecair dan pepejal bentuk), bentuk pepejal fotoluminasi (PL), analisis luas permukaan BET dan pengukuran konduktiviti proton. Pengukuran SCXRD dan PXRD membuktikan bahawa sebatian Bi-MOFs yang baru ini: (**1**) ke (**12**) adalah stabil air dan mempunyai struktur yang sama iaitu; $Bi(C_6H_2N_2O_4)$ $(C_6H_3N_2O_4)$ (H_2O) atau $Bi(pzdc)(Hpzdc)(H_2O)$ yang mempunyai dalam ruang kumpulan kristal $P2_1/n$ dengan (a = 14.1738(7) Å, b = 21.682(1) Å, c = 14.7988(8) Å, β = 109.2103(8)°), ianya berbentuk 2D dan telah dihubungkan dengan ligan Pzdc untuk menghasilkan bentuk 3D MOF yang bersaiz 10.5 Å× 8.9 Å. Kehadiran ikatan-hidrogen air disepanjang kristallographi arah-*c*, iaitu diantara papah 2D, kemungkinan konduktiviti proton boleh dilihat. Menariknya, ianya bercahaya dan warna fotoluminasinya adalah bergantung kepada kandungan air. Tiga MOFs baru yang menyerupai rangka organik-Pb telah dilaporkan bersama dengan perincian struktur, fotoluminasi, dan keupayaan penyerapan pewarna. Pengukuran SCXRD dan PXRD mengesahkan bahawa sebatian **13** dan **14** mempunyai formula yang sama iaitu, $C_{13}H_{13}O_9Pb$ atau $Pb(HBTC)(1,4\text{-dioxane})_{0.5}$, dan mempunyai ruang kumpulan kristal *C2/c* (a = 17.239(2) Å, b = 7.0225(8) Å, c = 19.911(2) Å, β = 104.74(1)°); Sebatian **18** mempunyai formula yang sama iaitu $C_{12}H_{11}NO_7Pb$ atau Pb(HBTC)(DMF), dikristalkan dalam ruang kumpulan kristal $P2_1/n$ (a =10.5004(3) Å, b =7.1398(3) Å, c =17.1285(5) Å, β =102.160(2)°); sementara sebatian **15** dan **17** mempunyai formula yang sama iaitu $C_{18}H_8O_{17}Pb_2$ or $Pb_2(HBTC)_2(H_2O)_5$, dan kristalnya dalam ruang kumpulan *P*-1 (a = 7.3989(4) Å, b =8.2196(4) Å, c =10.1437(5) Å, α =94.336(4)°, β =104.943(4)°, γ =108.270(3)°). Kesemua sebatian plumbum berbentuk struktur 1D dihubung oleh ligan BTC untuk berbentuk 3D MOFs dengan menghasilkan saiz pori yang berbeza dimana ditentukan oleh pelarut yang digunakan semasa sintesis. Diantara semua, hanya sebatian **17** yang menarik, hampir pelepasan cahaya-putih, komponen tunggal fosfur dengan koordinasi CIE (0.33, 0.36), manakala sebatian **14** menyerap pewarna metalina biru dan metil merah.

Katakunci: Koordinasi polimer berpori, logam blok P, konduktiviti proton, fotoluminasi, penyerapan pewarna.

ACKNOWLEDGEMENTS

First and final, all praises and graces to almighty Allah who gave me knowledge and strength to complete this work. I express my sincere gratitude to my scientific guidance Associate Professor Dr. Arief C. Wibowo for providing the proposal idea and all chemical materials and paying most of financial requirements for the measurements. I would like to introduce my deepest thank to my helpful supervisor Professor Dr. Azhar Bin Ariffin, for his unlimited moral support, expert guidance, constant encouragement and sincerity and enlightening discussions throughout the course of the completion of my work. A special thanks to Dr. Siti Nadiah Halim for her unlimited assistance, moral support, encouragement and intellectual help at many steps during my study period.

I gratefully acknowledge the Higher Education Commission of Iraq /Al-Mustansiriyah University in Baghdad for the financial support, and my sincere thanks to Universiti Malaya of Research Grant FRGS (Grant No.: FR037-2014A) for giving me this opportunity to continue my Doctoral study.

My deepest gratitude to my parents (who rest in peace) father who guided me to the path of rightness, who is the true source of wisdom, knowledge which is the only way to reach Allah, and mother for her love, courage, prayers and support throughout my life.

Foremost, I wish to express my most heartfelt gratitude and especial dedication to my family; my husband and my loved kids for their patience, sacrifices, moral support and motivation with positive energy throughout my research work. A tribute to my loving sisters and brothers for their affection, prayers, encouragement and moral support.

I'm also very thankful to all friends specially my brother Hamisu Aliyu Mohammed and my best friend and sister Olla H. S. Sharhan for their kindness and continuous help. All the respects to my lab mates for their valuable support and sustaining friendly atmosphere in the laboratory and for all UM staff for their kindness and help and well- wishers to who remember me in their prayers.

Finally, my special thanks to Muhammad Fauzan Bin Zainudin for his kind help to improve my plotting skill and developing ideas in PXRD study and to Madam Nor Lailah for her unlimited help in running my samples using FTIR technique, also for Mr. Zaidi for helping me to do the TGA measurements. I also need to acknowledge our collaborators abroad: from South Korea: Professor Dr. Kang Min Ok/ Chang- Ang University, from Canada: Professor Dr. George K.H. Shimizu/ University of Calgary and from Germany: Dr. Nicolo Minafra/ University Gie Ben.

TABLE OF CONTENTS

LIST OF FIGURES

LIST OF SCHEMES

LIST OF TABLES

LIST OF SYMBOLS, NOMENCLATURE AND ABBREVIATIONS

Å : Angstrom

° : Degree or bond angles (º)

°C : Degree centigrade

K : kelvin

θ : angle

λ : Wavelength

0D : Zero- dimensional (no extension)

1D : One- dimensional

2D : Two- dimensional

3D : Three- dimensional

Al^{3+} : Aluminum cation

An : Aniline

BDC : benzene-1,4- dicarboxylic acid

BET : Brunauer-Emmett-Teller method

Bi(Im)MOF : The batch of BiMOF synthesized using Imidazole as a modulator

Bi(ImZm)MOF : The batch of BiMOF synthesized using Imidazolium iodide as a modulator

$Bi(NO_3)_3.5H_2O$: Bismuth(III) Nitrate pentahydrate

Bi^{3+} : Bismuth (III) cation

BPDC : biphenyl-4,4'-dicarboxylic acid

Ce^{4+} : Cerium cation

CHNS/O : Carbon, Hydrogen, Nitrogen, Sulphur or Oxygen elements analysis

CIE : Commission Internationale l'Eclairage chromaticity diagram

CIF : Crystallography Information File

CN : coordination number

CO	:	carbon monoxide
CO_2	:	carbon dioxide
Co^{3+}	:	Cobalt cation
CP	:	Coordination polymer
Cr^{3+}	:	Chromium cation
Cu^{2+}	:	Cupper cation
d	:	crystal lattice spacing
DMF	:	Dimethylformamide
DSC	:	differential scanning calorimetry
DW or H_2O	:	Distilled water
Dy^{3+}	:	Dysprosium cation
EDTA	:	Ethylene diamine tetraacetic acid
EtOH	:	Ethanol
Eu^{3+}	:	Europium cation
Fe^{3+}	:	Ferric cation
FESEM-EDX	:	Field Emission Scanning Electron Microscope coupled with Energy Dispersive X-Ray Spectroscopy Analysis
FTIR	:	Fourier transform infrared
H^+	:	Hydrogen cation or proton
H_2	:	Hydrogen gas
H_2pzdc or Pzdc	:	pyrazine dicarboxylic acid
H_2S	:	hydrogen sulfide
H_3BTC or BTC	:	1,3,5-benzenetricarboxylic acid
H-b	:	Hydrogen bond
HCl	:	Hydrochloric acid
Hf^{4+}	:	Hafnium cation

HSAB : hard-soft acid base theory

I_2 : Iodide

ILCT : Intra ligand charge transfer

Im : Imidazole molecule

iMOFs : anionic MOFs

ImZm : Imidazolium iodide

L : Ligand

LMCT : ligand to metal charge transfer

M : metal

MB : methylene blue dye

MR : methyl red dye

MeOH : Methanol

Mg^{2+} : Magnesium cation

mL : milliliter

MLCT : Metal to ligand charge transfer

mmol : millimoles

MOCP : Metal-Organic coordination polymers

MOF : Metal-organic Framework

MOM : Metal- organic materials

MOPs : metal–organic polygons/polyhedra

MR : methyl red dye

N : Nitrogen atom

N_2 : Nitrogen gas

NaOH : Sodium Hydroxide

Ni^{2+} : Nickel cation

NMR : nuclear magnetic resonance

O : Oxygen atom

OLEDs : organic light–emitting diodes

$Pb(NO_3)_2$: Lead(II) Nitrate

Pb^{2+} : Lead (II) cation

PBUs : Primary Building Units

PCP : Porous coordination polymer

pH : The inverse logarithm of hydrogen cations concentration that measures how acidic or basic an aqueous solution is

Pip : Piperazine

PL : Photoluminescence

PXRD : powder X-ray diffraction technique

RT : room temperature

SBUs : Secondary Building Units

SCXRD : Single Crystal X-Ray Diffraction

SSUV-vis : Solid state ultraviolet visible

Tb^{3+} : Terbium cation

TEA^+ : Tetraethylammonium cation

TG/DTA : Thermo-gravimetric /Differential Thermal analyzers

TGA : Thermo-gravimetric analysis

TM : transition metal

UiO_2 : Uranium (IV) oxide

UV : ultraviolet

Vis : visible

Zn^{2+} : Zinc cation

Zr^{4+} : Zirconium cation

1-10 : Bi(Im)MOF

11, 12 : Bi(ImZm)MOF

13 : Pb(Dioxane)MOF

14 : Pb(Dioxane + Aniline)MOF

15 : Pb(MeOH)MOF

17 : Pb(MeOH + Imidazole)MOF

18 : Pb(DMF)MOF

LIST OF APPENDICES

CHAPTER 1: INTRODUCTION

1.1 Background study

Hybrid materials are developed by scientists in the early 21st century upon the availability and advances physico–chemical characterization methods, which enable better approaches to novel materials. The hybrid materials consist of two main building blocks: an inorganic part which provides mechanical strength and an overall structure and the organic part which delivers bonding between the inorganic and organic sections [1]. There are two different types of interaction that can be observed between the two components in the hybrid materials, weak and strong interactions. The weak interactions, such as Van der Waals forces [2], electrostatic interactions, π-π interaction, the intra and/or intermolecular hydrogen bonding, and another interactions that dubbed "supermolecules" [3]. Whilst, the strong interactions is chemical covalent bonds between them [4, 5], see Figure 1.1.

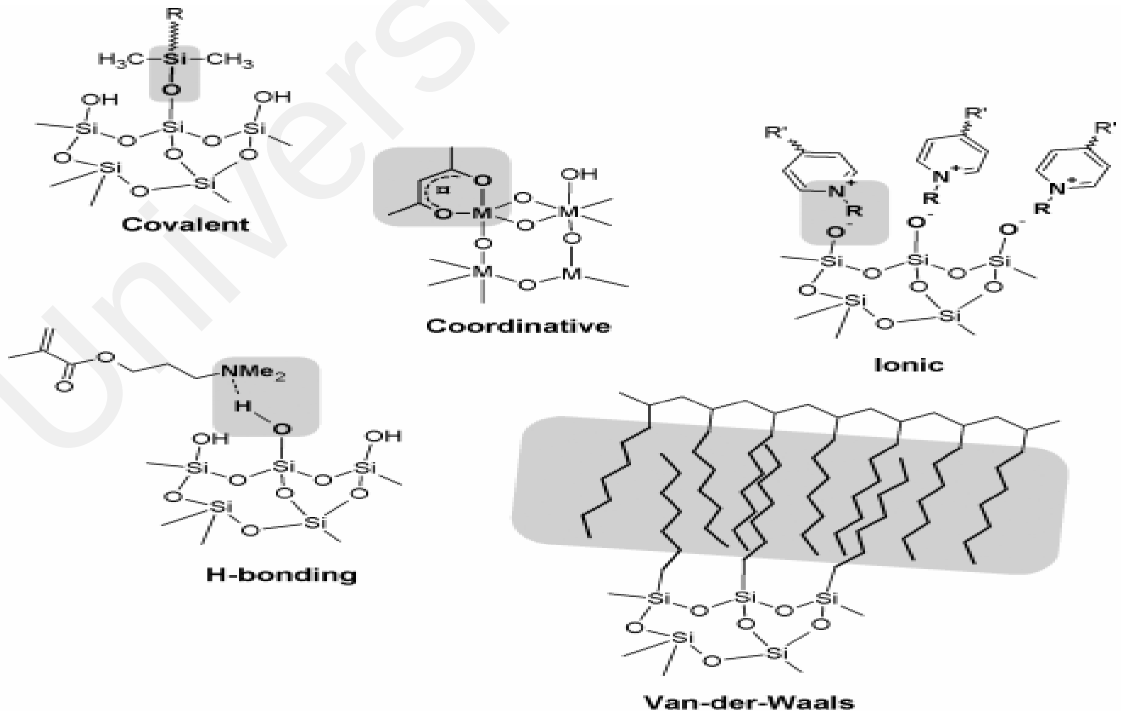

Figure 1.1: Selected interactions typically applied in hybrid materials and their relative strength [1].

A new class of inorganic-organic hybrid materials called metal organic materials (MOMs) have been investigated and rapidly developed in the past decade. MOMs is composed of metal-containing nodes connected by organic linkers through chemical bonds that built from a combination of metal moieties with organic ligands, the resulting properties often obtained from synergic combination of both constituents [6, 7].

MOMs can be divided into two main categories: I) the non-polymeric hybrid materials, which is called metal–organic polygons/polyhedra (MOPs), that have discrete structural features (display 0D means no extension), and II) the polymeric hybrid materials that have infinite structural features (display 1D-3D) which can also be divided into two categories: i) the polymeric porous materials, which is called metal–organic frameworks (MOFs) and ii) the polymeric non-porous materials that called coordination polymers (CPs) [8], see Scheme 1.1.

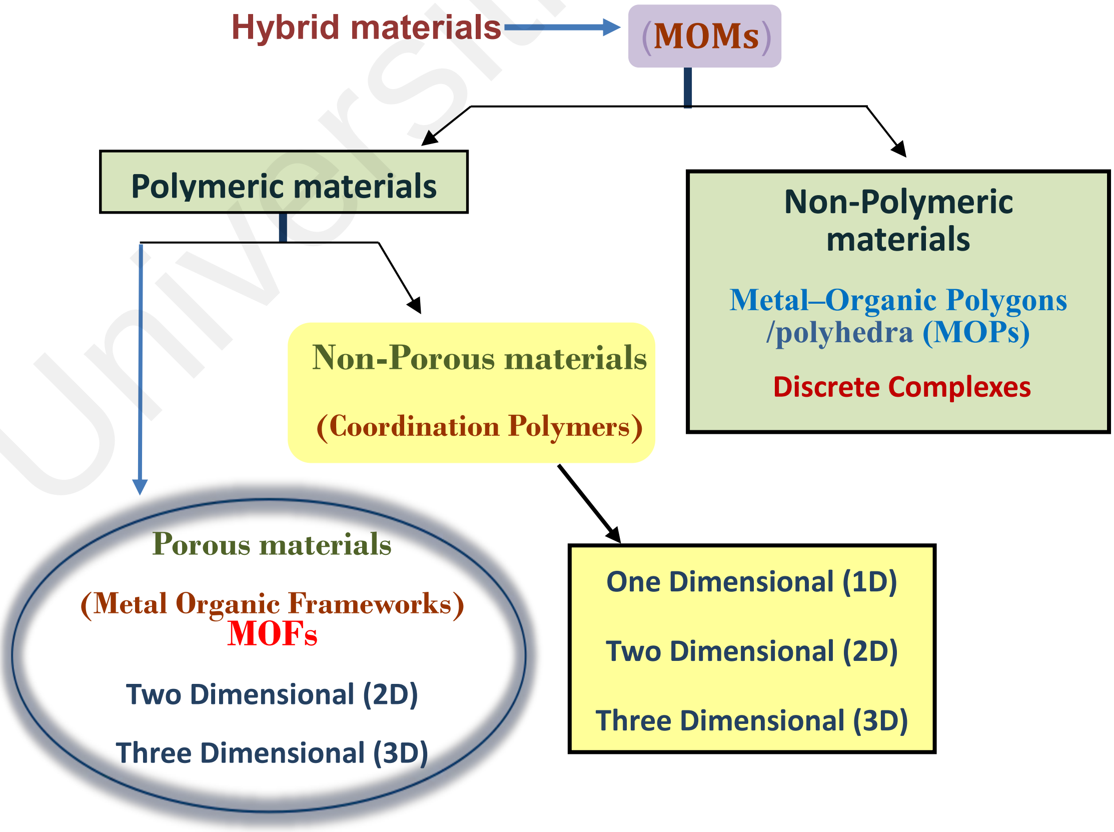

Scheme 1.1: Classification of hybrid materials according to the extension [9].

MOFs or porous coordination polymers (PCPs), a second generation of MOMs, is a three-dimensional extended structures with permanent porosity [10 - 13]. For more than two decades, MOF, predominantly transition metal (TM) and post TM base [14], has proven its importance through several groundbreaking discoveries in several applications such as gas storage and separation, luminescence, and magnetic properties [15 - 21] exploiting its versatile Reticular Chemistry [22].

MOFs can collaboratively combine the rigidity of inorganic compounds with the flexibility and tunability of organic matter to display the non-extended molecular solid state structures, contain potential voids [7], [23].

1.2 Classification and description of MOFs

MOFs can be categorized based on the charge of the framework into cationic [24], neutral and an anionic MOFs (iMOFs) [25]. MOFs, the second generation of MOM, belong to an important class of coordination network which can be considered as a subclass of CPs with special feature that they are always porous (have a permanent porosity) [10]. They have reported as special class of nano-porous materials [12] and named as “a periodic net” because they can be described as a separated type of graph [26].

Based on the ability of structural transformation, MOFs can be classified into flexible and robust/ rigid categories. The flexible class can shows the structural transformation phenomenon upon employing the external stimuli such as heat, guest molecules, electric or magnetic field, while the robust class of MOFs does not show this phenomena [27].

1.3 Why Lead (Pb) and Bismuth (Bi) metals

P-block metals-containing compounds protruded among the periodic table elements because they have a variety of applications in electroluminescence [28], photovoltaic conversion, crop protection agents, polymers, catalysts [29], disinfectants, fertilizers [30], solar cells, explosives, fluorescent sensors [31], medicines [32 - 34], and organic light–emitting diodes (OLEDs) [35]. However, little reports on p-block containing MOFs comparing to s-, d- and even f- block metal ions [36].

Tl^+, Pb^{2+} and Bi^{3+} cations, which belong to the sixth-row elements of periodic table, have the electronic configuration of [Xe] $4f^{14}5d^{10}6s^2$ in their lower oxidation states, featuring lone electrons pair in s-orbital, which typically form hemi-directed metal-organic polyhedra (distorted polyhedra) as building blocks of MOM with irregular network topologies, making them comparatively less explored [37 - 44]. In rare cases, however, these lone pair metals can form surprisingly regular network topologies, such as a Kagomé Lattice [45] and a paddle-wheel moiety [46 - 48] due to formation of only slightly distorted, holo-directed polyhedral, i.e. the lone pairs are not stereo-chemically active in most Bi^{3+} compounds, and there are only few compounds of Bi^{3+} with six coordination number that have a stereo-chemically active lone pair electron, which stimulates the Bi^{3+} cation to introduce versatile coordination geometries that form hemi directed MOPs (distorted polyhedral) as a building block [49]. Conversely, the lone electrons pair in Pb^{2+} compounds can be either active (hemi-directed) or inactive (holo-directed), which introduce numerous coordination geometries due to the ability of Pb^{2+} to form antibonding molecular orbital interactions (Pb 6s ligand np) [50, 51].

This lone electrons pair authorizes the metal ion to act as an electron pair donor (Lewis base) in addition reactions [52], and besides being a determining factor in the structural formation, lone electrons pair, also plays a very important role in responding to electric and mechanical field perturbations that provides important technological properties, such as ferroelectric and piezoelectric [53].

Among the p-block metals, Pb^{2+} merits other several advantages, include tolerant to defect, hence possibility of tunable electronic properties. According to Pearson’s hard-soft acid-base theory, $Pb^{2+}$and Bi^{3+} ions are border line metal ions that have a high affinity for both softer (:N) and harder (:O) donor ligands, thus, adaptable to a variety coordination environment [54, 55].

Due to their large ionic radius 1.16 Å for Bi^{3+} and 1.33 Å for Pb^{2+}, and the flexibility of Bi^{3+} and Pb^{2+} in coordination numbers (CN) ranging from 2–10 higher dimensionality cationic frameworks could easily be formed [56, 57].

Lead has two common oxidation states, +2 and +4, however, Pb^{2+} is more stable than Pb^{4+}, while the most stable oxidation state for bismuth is +3, which is govern its chemistry. The Bi^{3+} cation has a high Lewis acidity, which sometimes displays irregular coordination geometry. Other observed bismuth compounds’ oxidation states include +5, as well as the +2, +1 and even -3 [58].

Despite its identity as a heavy metal ion, bismuth compounds are generally nontoxic to humans and pose minimum threat to the environment. In spite of its low solubility, bismuth exists in wide applications as antibacterial and antifungal agents [35, 57].

Although lead is used in various technologies, it is poisoning to the human and the environment. Unfortunately, there is no oral chelator available to treatment of lead poisoning, but there is a growing interest to find selective lead binding materials. Simultaneously, many interesting lead-based coordination chemistry are under discovery [59- 61].

1.4 Why H_2Pzdc and H_3BTC ligands

The chemical stability and the structural rigidity as well as the appropriate connectivity of the two ligands that used in this study pyrazine -2,3-dicarboxylic acid (H_2Pzdc) and benzene tricarboxylic acid (H_3BTC), make them as the most successful multifunctional ligands which enable them to produce robust and stable frameworks [62]. They have multi donor sites (O and/or N) and their partially or fully deprotonated anions ($Hpzdc^{-}$ and $Pzdc^{2-}$) and (H_2BTC^{-}, $HBTC^{2-}$ and BTC^{3-}), respectively, enable them to extend in two and/or three dimensional (2D, 3D) structures and behave as poly-functional donors and/or bridging ligands with multi coordination modes in complexes and/or in coordination polymer compounds. ligands containing multi-carboxylates like H_2Pzdc and H_3BTC have been proven to be an effective strategy to construct intriguing MOFs due to the fact that carboxylic acid groups can provide reliable coordination modes to regulate pore size [63].

1.5 Problem statement

Considering the continues demand for energy production and in line with the key role of proton conductivity, which assumes in the production of electricity in hydrogen fuel cells, that some MOFs played because of the free proton inside their pores, besides the ability of the flexible MOFs to absorb different sizes of different molecules, like solvents, dyes or other toxic compounds, there is an obvious interest for designing and synthesis **adsorbing and storage** agent porous materials with a high capacity of H^{+} active sites, and acid and base stability.

1.6 Scope of study

This study deals with synthesis of some rare new BiMOFs which have ability to bear a water contents around 20% of their weight and remains stable that form an infinite network of hydrogen bonds inside its pores and also display different photoluminescence under UV and visible light. It deals also with some other new flexible/ breathing PbMOFs which exhibit an interesting near white light emission under UV light and can also absorb some organic molecules like dyes and some toxic compounds like aniline that makes them not only a good candidate to remove the aniline from environment but to be a promising candidate as aniline detector depending on the concentration of aniline in the medium.

1.7 Objectives

I. To develop and optimize the synthetic protocols for the synthesis of Bi and Pb-based functional MOFs featuring N and O donor atoms.

II. To characterize the structure as well as the physical and the chemical properties of the synthesized Bi and Pb-based functional MOFs.

III. To investigate the proton conductivity behavior of the individual functional MOF.

IV. To investigate the structure transformation behavior of the individual functional MOF using different solvents for synthesis.

V. To investigate the guest adsorption properties of the functional MOFs.

CHAPTER 2: LITERATURE REVIEW

2.1 Architecture of MOFs

MOFs are inorganic-organic hybrid extended networks that built from two main components called the primary building units (PBUs): the linker or “strut” which is the organic ligand and the metal ions/clusters. The construction of MOFs starts by choosing proper PBUs, then combining them together to link covalently and form a discrete metal-ligand cluster that generates a rigid existence with a simple geometry called secondary building units (SBUs) [64].

SBU is an organic-inorganic fragment of poly-nuclear cluster entities (metal moiety that is more complex than simple ions), which considered as molecular complexes that form the subunits or a template of MOFs [65]. These entities are normally formed when an organic linker connects two or more metal cations and arranges in a style/ layout of a rigid, 0D metal-ligand cluster with a simple geometry [66, 67], for instance, Zn_4O SBU, see Figure 2.1.

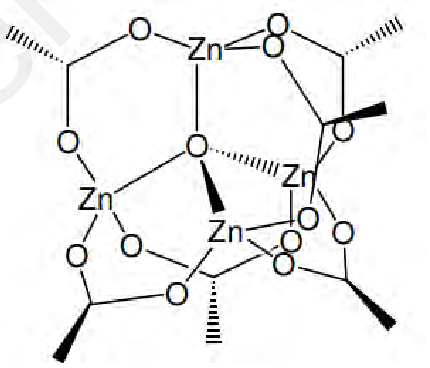

Figure 2.1: The Zn_4O cluster that named “ SBU” [68].

MOF is a coordination network that containing potential voids formed by the connection between an organic ligand and a metal atom [69]. This network can be extended through repeating coordinated entities, with cross links between two or more individual chains/loops, in a 1D, 2 or 3D structure [21, 70], see Figure 2.2.

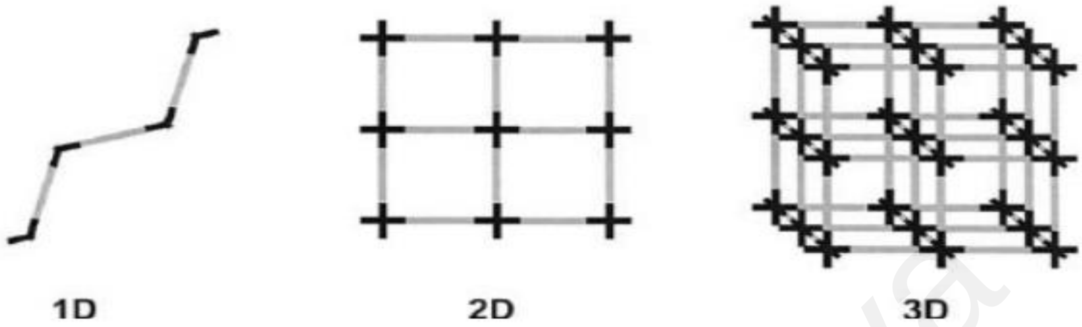

Figure 2.2: 1D, 2D and 3D frameworks based on two different metal coordination geometries with a linear organic bridge (black: metal; gray: organic bridge) [71].

The structures of MOFs can be designed as directional, stable and rigid building units in the architecture of predetermined robust crystalline composites, with potential properties depending on the poly-nuclear nature of the SBUs [65]. Therefore, the metal coordination environment and the ligand coordination mode can be exploited for the transformation of these discrete fragments into an extended porous network using multitopic linkers /or bridging ligands, such as terephthalic acid /benzene-1,4-dicarboxylic acid (BDC), biphenyl-4,4'-dicarboxylic acid (BPDC), pyrazine dicarboxylic acid (PzDC) or trimesic acid/ benzene -1,3,5-tricarboxylic acid (BTC) [72]. These organic linkers can be classified into rigid, semi-rigid and flexible categories [73].

There are three types of linkers are often used in designing a MOF: the cationic ligands (like imidazole, triazole or tetrazole), the neutral ligands (like pyrimidine, pyrazine, 4,4'-bipyridyl) and the anionic ligands (which usually contain carboxylate COO^-, sulphate SO_4^{2-} or phosphate PO_4^{3-} groups) [27]. It is very obvious that rigid N-donor ligands are mostly used for synthesis of high dimensional coordination polymers, unlike the flexible N-donor, which are stronger due to their space orientation [74].

Usually, the rigid or semi-rigid ligands [75, 76] are used to design a crystalline robust MOF that feature high porosity [77- 79]. However, using flexible ligands leads to produce a kind of MOFs that tend to be amorphous [80, 81]. Besides that, the aromatic linkers are favorable because an aliphatic part is less rigid than an aromatic part of the ligand.

2.2 Introduction to the synthesizing approaches of MOFs

The synthesis of MOFs has been advanced from the synthesis of zeolite where it usually needs organic "template" that is typically quaternary ammonium cations such as tetrapropyl ammonium hydroxide (TPA), cetyl trimethyl ammonium bromide (CTABr) or tetraethyl ammonium (TEA^+) cations. These quaternary cations are used to develop the inorganic framework and will be removed later. In contrast with zeolites, MOFs are assembled from the SBU and bridging organic ligands that consider as a template of MOFs and remain intact/integral throughout the synthesis [82- 84].

Zeolites and MOFs are created mostly by using conventional hydrothermal, solvothermal and non-solvothermal techniques in which the crystals are grown slowly from a hot solution of the starting materials with the solvents. A small scale of MOF precursor solution is heated within a temperature range (below/or at) boiling point of the solvents that generates autogenous pressure for different periods of time. Some materials are slowly developed as a result of many numerous conditions like temperature, pressure, time, concentration of precursor choice [85]. In order to minimize the reaction variables and/or optimize the product yield and/or control particle size, morphology and topology of MOFs, microwave assisted synthesis, electrochemical, mechanochemical, sono-chemical and ligand exchange methods have been used [86].

Hydro-and solvothermal synthetic methods are convenient techniques for preparing metal-organic frameworks (MOFs) using aromatic dicarboxylic acid based ligands and transition elements, in particular post transition elements, with reported applications such as gas storage [19, 87, 88], magnetic [16, 22, 89, 90] and luminescent applications [91], [18, 92]. The dissolution-crystallization, a rather less popular technique and yet requires less synthetic equipment, could potentially produce new, kinetically stable MOF that may merit its own structural library and applications [93, 94]. By similar token of facile dissolution-(re)-crystallization technique, post synthetic modification of MOFs exploits the relatively weak coordination bond of certain metal center to synthesize new compounds with tunable properties that are not possible to be made through conventional synthetic pathways [95, 96].

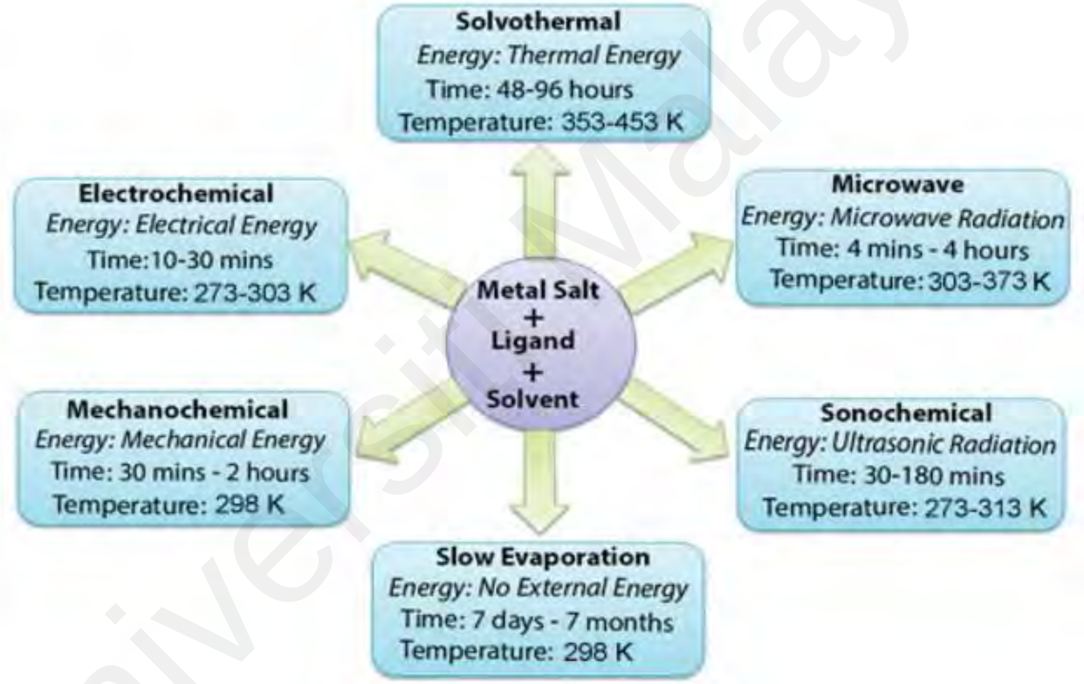

Scheme 2.1: A summary of the various approaches for MOFs preparation [97].

2.3 Nomenclature of MOFs

The Reticular Chemistry Structural Resource (RCSR) database task group has developed a terminology and nomenclature system for MOFs and/or CPs. This system can designate the subunits of a MOF (SBUs) as a fragment, which organizes and describes the framework structure in a way that can make it easier to illustrate the common topologies of several structures [26, 65].

The analysis and descriptors of these topologies is called “a net**”,** where atoms act as vertices of the net and the bonds act as links/ edges between atoms [98]. The topology assign/ or allocated as a symbol of three lower-case bold letters (sometime with a fourth letter after a hyphen) [70]. The **pcu** (Primitive Central Unit) topology net has been displayed by, for instance, MOF-76, MOF-5, MOF-1114(RE) and MOF-1115(RE) [69], while some others MOFs like MIL-47 and MOF-72 are featuring a **hex** topology, as shown in Figure 2.3.

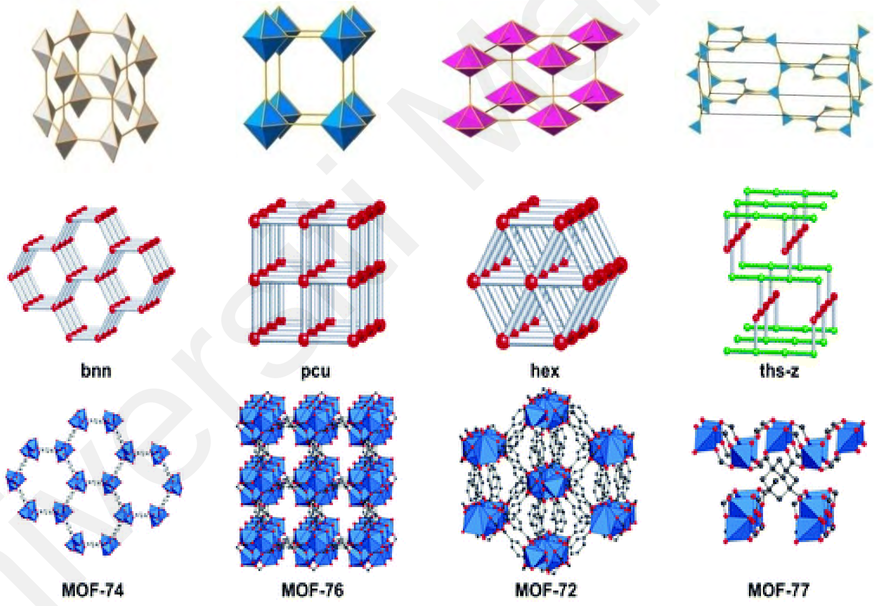

Figure 2.3: Correlation matrix (topologies) of some MOFs and their respective nets [99, 100].

The modular nature of MOFs, the chemical and geometrical attributes of the multitopic linkers and the SBUs make the framework topology not only nicely predicted, but also allowed for synthesis and designing of a new targeted class of porous materials with high porosity and robust structures [66].

2.4 Properties and applications of MOFs

Recently, MOFs have received a significant attention as a new family of nano-porous materials, largely due to variations in compositions, size, geometry, physicochemical properties and chemical functionality [101].

In storage technologies, MOFs are attractive platform that suffice the continuous need of energy for the next generation [102]. These variations enabled material scientists to investigate several thousands of different MOF structures.

A careful selection of both the metal center and the multifunctional linkers with the appropriate properties for the construction of MOFs is essential to produce the targeted and a prerequisite properties of the produced structure [102]. It can be tailored for not only the fascinating topologies and structures but largely due to their potential applications in various fields, such as luminescence, volume specific applications in gas adsorption (capture, storage, purification, sensing etc.) [103], ion exchange, conductivity, magnetism, catalysis, membrane design and molecular recognition using surface modified MOF as well as biomedical applications due to their biocompatibility and biodegradability [22]. Moreover, the choice of an appropriate exchangeable solvent (should be volatile), which is used for synthesizing of MOFs and/or removing the guest molecules from the pores of the framework, plays a key role in the architecture of some MOFs, while some frameworks collapse after removing the guest molecules [104]. Exploiting of various solvents controls the shape and the size of pores in MOFs architecture, where the solvent could sometimes consider as a template for designing a proper framework and prevents catenation, for producing an open structure [105]. Therefore, there are some important factors to achieve a target MOF and aligned together for best results, such as a successful selection of the metal ion, the ligand, the counter ions and the solvent, then chose a proper molar ratios of these components [27].

MOFs architecture are newly emerging and fast-growing field due to their intriguing benefits over the existing porous materials, such as zeolite and activated carbons. MOFs usually show interested properties like higher surface areas (due to the high porosities), reasonable higher thermal and mechanical stabilities, structural robustness, flexibilities, potential activities, which are intrinsic advantages for a wider range of applications in different fields rather than other types of general polymers or porous materials. In addition, MOFs offer a shape and size selectivity which required for both catalysis and separation applications [69, 106].

MOFs are classified as crystalline microporous materials [107], and the pores in most MOFs still stable during elimination of the guest molecules, i.e. solvents and other molecules could be refilled [108, 109]. Therefore, they are ideal for several volume-based related applications, such as adsorption-based gas separations [110], storage/capture of gases and/or fuel, such as carbon dioxide, methane and hydrogen [111, 112], gas/ liquid storage [113], separation/ purification [114, 115], super capacitors [116], chemical catalysis [117], catalysis [118, 119], sensing [120], luminescence [121], ion- exchange [122], cathode materials in lithium-ion batteries (LiBs) as lithium storage, [123], water desalination and purification, dehumidification and adsorption cooling technologies [105]. As well as, encapsulation, delivery and release of drugs [124- 127].

Besides the vital features of MOFs like large surface areas, tunable pore sizes, and permanent porosity, some flexible MOFs show a unique gate-opening effect behavior i.e. breathing phenomena. In which, MOF undergoes expansion and contraction that cannot observed in rigid frameworks like Zeolite [128]. Such breathability occurs by changing of mechanical pressure/temperature/ adsorption of the guest (usually the solvent or any external stimuli), which filled the voids [129]. This structural transformation depends on a number of factors, such as the nature of organic linkers, the nature of SBUs, the nature of solvent molecules and on the pore geometry [130].

2.5 Features of MOFs

MOFs can offer some unusual features, such as conductivity [131, 132], high surface areas and large pore size for guest adsorption [133], luminescence [134, 135], structure transformation [130].

2.5.1 The Proton Conductivity phenomenon and its mechanism

Physically, the liquid properties of water come from the presence of intersecting lines of hydrogen bond between its molecules, which make it a precious protons conductor [136]. The H-b forms as a dynamic attraction between two neighboring molecules involving one oxygen atom located between two hydrogen atoms called protiums in the water lattice [137]. Typically, the proton conductor is a solid electrolyte, in which the protium (H^+ cation) is the primary charge carrier. The protium is a nucleus which has only one proton inside and no electron shell around it, therefore, it strongly interacts with the electron density of its environment [138].

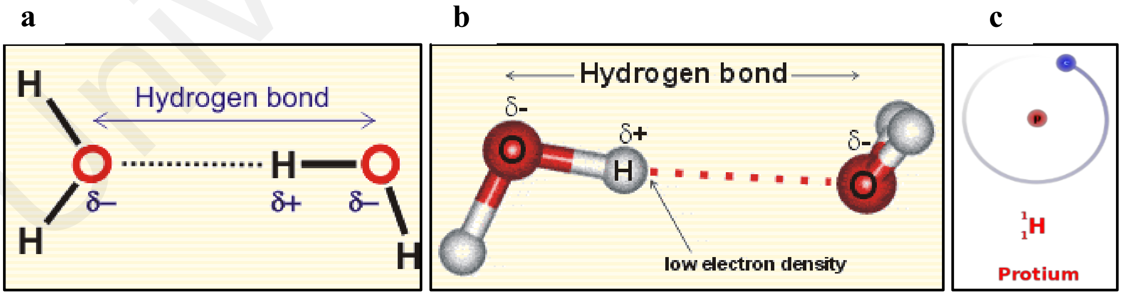

Figure 2.4: The electronic structure of water molecule; a and b: the hydrogen bonds formation, c: the protium atom.

In 1804 A.D, the conduction mechanism was studied first by Theodore von Grotthuss who suggested a “hop-turn” steps for this mechanism incidence by H^+ transport across a tunnel between water molecules (H_2O) and hydronium ions (H_3O^+), which involved a covalent bond exchange between H and O with a hydrogen bond [139].

Usually, at the end of hydrogen bond network, a proton bounces to an adjacent group, as shown in Scheme 2.2 (a); subsequently the hydrogen bond power authorizes this H^+ to substitute with another H^+ that binds at the other/opposite end of the network, Scheme 2.2 (a). This mechanism is named hop phase, then an alternation between water molecules in Scheme 2.2 (b) repeats structure (a) again, which is called turn phase [140]:

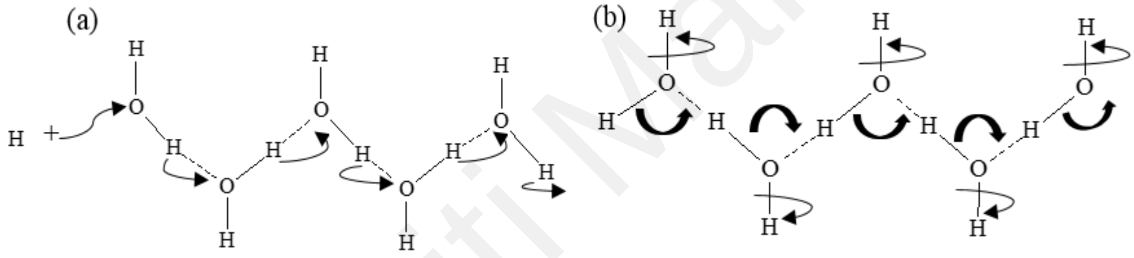

Scheme 2.2: The proton conduction which occurs through a "hop-turn" mechanism, I is the hop phase; and II is the turn phase.

The proton conductivity happens by the proton selective channels which conducts protons as H^+ rather than the form H_3O^+, even though the protons almost subsist in the solution as H_3O^+ (vehicles of hydronium ions) [141]. A proton diffuses together via a vehicle to a water molecule by tunneling in a hydrogen bond in the aqueous solution. The water molecule subsequently suffers reorientation in order to be able to take up the next proton. A counter diffusion of the un-protonated vehicles (e.g., H_2O) allows a net transport of protons, and the “vehicles” show pronounced local dynamics of protiums while they reside in their sites, see Figure 2.5a, then protons being transferred within hydrogen bonds from one “vehicle” to another, see Figure 2.5b [142].

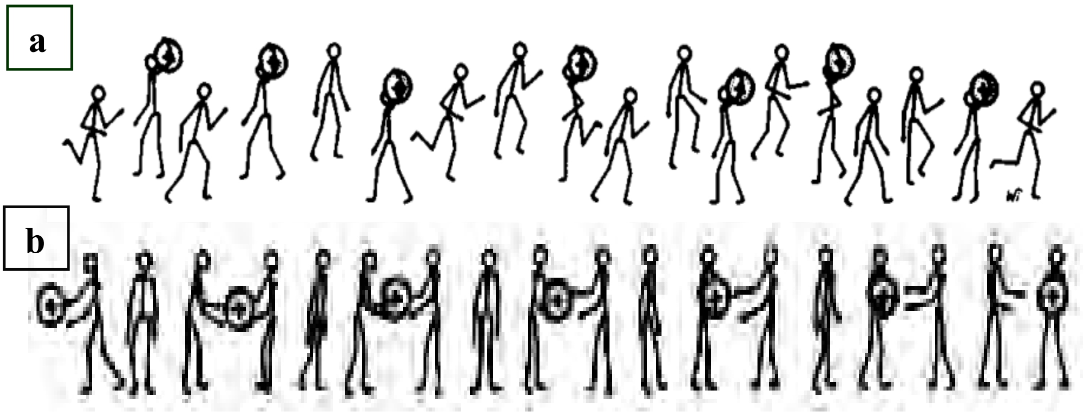

Figure 2.5: Model of proton conduction. a) Vehicle Mechanism: the movement takes place with the aid of a moving “vehicle”, e.g. H_2O or NH_3, as complex ions (H_3O^+ or NH_4^+); b) Grotthuss Mechanism; the protons are passed along the hydrogen bonds [142].

The concept of the Vehicle Mechanism leads to new applications in many technological innovations of solid proton conductors, such as hydrogen permeation membranes, membranes for water electrolyzes [143], hydrogen and humidity sensors [144] and for high efficiency electrochemical energy conversion in fuel cell [145].

The protons move inside the pores of MOFs in an infinite reticular pathway of H-bs caused by the presence of water molecules/ or any source of the deprotonated hydrogen (protium /H^+) like the quaternary cations (NH^{4+}) or the Imidazole molecule (Im) in the pores cavity of the MOF [146]. Figure 2.6 shows the chain of hydrogen bonds in its ground state (a) then a proton enters from one side of the chain (b), and the hydrogen bonds re-arrange such that a proton on the other side of the chain is released (c), the water molecules have to turn (d) in order for changing back the chain to its ground state (e).

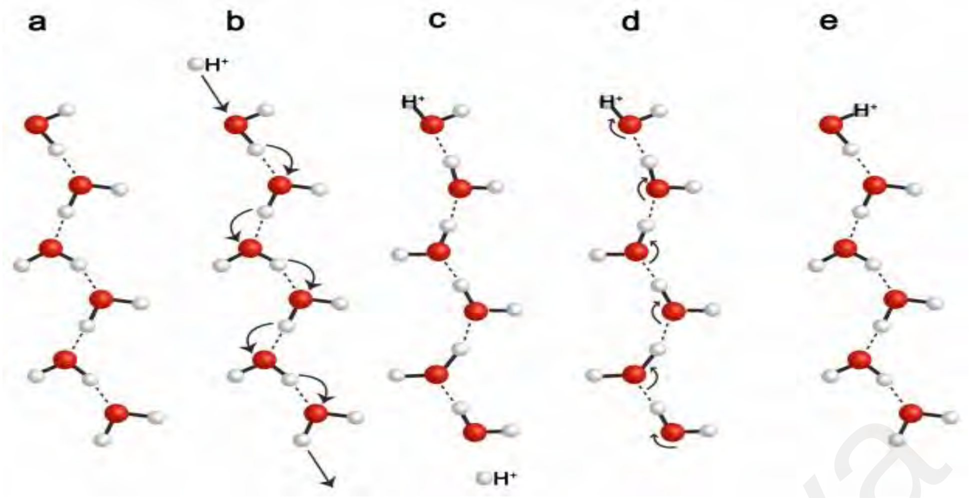

Figure 2.6: A schematic illustration of proton transferring through a hydrogen-bonded water chain via Grotthuss mechanism.

Considering the key role assumed by the proton conductivity in the photosynthesis process in green plants and electricity generation of the hydrogen fuel cells, which are promising future source of energy, the lanthanide contraction was employed by George K. H. Shimizu group (2017) to vary the unit cell dimensions systematically and tune the proton conducting pathways of crystalline MOFs series consisting of seven isomorphous members in PCMOF-5 family, $[Ln(H_5L)(H_2O)_n](H_2O)$ (L=1,2,4,5-tetrakis (phosphonomethyl) benzene, Ln =La, Ce, Pr, Nd, Sm, Eu, Gd) [147].

PCMOF-5 family contains 1D channels filled with water and terminated with free hydrogen phosphonate groups that gives a low activation energy pathway for proton transfer. The presence of water molecules and free acid groups positions in the frameworks have been confirmed by single crystallographic studies and the differences in particle size among the different members of the Ln series affirmed by SEM technique. The proton conductivities for La and Pr PC-MOFs were roughly an order of magnitude higher than other members of this series (10^{-3} S cm^{-1} vs. 10^{-4} S cm^{-1}) and the measurements of proton conductivity have assured that the high conducting La and Pr MOFs have the largest particle sizes.

Recently, there is an exciting achievement in proton conductive materials with coming of MOFs as promising materials, although the exact mechanism in proton transfer in MOFs remains challenging and not well understood. Wei and coworkers (2017) report a successful solvothermal synthesis of proton conducting MOF $(Me_2NH_2)[Eu(L)]$ (H_4L = 5-(phosphono methyl) isophthalic acid). This MOF composed of a layered anionic framework and counter cations embedded in the interlayer interact with phosphonate group to form strong hydrogen bonding chains, parallel to *c*-direction, Figure 2.7 (a, b). At 150 °C, the single crystal of this material was found to have anhydrous conductivity of 1.25×10^{-3} $S.cm^{-1}$ and a water mediated proton conductivity of 3.76×10^{-3} $S\ cm^{-1}$ at 100 °C and 98 % relative humidity RH using a compacted pellet. Herein, authors observed directly the proton dynamics involved vibration and transferred with the N–H···O chains of the material using controlled experiments and an isotropic conductivity measurements using single crystal and pellets [148].

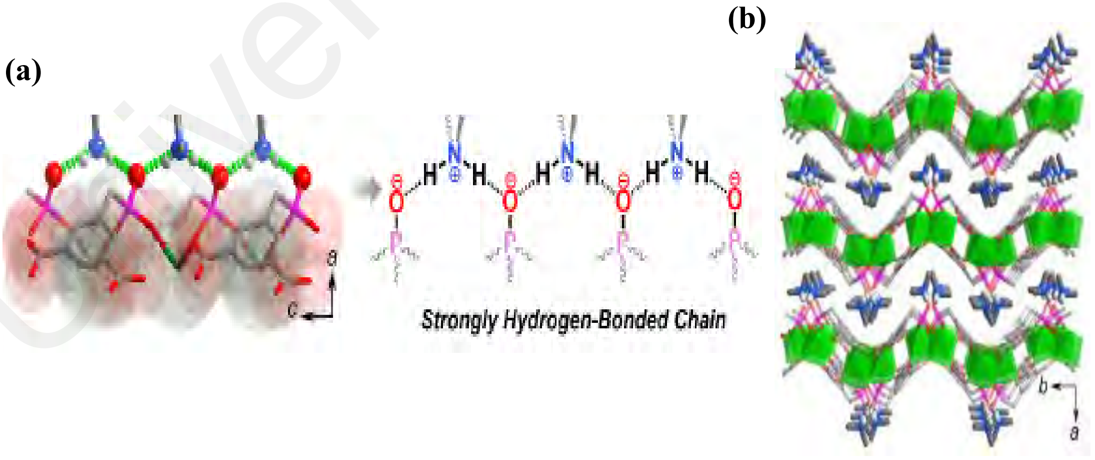

Figure 2.7: a) strongly hydrogen-bonded (N-H…O) chain assembled alternately by $(Me_2NH_2)^+$ cations and uncoordinated O7 atoms of phosphonate groups of anionic host framework, b) sandwich-type structure along the *c*-axis with the counter cations $(Me_2NH_2)^+$ periodically aligned in the interlayers.

Depending on imidazole molecules ability to be incorporated frequently into porous materials to improve their proton conductivity, Zhang and co-workers have designed Fe−based MOF exhibited a high proton conductivity. The Im@Fe−MOF with physically adsorbed imidazole has been prepared by encapsulating the free imidazole molecules into the pores of the parent Fe−MOF, where Im−Fe−MOF formed in which imidazole co-ligand molecules coordinated to the metal nodes of the framework. The proton conductivity of Im−Fe−MOF (1.21×10^{-2} S cm^{-1}) was two orders of magnitude greater than those of Fe−MOF and Im@Fe−MOF at room temperature. The density functional theory calculations suggested that coordinated imidazole molecules in Im−Fe−MOF can provide greater proton concentrations for the proton transportation than that of the coordinated water molecules in Fe−MOF alone, and the immobilized imidazole molecules by coordination bonds in the framework were more prone to form proton−conduction pathways and thus performed better and steadier in water-mediated proton conduction [149].

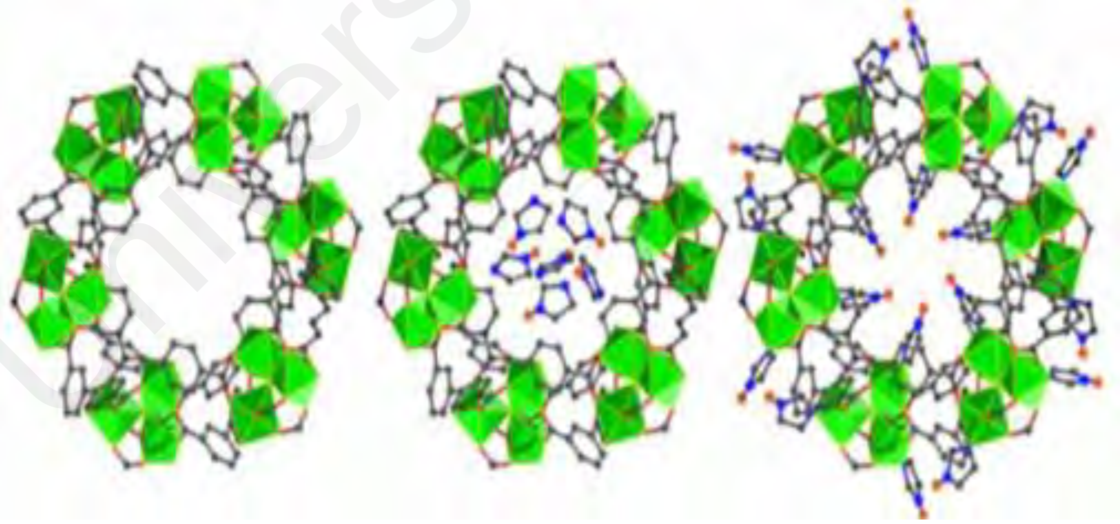

Figure 2.8: The variation in Imidazole incorporation inside Fe-MOF, Im-Fe-MOF, and Im-Fe-MOF hosts (left to right) respectively [149].

2.5.2 The porosity and high surface areas

2.5.2.1 The role of MOFs in Gases adsorption and separation

Considering the rapid increase of carbon dioxide (CO_2) emissions, especially from power plants, extensive attention for low cost and effective materials that can efficiently eliminate the post combustion CO_2, is of increasing. The importance of CO_2 storage, subsequent fixing and capture, for a clean energy, is of a great interest to scientists and engineers due to its economic importance. MOFs has shown to have a very promising potential for CO_2 capture and conversion; largely, unsaturated open metal and abundant N, O-rich Lewis basic sites in the network are prerequisite for proper and effective interaction with CO_2 that can pasture capturing of CO_2 molecules in the pores [150]. Molecular simulations can guide experimental studies by providing insights into MOFs separation mechanisms of gas adsorption. A lot of molecular simulation studies have tested MOFs for adsorption-based CO_2 separation that enable to identify MOFs. This was one of the most promising molecular properties for CO_2 separation to extensive experimental efforts [111].

Considerable effort has been exerted to improve the adsorption capacity and to incorporate different types of high-density open metal sites and Lewis basic sites. Liang and coworkers have recently, successfully synthesized a Cu-based MOF (FJI-H14) featuring high water stability, high density active sites with rare acid/base and high volumetric uptake of CO_2 (171 cm^3g^{-1}) at 298 K and 1 atm. In addition, it was easily being synthesized in a large quantity. FJI-H14 can efficiently converts CO_2 from the post combustion flue gas to the corresponding cyclic carbonates in ambient condition and remarkable selectivity of CO_2 over N_2. These activities were attributed to the synergetic effect of multiple high density active sites [151].

In a related study, two MOFs were synthesized that showed very promising thermal and solvent stability, high CO_2 uptake and excellent emission property [152]. They were basically Mg-based MOFs isomers with a molecular formula $[Mg_2(HCO_2)_2(NH_2\text{-}BDC)(DMF)_2]_n$ (NH_2-BDC = 2-amino-1,4-benzene dicarboxylate) constructed using a 6 connected metalla-crown SBUs, which resulted in 2D and 3D frameworks, due to different extended orientation of the SBUs.

A solvothermal reaction between Pb^{2+} and H_3L [(L=2-(pyridine-2-yl)-1H-imidazole-4,5-dicarboxylic acid] have generated three new 3D PCPs, $[Pb_2(L)_2]_n$; **1**, $[Pb_3(L)_3]_n$; **2** and $[Pb(L)]\cdot H_2O$; **3** see figure 2.9. The three MOFs offered numerous architectures influencing by utilizing various solvents; a multi-nodal 3,3,4,4-connected net for **1** and binodal 3,4- connected topological net with helices for **2**, while a uni-nodal 3-connected net had displayed by **3**, which possessed a micro pore that decorated with pyridyl and uncoordinated carboxylate oxygen atoms from the ligand. MOF **3** exhibited small size and highly polar pores, which attracted CO_2 strongly and led to a high sorption heat and significant selectivity for CO_2 over N_2 and H_2 at 293 K [133].

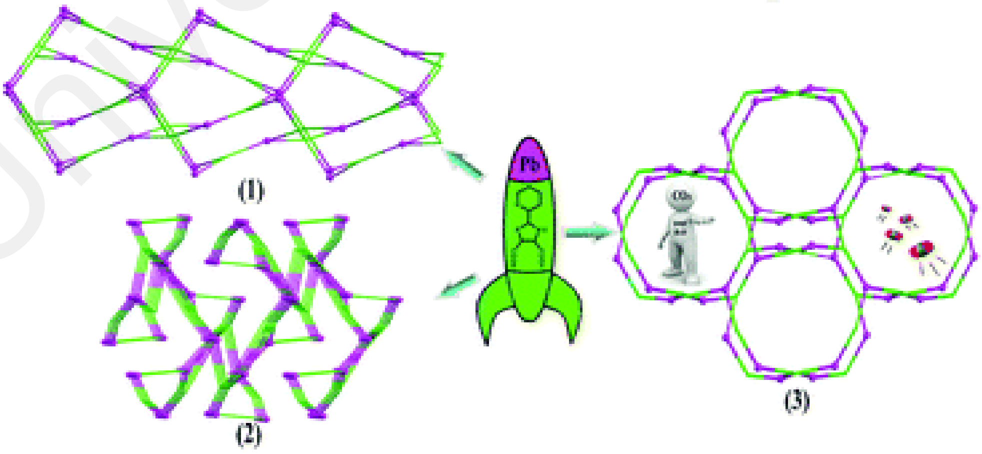

Figure 2.9: A multi-nodal 3,3,4,4-connected net (1), helices of binodal 3,4- connected net (2), and uni-nodal 3-connected net (3).

Recently, a series of highly porous MOFs have been built successfully using multi-functional linkers. For instance, a new MOF with NbO topology; Cu_2L (**ZJU-32**); H_4L = 5′-((3,5-dicarboxyphenyl) ethynyl)- [1,1′:3′,1″-terphenyl]-4,4″-dicarboxylic acid) was solvothermally synthesized using a tetra topic ligand. ZJU-32, see Figure 2.10, was found to exhibit a BET surface area of 3831 m^2 g^{-1} and pore volume of 1.482 cm^3 g^{-1} made it a very suitable material for CO_2 capture and CH_4 storage at the room temperature [153].

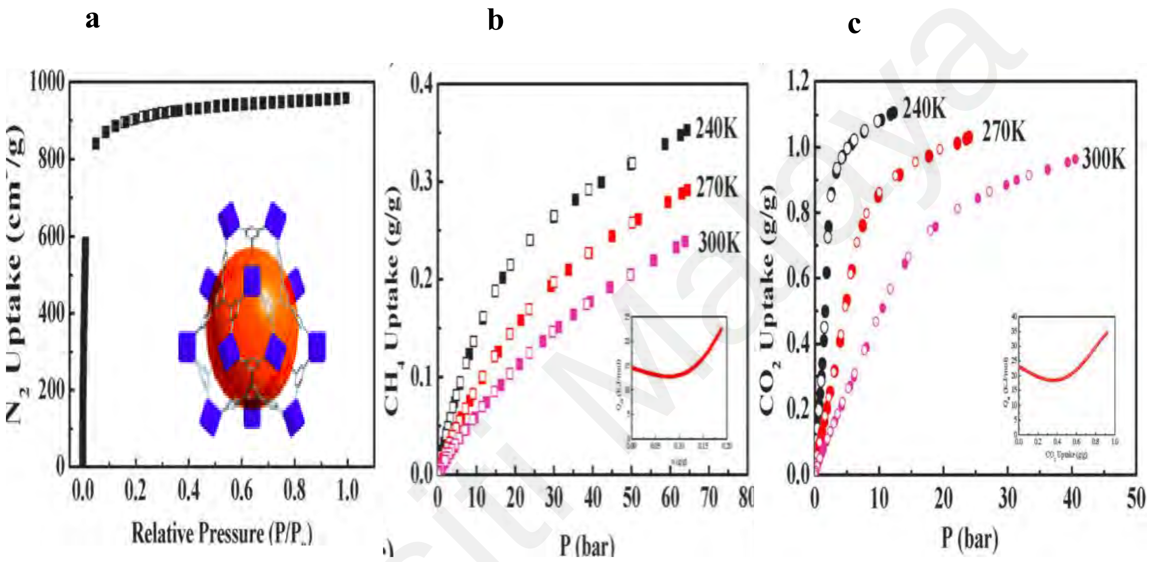

Figure 2.10: Gas adsorption isotherms of ZJU-32 for (a) N_2 at 77 K, (b) high-pressure methane at different temps (c) high-pressure CO_2 at different temperatures.

Walton and co-workers vote the IRMOF-1, Cu-BTC, IRMOF-3, and $Zn_2[bdc]_2[dabco]$ MOFs for comparison to understand the reciprocation of the factors (open metal sites, electrostatics, pore size, ligand functionalization, and heat of adsorption), which participate in CO_2, CO, and N_2 gases adsorption by MOFs using the atomistic grand canonical Monte Carlo simulations [154]. Discriminatory CO_2 was adsorbed over CO and N_2 in all these MOFs. CO_2 selectivity increased with increasing CO_2 concentration in the gas mixtures at a total pressure above 5 bar. The armature of the smaller pore size of MOFs, which included open metal sites or functionalized groups, can lead to greater reinforcement of these adsorption separation systems.

Two isomorphic MOFs, $[Co_2(4\text{-}Ptz)_2(BDC)(DMA)]_n$; **1** and $[Co_2(4\text{-}Ptz)_2(2\text{-}NH_2\text{-}BDC)(DMA)]n$; **2** [4-Ptz = 5-(4-Pyridyl)tetrazole, H_2BDC = Terephthalic Acid, DMA = N,N-dimethyl acetamide and $2\text{-}NH_2\text{-}H_2BDC$ = 2-Aminoterephthalic Acid,] have been successfully erected through solvothermal reactions [155]. The crystallographic data confirmed that a tetrazole ring of 4-Ptz ligand which interacted with oxygen atom of DMA and two bridged neighboring Co^{2+} has resulted in a binuclear Co^{2+} cluster for both **1** and **2**. Higher adsorption quantities for **2** (33.8 cm^3/g) than for **1** (26.2 cm^3/g) has proven by measuring of CO_2 adsorption isotherms at 273 K, which was assigned due to the presence of NH_2- functional group in **2**.

It is necessary to remove hydrogen sulfide (H_2S) in various industry applications, like syngas purification to avoid its toxicity and corrosion. The design of adsorbents which can bear the corrosion of H_2S and control the competitive adsorption from carbon dioxide (CO_2) is still a challenge. To achieve a steady adsorption mechanism and keep stability of MOFs during H_2S separation process, 11 MOFs based materials were utilized to capture H_2S from CO_2. Molecular dynamic studies, dynamic separation experiments and density functional theory were employed to inspect selective H_2S/CO_2 separation. Results showed that most of these MOFs displayed one-off high capacity and selectivity of H_2S, when disposable chemical reaction occurred on HKUST-1, Cu-BDC(ted), Zn-MOF-74, MIL-100(Fe) gel and MOF-5. A complete reversible physical adsorption was definite on Mg-MOF-74, MIL-101(Cr), UiO-66, ZIF-8 and Ce-BTC, and an incomplete reversible adsorption happened on UiO-66(NH_2).

2.5.2.2 The role of MOFs as a Catalyst

Two new porous coordination polymers based on cobalt, $[Co_6(oba)_5(OH)_2(H_2O)_2(DMF)_4.5DMF]$ (TMU-10) and $[Co_3(oba)_3(O)(Py)_{0.5}]_n$. 4DMF.Py (TMU-12) ($H_2$oba=4,4'-oxybisbenzoic acid), have been solvothermally synthesized using a nonlinear dicarboxylate linker [156]. Under mild reaction conditions (at atmospheric pressure and below 100°C), both MOFs exhibited good catalytic activity and reusability in oxidative desulfurization (ODS: an efficacious process that operates at mild reaction conditions and offers high sulfur removal efficiency). FTIR and mass analysis confirmed that the main product of dibenzothiophene (DBT) oxidation, which was prepared by dissolving DBT in n-hexane, was its corresponding sulfone that adsorbed on the surfaces of the catalysts, where the resulted activation energy was 13.4 kJmol^{-1}.

The architecture design of a MOF that can feature a high stability and reusable heterogeneous catalysts without losing performance remains a challenge. However, by adopting a modulated synthetic strategy, it was possible to build two new robust 3D porous metal-cyclam-based zirconium MOFs, VPI-100 (Cu) and VPI-100 (Ni) by Zhu et al (2018). These two frameworks are featuring eight-connected clusters of Zr_6 that connect to metallocyclams organic linkers. This linker has accessible axial coordination sites in the cyclam core which enabled the framework to interact with the guest molecules. Both MOFs displayed a vital chemical stability in numerous aqueous and organic solvents with different pH environments and offer a high CO_2 uptake capacity [157].

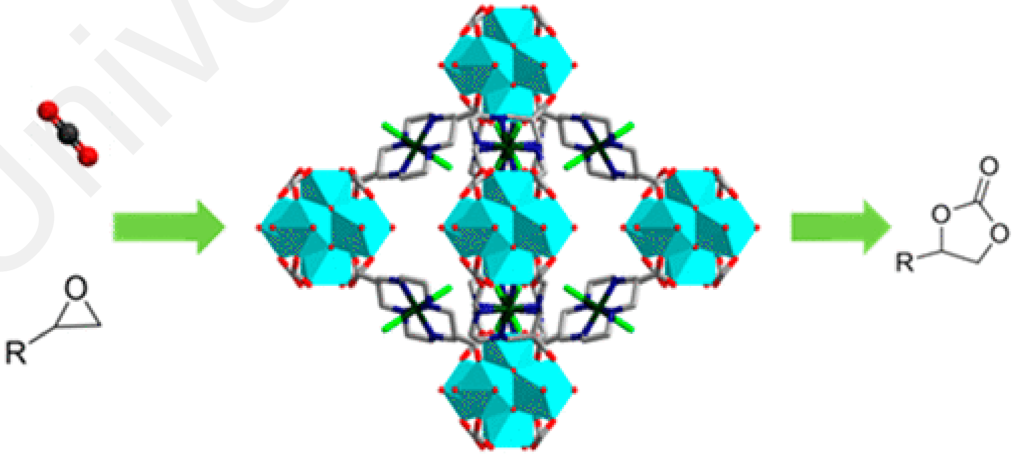

Figure 2.11: A porous metal- cyclam- based MOF that offer the highest catalytic activity values for the chemical fixation of CO_2 with epoxides [157].

2.5.2.3 The role of MOFs in removing the environment pollutants

According to World Health Organization, about one billion people do not have access to clean drinking water, a concern expected to be high with the climate change. Excessive use of heavy metals and higher energy by industrial processes have escalated the chances of human exposure to these pollutants [158]. Currently, there are various sources of exposure to these heavy metals [159]. For instance, lead (Pb) in particular has been an ingredient in many industries, such as ceramic glaze, paints, toys, jewelry and pipes [60, 61]. An increase in heavy metal pollution was also reported through improper industrial effluent disposals from industries, such as fertilizers, pesticides, tannery, dye and paint coatings, drugs, mining fossil fuel processes, electronics and battery manufacturing [160]. Heavy metals such as mercury, lead, cadmium, cobalt, copper, chromium, zinc, … etc, exhibit toxic effect and have relatively high density and of environmental concern due to their detrimental effects. Generally, these metals are non-biodegradable and need to be efficiently remove from the environment especially the water [161]. Scientist deployed considerable efforts to hit this problem using various methods, amongst which, adsorption technique was the most extensively used due to its low cost and easy to handle [162].

Recently, Zhong and coworkers (2018) had developed a tap with a broad- spetrum for heavy metal capture by slotting the EDTA (ethylenediaminetetraacetic acid) inside a robust MOF structure. This trap is very effective, that it can captured various kinds of heavy metal ions, with high efficiency >99%, including the soft, hard and also the borderline Lewis metal ions via the breakthrough or the adsorption processes. This trap can be a platform candidate for removal and/or separation of versatile heavy metals or for catalysis applications [163].

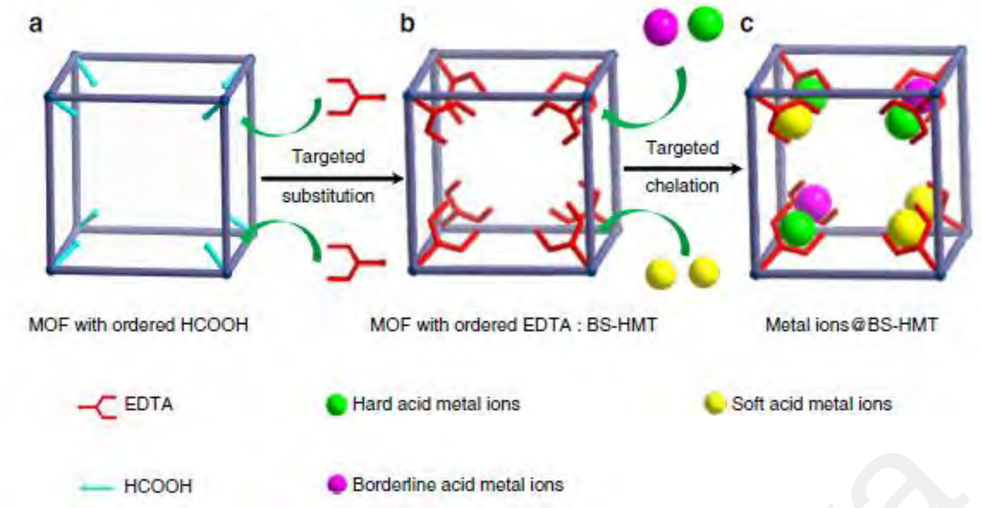

Figure 2.12: Schematic illustration of the BS-HMT concept [163].

Wendy Queen's group (2018) used a water stable MOF built with biologically and environmentally friendly materials by pining the dopamine on the internal surface of Fe-BTC MOF. The dopamine can spontaneously polymerize to polydopamine through the pores by Fe^{3+} open site of this MOF. It was demonstrated that the material can remove heavy metals from water in seconds and render it safe for drinking. It displayed an efficient removal of heavy metals compared to other materials to date, where it removed mercury more than 1.6 times its weight and lead 40 percent of its weight [164].

Dyes and toxic materials removal by adsorption technologies, such as removal of iodine or aniline from contaminated water, is one of the competitive methods in industry because of simplicity and high efficiency of this operation [165]. The hydration and dehydration of new porous 3D CPs based on lead, observed a reversible crystal to crystal transformation from $[Pb(4\text{-}bpdh)(NO_3)_2]n$ ($HMTI^{-2}$) to $[Pb(4\text{-}bpdh)(NO_3)_2(H_2O)]n$ ($HMTI^{-1}$). These MOFs, which have the same crystalline lattice, was synthesized by hydration and dehydration reaction via combining Pb^{2+} ions with 2,5-bis(4-pyridyl)-3,4-diaza-2,4-hexadiene (4-bpdh) as a linker. Morsali's group (2012) were successfully loaded $HMTI^{-2}$ and $HMTI^{-1}$ with I_2 and determined I_2 delivery by UV-vis spectroscopy. They observed from the adsorption and desorption rate of iodide in these two MOFs that the presence of H_2O molecules had an effective role in increasing of iodine adsorption in $HMTI^{-1}$ [166].

An increasing concern on the release of toxic chemicals from different manufacturing industries such as rubber, dye, paint, pesticides and many more. Such chemicals like aniline, though very important intermediate and widely used in these industries, its discharge into the environment, even at low concentration can be very dangerous may result into health related issues such as anemia, liver damage or skin cancer [167]. It is imperative to device efficient and effective technique that can detect and monitor aniline directly using naked eyes. This may help in avoiding the adverse effects on the environment and therefore human health. In light of this, MOFs were considered as a preferred candidate due to their high visible emission and long emission lifetimes. Vast number of MOFs were exploited for various application for the detection, capturing and sequestration of various environmental pollutants, however, MOFs based sensors for aniline detection are still very rare [168].

In a recent report, two lanthanide based isostructural MOFs were shown to exhibit and outstanding stability in solvents and efficient aniline sensing (Eu-based MOF), based on the analysis of the photoluminescence emissions. This MOF can be reused up to four times making it very promising detector for aniline. The two isostructural MOFs $[(Ln(BTB)(H_2O)]_n$ (Ln = Eu and Dy) were constructed using try topic ligand 1,3,5-benzenetribenzoic acid (H_3BTB). Following the characterization, it reveals that, two lanthanide ions are bridged from four carboxylic group oxygens of different BTB ligands forming a binuclear SBUs. The SBUs extends in one dimensional chain via two bridging carboxylic groups that are subsequently linked by BTB^{3-} to generate the three periodic networks [165]. Furthermore, the Dy-based MOF show excellent slow magnetic relaxation behaviors with the energy barrier of 9.36 K.

Iron, cobalt and copper as central metal ions in MOFs based on 1,2,4,5-tetrabenzene carboxylic acid as a linker, was successfully synthesized by Shooto and coworkers (2015 & 2017). The new MOFs, which offered the creating of charges and functionalities on MOFs surface for adsorption, have been characterized by FTIR, TGA, x-ray diffraction and SEM/EDX techniques. The thermodynamic and kinetic studies, equilibrium and isotherm batch adsorption experiments were carried out to determine concentration, temperature and time effects. These MOFs have been employed as adsorbent for lead ions removal from aqueous solution. Results showed a remarkable fast adsorption affinity of Pb^{2+} by all MOFs, in which, Cu-MOF was more effective adsorbent than Co-MOF [169, 170].

In another study on dye adsorption properties, three new cobalt based coordination complexes i.e. $\{[Co(tib)_2].2HNO_3.2H_2O\}_n$, $\{[Co(tib)(4,4'\text{-dpt})(H_2O)_2].5H_2O\}_n$, and $\{[Co_2(tib)_2(1,3\text{-dpt})_2].H_2O\}_n$ (tib = 1,3,5-tri(1-imidazolyl)-benzene, 4,4'-dpt = p-terphenyl -4,4'-dicarboxylate and 1,3-dpb = 1,3-di(4-carboxyl-phenyl)benzene), constructed using hydro/solvothermal technique. The first structure featured a rare two-dimensional **kgd** network which was further connected by hydrogen bonds and C-H---O bonds to form 3D network. While the second structure featured **hcb** 2D structure, which was further linked by H-bs to assemble into a 3D supramolecular network. However, the third structure showed rather a novel 3 nodal (3,4,6)-connected 3D network. The study on dyes (GR and MGO) adsorption capability showed that the first and second frameworks were efficiently and selectively adsorbed GR and MGO dyes while the third framework was selectively adsorbed MGO [171].

2.5.2.4 The role of MOFs in drug delivery

The highly unprecedented porosity feature, surface modification, some unique chemical and physical characteristics, chemical composition, biological stability, high drug loading capacity, encapsulation efficiency, biodegradability, toxicological compatibility, and versatile functionality of many MOFs make them potential as a promising platform in medical and biomedical applications, such as drug storage, delivery, release and encapsulation, nitric oxide gas storage and delivery, imaging, and sensing [172].

The MOFs might also consist of biologically active moieties in their framework structure which can be released via distraction/or degradation of the MOF framework, during therapeutic process. Therefore, Horcajada and coworkers had overviewed the drug administration routes and the controlled drug carriers in pharmaceutical technology. They had also introduced the formulation, synthesis, stability, toxicity and bio-applications of MOFs, then analyzed the efficiency of MOFs, in vitro and in vivo [173], Scheme 2.3.

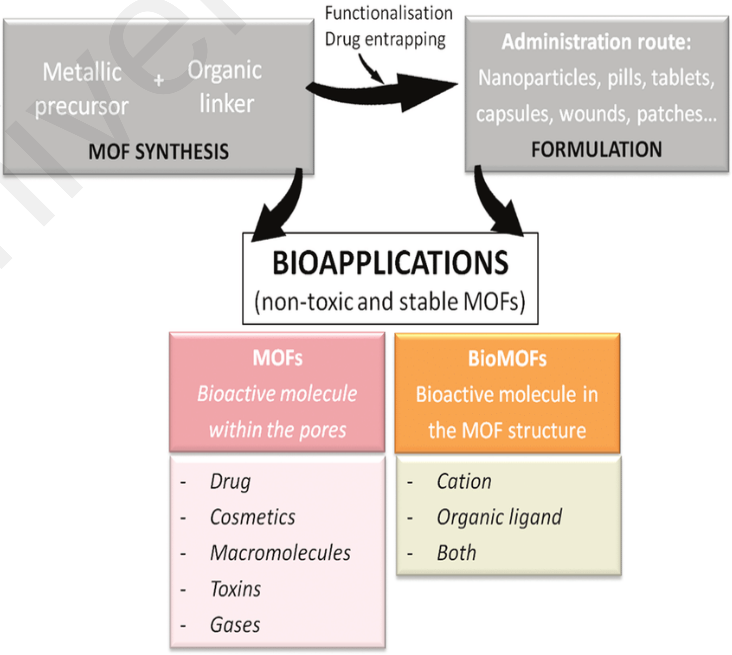

Scheme 2.3: The MOF manufacturing process for bio-applications.

Morris' group described how triggered release methods in Co, Ni and Cu-based MOFs can be employed to deliver relevant amounts of NO (as a therapeutic agent) and they displayed the biological activity potential applications in several different areas, such as anti-thrombosis, dermatology and wound healing, anti-bacterial, and vasodilation [174]. Considering the non-toxicity of most MOFs and their excellent properties in release and encapsulation drugs efficiencies, they have recently been introduced in biomedicine applications [126].

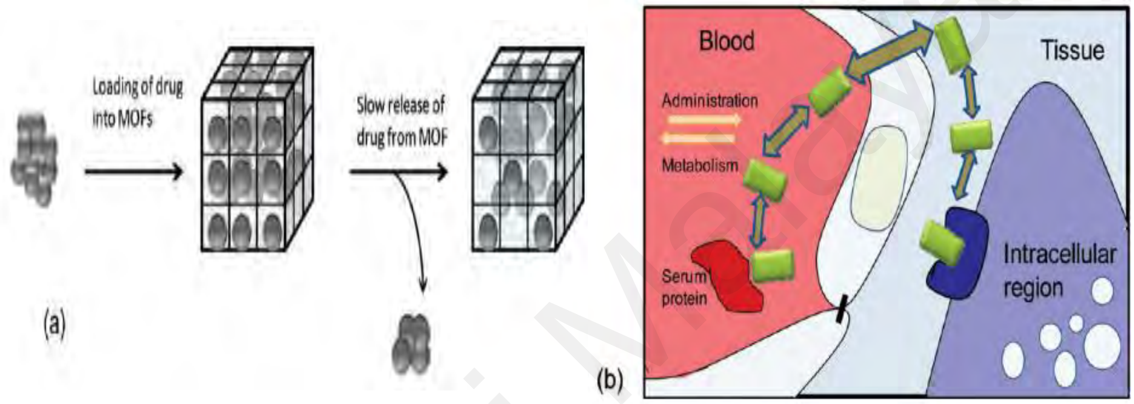

Scheme 2.4: (a) General scheme for using of MOFs as drug delivery vehicles. (b) In vivo conditions involved in the slow releasing of drugs [172].

2.5.3 The photoluminescence phenomenon

Luminescence, defined as a soft, glowing light that does not derive energy from the temperature of the emitting body or as emission of light by a substance not resulting from heat [175]. It is a form of cold-body radiation caused by jumping of material's electrons from their origin level (ground state) to a higher energy level (excited state) when absorbing energy from some sources. The excited electrons are dropped down from the excited state to the ground state and emitted an energy they had previously absorbed as a light [176].

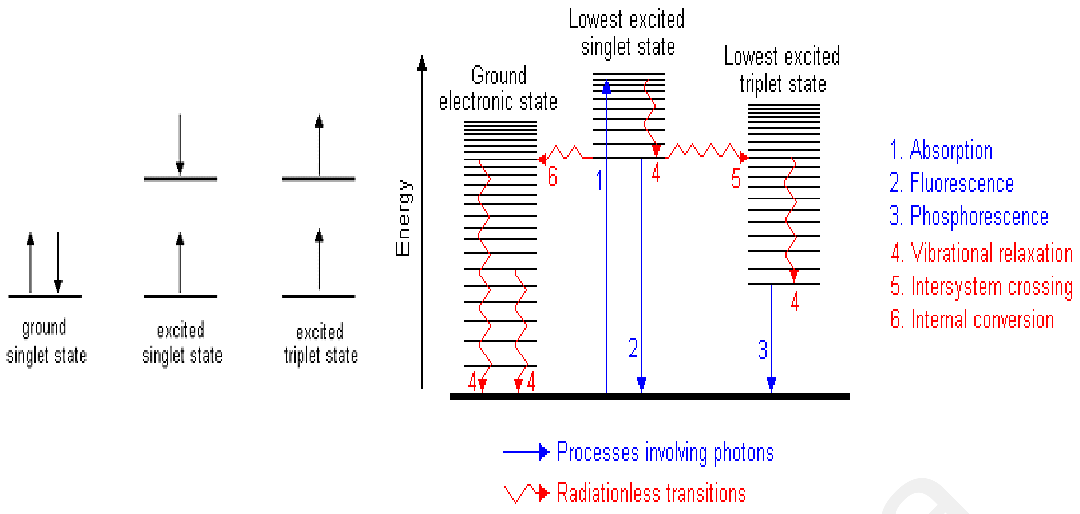

Figure 2.13: The possible physical process of absorption of a photon by a molecule. In the Singlet state: All electrons in the molecule are spin-paired, while in the Triplet state: One set of electron spins is unpaired.

Luminescence can be caused by photoexcitation process, such as chemical reactions, electrical energy, subatomic motions or stress on a crystal, which all are ultimately caused by spontaneous emission. Luminescence is divided into two categories, fluorescence and phosphorescence. The fluorescence is a rapid process that defined as luminescence, which stops within 10 nanoseconds after an energy source has been removed, while the phosphorescence is a slow process that defined as luminescence, which continues for more than nanoseconds after an energy source has been removed [7, 28].

2.5.3.1 The photoluminescence phenomenon in MOFs

Luminescence is a common property in many MOFs because of the multifaceted nature of their structure, i.e. almost the MOFs structures incorporate luminescent lanthanide ions or contain aromatic groups of a conjugated linker that is readily fluoresce (chromophoric) [31, 177]. The organic chromophoric ligands usually absorb the light and excited, then transfer this excitation energy to the metal ions in a process called Ligand to Metal Charge Transfer (LMCT); in which, the electronic transition in the excitation state in a metal complex are populating the electronic state, where electron transfer from a ligand to metal center has occurred. In contrast, there is a Metal to Ligand Charge Transfer (MLCT) process (whereas, the electronic transition in a metal complex are populating an electronic state in which considerable electron transfer from a metal to ligand has occurred) [178].

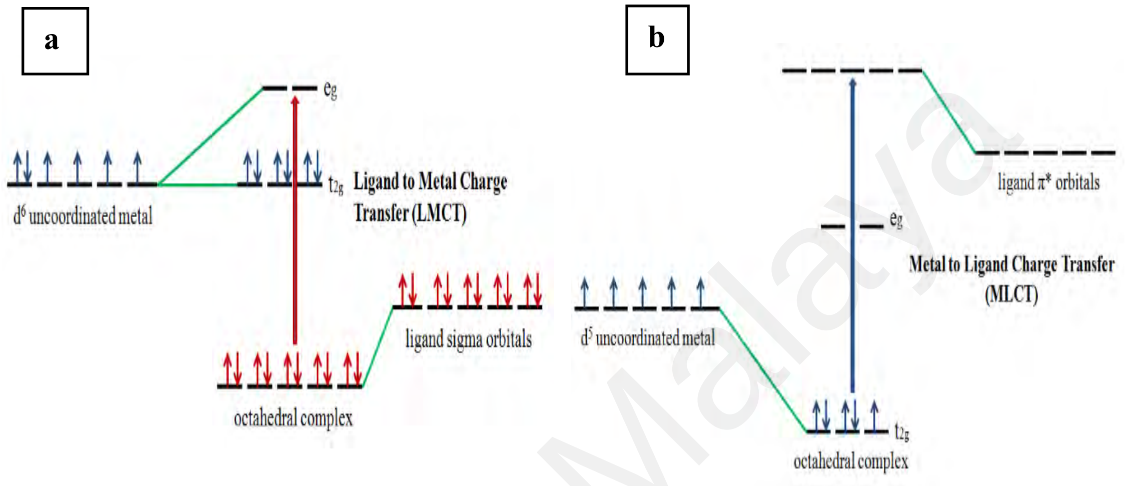

Figure 2.14: a) LMCT involving an octahedral d^6 complex, b) MLCT involving an octahedral d^5 complex.

Two photo luminescent MOFs based on Lead; 3D anhydrous MOF $[\mathrm{Pb(fum)}]_n$ (**1**) and 3D hydrous MOF $\{[\mathrm{Pb_2(fum)_2(H_2O)_4}]\cdot 2\mathrm{H_2O}\}_n$ (**2**); (fum= fumarate), were synthesized by the reaction of the fum anions with the Pb^{2+} cations in the presence of pyrazine and pyrazole, respectively.

The fum ligands in **1** arranged to offer six- coordinated bonds around the lead atom and displays a hemidirected geometry, while the fum ligands' arrangement in **2** exhibits a coordination gap around the atom of metal center which occupied by the stereoactive lone pair electrons on Pb^{2+} and displays eight-coordinated bonds, see Figure 2.15. These MOFs were characterized by solid-state photoluminescence spectra which exhibit a maximum emission photoluminescence that located in UV region [179].

Figure 2.15: a) The octa-coordination environment of Pb(II) by fumarate ligands in 2, b) the polyhedral representation of PbO_8 in 2. c) the Hexa-coordination environment of Pb(II) by fumarate ligands in 1, d) the polyhedral representation of PbO_6 in 1.

A self-assembly of 4,4'-biphenyl dicarboxylic acid (4,4'-H_2BPDC) and $Pb(NO_3)_2$ under solvothermal reaction has produced a new 3D pillared MOF, which has been characterized by IR spectroscopy, element analysis, TGA and SCXRD. The SCXRD results showed that the Pb^{2+} connected to six oxygen atoms from carboxylate groups in the ligand to obtain metal-carboxylate layers connected by (4,4'-BPDC) linkers that act as pillars to offer a novel 3D pillared framework and displayed a rare μ_6 coordination mode. This 3D pillared MOF has a high thermally stable structure and showed blue photoluminescence at room temperature in the solid state [180].

Terephthalic acid (TA) and nitro terephthalic acid (NO_2TA) have been reacted with Bismuth nitrate hydrothermally to produce two new 3D bismuth-based CPs consist of Bi_2O_2 layers and Bi_4O_3 chains, respectively. The bridge ligand (TA) has linked Bi_2O_2 layers to form Bi_2O_2(TA), **1**, which showed red-shifted photoluminescence comparing with that of (TA). Whilst, (NO_2TA) bridge ligand has connected Bi_4O_3 chains to offer a novel compound $Bi_4O_3(NO_2TA)_3(H_2O).(H_2O)_{0.68}$, **2**, which quenched the photoluminescence [38], Figure 2.16.

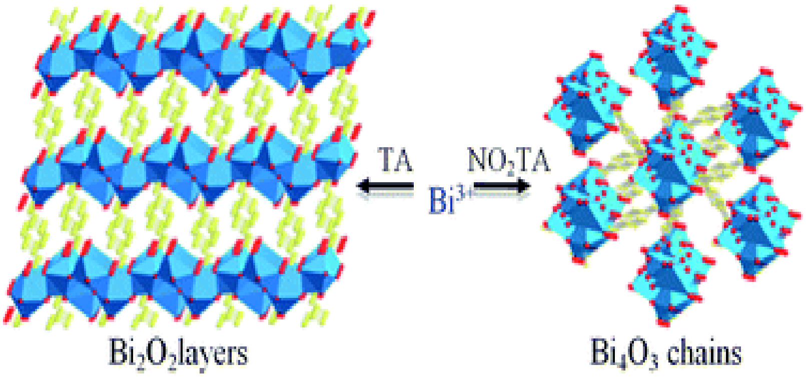

Figure 2.16: The Bi_2O_2 layers and Bi_4O_3 chains that formed by changing the bridge liker [38].

A rare Bi-fluorophore luminescent MOF (LMOF-401) has been synthesized by interaction between 9-coordinated Bi^{3+} cations and H_2tcbpe (H_2tcbpe=4’,4’’,4’’’,4’’’’-ethene- 1,1’,2,2’-tetrayl) tetrakis (1,1’-biphenyl-4-carboxylic acid) linker which had a strong yellow aggregation induced emission (AIE). LMOF-401, featuring strong blue emission that converted to green then to yellow upon DMF solvent molecules removal within the structure. The activated MOF promises to be a candidate as phosphor coating in phosphor converted white light emitting diodes (PC-WLEDs) because it displays strong yellow emission with quantum yield (~74%) under the blue light excitation [181].

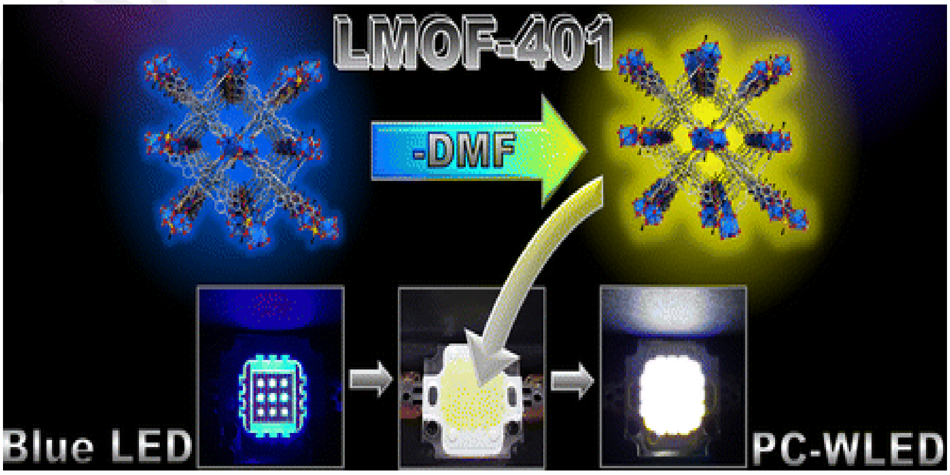

Figure 2.17: A Bi-fluorophore luminescent MOF [181].

A novel 3D MOF which exhibited (Pb_6O_2) clusters as SBUs was prepared when Pb^{2+} cations as metal centre reacted with 4,4’-dicarboxy-2,2’-dimethoxy-1,1’-biphenyl (LH_2) as a linker in a mixture of solvents H_2O/EtOH (10:2) at pH 4 in the presence of triethyl amine and 2,2’-bipyridine. An emission and excitation properties observed with the luminescence spectra of this network (which was similar to the spectra of ligand) that can be attributed to the linker (LH_2) only, but not to the metal. There was a little blue shifting of λ_{max} in the MOF luminescence spectra (due to linker interaction with the cluster or with the polar organic EtOH solvent molecules) that in turn made this MOF be a promising candidate as a sensor for different organic solvents [182].

MOFs have also some scintillation properties which caused luminescence when excited by ionization radiations. In this example, a Zr and Hf-based MOFs $M_6(\mu_3\text{-}O)_4(\mu_3\text{-}OH)_4(\text{carboxylate})_{12}$ (M = Hf or Zr) using anthracene dicarboxylate linker to form the SBUs, which was found to have an excellent and effective X-ray antenna due to Zr and Hf large atomic number that served as an efficient to a visible light luminescence property. The mechanism depended on the absorption of x-ray photons by the SBUs and subsequently converted them to fast moving electrons by photo-electric effect. The generated electrons then excited multiple anthracene-based emitters in the MOF through inelastic scattering, leading to efficient generation of detectable photons in the visible spectrum. The MOF materials thus served as an efficient X-ray scintillators via synergistic X-ray absorption by the metal cluster SBUs and optical emission by the bridging ligands [183].

Koppen and coworkers conducted a high throughput experiment by using triazine-2,4,6-triyl-tribenzoic acid (H_3TATB) and bismuth nitrate and investigated two Bi-based MOFs. Both structures were isolated by changing the solvent composition and the reaction time. The solvent mixture of water/DMF over 5 days formed the CAU-35 MOF;

$[Bi_2(O)(OH)(TATB)].H_2O$, Figure 2.18a. Whilst, the solvent mixture of methanol/DMF and shorter the time of synthesizing afforded the CAU-7-TATB MOF; $[Bi(TATB)].DMF.6H_2O$, Figure 2.18b. On the other hand, using an amino functionalized H_3TATB ligand, and cyclic anhydrides (phthalic and succinic anhydride), anhydrides (valeric and acetic anhydrides) and 1,3-propane sultone resulted a functionalized porous Bi-based MOF $[Bi(TATB\text{-}NH_2)].5H_2O.0.5DMF$ via post synthetic modification. The conversion efficiency ranged between 33 % to 79 % REF [184].

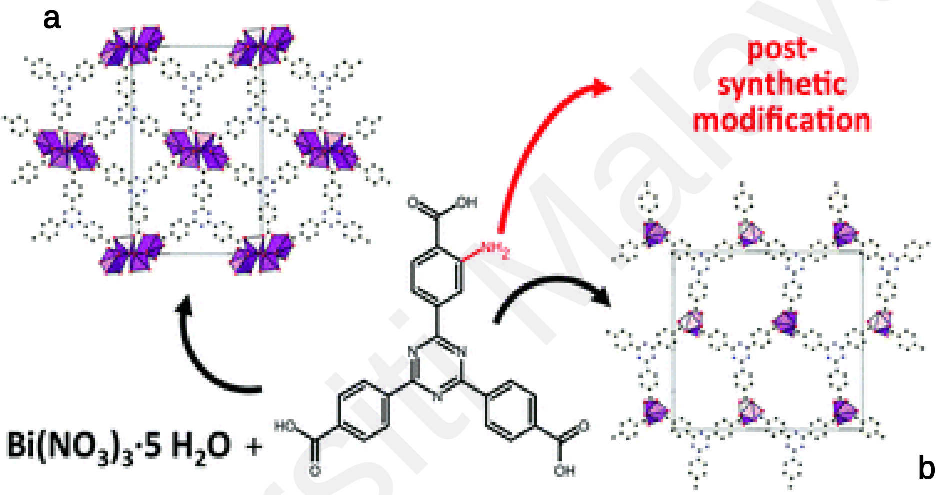

Figure 2.18: a) The crystal structure of CAU-35, b) the crystal structure of CAU-7-TATB.

Casado's group (2012) were successfully synthesized two new lead(II) butyrate compounds $[Pb_2(but)_4(4,4'\text{-bipy})(H_2O)]_n$(1) and $[Pb_2(but)_4(bpe)(H_2O)]_n$ (2) using (4,4′-*bipy* and *bpe*) as N bridging ligands [*but* = butyrate; 4,4′-*bipy* = 4,4′-bipyridine and *bpe*= 1,2-bis(4-pyridyl)ethene]. Results showed various 3D structures from 2D lamellar for most of metal alkanoates and enhancing the properties of the synthesized composites [185]. The new compounds had characterized using UV-visible spectroscopy, differential scanning calorimetry, thermogravimetric analysis, steady-state fluorescence, lifetime measurements and single crystal x-ray diffraction which confirmed that both MOFs showed a similar 3D ($4^2 6^3 8$)-**sra** network in a monoclinic lattice ($C2/c$) with interesting photo-physical properties.

Aggregation induced emission (AIE) involved a deliberate engineering and manipulation of fluorescence emission in materials. For example, a study was conducted using a hydroxyl functionalized ligand, the resulted MOFs featured AIE, where the emission can be tuned intentionally. This MOF can be turned “on” and “off” up on the removal or addition of 4,4'-bypyridine in the framework. Herein, the incorporating of this heterocyclic auxiliary ligand caused quenching of the emission (turn off), while its removal triggered the emission (turn on). The group workers revealed that by using the time-dependent DFT studies, the origin of the emission quenching was due to the occurrence of the excitation transference between AIE ligand and the conjugated 4,4'-bypyridine ligand. This MOF was successfully applied as an “on”-“off” sensing probe for Al^{3+} detection in aqueous media. The sensing mechanism involved hydroxyl group played a vital role for selectively chelating Al^{3+} [186].

Main group, p-block based MOFs has also been successfully engineered and reported to have very interesting emissions for solid state lighting applications. The multi topic linker pyridine-2,5-dicarboxylic acid (Hpydc) has been employed to react hydrothermally with bismuth nitrate and/or lead nitrate to obtain a 2D (CP) based on bismuth $Bi_3(pydc)_2(Hpydc)(H_2O)_2$; **1** and 3D (CP) based on lead $Pb(pydc)(H_2O)$; **2**, respectively. The structures of these CPs have been confirmed by SCXRD which assured that the bismuth-based polymers crystallized with $P2_{1/c}$ space group and the Bi_6O_4 clusters in **1** were connected by bridging ligands into 2D sheets. This offered a 3D supramolecular structure via hydrogen bonding along z-axis. On the other hand, the lead-based polymer crystallized with $P1$ space group and a 1D chains of corner-sharing distorted face capped trigonal prisms of **2** were linked into 3D framework by (pydc) ligand. Both CPs displayed a white photoluminescence that extended to display a wide spectral range comparing with the ligand spectra and attractive luminescence materials for solid state lighting applications [37].

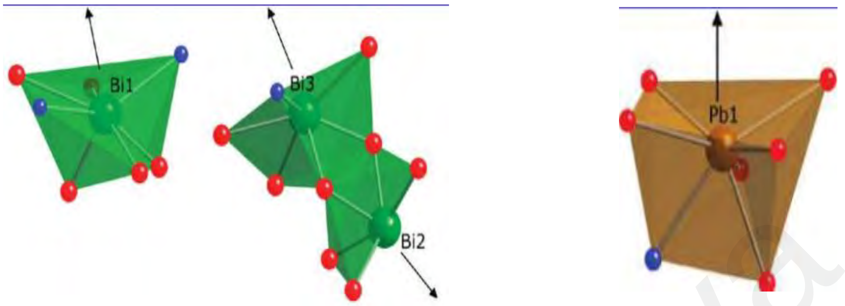

Figure 2.19: The stereochemically active lone pair formation of the compounds, the arrow shows the approximate location of lone pair electrons.

Wang and co-workers (2015) were synthesized a novel topology MOF based on bismuth ([Bi(BTC)(DMF)].DMF.$(CH_3OH)_2$,Bi-BTC) using a solvothermal reaction. Single crystal x-ray diffraction confirmed that Bi-BTC presented a novel 3D framework erected by {Bi_2O_{14}} SBUs which regularly assembled and connected to trimesic acid (H_3BTC) and crystallized in $P2_1/n$ space group to form two helix chains. The photo-physical properties of Bi-BTC MOF have been studied and showed high activity of O_2 production as photo-catalysis [8].

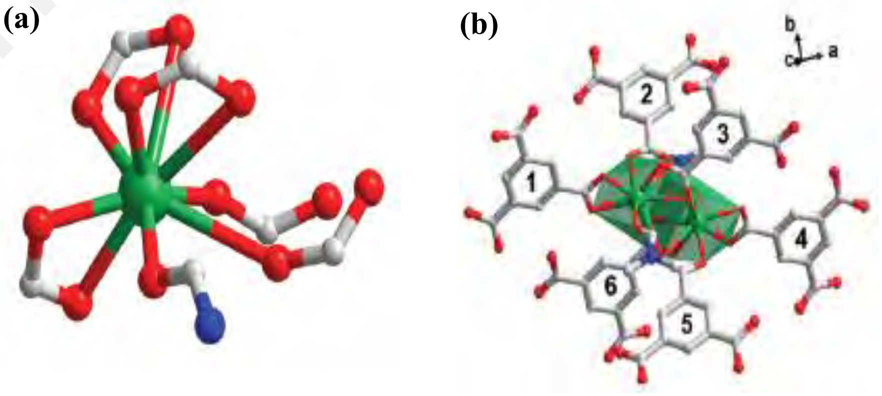

Figure 2.20: The Coordination Environment of (a) Bi^{3+} cations, b) polyhedral view of the centrosymmetric dimeric {Bi_2O_{14}} unit and the linked six BTC^{3-} molecules.

The combination of Zn^{2+} ions and the 1,3,5- benzene tricarboxylic acid (H_3BTC) under a solvothermal condition produced a new 3D trinodal (3,5,6)-c framework based on Zn with two different kinds of cluster nodes Zn_3O and Zn_4O, $[Zn_{21}(BTC)_{11}(\mu_3\text{-}OH)_3(\mu_4\text{-}O)_3(H_2O)_{18}].21EtOH$ (**1**). The SCXRD measurements confirmed that this MOF displayed a large octahedral cage, which resulted from a connection of nine Zn_3O and nine of Zn_4O nodes of SBUs with twenty- four triangular BTC linkers. The incorporation of Eu^{3+}/Tb^{3+} cations produced a new derivative of **1** with 0.251% Eu^{3+} and 0.269% Tb^{3+}, respectively. By changing the excitation wavelength from 308 to 315 nm it was possible to display a tunable luminescence from yellow to white and then to blue green. Besides, this MOF can consider as a selective luminescent sensor for Al^{3+} and Cu^{2+} cations. Moreover, an isomorphous Cu-based MOF, which offered a good adsorption capacity of CO_2 and N_2 gases can be produced from the metal ion exchange of this MOF with Cu^{2+} cation [101].

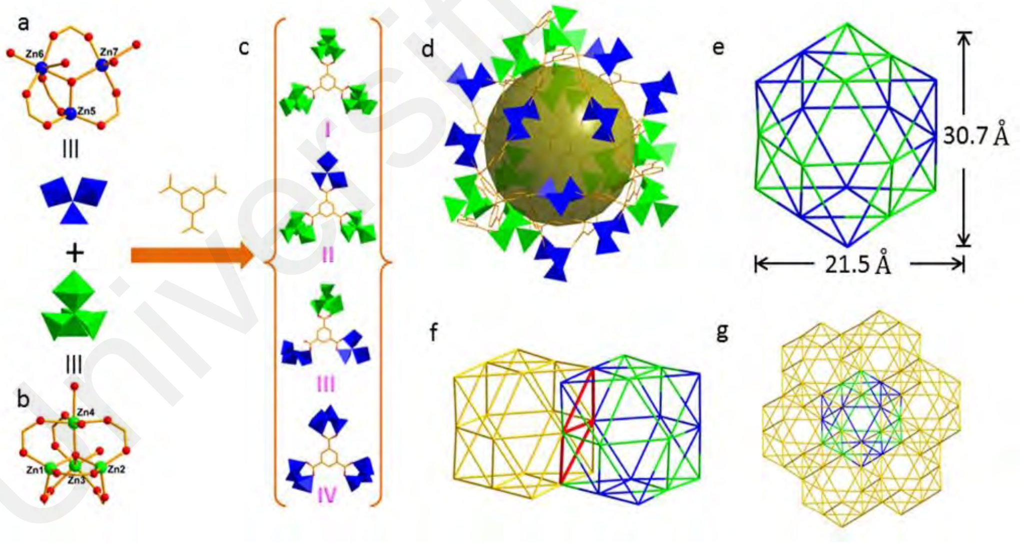

Figure 2.21: **a) Zn_3O SBU, b) Zn_4O SBU, c) linking modes of BTC^{3-} ligand, d) octahedral cage constructed by Zn_3O and Zn_4O cluster nodes and BTC^{3-} linkers, e) octahedral cage by connecting Zn_3O and Zn_4O cluster nodes, f) Two octahedral cages are connected by sharing two edge-fused triangles, g) one octahedral cage surrounded by six identical cages.**

2.5.4 Structure Transformation (breathing behavior)

A subclass of MOFs undergoes a “breathing” phenomenon, which is a reversible flexing of the framework as a function of adsorbed guest. Besides the evident application of selective gas adsorption, breathing MOFs have also been utilized in applications such as chemical sensing and hazardous waste adsorption. Through gas adsorption/desorption processes, it became possible to synthesis many MOFs that can dynamically change in structure and offer identical changes in potential porosity that represent adsorption induced reversible structural transformations between large/wide-pore and small/narrow pore conformations in bistable frame systems. These MOFs have the ability to switch between both open and close (or wide and narrow) pore states upon gases and/or solvents adsorption that stimulates a design of multifunctional host materials. This design combines the large surface areas with periodic and flexible frameworks in the gas storage for a renewable energy [187- 189].

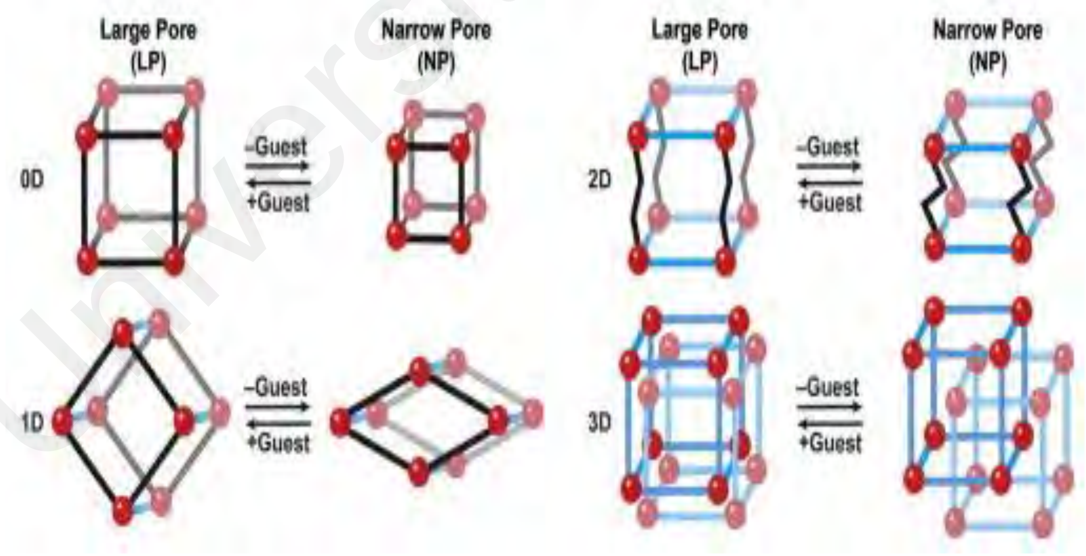

Figure 2.22: The breathing phenomena in some MOFs [129].

The design of flexible MOFs can be done by the judicious selection of organic linkers and/or the metal ions that can control the pores shape and sizes in a flexible manner. Barbour's group (2018) have been designed a Zn(II)-MOF (**1**) which displayed special three-steps different breathing behaviors, Figure 2.23. Pressure-gradient differential scanning calorimetry (DSC), variable pressure PXRD and in situ single crystal x-ray diffraction (SCXRD) analyses were employed to explain these numerous porous forms of structure transferring using an environmental ethane gas cell pressure at the ambient temperature [190].

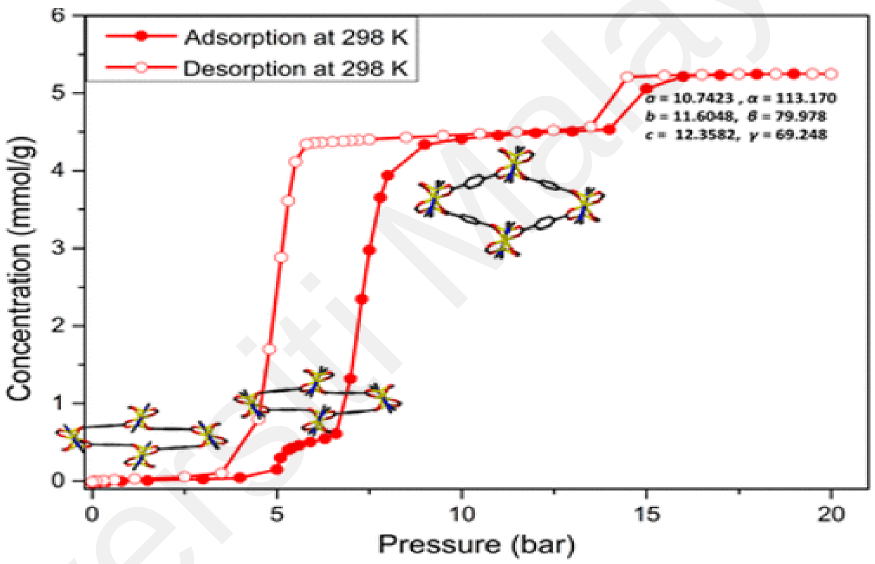

Figure 2.23: The three-step hysteretic breathing behavior under ethane gas pressure at ambient temperatures [190].

Most breathing MOFs which considered as an emerging class of soft porous crystals (SPCs), however, they have low surface area and/or low stability, unfortunately. Farha and co-workers (2015) were introduced a water-stable breathing MOF with a high surface area featuring **ftw** topology (NU-1105) [191]. The presence of fluorene units in FP arms of pyrene-tetracarboxylate (Py-FP) ligand offered significant potential properties, i.e. high surface area and played a key role in the promoting breathing behavior. Whereas, Zr$_6$-oxo clusters exhibited water stability. The closed pore (cp) ↔ open pore (op) transition of NU-1105 was tracked using in situ powder x-ray diffraction during propane sorption at ~3 bar pressure. Result affirmed that NU-1105 in (cp) mode at 1 bar has adsorbed less propane than in (op) mode, Figure 2.24.

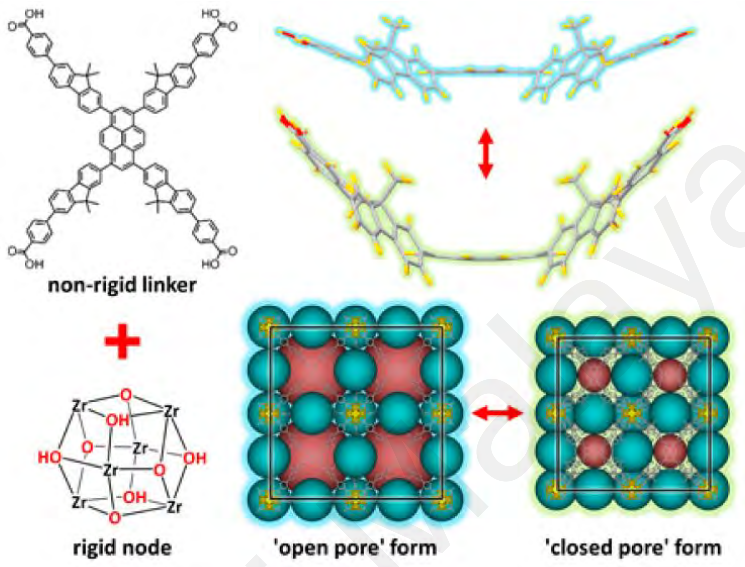

Figure 2.24: The open pore (op) & the closed pore (cp) modes in "Breathing" MOF (NU-1105) which display ftw topology.

2.6 Introduction about the ligands that used in this study

The various coordination modes of H$_2$Pzdc ligand can be generated by the five donor atoms of this linker and ranged from bidentate chelating passion (a/c= μ_2: η^1, η^2), b=μ_2: η^2, η^2, tridentate (d/e/f= μ_3: η^1, η^1, η^2, g=μ_3: η^1, η^1, η^1), which represented in Scheme 2.5, to multi-dentate chelating bridging passion (h= μ_4: η^1, η^2, η^2, η^2, i/k=μ_4: η^1, η^1, η^2, η^2, j=μ_4: η^1, η^1, η^1, η^2, l/m=μ_4: η^1, η^2, η^2, η^2, n=μ_5: η^1, η^1, η^1, η^1, η^2, o= μ_5: η^1, η^2, η^2, η^2, η^2,), or bridging passion (p= μ_7: η^1, η^1, η^1, η^1, η^1, η^1, η^1) [192, 193], which represented in Scheme 2.6:

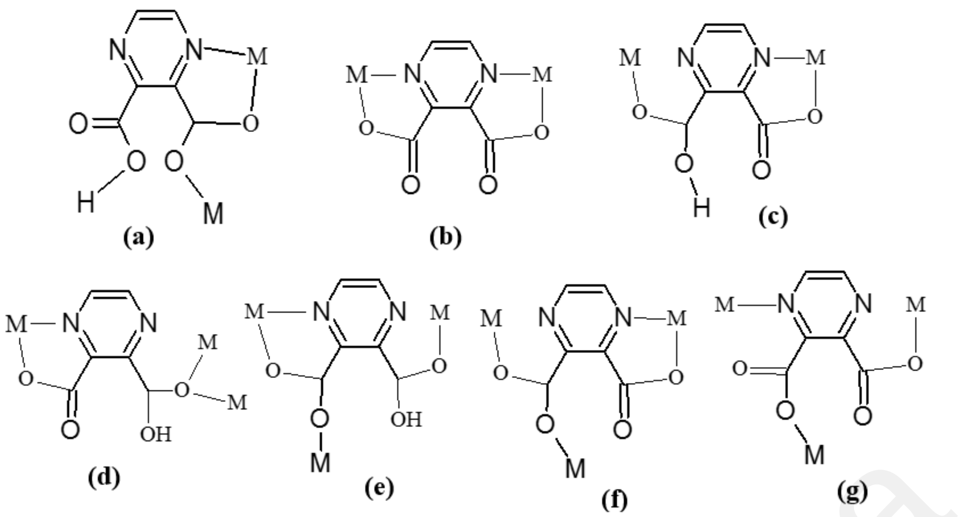

Scheme 2.5: 2,3-pyrazine dicarboxylic acid (H_2pzdc) with 3 or 4 donor atoms that exhibit 7 different coordination modes [192, 193].

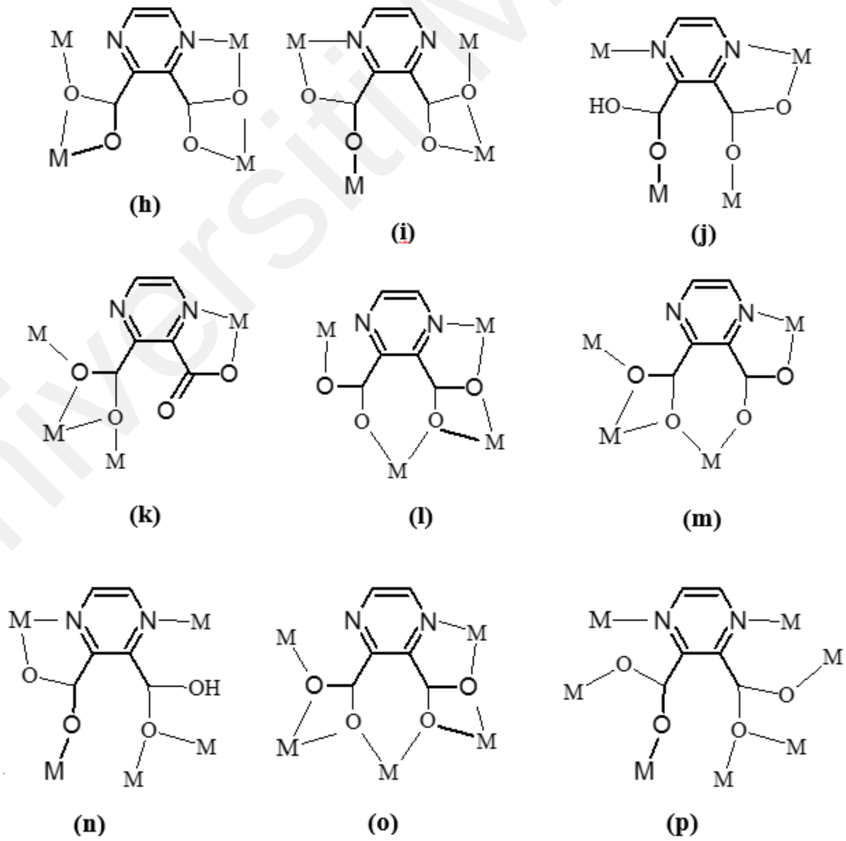

Scheme 2.6: H_2pzdc with 5 or 6 donor atoms that exhibit different 9 coordination modes.

Recently, a novel coordination mode of H_2Pzdc, which is monodentate (μ_1: η^1) has been synthesized by Mutlu group [194]. These sixteen coordination modes (a-p) can form mono/dinuclear or polymeric materials with p, d-block and even f-block metals ions. H_2Pzdc ligand, with or without co-ligand, is one of the most frequently used ligands to construct MOFs and/ or CPs, including catalytic properties of MOFs [195], photo luminescent CPs [196, 197], photonics applications of MOFs [197], MOFs hysteretic CO_2 adsorption [198], … etc.

Conversely, H_3BTC with its partially or fully deprotonated anions (H_2BTC^-, $HBTC^{2-}$ and BTC^{3-}) exhibit multi donor sites that enable it to offer 3 to 6 donor atoms with different coordination modes, Scheme 2.7:

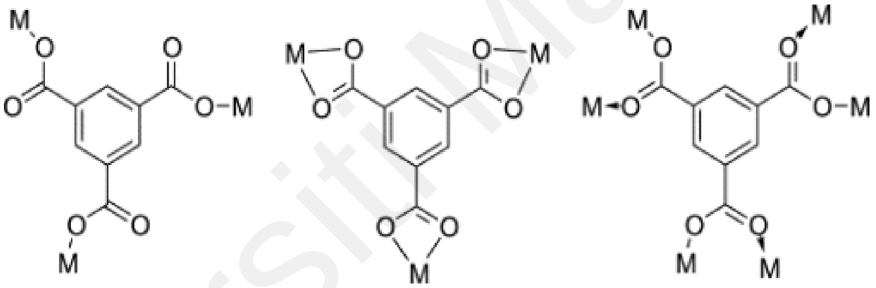

Scheme 2.7: The coordination modes expected for Benzene 1,3,5-Tricarboxylic acid H_3BTC [113].

H_3BTC ligand, with or without co-ligand, is one of the most frequently used ligands to construct MOFs, including world-famous HKUST-1, $Cu_3(BTC)_2(H_2O)_3$ MOF. To date, HKUST-1 has been reported for catalytic [199], photocatalytic [200], enzyme encapsulation [201], and semiconducting applications [202].

H_2Pzdc has two carboxylate groups and H_3BTC has three carboxylate groups that, each one could be coordinated to metal centers at least in one of the following modes, Scheme 2.8:

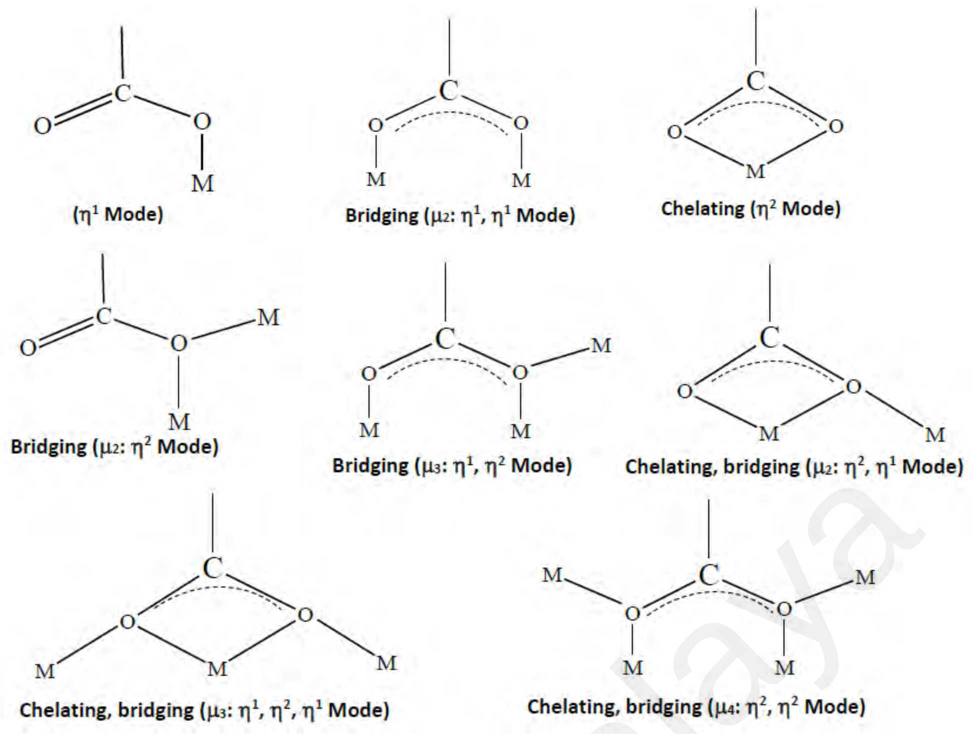

Scheme 2.8: The coordination modes expected for the carboxylate group [36].

Thus far, there are only five reports about Pb-based BTC, synthesized by solvo- or hydrothermally with four disclosed crystal structures and potential uses in luminescence applications [150, 176, 203- 205]. Our interests lie in discovering new bismuth and lead-based MOF with exotic properties, using a less preferred, but a facile dissolution-crystallization method.

The researcher could conclude that; MOF is a subclass of (CPs) with special feature that they are always porous which both can consume as new classes of inorganic organic hybrid materials. MOF combines the rigidity of inorganic materials with the flexibility and tunability of organic matter to display 3D extended solid state structures, contain potential voids. It is built from organic ligand/ bridging linker “strut” that links/ connects two or more atoms (metal ions/ clusters) to form discrete metal-ligand cluster which generate a rigid existence with simple geometry named secondary building unit (SBU) that used as a template for architecture of MOF.

MOF exhibits interesting phenomena like; luminescence which is a spontaneous emission of light that a substance can emits and it is a form of cold-body radiation not resulting from heat, proton conductivity which occurs by the protons movement in an infinite network of hydrogen bonds caused by presence of water/any source of deprotonated hydrogen (H^+) like imidazole (or any quaternary cation) in the pores of MOF, structural transformation/ gate-opening/ breathing, this breathability occurs by changing of mechanical pressure/ temperature or adsorption of guest / solvent or any external stimuli.

MOF displays vital features and has many interesting properties/ features that offers potential activities, like; higher surface areas, higher thermal stability, structural robustness and diversity, tunable pore sizes and permanent porosity. Therefore, MOF can be used in various applications such as: gas/liquid purification, water desalination, dehumidification and adsorption cooling technologies, as super capacitors: storage/capture/ separation of gases/fuel, in catalysis: photo-catalysis, electro-catalysis and catalyst for production fine chemicals, as ion-exchanger, in sensing and cathode storage in lithium batteries.

CHAPTER 3: METHODOLOGY

3.1 Materials

Some of chemical used for synthesis were purchased commercially form Sigma Aldrich (St. Louis, USA) as analytical grade, others were commercially available at reagent grade and used as received without further purification.

3.1.1 Chemicals and Reagents

The inorganic materials: Bismuth(III) nitrate pentahydrate, $Bi(NO_3)_3.5H_2O$ ≥98%, Sigma-Aldrich; Lead(II) nitrate, $Pb(NO_3)_2$, ≥99%, Sigma-Aldrich; hydrochloric acid, HCl; sodium hydroxide, NaOH, 99%, EMSURE.

The organic materials: 2,3-Pyrazine dicarboxylic acid (H_2Pzdc), $C_6H_4N_2O_4$, 97%, Aldrich; Trimesic acid (benzene-1,3,5-tricarboxylic acid) (BTC), $C_6H_3(CO_2H)_3$, 95%, Aldrich; Imidazole, $C_3H_4N_2$, ≥99%, Sigma-Aldrich; Imidazolium Iodide, $C_3H_5IN_2$; Aniline ($C_6H_5NH_2$), ≥99.5%, C_6H_7N; methyl red dye (azo compound), $C_{15}H_{15}N_3O_2$; methylene blue dye (methyl thioninium chloride), $C_{16}H_{18}ClN_3S$.

The solvents: 1,4-Dioxane, $C_4H_8O_2$, ≥99.5%, EMSURE; Methanol (MeOH), CH_3OH, ≥99.8%, EMPARTA; Acetone (CH_3COCH_3), C_3H_6O; N,N-Dimethylformamide (DMF), C_3H_7NO, ≥99%, EMSURE; Distilled water, H_2O, Lab. grade; Ethyl acetate ($CH_3COOC_2H_5$), $C_4H_8O_2$.

3.2 The instrumentations and measurement parameters

Elemental analyses of the new MOFs were performed using Perkin Elmer precisely 2400 series II CHNS/O elemental analyzer instrument and employing acetanilide as an internal standard and using EA 2400 Data Manager software (Version 1.0.0095). All measurements were taken under a constant flow of pure O_2 gas (Chemistry department, Malaya University, Malaysia).

Thermo-Gravimetric analysis (TGA) which displays the mass loss data with jumping in temperature every 5 minutes (the heating rate), was conducted under nitrogen atmosphere in the range of room temperature (RT) to 900°C using Perkin Elmer TGA 6 Thermo-gravimetric and Perkin Elmer SII Pyris Diamond and TG/DTA Thermo-gravimetric /Differential Thermal analyzers (Chemistry department, Malaya University, Malaysia).

The photoluminescence characterizations were measured using photoluminescence spectroscopy (PL) FLS920 Edinburgh instrument (CRIM-INS, University Kebangsaan Malaysia), then the raw data were plotted on Origin Lab software.

Solid state ultraviolet-visible (SSUV-Vis) measurements for these new compounds were conducted using UV-Vis-NIR Lambda 950/ Perkin Elmer spectrophotometer (CRIM-INS, University Kebangsaan Malaysia), then the raw data were plotted on Origin software. While the solution ultraviolet-visible (UV-Vis) absorption spectroscopy analyses were performed on UV-Vis spectrophotometer UV-2600 SHIMADZU and UV Probe software were used to draw the pattern chart from 200 to 800 nm for dyes adsorption measurements (Department of Chemistry, University of Malaya, Malaysia), then the raw data were plotted on Origin Lab software.

Single crystal X-ray diffraction (SC-XRD) data for the new MOFs (**1, 13**, **15**, **18**) was collected using Oxford Supernova Dual Wavelength BURKER diffractometer (λ_{Mo} K_{α} = 0.7107 Å). High quality, fractured, optically clear crystal was selected under a polarizing microscope and mounted on a tip of a thin glass fiber using an epoxy, then this fiber is attached to a brass mounting pin and the pin was inserted then into goniometer head which then affixed to a diffractometer. Data processing and absorption correction was performed by multi-scan method using CrysAlis PRO, with empirical absorption correction using spherical harmonics. X-ray intensity data from colorless crystals of all synthesized compounds were measured between 203(2) to 296(2) K using a Bruker SMART APEX diffractometer ((λ_{Mo} K_{α},λ= 0.7107 Å). Direct methods structure solution, difference Fourier calculations and full-matrix least-squares refinement against F^2 were performed with SHELXT (Department of Chemistry, Chung-Ang University, Seoul, South Korea).

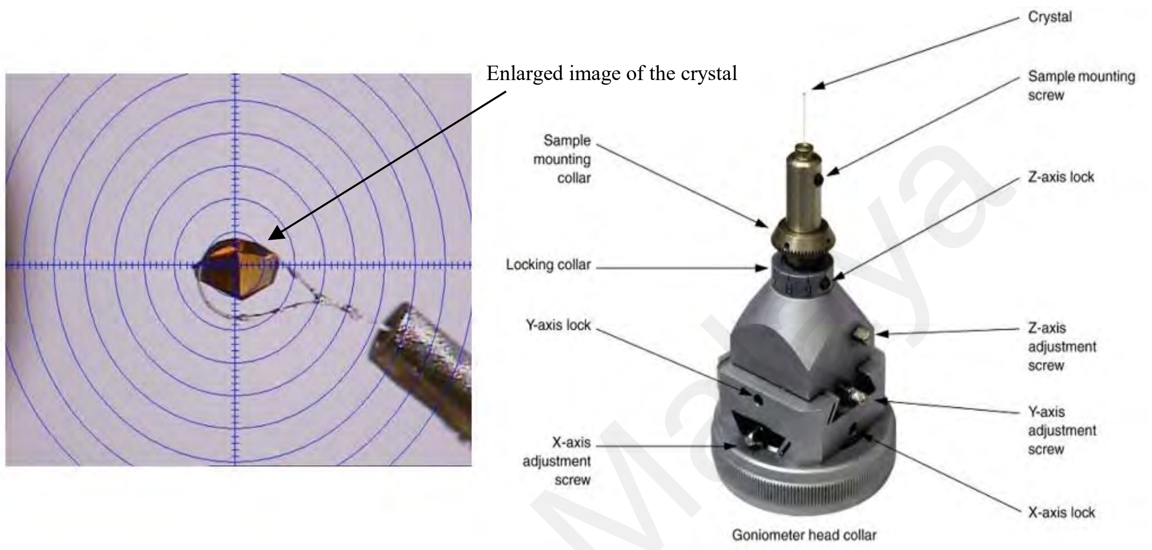

Figure 3.1: Huber model 1004 goniometer head for SCXRD [206].

The crystallinity and the purity of the new compounds were measured by powder X-ray diffraction technique (PXRD) using PANalytical, X'Pert Pro Powder diffractometer with primary monochromatic high intensity Cu-$K\alpha_1$ (λ=1.5406 Å), $K\alpha_2$ (λ=1.54443 Å) and K_β (λ=1.39225 Å) radiation. Ground mixtures of polycrystalline powders and/or single crystals of the samples were used to collect PXRD patterns using a PanAnalytical X'Pert Pro powder Diffractometer (Cu $K\alpha$ radiation λ= 1.5418 Å) over the scanning range of (5-70) ° and step size (2θ) = 0.026 ° for 30 minutes scan rate with a scan speed of 0.25 °/min. (Department of Chemistry, University of Malaya, Malaysia). These patterns then compared to the simulated diffraction patterns using the respective single crystal data and High Score plus software, after that the raw data were plotted on Origin Lab software.

Attenuated Total Reflectance Fourier Transform Infrared spectroscopy (ATR-FTIR) was employed to collect the infrared spectra by using Perkin Elmer Spectrum 400 FTIR/FT-FIR spectrometer and Spectrum software were used to draw the pattern chart (Department of Chemistry, University of Malaya, Malaysia), then the raw data were plotted on Origin Lab software.

Surface morphology and elemental percentage were determined by Field Emission Scanning Electron Microscope coupled with Energy Dispersive X-Ray Spectroscopy Analysis FESEM-EDX using Hitachi SU8220 machine (Department of Chemistry, University of Malaya, Malaysia).

For Specific Surface Area, Pore Sizes and Pore Volume, the Brunauer-Emmett-Teller (BET) method was employing using Micromeritics instrument and N_2 gas as Analysis Adsorptive by using nitrogen adsorption-desorption isotherms method with analysis bath temperature = 77.315 K (IPPP, University of Malaya, Malaysia).

Electrochemical impedance measurements were performed on a Princeton Applied Research VersaSTAT3 potentiostat/ galvanostat with environment maintained by an E-Spec BTL-433 humidity-controlled oven to measure the proton conductivity of BiMOF. Experiments were performed in air, at temperatures between 25 °C and 85 °C while humidity levels were maintained at 95 % relative humidity (RH), after a full cycle of RH variation (from 35 to 95 %) at constant 25 °C. Samples were finely ground to a powder by mortar and pestle prior to loading in custom dual-sample 2-probe cells with titanium electrodes. Electrodes were hand tightened, then tightened to an unknown pressure (with a screw driver) to ensure good contact. Cell (sample) lengths were approximately between 0.15- 0.3 cm, with a 0.317 cm diameter. At minimum two full heating/cooling cycles were performed with a minimum of 24 hours between temperature points. Duplicate measurements were obtained sweeping from 1 MHz to 0.1 Hz and then in reverse. Data was collected using Versa Studio software (version 2.1). ZView Software was used to fit impedance data sets by simulating an equivalent circuit (University of Calgary, Alberta, Canada); then the proton conductivity improvement measurements were conducted at (Physical-chemical institute, Justus Liebig-University, GieBen; Germany).

3.3 Synthesis of Compounds

3.3.1 Syntheses of Bi-MOFs (1-12)

Bismuth nitrate $Bi(NO_3)_3 \cdot 5H_2O$ precursor (is amongst the most common starting materials for synthesizing other bismuth complexes and frameworks), H_2Pzdc ligand as O donor and imidazole (Im)/ or imidazolium iodide (ImZm) as N-containing ligand and/ or modulator agents would be employed to synthesize Bi-MOF by using slow evaporation method. The reaction conditions optimization would be taking place by varying solvents stoichiometric molar ratios to get fast and big crystals of product.

A mixture of $Bi(NO_3)_3 \cdot 5H_2O$ (0.1213 gm, 0.25 mmoles); H_2Pzdc (0.1009 gm, 0.6 mmoles) and Im (0.0204 gm, 0.3 mmoles) was dissolved in 10 mL of DMF, followed by slow addition of 10 mL of distilled water (DW) with stirring at ambient temperature. A white precipitate started to show up inside the solution as soon as the H_2O were added to DMF and the temperature of mixture increased up to 43 °C (nucleic temperature). The mixture was then heated to 50 °C (before boiling point of solvents mixture) and it was left to cool down to RT with continuous stirring. The precipitate which is the amorphous BiMOF was isolated upon filtration and the filtrate was kept in a vial covered by para film with some small holes and left for slow evaporation crystallization process. Plate shining crystals were formed after ca. 4-7 days. The final products (BiMOF crystals), Scheme 3.1, were washed thoroughly with fresh DW, isolated by vacuum filtration, and dried at RT.

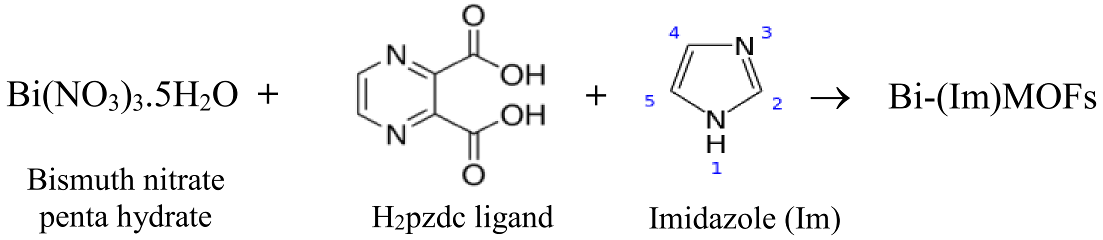

Scheme 3.1: The pathway of synthesizing the Bi(Im)MOFs.

3.3.1.1 Optimization of Reaction Conditions for Bi-MOFs (1-10)

Attempts in optimizing the reaction conditions to obtain the different colored Bi-MOFs were performed systematically in order to discover suitable procedure that can increase the yield, quality of the crystals and reducing the reaction time. Therefore, a constant total volume of solvents mixture (20 mL) with variety of the stoichiometric molar ratio of the solvents (H_2O: DMF) were used for synthesizing different batches of Bi-MOFs:

Starting first with (10:10) molar ratios for the solvent's mixture (DMF: H_2O) then reduce the volume of one solvent and increase the volume of the other solvent; with fixed total volume of the solvents' mixture (20 mL), e.g.

Table 3.1: The molar ratios of the solvent's mixture (DMF: H_2O)

The solvents mixture in mL		**The solvents mixture in mL**	
DMF	**H_2O**	**DMF**	**H_2O**
11	9	12	8
13	7	14	6
15	5	16	4
17	3	18	2
19	1	20	0
9	11	8	12
7	13	6	14
5	15	4	16
3	17	2	18

3.3.1.2 Improving the ionic conductivity of Bi-MOFs (1-10)

*(a) **Replacing the N- containing (Im) with (ImZm) to synthesis (11&12):***

Attempts for improving the proton conductivity of compounds (**1-10**) were done by replacing the N donor Im with ImZm, a mixture of $Bi(NO_3)_3 \cdot 5H_2O$ (0.1213 gm, 0.25 mmoles); H_2Pzdc (0.1009 gm, 0.6 mmoles) and (ImZm) (0.0588 gm, 0.3 mmoles) would be dissolved by adding a mixture of (10 mL /or 14 mL) DMF and (10 mL /or 6 mL) of H_2O with stirring at ambient temperature, a red solution formed and a yellow precipitate started to show up inside the red solution. The mixture then was heated to 50 °C (before boiling point of solvents mixture) and it was left to cool down to RT, filtered, and the filtrate kept in a vial covered by para film with some small holes to allow a slow evaporation for solvents and after 7-10 days shining yellow crystals formed. To check the I^- anions incorporation inside the MOFs for different time periods the EDX then proton conduction measurements were used.

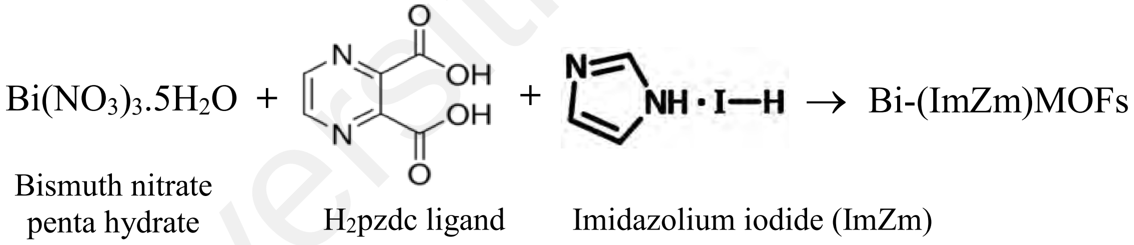

Scheme 3.2: The pathway of synthesizing the Bi-(ImZm)MOF.

*(b) **Soaking the BiMOFs with $NaCOOCH_3$ or Na_2SO_4:***

A (0.1213 gm, 0.2 mmoles) of $NaCOOCH_3$ or (0.1213 gm, 0.2 mmoles) of Na_2SO_4 was dissolved in 10 mL DW and added after filtration on (0.1213 gm, 0.1 mmole) of Bi(Im)MOF or Bi(ImZm)MOF in two separated beakers to improve the ionic conductivity of these Bi-MOFs by checking the Na^+ cations and/ or SO_4^{2-} anions incorporation inside the MOFs for different time periods using EDX then proton conduction measurements.

3.3.1.3 Study of stability of BiMOF (1-10)

To investigate the stability of the different batches of BiMOF the researcher used various ways:

(a) Soaking different batches of the BiMOF in different solvents

A (0.028 gm, 0.05 mmoles) from different dry batches of Bi(Im)MOF was soaked in 20 mL of different solvents (H_2O, EtOH, Dioxane, Ethyl ether and DMF) in separated beakers for more than one month; the pH of the resulted solutions after soaking this MOF in these different solvents were (4, 4.5, 5, 6 and 6.5), respectively.

(b) Soaking different batches of the BiMOF in different pH environments

A (0.028 gm, 0.05 mmoles) from different dry batches of Bi(Im)MOF was soaked in different concentrations of diluted HCl and diluted NaOH solutions.

(c) Investigating the stability of BiMOFs using reflux

A (0.028 gm, 0.05 mmoles) from two dry batches of BiMOFs crystals (10D:10H, 17D:3H and 13D:7H) were put in a round bottom flask then 15 mL of DW was added to each flask and start water refluxing for 3 days. The samples then filtered, dried and check its stability via the PXRD analysis.

3.3.2 Syntheses of Pb-MOFs (13-21)

The syntheses of Pb-MOFs were implemented by combination of $Pb(NO_3)_2$ with BTC linker, employing layering method, as procedure for synthesis, and adopting aniline (An), imidazole (Im) and piperazine (Pip) as modulating agents [207]. The compounds are made using a facile dissolution-crystallization method, exploiting the use of hard-soft acid base (HSAB) principle to find a suitable modulator to yield a phase pure product [208].

3.3.2.1 Synthesis of compound 13 [Pb(HBTC)(1,4-dioxane)$_{0.5}$]

A $Pb(NO_3)_2$, (0.0331 gm, 0.1 mmole), was dissolved in 4 mL of Distilled Water (DW) then carefully and slowly this solution layered on the top of a solution contains H_3BTC (0.021 gm, 0.1 mmole) that dissolved in 8 mL of 1,4-dioxane, (the layering process have conducted by dropping the solution on the inner wall of the beaker). White shining crystals, Scheme 3.3, was formed after 3 days with nearly quantitative yield.

(a) ***Improving the PXRD pure phase of 13 by adding N-containing ligand***

A (0.0465 gm, 0.5 mmole; 0.0931 gm, 1 mmole; 0.0372 gm, 0.4 mmole) of (An) was weighed in three separated beakers and added as N- containing ligands to the same stoichiometric ratios of synthesizing **13** to produce compound **14a**, **14b** and **14c** in order to get very pure phase of **13**.

3.3.2.2 Synthesis of compound 14 [Pb(HBTC)(1,4-dioxane)$_{0.5}$]

A $Pb(NO_3)_2$ (0.331 gm, 1 mmole) was dissolved in 4 mL of DW then carefully and slowly layered on the top of a solution contains H_3BTC (0.21 gm, 1 mmole) that dissolved in 20 mL of 1,4-dioxane, after that a careful addition of An (0.0372 gm, 0.4 mmol) have conducted. White ribbon-like crystals were formed after 3 hrs. with nearly quantitative yield. The final product (compound **14**) was washed thoroughly with fresh DW, isolated by vacuum filtration, and dried at RT. A quantitative analysis of the crystals obtained was performed by CHN analysis. Anal. Calc. (Found) for $C_{13}H_{13}O_9Pb$: C, 29.99 (30.02); H, 2.52 (2.49).

3.3.2.3 Synthesis of compound 15 [$Pb_2(HBTC)_2(H_2O)_5$]

A (0.0331 gm, 0.1 mmole) of $Pb(NO_3)_2$ dissolved in 4 mL of DW then carefully layered and slowly added on the on the top of a solution contains H_3BTC (0.021 gm, 0.1 mmole) which previously have dissolved in 4 mL of methanol (MeOH). White block crystals, Scheme 3.3, with near quantitative yield were formed after 5 hours.

(a) ***Improving the PXRD pure phase of 15 by adding N-containing ligand***

A (0.0465 gm, 0.5 mmole; 0.0931 gm, 1 mmole; 0.0372 gm, 0.4 mmole) of An was added as N donor ligands to the same stoichiometric ratios of synthesized **15** to produce compound **16**. Then a (0.0341 gm, 0.5 mmole; 0.0681 gm, 1 mmole; 0.0272 gm, 0.4 mmole) of Im was added as N donor ligands to the same stoichiometric ratios of synthesizing **15** to produce compound **17**.

3.3.2.4 Synthesis of compound (17) $Pb_2(HBTC)_2(H_2O)_5$

A $Pb(NO_3)_2$ (0.331 gm, 1 mmole) dissolved in 4 mL of DW was carefully and slowly layered on the on the top of a solution contains H_3BTC (0.21 gm, 1 mmole) which dissolved in 8 mL of MeOH, after that a careful addition of Im (0.0272 gm, 0.4 mmol) have done. White block crystals with near quantitative yield were formed after ca.1day. The final product (compound **17**) was washed thoroughly with fresh DW, isolated by vacuum filtration, and dried at RT. A quantitative analysis of the crystals obtained was performed by CHN analysis. Anal. Calcd (Found) for $C_{18}H_8O_{17}Pb_2$: C, 23.74 (23.65); H, 0.89 (0.90).

3.3.2.5 Synthesis of compound 18 [Pb(HBTC)(DMF)]

A $Pb(NO_3)_2$ (0.0331 gm, 0.1 mmole) was dissolved in 4 mL of DW then carefully and slowly layered on the top of a solution contains H_3BTC (0.021 gm, 0.1 mmole) that dissolved in 2 mL of DMF. Small white plate-like crystals were formed in close to quantitative yield after ca.1 day. The final product (compound **18**), Scheme 3.3, was either kept as it is in mother liquor or washed thoroughly with fresh DW, isolated by vacuum filtration, and dried at RT. A quantitative analysis of these crystals was not performed due to decomposition of the product outside of mother liquor.

(a) Improving the PXRD pure phase of 18 by adding N-containing ligand

A (0.0465 gm, 0.5 mmole; 0.0931 gm, 1 mmole; 0.0372 gm, 0.4 mmole) of An was added as N donor ligand to the same stoichiometric ratios of synthesized **18** to get a pure phase of compound **18** and produce compound **19**. Then a (0.0341 gm, 0.5 mmole; 0.0681 gm, 1 mmole; 0.0272 gm, 0.4 mmole) of Im was added as N donor ligand to the same stoichiometric ratios of synthesized **18** to get a pure phase of compound **18** and produce compound **20**. Then a (0.0431 gm, 0.5 mmole; 0.0861 gm; 1 mmole; 0.0345 gm, 0.4 mmole) of Pip was added as N donor ligand to the same stoichiometric ratios of synthesized **18** to get a pure phase of compound **18** and produce compound **21**.

3.3.2.6 Synthesis of compound 22

A $Pb(NO_3)_2$ (0.0331 gm, 0.1 mmole) was dissolved in 4 mL of DW then carefully and slowly layered on the top of a solution contains H_3BTC (0.021 gm, 0.1 mmole) dissolved in 3 mL of Acetone. Large white shining crystals was formed immediately and change to white plate-like crystals were formed in close to quantitative yield after ca.1 day. The final product was either kept as it is in mother liquor or washed thoroughly with fresh DW, isolated by vacuum filtration, and dried at RT.

3.3.2.7 Synthesis of compound 23

A $Pb(NO_3)_2$ (0.0331gm, 0.1mmole) was dissolved in 4 mL of DW then carefully and slowly layered on the top of a solution contains H_3BTC (0.021 gm, 0.1 mmole) dissolved in 4 mL of Ethyl acetate. Large colorless plate-like crystals were formed in close to quantitative yield after ca.7 days. The final product (compound **23**) was either kept as it is in mother liquor or washed thoroughly with fresh DW, isolated by vacuum filtration, dried at RT.

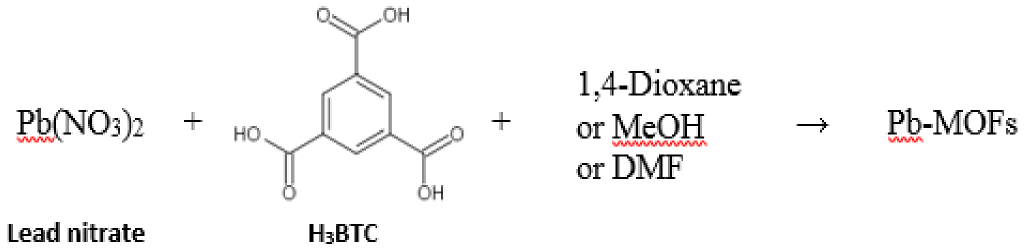

Scheme 3.3: The pathway of synthesizing the Pb-MOFs.

3.3.2.8 Investigating the guest absorbance efficiency of the new Pb-MOFs

The compounds **14** and **17** have been chosen for this study because both of them have a pure phase pattern pxrd, therefore, they have known structures while compound **18** did not have a pure phase pattern of pxrd so it is unknown compound, therefore, it was not chosen. The dyes sorption experiments were carried out by using the following procedure:

a) A (50 mg) of compound **14** was soaked into two separated solutions of 10 ppm from the two selective dyes; methyl red (MR) and methylene blue (MB) which were prepared in 10 mL volumetric flask, then the mixture of compound **14** with the dye solution were sealed tightly and shaken well then left to check the dyes absorption ability of compound **14** after (1, 3, 5 and 7 days).

b) A (50 mg) of compound **17** was soaked into two separated solutions of 10 ppm from the two selective dyes; methyl red (MR) and methylene blue (MB) which were prepared in 10 mL volumetric flask, then the mixture of compound **17** with the dye solution were sealed tightly and shaken well then left to check the dyes absorption ability of compound **17** after (1, 3, 5 and 7 days).

c) The UV-vis spectroscopy equipped with 1 cm quartz cells at λ= 525 nm for MR dye and λ= 660 nm for MB dye were then conducted.

CHAPTER 4: RESULTS AND DISCUSSION

4.1 General Characterization of the synthesized MOFs

The physical and chemical features and the solid state properties of the new compounds (**1**-**18**) were performed, by using optical microscope, black box for UV light, Scanning Electron Microscope, coupled with Energy Dispersive X-Ray Spectroscopy SEM/EDX, Single Crystal and Powder X-ray diffraction (SC-XRD and PXRD), Thermo-gravimetric Analysis (TGA), elemental analysis (CHN), solid state Nuclear Magnetic Resonance (SS-NMR), Fourier Transform Infrared Spectrometry (FTIR), Ultra Violet-Visible (UV-Vis) spectrophotometry (solid and liquid state), solid state photoluminescence (PL), BET surface area analysis and proton conductivity measurements.

4.2 Synthesis, characterization and properties of Bi based-MOFs

Till date, there are only few Bi-based MOFs reported [8, 181, 209- 212]. Herein, we report a new, rare, and highly water stable bismuth-containing organic framework; Bi(pzdc)(Hpzdc)·xH_2O, compound **1**, which was successfully synthesized by using Bi(III) ions with H_2Pzdc as O-donor ligand and with imidazole (Im)/ or imidazolium iodide (ImZm) as a modulation agent via a simple dissolution-slow evaporation method, unlike most of the Bi(III)MOFs that have been made by hydro- or solvothermal method. Such Bi MOF was synthesized by using an optimized, facile slow evaporation method showcasing highly water stable compound, that, together with hydrogen-bonded water feature along the crystallographic c-direction, lead to proton conductivity of 8.41 $\times 10^{-6}$ S.cm^{-1} at 85°C and 95% RH. Its optimized synthetic condition, structural, thermal, and photophysical characterizations in relation to water content and water stability, as well as proton conductivity property are presented.

Lattice water content, hence, the resulting color of the product, could be varied (x = 0.5, 0.78, 0.86, 0.90, 1.0, 1.26, 1.5 and 6.0 based on TGA measurements) from white to yellow color, respectively by changing DMF: H_2O molar ratios. Prior to this discovery, attempts were made to obtain quantitative yields, which involved combinations of the following variables, such as (a) molar ratio of $Bi(NO_3)_3.5H_2O$ and H_2pzdc, (b) variety of solvent or mixture of solvents. The compound was found to contain unknown impurity and/or amorphous phase. Inspired by the use of monocarboxylic acid modulator, to obtain pure and stable transition metal-based MOFs [213- 216]. Additional trials were attempted, following Pearson's hard-soft acid base concept, in which borderline organic bases are suitable for borderline acids, e.g. Bi^{3+}, and found that, the use of imidazole was required to make phase pure and stable compound of **1**. Adding the suitable N-donor ligand resulted in the gradual disappearance of the unidentified impurity peaks, that eventually reached phase pure with nearly quantitative yields, achieving optimum synthetic condition. Activation attempts for **1**, starting from rather harsh thermal activation, to relatively milder supercritical CO_2, as well as, solvent exchange activations were unsuccessful, despite the fact that, there was 37% void space as analyzed by Platon [217].

The combination of $Bi(NO_3)_3.5H_2O$ and H_2Pzdc ($C_6H_4N_2O_4$) linker, Figure 4.1 (a), with (Im)/ or (ImZm) in a mixture of DMF/H_2O (with different stoichiometric molar ratios) produced a new porous coordination polymer /MOF, with a molecular formula of Bi (pzdc)(Hpzdc)·xH_2O or $[(C_{12}H_5BiN_4O_9)(H_2O)_X]$; **1-12**, and with molecular mass of 560.20 gm/ mol, Figure 4.1 (b) show the expected coordination modes of H_2Pzdc with Bi metal ions in compounds **1-12**. The varying of the solvents molar ratios enables the researcher to get different crystals of Bi-Im-MOFs (**1-10**) and by changing the modulation agent (Im) with (ImZm) it was able to get Bi-ImZm-MOFs (**11**, **12**). The compounds (**1-12**) show different colors, under visible light and potential different photoluminescence

(PL) under the long wave length of UV light (365nm), with similar PXRD patterns, which matching with the simulated one, means that all of the synthesized Bi compounds have the same structure.

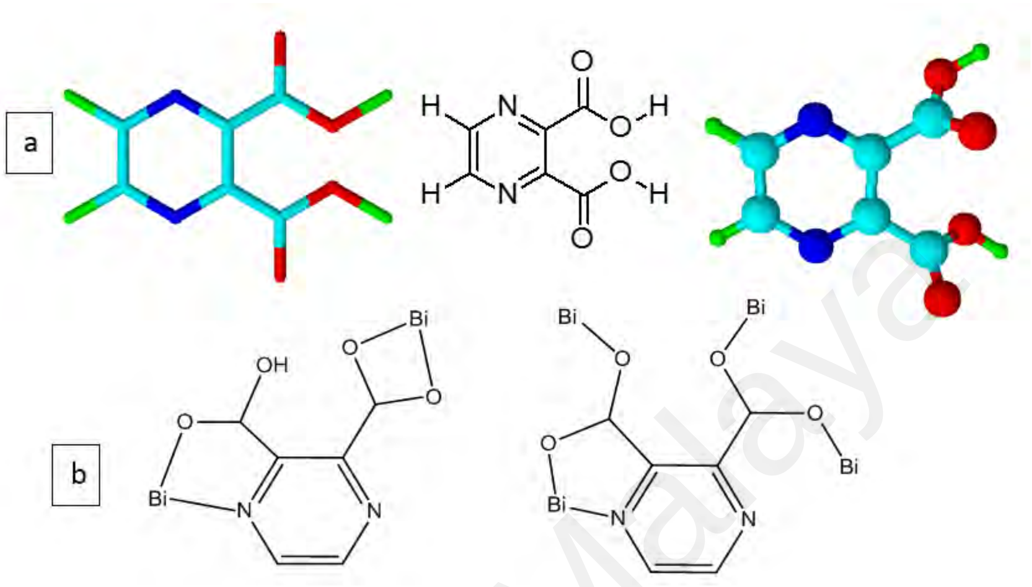

Figure 4.1: (a) The sticks and the ball modules of the free linker H_2Pzdc, (b) The expected coordination modes of H_2Pzdc with Bi metal ions in compounds 1-12.

The visual observation confirmed that, (10:10) (DMF: H_2O) batch, **1**, could give a large amount with small quality crystals in 4 days while (14:6) (DMF: H_2O) batch, **5**, can give a smaller amount comparing to (10:10) (DMF: H_2O) batch, but big quality crystals in 5-6 days. Besides that, (9:11) (DMF: H_2O) batch, **3**, can give good quality crystals within 4-5 days at room temperature and within 2 days when it is kept at oven 38°C. The exchange of the auxiliary ligand (Im) with (ImZm) gave big crystals of Bi-ImZm-MOF which have the same PXRD pattern, that matches with the simulated one of compound **1**, with (0.35- 0.46) % doping amount of iodide ions that displays dark yellow color under visible light and quenched PL under UV light because the iodide is a heavy metal ion, that has a significant fluorescence quenching of general fluorophores/ chromophore [218].

4.2.1 Elemental analysis (C.H.N) of BiMOFs

Results tabulated in Table 4.1 are summarized the molecular formula, molecular weight, %yield, color and appearance and elemental analyses for the new synthesized Bi-MOFs. The molecular formula and molecular weights of the new compounds have been obtained from the SCXRD analyses. The elements analysis CHNO that run for both kind of Bi-MOFs (Im and ImZm) ensure that both MOFs have same kind of elements with nearly same percentage amounts, which are matched well the calculated values theoretically for both of them, indicating that both compounds have same structure.

Table 4.1: The physical data of the new synthesized compounds.

Comp. code	**Molecular formula, colour and appearance**	**Molecular weight g/mole and Yield%**	**Percentage of element (%) Experimental (Theoretical)**		
			C	**H**	**N**
Bi(Im) MOFs **= 1, 2, 3, 4, 5, 6, 7, 8, 9 & 10**	$Bi(C_6H_2N_2O_4)(C_6H_3N_2O_4)$, (H_2O) white, light yellow, dark yellow and orange crystals (depending on the water contents)	560.20 65-74%	25.99 (25.73)	1.16 (1.19)	10.10 (10.05)
Bi(ImZm) MOFs **= 11&12**	$Bi(C_6H_2N_2O_4)(C_6H_3N_2O_4)$, (H_2O) big yellow crystals	560.20 89, 93%	25.57 (25.73)	1.17 (1.29)	10.23 (10.00)

4.2.2 FTIR Vibrational spectra of BiMOF

Generally, the carboxylic acids usually show a strong, wide band for the OH stretching ν(O-H) appears as a very broad band (because the carboxylic acids usually exist as hydrogen-bonded dimers) in the region between 3300-2500 cm^{-1}. It is centered at about 3000 cm^{-1} and the exact position of this broad band, depends on whether the carboxylic acid is saturated or unsaturated, dimerized, or has internal hydrogen bonding [219].

The FTIR spectral data of the free ligand linker H_2Pzdc, Figure A-1; Appendix A, was compared with those of the new synthesized BiMOFs, Figures A-2 to A-6. It was observed that, IR spectra of Bi(Im) and Bi(ImZm) depicts peaks nearly in similar region, which beside the CHN values, PXRD patterns and TGA charts, confirmed that both of these compounds (Bi(Im) and Bi(ImZm)) have the same structures. The FTIR spectrum of the free ligand H_2Pzdc, Figure A-1, shows a strong absorption band appears at 3099 cm^{-1} which is attributed to ν(C-H) vibrations of sp^2 C in the ring and also shows a broad band appears around 3263-2843 due to ν(O-H) of the COOH group. The δ(CH) vibrations of pyrazine ring generally appear as strong bands at 1000-1280 cm^{-1} [161], for H_2Pzdc it appears at 1096 cm^{-1} region. The strong absorption bands that appear at the region 1751-1688 cm^{-1} due to the stretching vibrations of ν(C=O) mode, while the bands at 1398-1357 cm^{-1} due to ν(C-O) mode; both are attributed to the asymmetric and symmetric stretching vibrations of carboxylate group $\nu_{as,sy}$(COO) of the free ligand [220].

The $\nu_{as,sy}$(COO) are shifted to the lower wavenumbers after coordination between the free linker and Bi(III) metal ions to form the Bi-MOF network, Figure A-2 and A-4. They shifted and observed at the region around 1601-1556 cm^{-1} for C=O and 1393 cm^{-1} for C-O of Bi(Im)MOF, Figure A-2, while they shifted and observed at the region around 1600-1554 cm^{-1} for C=O and 1352 cm^{-1} for C-O of Bi(ImZm), Figure A-4 [221]. The differences between the ν_{as} and ν_{sy} frequency of the (COO) of H_2pzdc, [$\Delta\nu = \nu_{as}$ (COO) - ν_{sy} (COO)], is < 300 cm^{-1}; ($\Delta\nu$ = 226 -163 in Bi(Im) and 164 -160 cm^{-1} in Bi(ImZm) suggest a multi-dentate binding of the carboxylate group to the Bi(III) metal ions in these two new compounds [222]. The ν(COO) vibrations of multi carboxylate groups which connected to the pyrazine ring of H_2Pzdc and the clear shifting, that observed for these stretching vibrations in the IR spectrum of BiMOFs, Figure A-2 and A-4, provide a good evidence that H_2pzdc coordinated to Bi(III) cation and display a different coordination modes. The pyrazine ring of the free ligand is aromatic in nature, therefore, the C=N frequency of this moiety could be assigned as the ring skeletal at 1577 and 1542, which are overlapped and shifted to appear at 1435 cm^{-1} in the MOF spectrum [223]. The peak at 1445 cm^{-1} is ascribed to the C-C vibration in the aromatic ring [223].

The new bands that appeared at 466 cm^{-1} due to Bi-N stretching vibrations and at 550 cm^{-1} due to Bi-O stretching vibrations in spectrum of Bi(Im). Besides, the new bands at 445 cm^{-1} due to Bi-N stretching vibrations and 547 cm^{-1} due to Bi-O stretching vibrations in the spectrum of Bi(ImZm) confirmed the interaction between N and O atoms of the ligand with the Bi(III) metal ion [27] in these two MOFs, Figure A-6.

The FTIR spectrum of BiMOF shows broad peak of ν(OH) vibrations of hydrogen bonded covering from 3600 to 3000 cm^{-1}, Figure 4.2, is further supported by Figure 4.9 in SCXRD study.

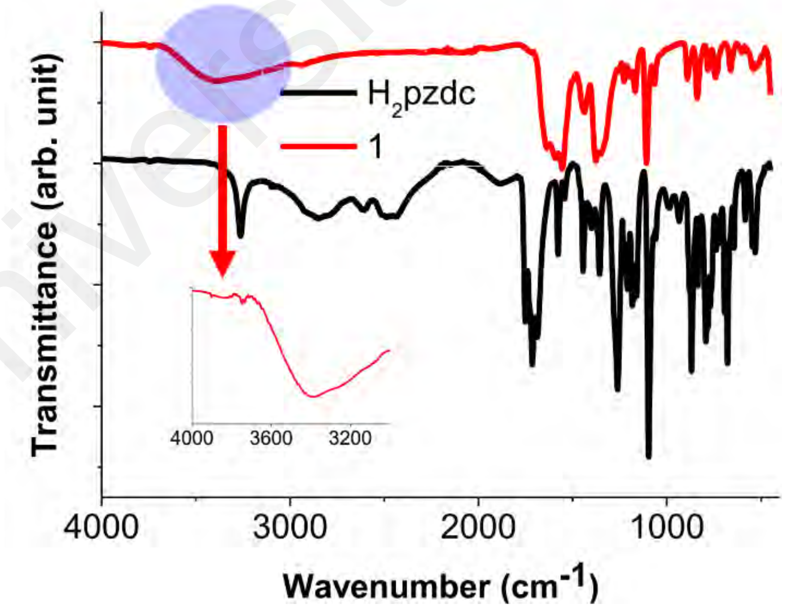

Figure 4.2: FTIR of 1 with a zoom-in inset showing hydrogen-bonded lattice water peak extended from 3600-3000 cm^{-1}.

- ➢ Note: The FTIR patterns of other BiMOF compounds uploaded at Appendix A

4.2.3 Single Crystal X-Ray Diffraction (SCXRD) analysis

The reactions of H_2pzdc with $Bi(NO_3)_3\cdot 5H_2O$ under a simple slow evaporation resulted in Bi(pzdc)(Hpzdc)·xH_2O or $Bi(C_6H_2N_2O_4)(C_6H_3N_2O_4),(H_2O)$ (pzdc = pyrazine-2,3-dicarboxylate; x = 0.5, 1.0, 1.5 and 6.0), compound **1**, whose structure was determined by SCXRD. The SCXRD structure determination confirms that compounds (**1**-**12**) which all have same structures (according to the PXRD patterns); crystallize in the monoclinic, $P2_1/n$ space group (a =14.1738(7) Å, b =21.682(1) Å, c =14.7988(8) Å, β =109.2103(8)°) and built from 2D slabs which contain layers of Bi polymers that interlinked via H_2pzdc ligands into 3D MOF with unit-cell volume = 4294.554141 Å^3 and ~6Å× ~8Å aperture size occupied by water molecules with varied contents. Relevant crystallographic data from the single-crystal structure refinement are found in Table 4.2. Selected interatomic distances and angles of **1** are summarized in Table B-1 (Appendix B).

Figure 4.3 (a) depicts the asymmetric unit cell and atom labels of **1**, that consists of two unique bismuth atoms, two deprotonated pzdc and two monoprotonated Hpzdc ligands, and two lattice water molecules. The overall structure is built around Bi polymer layers extended along the *c*-axis. The nitrogen and oxygen atoms of the pzdc^{2-} and Hpzdc^{-} ligands complete the coordination sphere around the bismuth cations in the Bi polymer slabs to form Bi(1)O_7N_2 and Bi(2)O_7N_2 tricapped trigonal bipyramid, Figure 4.3 (a), with Bi-O distances ranging from 2.235(8)-2.775(8) Å, and Bi-N distances are between 2.519(9) to 2.677(9) Å, typical of Bi compounds [46 - 48, 181, 210, 224, 225]. All the Bi^{3+} polyhedra are holo-directed and contain stereochemically inactive lone pairs shown in Figure 4.3 (b).

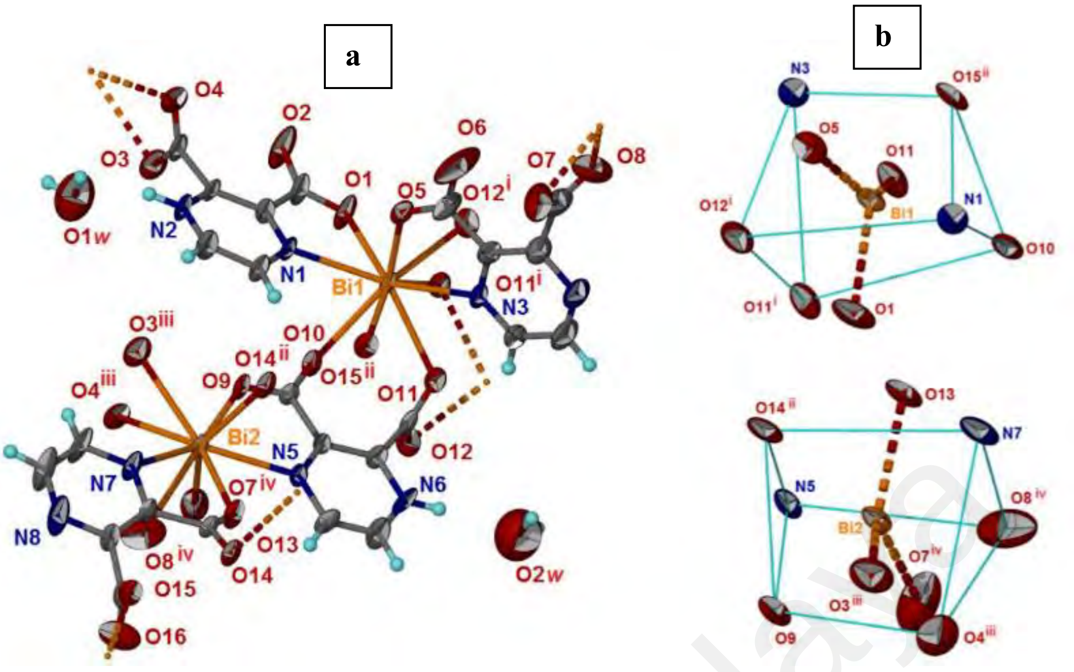

Figure 4.3: (a) Asymmetric structure and atomic labeling of compound 1, Displacement ellipsoids are drawn at the 50% probability level. (b) The holo-directed bismuth centered polyhedra of the compound 1, Bi(1)O$_7$N$_2$ and Bi(2)O$_7$N$_2$.

In fact, there is two crystallographically independent Bi units, the Bi(1) atoms are interlinked by the ligands to form polymers that featuring dioxo bridging from O(11) of the ligand. The Bi(1) polymer is correlated through inversion symmetry, Figure 4.4(a). Bi(2) atoms also form polymers, related by inversion symmetry, through the ligand. Unlike Bi(1) polymers, however, Bi(2) polymers do not exhibit dioxo bridging, Figure 4.4(b). Both dimers are then connected by the ligand to form 2D structure along the *ac*-plane, Figure 4.5, in which hydrogen-bonded water molecules are extended along the *c*-direction, Figure 4.6. The existence of hydrogen bonds between free oxygen atoms of pzdc carboxylic acids and hydrogen atoms of lattice water, O(2)···H(21) and O(10)···H(11) with bond distance of ~1.965 Å.

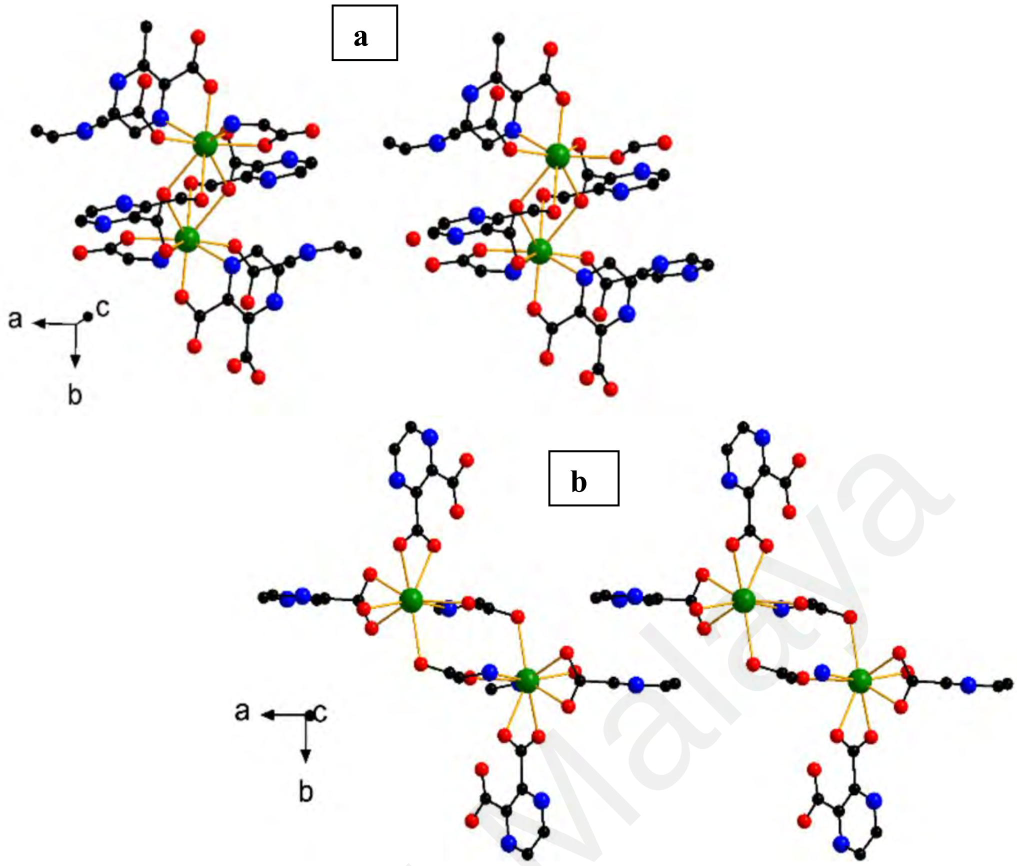

Figure 4.4: (a) Bi(1) dimers linked by pzdc ligand in compound 1. (b) Bi(2) dimers linked by pzdc ligand in compound 1. Bi =green, O = red, N =dark blue, C = black.

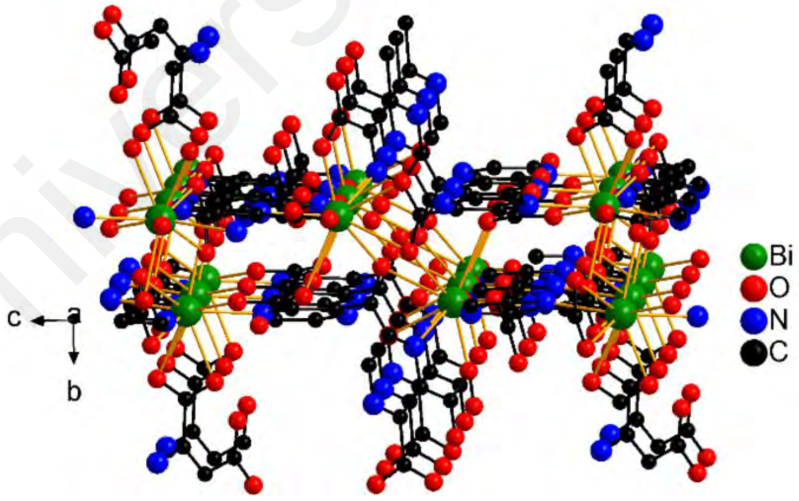

Figure 4.5: Combination of Bi(1) and Bi(2) dimers to form 2D structure of compound 1.

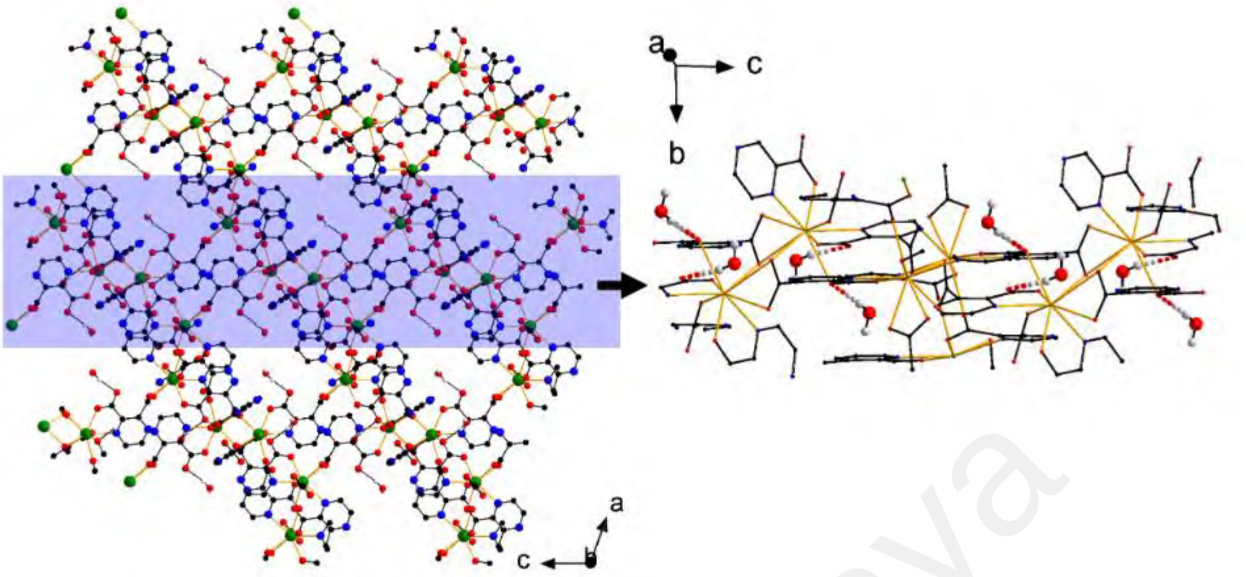

Figure 4.6: 2D structure of 1 along the ac-plane showing the hydrogen-bonded lattice water extended along the c-axis.

The 2D slabs are further connected by the ligand along the b-axis to form 3D structure in which the 2_1 screw axis along the diagonal of the unit cell could be viewed, Figure 4.7. Zooming into the pore with approximate aperture size of ~6 Å × ~8 Å, there are uncoordinated N (N(4), (6), and (8)) and O atoms (O(2), (6), and (16)) of the ligands.

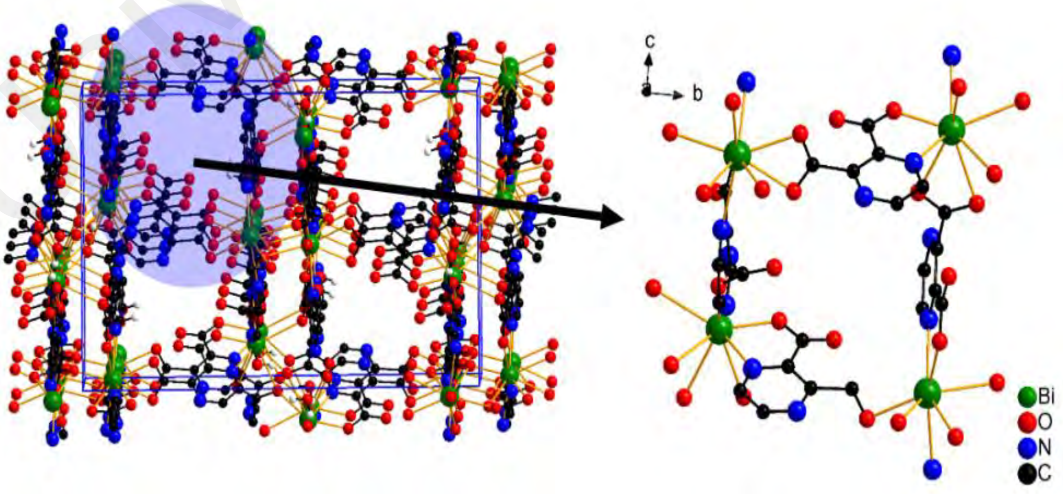

Figure 4.7: 3D structure of compound 1, with a zoom-in picture of pore formation with uncoordinated N and O atoms.

Table 4.2: The Crystal data and structure refinement parameters of compound 1.[a]

Empirical formula	$C_{12} H_7 Bi N_4 O_9$
Formula weight	560.20
Temperature	295(2) K
Wavelength	0.71073 Å
Crystal system	Monoclinic
Space group	$P\ 2_1/n$
Unit cell dimensions	a = 14.1738(7) Å, α = 90.00° b = 21.6814(12) Å, β = 109.2103(8)° c = 14.7988(8) Å, γ = 90.00°
Volume	4294.6(4) $Å^3$
Z	8
Density (calculated)	1.733 g/cm^3
Absorption coefficient	8.255 mm^{-1}
F(000)	2096
Crystal size	0.20 x 0.15 x 0.10 mm^3
θ range for data collection	2.38 to 27.71°
Index ranges	-18<=h<=18, -28<=k<=28, -19<=l<=18
Reflections collected	42068
Independent reflections	10002 [R_{int} = 0.0692]
Completeness to θ = 27.71°	99.3%
Refinement method	Full-matrix least-squares on F^2
Data / restraints / parameters	10002 / 12 / 469
Goodness-of-fit	1.046
Final R indices [I>2σ(I)]	R_{obs} = 0.0582, wR_{obs} = 0.1544
R indices [all data]	R_{all} = 0.0829, wR_{all} = 0.1696
Largest diff. peak and hole	4.741 and -1.399 e·$Å^{-3}$

$$^{a}R = \sum \| F_0 | - | F_C \| / \sum \| F_0 \| . wR_2 = \left\{ \sum \left[w\left(F_0^2 - F_C^2\right)^2 \right] / \sum \left[w\left(F_0^2\right)^2 \right] \right\}^{1/2}$$

4.2.4 Microscopic Features

The different colored crystals from different batches of BiMOF (which have same PXRD patterns) displayed different plated crystal shapes and morphologies with different crystal sizes that observed under the electrical microscope which can explain the difference in colors that these different batches exhibited, Figure 4.8.

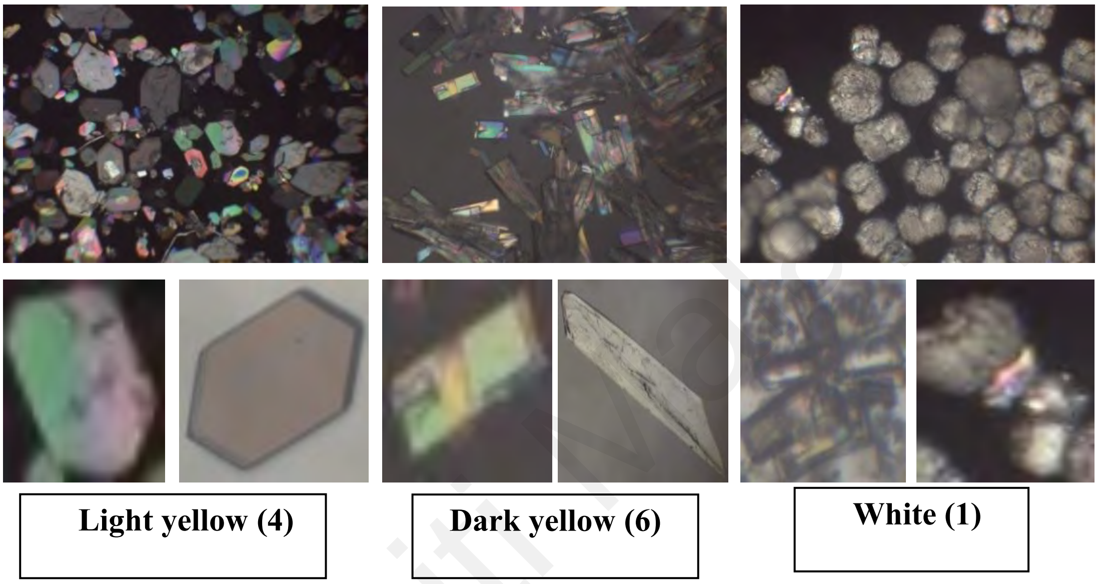

Figure 4.8: Optical-images of different batches of Bi-(Imi)MOFs took by the microscope.

4.2.5 Photoluminescence (PL) Observation

The different colored crystals from different batches of BiMOF (which have same PXRD patterns) displayed various PL colors under UV and visible light. The emission mechanism of this PL attributed to the presence of the organic fluorophores [226] and to the presence of different water contents in the pores of the new BiMOF framework. This feature could make the new BiMOF as promising candidate as a moisture sensor and/or proton conductor, Figures 4.9 and 4.10.

PL under **visible** light for **1**, **4** & **6**

PL under **UV** light for **1**, **4** & **6**

Figure 4.9: photo-images of the different colored crystals of Bi-(Im)MOFs.

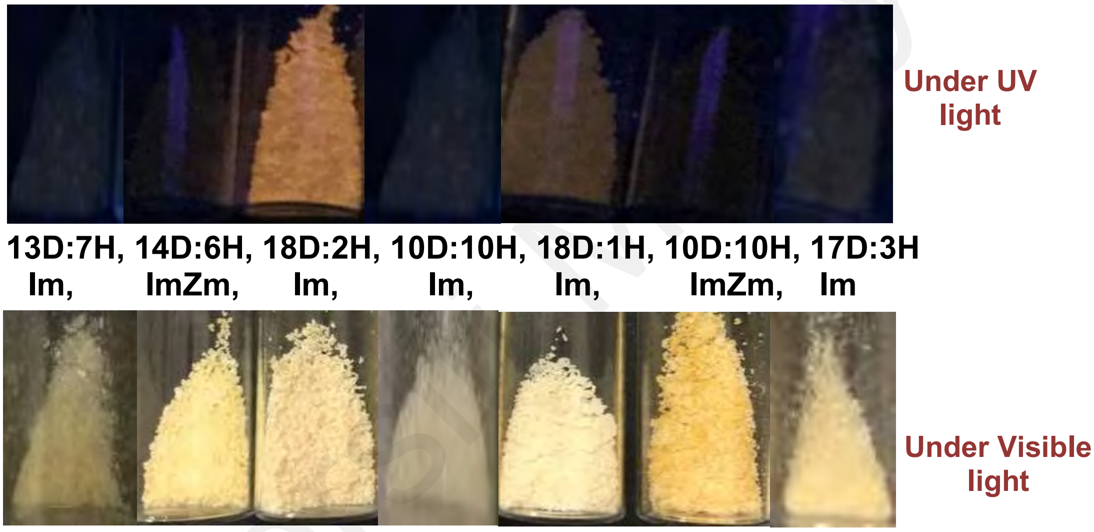

Figure 4.10: Photo images of the different colored crystals from various batches of BiMOF.

4.2.6 Powder X-ray diffraction (PXRD) analysis

The combination of only $Bi(NO_3)_3 \cdot 5H_2O$ and H_2pzdc to generate BiMOFs were found to contain unknown impurity and/or amorphous phase. Inspired by the use of monocarboxylic acid modulator to obtain pure and stable transition metal-based MOFs [213- 215] the researcher attempted additional trials. Following Pearson's hard-soft acid base concept in which borderline organic bases are suitable for borderline acids, e.g. Bi^{3+}, The researcher found that the use of (Im) was required to make phase pure and produce stable compound of **1-12** via modulating the framework of these compounds. The powder

X-ray diffraction measurement (Figures 4.11-4.15) can show that Bi-MOFs (with all different molar rations) display a high degree of crystallinity with sharp and well-defined peaks in XRD patterns comparing with the simulated patterns which obtained from single crystal x-ray diffraction analysis (Crystallographic Information Framework, CIF file).

4.2.6.1 Phase purity, water stability, and water content vs. resulting color

Phase purity and the presence or absence of polymorph can be detected by PXRD. The purity of compound **1**, plate crystals, was checked using PXRD. The PXRD pattern of compound **1** match the calculated pattern based on the single crystal structure as shown in Figure 4.11, demonstrating that within the resolution and detection limit of PXRD, the reaction products used for further physical characterizations are of single phase, and no additional polymorph is present, and no unreacted starting material remains in the samples.

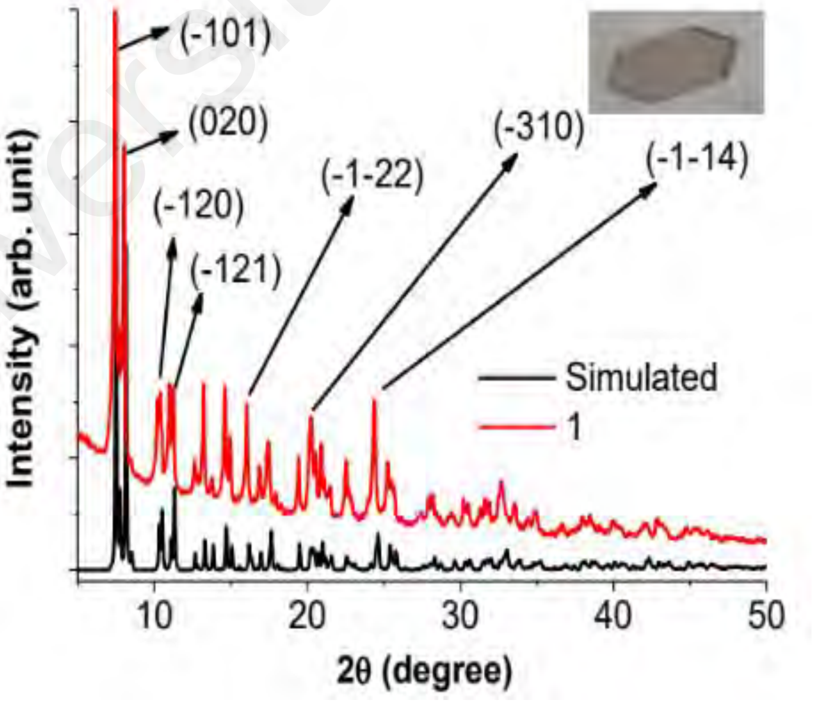

Figure 4.11: PXRD patterns of compound 1 showing: simulated vs. observed, with an inset shows plate crystal of 1.

The PXRD patterns' results confirmed that the compounds **1** to **10** (Figure 4.12) have the same structures. Furthermore, they confirmed that compounds **11** and **12** crystallize with high dense phase that share structural similarity with **1**, (Figure 4.13).

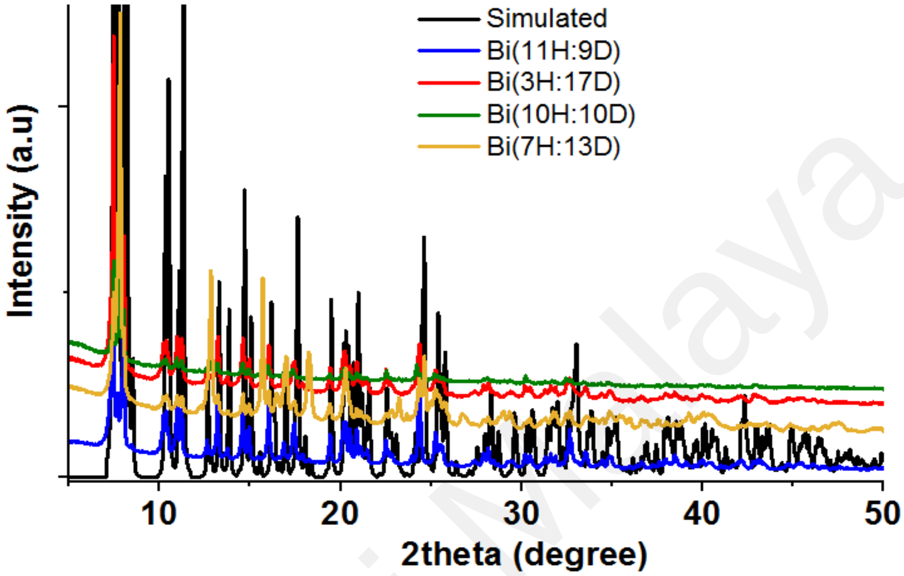

Figure 4.12: The PXRD measurement showing: simulated vs. observed patterns of various batches of synthesized BiMOFs.

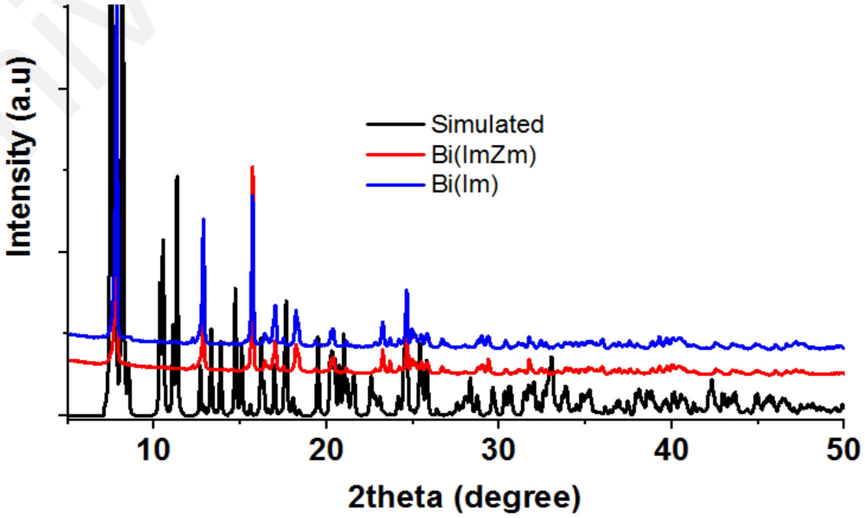

Figure 4.13: The PXRD measurement showing: simulated vs. observed and comparison between compound 1 and 11 patterns.

Realizing the moisture stable product with fully 3D coordination bond in the structure of **1** featuring an extended, hydrogen-bonded lattice water within the pores, Figure 4.6, the research went ahead to check the compound water stability by soaking it in water for 2 months at RT as well as refluxing it in water for 1 day. The research also went ahead to check the compound stability in other solvents by soaking some crystals (0.05 mmol) of different batches from BiMOFs in 1,4-dioxane, ethyl acetate and DMF for 2 months at RT, the pH of these resulting solutions was 5.5, 6 and 6.5, respectively, whilst, the pH of water solution of BiMOF was 4, Figure 4.14 shows the robustness and structural integrity of **1** after soaking for 2 months and 1 d reflux, while Figure 4.15 shows the robustness and structural integrity patterns of BiMOFs after soaking for 2 months in different solvents in which in all patterns, there is no indication of product decomposition and the crystallinity is preserved. Interestingly, during the 2 months course of water soaking, we noticed there was some change in color of **1** from white to yellow and based on PXRD and TGA analysis, the structure was intact. From such finding, a successful synthetic procedure, as mentioned in Experimental section, was obtained to synthesize **1** with varied lattice water contents based on DMF: H_2O used during synthesis.

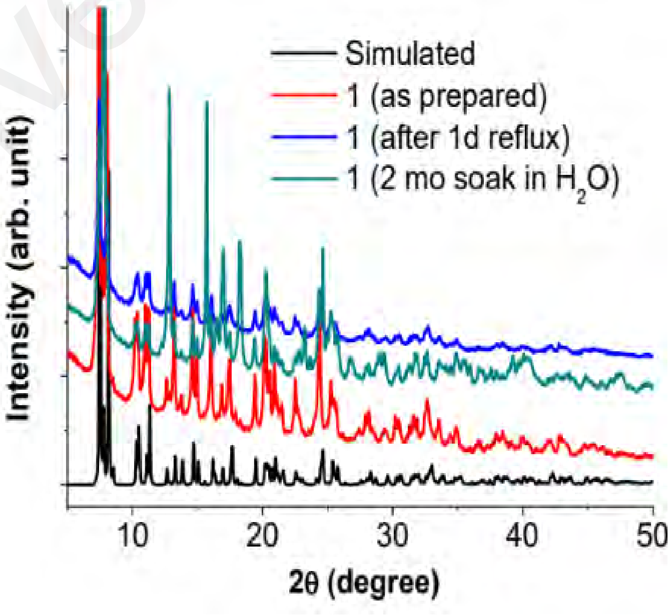

Figure 4.14: PXRD patterns of compound's water stability after 1d reflux and 2 months of soaking.

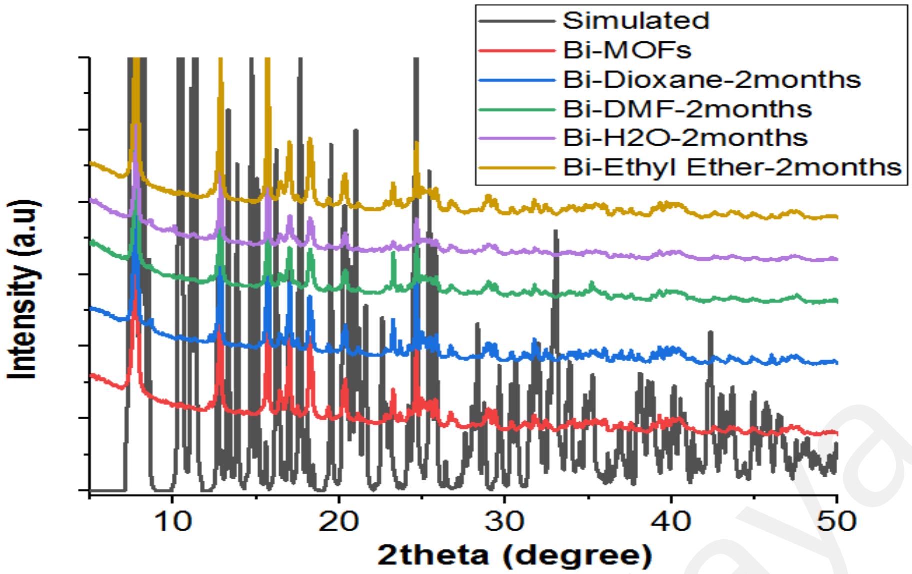

Figure 4.15: PXRD patterns of a mixture from compounds 1-10 show: simulated vs. observed for compounds' stability after 2 months of soaking in different solvents.

Furthermore, in attempt to check the stability of compound **1** in different pH environments, the soaking of **1** in different pH solutions (the pH of the produced solutions was 7-1.5) was done using $NaOH_{dil}$ and HCl_{dil} was done. The PXRD results of soaking the various batches of BiMOF in different pH environments showed that the structure of this MOF collapsed at pH below 4 and it lose its crystallinity and became amorphous compound at pH around 7, Figure 4.16. Therefore, the researcher could conclude (from the soaking of this framework in different solvents and different pH environments) that this framework remained to maintain its structure at the acidic environment only with pH between (6.5 - 4) and it is not stable (became amorphous) in the basic environment.

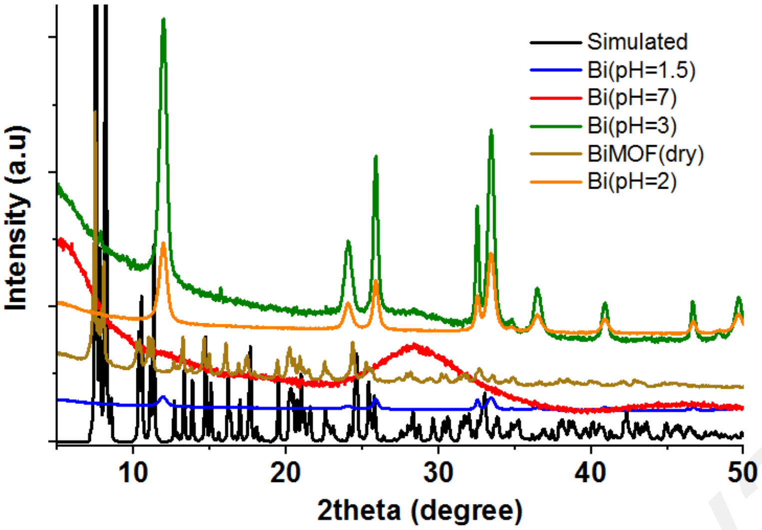

Figure 4.16: PXRD patterns of compounds 1-10 showing simulated vs. observed for compound's stability in different pH environments.

4.2.7 TGA measurements

To determine the thermal stability of the studied compounds, the thermo-gravimetric analysis was performed. Interestingly, the observation of variety in colors from by the different batches of BiMOFs, which produced via changing the molar ratios of the solvents' mixture, led to exhibit different TGA thermograms patterns based on the variety in water contents inside the pores (H_2O molecules) for each framework that in return it gives different colors under UV and visible lights, which could be anticipated to employee them as moisture sensors or proton conductors.

Highly water- stable compound (reach to about 20% of its weight) with nearly quantitative yield was identified by the reaction of DMF/H_2O -based $Bi(NO_3)_3 \cdot 5H_2O$ with H_2pzdc in the presence of Im or ImZm under slow evaporation with optimized condition. The studied compounds of BiMOFs (**1-12**) were analyzed at TGA machine under 20 ml/min flowing nitrogen gas (N_2) with temperature ramping at a rate of 5 °C/min starts from RT to 900 °C. The bulk phase purity of **1-12** was further confirmed by TGA analysis in which, the observed weight losses of the corresponding solvent and the ligand are closely matched with the theoretically expected values that was calculated from formulas obtained from crystallographic refinements, Figures 4.17, 4.18 (a - g). This may also support that, within the synthetic conditions, used in here, neither of the modulator is presented in the structure, in conjunction with crystallographic refinement results, as well as CHN analysis. Figure 4.17 displays TGA thermograms of **1** with varied water content; x = 0.5, 1.0, and 6.0 H_2O molecule per formula unit that leads to change in color from white to yellow as the lattice water content increases.

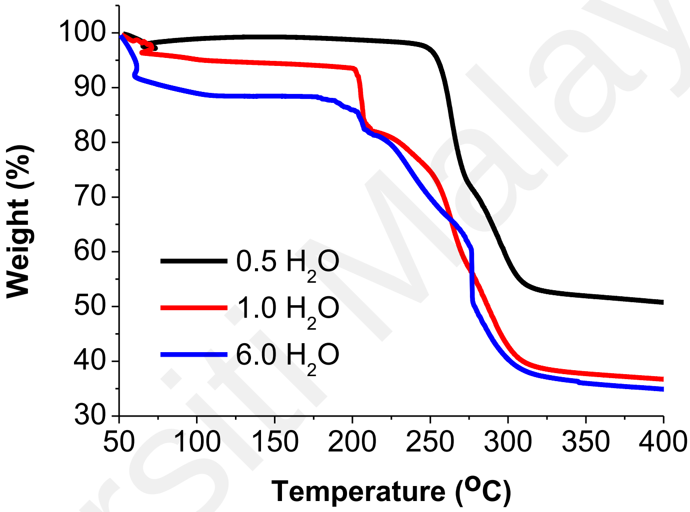

Figure 4.17: TGA thermograms of compound 1 showing varied lattice water contents.

4.2.7.1 Discussion of TGA measurements patterns of other batches of BiMOF

The first mass losing for the other different batches of BiMOF was around (100-85) % which started at around (60-90) °C corresponding to the releasing of hydrated water molecules that exist inside the pores of the frameworks. The frameworks of these MOFs remain stable until around (220-260) °C, when the organic ligand H_2pzdc starts to decomposed and lose its mass from around (90-25) %, then at 315 °C, the bismuth or bismuth oxide started to precipitate, Figure 4.18 (a - g). TGA measurements results are summarized in table 4.3.

Table 4.3: The summarized results of the TGA charts for different batches of BiMOF.

Comp. no.	first mass losing % = solvent formula weight (g/mole)	Temp. °C	No. of solvent molecules	Second mass losing % = ligand formula (g/mole)	Temp. °C
1	2.5% = 14 (g/mole)	60	0.78 H_2O	67 ≈ (Hpzdc + pzdc)	250
4	6% = 33.6 (g/mole)	50	1.87 H_2O	65 ≈ (Hpzdc + pzdc)	230
6	19.9% = 111.64 (g/mole)	55	6 H_2O	63 ≈ (Hpzdc + pzdc)	220
7	5% = 28 (g/mole)	85	1.6 H_2O	60 ≈ (pzdc + pzdc)	250
10	4% = 22.4 (g/mole)	120	1.25 H_2O	59 ≈ (Hpzdc + pzdc)	260
11	4% = 22.4 (g/mole)	130	1.25 H_2O	61 ≈ (Hpzdc + pzdc)	265
12	3% = 16.81 (g/mole)	110	0.9 H_2O	60 ≈ (Hpzdc + pzdc)	260

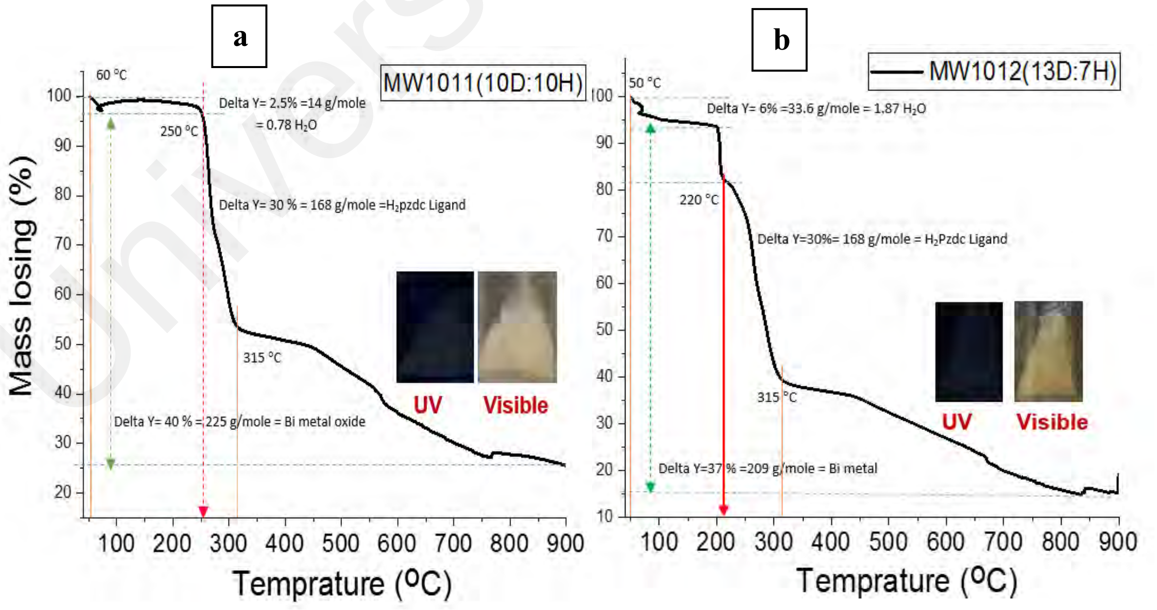

Figure 4.18: (a), (b) TGA thermograms of compounds 1, 4 respectively, (c), (d) TGA thermograms of compounds 6, 7 respectively, (e), (f) TGA thermograms of compounds 10, 11 respectively, (g) TGA thermograms of compound 12.

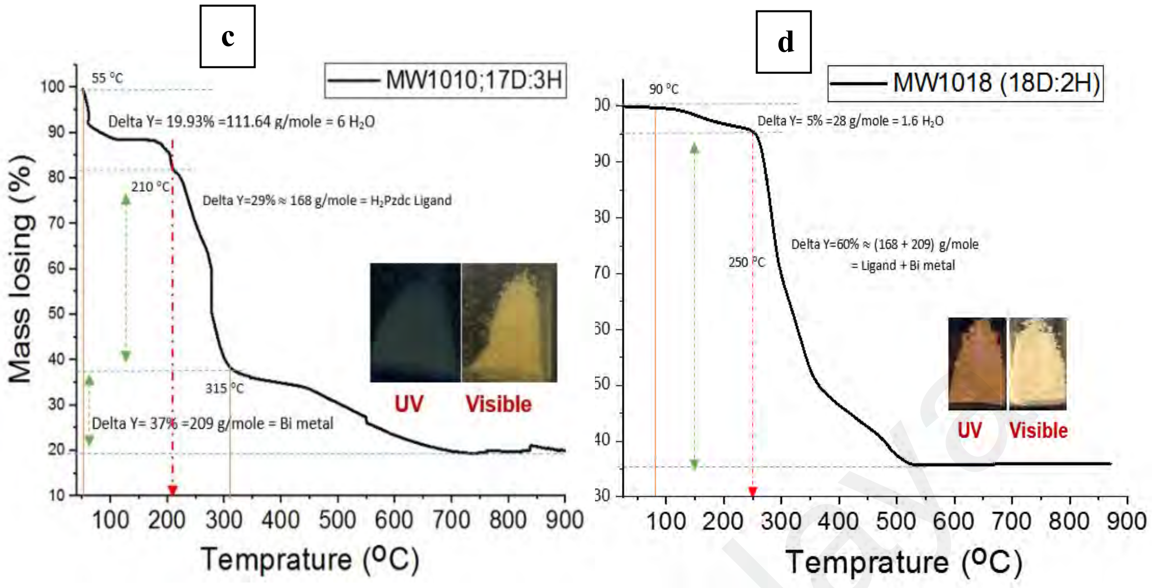

Figure 4.18: Continued.

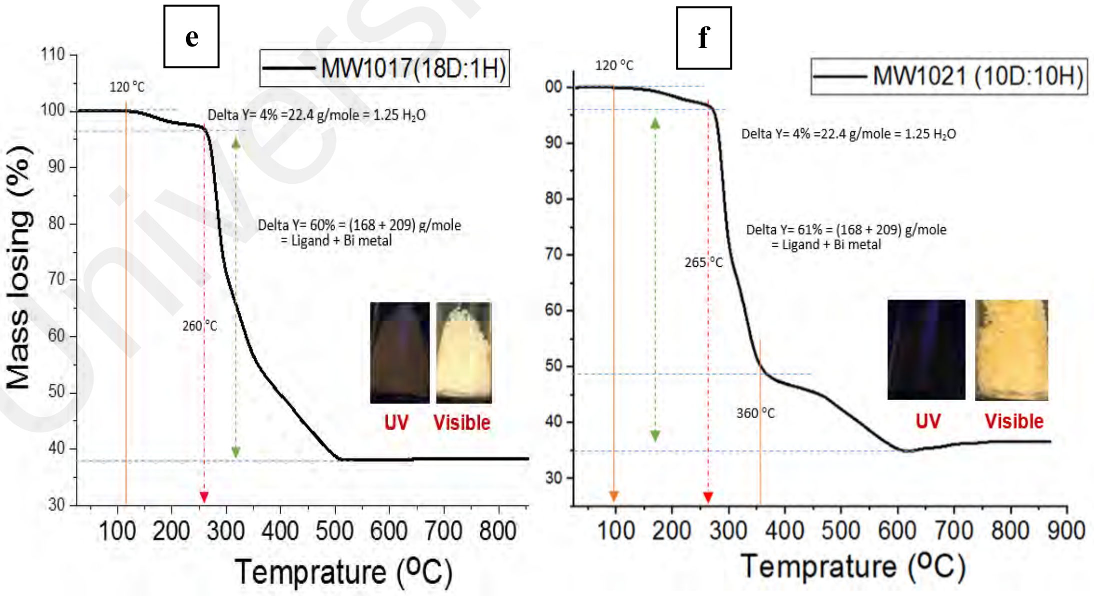

Figure 4.18: Continued.

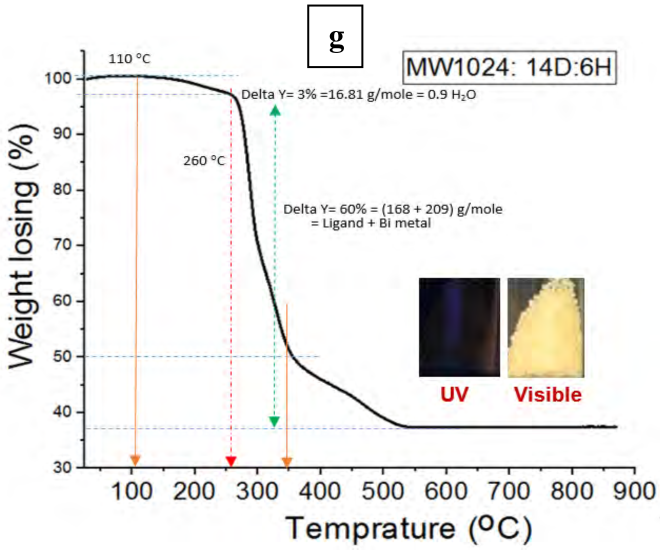

Figure 4.18: Continued.

4.2.8 Solid state UV-Vis analysis

As expected, the absorbance of yellow colored **1** is red-shifted [or Bathochromic Effect, which is a change in absorbance to a longer wavelength (λ)] from UV for (H_2pzdc) to violet region for (**1**), as shown in the solid-state UV-Vis spectra of as received H_2pzdc, **1** (white, x= 0.5), and **1** (yellow, x = 6.0), Figure 4.19.

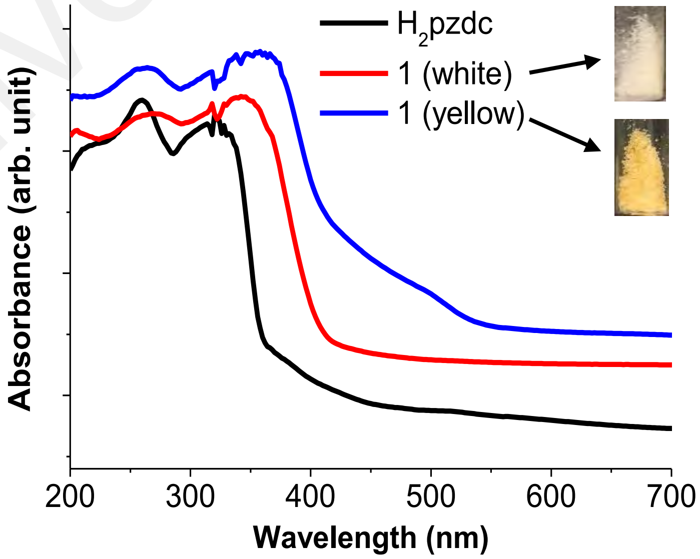

Figure 4.19: Solid state UV-Vis spectra of H_2pzdc (as received), 1 (white), and 1 (yellow) with insets showing the digital images of sample's color.

4.2.9 FESEM /EDX analysis

As the researcher got a proton conductivity value of 8.41 x 10^{-6} S.cm^{-1} for compound **1** and in order to improve/increase this value, there were some trials via the incorporating of Na$^+$ cations and/ or SO$_4^{2-}$ anions inside the pores of the framework of BiMOF. The proton or ionic conductivity of **1** maybe increased by cation exchange with highly mobile ions or incorporating highly mobile guest cation that facilitate ion conductivity. Therefore, the researcher conducted the following ways:

4.2.9.1 Soaking the BiMOFs [Bi-(Im) and/or Bi-(ImZm)] with NaCOOCH$_3$:

After soaking Bi(Im)MOF with aqueous solution of sodium acetate NaCOOCH$_3$ for 1 day, the highest percentage of Na$^+$ cations doping amount was 2.24% while the highest percentage of Na$^+$ cations doping amount was 5.62% after soaking this batch with NaCOOCH$_3$ for 1 week using FESEM /EDX. The structure of the framework kept its crystallinity with some missing peaks (maybe because the solvent of soaking (H$_2$O with Na$^+$) effects on the coordination order of the metal inside the framework or cause a strong orientation texture, which will result in peak intensities very different from a randomly oriented crystalline sample), that confirmed by PXRD pattern, Figure 4.20.

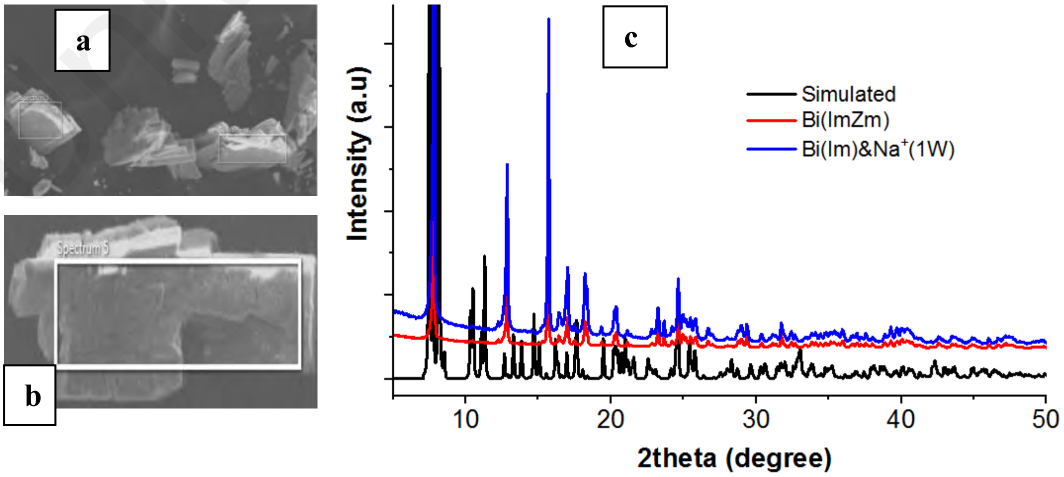

Figure 4.20: a), b) SEM image of Bi(Im)MOF after 1day, 1 week soaking with NaCOOCH$_3$ solution, c) PXRD analysis showing: simulated vs. observed patterns after 1week soaking.

The highest percentage of Na^+ cations doping amount after soaking Bi(Im)MOF with an aqueous solution of $NaCOOCH_3$ for 3 weeks (until it became nontransparent) using FESEM /EDX was 6.20 %. The structure of BiMOF was collapsed and became amorphous, the blue PXRD pattern, Figure 4.21, because the solution which used for soaking this framework is alkaline (the pH up to 6.5) and BiMOF is not stable at this range of pH as mentioned previously in the section of checking its stability in different pH environments.

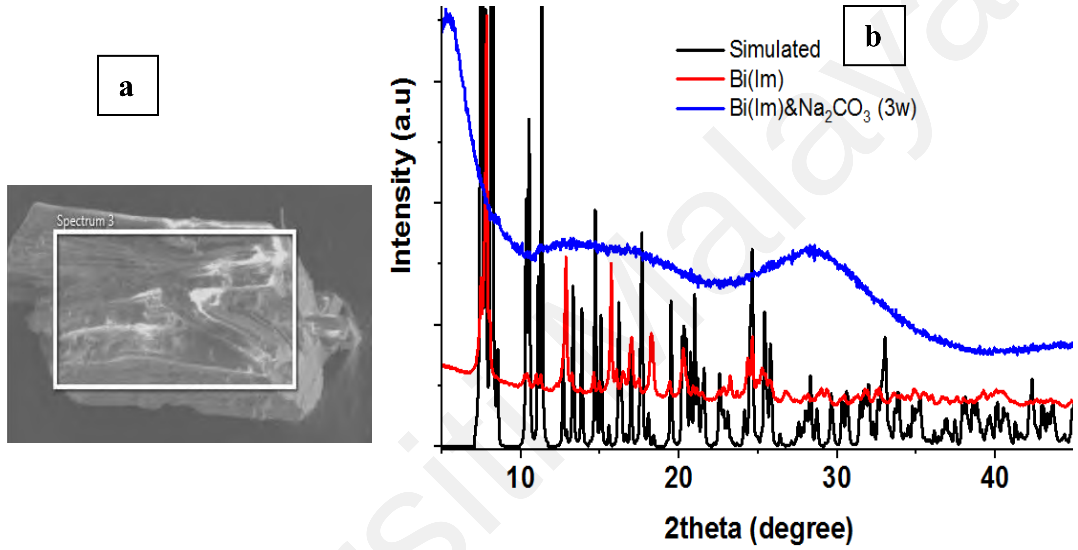

Figure 4.21: a) SEM image of Bi(Im)MOF, b) PXRD measurement showing: simulated vs. observed patterns of soaking various batches of synthesized Bi(Im)MOFs in $NaCOOCH_3$ after 3 weeks.

The highest percentage of doping amount for Na^+ cations after soaking Bi(ImZm)MOF with an aqueous solution of $NaCOOCH_3$ for 2 days was 9.26 % using FESEM /EDX, the structure that confirmed by PXRD pattern still maintain, Figure 4.22.

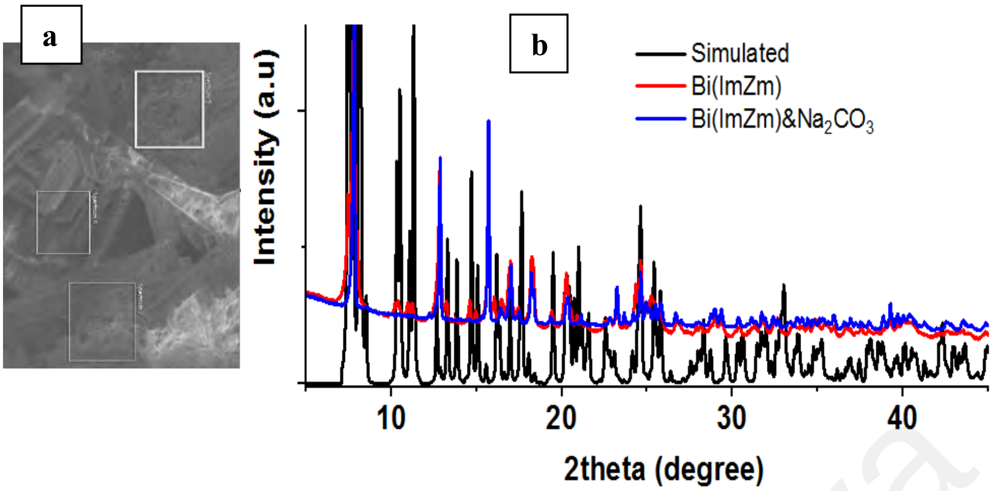

Figure 4.22: a) SEM image of Bi(ImZm), b) PXRD measurement showing: simulated vs. observed patterns of soaking of Bi(ImZm)MOFs in $NaCOOCH_3$ for 2 days.

4.2.9.2 Soaking of BiMOFs [Bi-(Im) and/or Bi-(ImZm)] with Na_2SO_4:

The highest percentage of doping amount for Na^+ cations after soaking various batches of synthesized Bi(Im)MOF with an aqueous solution of sodium sulphate Na_2SO_4 for 1 day was 8.33 % using FESEM /EDX, the structure kept its crystallinity with some missing peaks, confirmed by PXRD pattern, Figure 4.23.

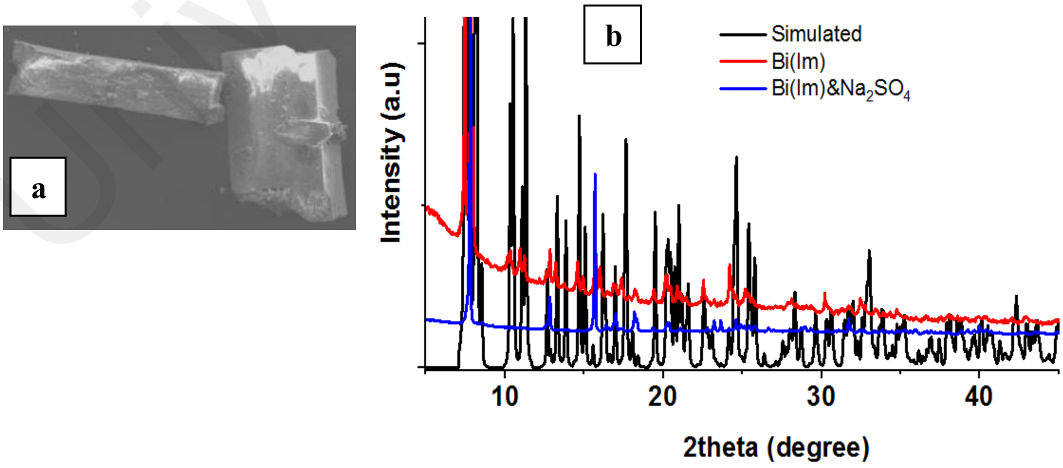

Figure 4.23: a) SEM image of Bi(Im), b) PXRD measurement showing: simulated vs. observed patterns of synthesized Bi(Im)MOFs soaked in Na_2SO_4 after 1day soaking.

The highest percentage of Na^+ cations doping after soaking Bi(ImZm)MOF with an aqueous solution of Na_2SO_4 for 2 days using FESEM /EDX was 10.73 %, while it was 21.60 % after soaking this MOF with same cations during 1 week and the structure reminded keep its crystallinity with some missing peaks according to the PXRD pattern, Figure 4.24.

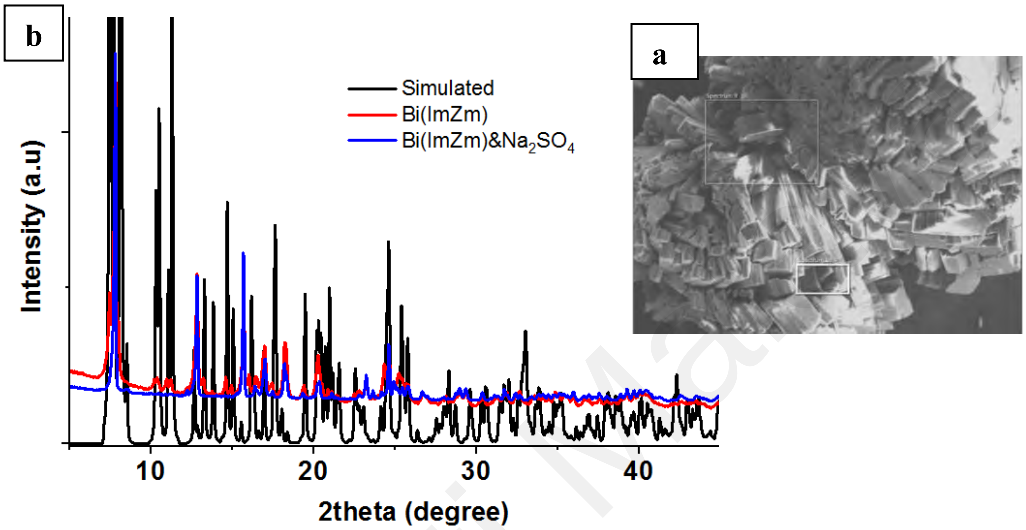

Figure 4.24: a) SEM image of Bi(ImZm) after 1 week soaking with Na_2SO_4 solution, b) PXRD measurement showing: simulated vs. observed patterns of soaking various batches of synthesized Bi(ImZm)MOFs in Na_2SO_4 for 1 week.

Finally, the research can conclude from this study that even after soaking BiMOF with Na^+ cations or SO_4^{2-} anions, there were no improving for the proton conductivity of this compound maybe because these ions could not incorporate inside the pores of the framework. Furthermore, the soaking of Bi(ImZm)MOF batch in an aqueous solution of Na^+ cations is better than the soaking of Bi(Im)MOF batch, also the soaking of these two batches (Im and ImZm) in Na_2SO_4 solution is better than soaking them in $NaCOOCH_3$ solution because it gave a high percentage of doping amount.

4.2.10 Proton Conductivity measurements

The presence of an extended, hydrogen-bonded lattice water along the *c*-direction (Figure 4.6) that attract more dynamic lattice water into the pore (up to 4.5 water molecules per formula unit in this case) and the fact that the resulting compound is highly stable after 2 months of soaking and 1day reflux in water (Figures 4.14, 4.15), fulfill the general pre-requisite for proton conductivity [227, 228]. AC impedance analysis with controlled relative humidity (RH) and temperature was used to measure proton conductivity of **1** using a pelletized sample, the resulting conductivities were calculated from fitting of the Nyquist plots, Figure 4.25. As shown in Table 4.4, the room temperature conductivity increases with the increasing of RH with a highest value 6.11 x 10^{-7} S·cm^{-1} at 95 % RH. A cycle of heating and cooling at maintained 95% RH results in the highest proton conductivity of **1**, 8.41 x 10^{-6} S·cm^{-1}, at 85°C and 95% RH, Table 4.5. Post measurement PXRD (Post PC), Figure 4.26, shows that, within the limit of PXRD, the structure integrity and the original phase of **1** is maintained with lowering of the crystallinity as the peaks broadened and there are some new unidentified peaks appear, which may indicate an additional phase co-exist within the compound after proton conductivity measurement (Post PC).

From the single crystal structure, there are two features that suggest why the proton conductivity for this MOF is not higher. First, the channels only propagate in one dimension, meaning that multidirectional efficient transport is a challenge and consequently, grain boundary resistances would be enhanced [229]. Secondly, the hydrogen-bond pathway between the included water molecules is not continuous with significant jumps between dimeric units; the shortest distance between them is 11.5863(8) Å, Figure 4.9. The activation energy for the proton transfer is calculated as 0.31 eV, Figure 4.34 (b), which is in the higher end of that generally regarded for a Grotthuss mechanism, i.e. a less efficient proton hopping mechanism consistent with the crystal structure. Although the proton conductivity of **1** is of moderate value for proton conducting MOFs, [227, 228, 230] its high water stability and the fact that lone-pair containing compounds are adaptable to defects [95, 144, 231, 232].

Table 4.4: Proton conductivity of 1 at 25 °C under variable humidity.

Temperature (ºC)	Humidity (% RH)	Conductivity ($S \cdot cm^{-1}$)
25	35	5.08×10^{-10}
25	45	6.61×10^{-10}
25	55	1.56×10^{-9}
25	65	3.95×10^{-9}
25	75	1.27×10^{-8}
25	85	5.35×10^{-8}
25	95	6.11×10^{-7}

Table 4.5: Proton conductivity of 1 at 95% humidity RH under variable temperature.

Temperature (^{o}C)	**Humidity (% RH)**	**Conductivity (S·cm^{-1})**	**Δ (S/cm)**
25.0	95	6.11×10^{-7}	1.38E-08
35.0	95	1.43×10^{-6}	3.24E-08
45.0	95	2.16×10^{-6}	4.88E-08
55.0	95	2.92×10^{-6}	6.58E-08
65.0	95	3.72×10^{-6}	8.40E-08
75.0	95	1.76×10^{-6}	3.98E-08
85.0	95	8.41×10^{-6}	1.90E-07
75.0	95	2.96×10^{-6}	6.67E-08
65.0	95	2.22×10^{-6}	5.02E-08
55.0	95	1.82×10^{-6}	4.11E-08
45.0	95	1.41×10^{-6}	3.18E-08
35.0	95	2.08×10^{-6}	4.70E-08
25.0	95	1.56×10^{-6}	3.53E-08
25.0	95	6.96×10^{-6}	1.57E-08

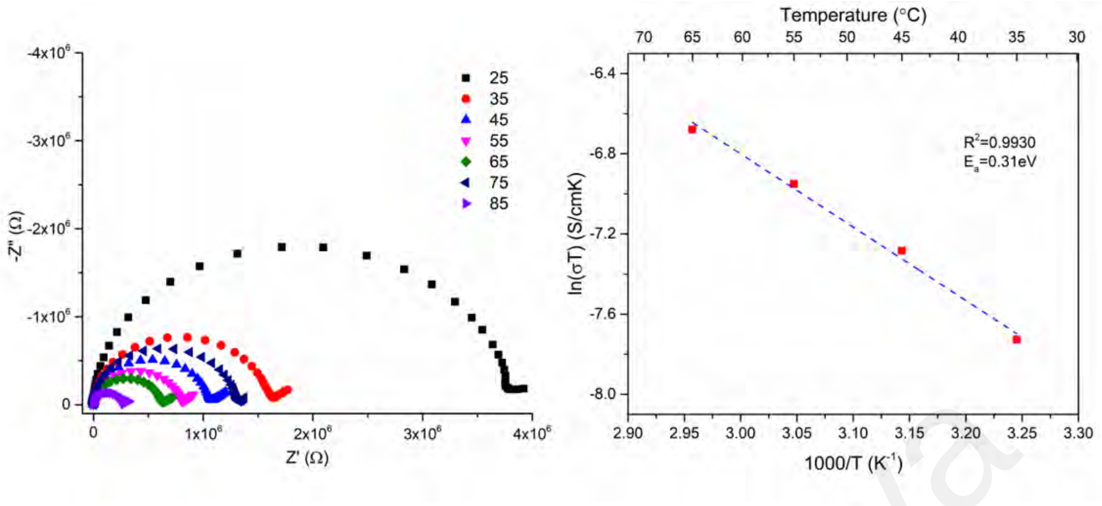

(a) (b)

Figure 4.25: (a) Nyquist plot at 95% RH with varied temperatures, and (b) Arrhenius plot of compound 1.

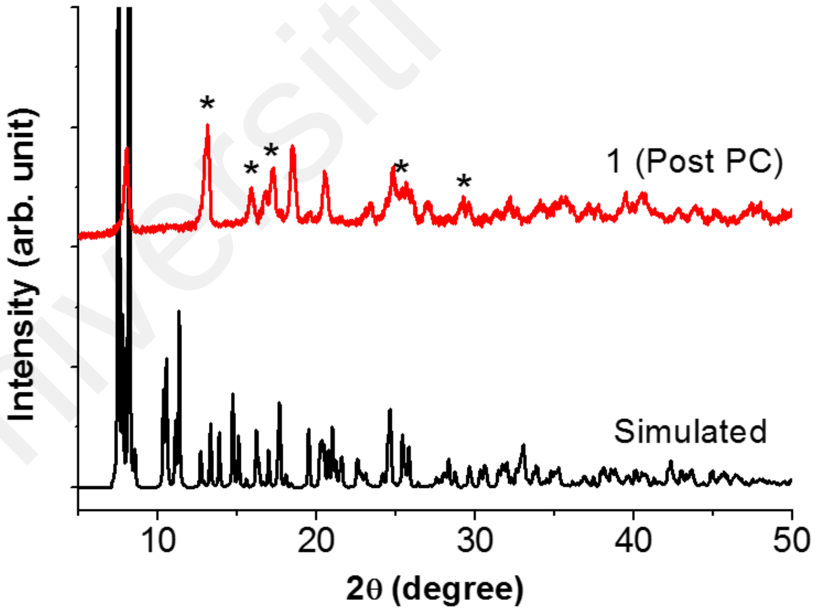

Figure 4.26: PXRD pattern of 1 after proton conductivity (Post PC) measurements: Simulated vs. Post PC.

4.3 Synthesis, characterization and properties of Lead based-MOFs

Three new lead-based MOF; (**14**, **17**, **18**), with exotic properties by using a simple facile and optimized dissolution-crystallization method were successfully synthesized by using H_3BTC, with or without aniline (An) or imidazole (Im). These new PbMOFs are reported along with their structural characterizations and photo luminescent properties.

In recent years, there is an immense interest in discovering white-light single phosphors from Pb-based compounds, due to its intrinsic broadband emission originated from self-trapping excision and defects [233]. Several white emitting Pb-based MOCPs have also been reported [234]. Enriching the library of single component, near white-emission Pb MOFs, herein the author reports three new BTC-containing PbMOFs, in which, compound **17** displays near white-light emission.

It was able to get different porous compounds based on lead(II) that show different structures with different pore sizes and potential different photoluminescence (PL) under the long wave length of UV light (365nm) via only varying the solvents mixtures and employing simple and optimized solution layering approach [235].

The combination of lead(II) nitrate, $Pb(NO_3)_2$, and benzene 1,3,5-tricarboxylic acid ($H_3BTC= C_9H_6O_6$) as O-donor ligand, Figure 4.27, with or without N-donor ligand (like aniline, imidazole) in a mixture of (H_2O/1,4-dioxance), (H_2O/methanol (MeOH)) or (H_2O/DMF) produced three different new porous coordination polymers (**13, 14**, **15**, **17** and **18**). The pores of these compounds was governed by the solvent, that used during the synthesis. Air stable compounds **14** and **17** with nearly quantitative yield were identified, by the reaction of aqueous-based $Pb(NO_3)_2$ with 1,4-dioxane or MeOH solution of H_3BTC in the presence of aniline (An) or (Im) for compounds **14** or **17**, respectively, under dissolution-crystallization with optimized condition. Compound **18**, on the other hand, was found to be relatively unstable at ambient condition; fresh batch with the use of mother liquor is required for structural characterizations.

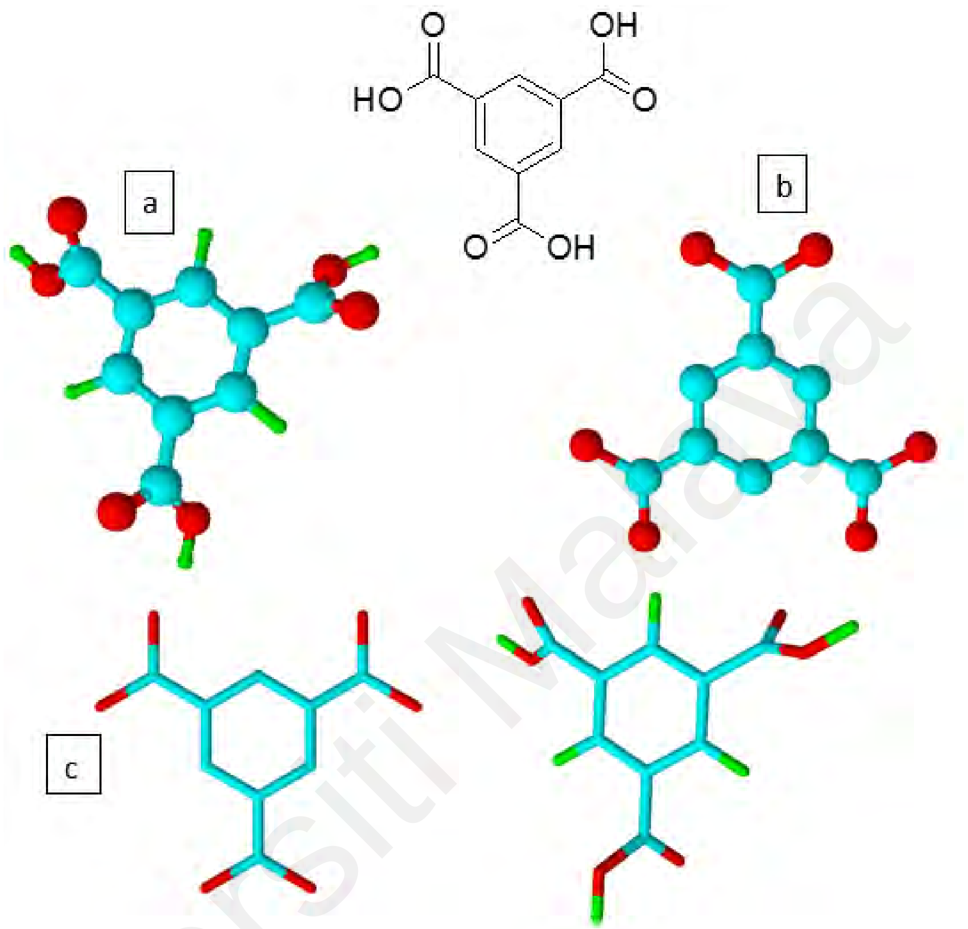

Figure 4.27: (a, b) The ball and sticks module, (c) the sticks module of the free linker H_3BTC.

The structure was determined, by single crystal X-ray diffraction, and its single-phase purity was examined by bulk sample measurements, by using powder X-ray diffraction coupled with TGA and CHN analysis. Prior to this discovery, the researcher attempted several synthetic conditions to obtain quantitative yields, that involved combinations of the following variables, such as (a) molar ratio of $Pb(NO_3)_2$ and H_3BTC, (b)variety of solvent or mixture of solvents. All three compounds were found to change their structures, during storage, even in the presence of mother liquors.

The use of modulator, such as mono-protic acid or monocarboxylic acid, is often adopted to produce an air stable transition metal (TM)-based MOFs with quantitative yield [213- 216]. Further, Li et. al clarified that the use of an appropriate modulator, in some cases without being present in the structure, could modify the surface structure of TM-based MOFs, thus greatly enhances the stability and performance of the resulting MOF [236].

Based on the previous report, a borderline organic base is a suitable modulator for a borderline acid of Pb-based MOCP resulting in a stable and phase pure compound [94], in accordance with Pearson's hard-soft acid base (HSAB) concept [237, 238]. Adopting the above, the researcher found that, the use of (An) or (Im), after several trials using other N-containing organic molecules as modulation agents, was required to make stable compounds of **14** and **17**, respectively.

The unidentified peaks in the PXRD patterns of **13** and **15** were gradually disappeared as the suitable, a modulation agent was added during reaction, that eventually, after optimizing the synthetic conditions, reached the PXRD phase pure patterns for **14** and **17** respectively with close to quantitative yields. At the moment, using the above-mentioned synthetic conditions for **14** and **17**, the researcher could not detect the presence of aniline nor imidazole within the structures crystallographically nor by TGA nor CHN analysis, which supports the role of modulation for aniline and imidazole in these cases. Further investigations to examine the role of the modulator during synthesis, reaction mechanism, and resulting structural defect vs. performance are currently on-going.

The use of N-containing molecules as modulation agents gave big crystals of **14** and **17** from the same stoichiometric ratios of **13** and **15** respectively, which both have pure phase PXRD patterns that matches with the simulated one with potential PL.

Unfortunately, attempts to make an air stable compound **18** was unsuccessful. Attempts to obtain these three phases by simple solvent exchange were unfruitful either. Activation attempts for **14** and **17**, starting from rather harsh thermal activation to relatively milder supercritical CO_2, as well as, solvent exchange activations were unsuccessful.

4.3.1 Elemental analysis (C.H.N)

Results tabulated in Table 4.6 summarized the molecular formula, molecular weight, %yield, and elemental analyses for the synthesized MOFs. The molecular formula and molecular weights of the new compounds was obtained from the SCXRD analyses. The elements analysis ensures that, the experimental results are matched well with the calculated values theoretically.

Table 4.6: The physical data of the new Lead synthesized compounds.

Comp. code	**Molecular formula, colour and appearance**	**Molecular weight** g/mole **Yield %**	**Percentage of element (%) Experimental (Theoretical)**		
			C	**H**	**N**
13	$C_{13}H_{13}O_9Pb$ **white small crystals**	520.46 24.30%	30.23 (29.98)	2.20 (2.50)	0.20 (-)
14	$C_{13}H_{13}O_9Pb$ **Light blue big crystals**	520.46 88.37%	30.02 (29.98)	2.52 (2.50)	0.00 (-)
15	$C_{12}H_{11}NO_7Pb$ **white tiny crystals**	488.44 58.50%	A quantitative analysis of the crystals was not performed due to decomposition of the product outside of mother liquor.		
17	$C_{12}H_{11}NO_7Pb$ **white small crystals**	488.44 79.68%	23.59 (23.74)	0.89 (0.90)	-0.01 (-)
18	$2(C_9H_4O_8Pb),O$ **white big crystals**	910.66 91%	23.65 (23.74)	0.89 (0.90)	0.00 (-)

4.3.2 FTIR Vibrational spectra of PbMOFs

The FTIR spectral data of the free ligand/ linker (H_3BTC), Figure A-9 in Appendix A, were compared with those of the new synthesized Pb MOFs. It was observed from the FTIR spectra of **13** and **14**, Figures A-10 and A-11, respectively, and also from the spectra of **15** and **17** Figures A-12 and A-13, respectively, that each pair of these compounds depict peaks nearly in similar region, which confirmed (beside the PXRD, TGA charts and CHN measurements) that, each pair of these compounds have the same structures.

The FTIR spectrum of the free ligand H_3BTC, shows also a broad band appears around 3100-2546 cm^{-1} assigned to ν(O-H) of the COOH group. A weak band of absorption appears at 2993 cm^{-1} which is overlapped with the ν(O-H) and attributed to ν(C-H) vibrations of sp^2 C of the ring. The δ(CH) vibration of benzene ring generally appears as strong sharp band at region 1271 cm^{-1} [161].

The FTIR spectrum of the free ligand H_3BTC shows also the characteristic symmetric and asymmetric stretching vibrations of carboxylate groups (Figure A-9). The ν(COO) vibrations of multi carboxylate groups, that connected to the benzene ring of the free H_3BTC ligand appeared as a strong bands at 1715- 1694 cm^{-1} due to the out of plane vibrations of ν(C=O) mode and the bands that appear at 1402-1325 cm^{-1} due to ν(C-O) mode; both attributed to the asymmetric and symmetric ν(COO) vibrations of the free ligand [26].

The ν(C=O) vibrations are shifted in the spectrum of PbMOFs with 1,4-dioxane to the lower wavenumbers and observed at the region 1695-1608 cm^{-1} for **13** and as a sharp peak at the region 1693 cm^{-1} for **14**, an overlapped peak of ν(C-O) vibrations appear at 1367 cm^{-1} for **13**, Figure A-10, and at 1375 cm^{-1} for **14**, Figure A-11. The ν(C=O) vibrations in the spectrum of PbMOFs with MeOH are also shifted and observed at the region 1696-1607 cm^{-1} for **15** and 1699-1608 cm^{-1} for **17**, respectively, whilst an overlapped peak appears at 1368 cm^{-1} for **15**, Figure A-12 and at 1369 cm^{-1} for and **17**, Figure A-13, respectively. The ν(C=O) vibration in the spectrum of PbMOFs with DMF, compound **18**, Figure A-14, is shifted to the region 1695-1606 cm^{-1} and an overlapped peak appears at 1368 cm^{-1} attributed to ν(C-O) vibration, which provide a good evidence that, the ligand coordinated to the metal cations and display a different coordination modes [220, 221]. The peak at 1452 cm^{-1} is ascribed to the C-C vibration in the aromatic ring [223]. Furthermore, the band around 741 cm^{-1} is related to the bending vibration of C-H group of the tri-substituted ring [239].

The coordination between the Pb metal ion and O atom of COO^{-} group of the ligand H_3BTC to form the new PbMOFs could confirmed also by observing some new bands, that appear in the spectra of the new compounds; at: 514 cm^{-1} for **13**; 515 cm^{-1} for **14**; 522 cm^{-1} for **15**; 535 cm^{-1} for **17** and at 516 cm^{-1} in the spectrum of **18**, Figures A-10 to A-14, respectively. All these new bands attributed to a vibrational mode, that involving the metal center and confirm the formation of Pb-O interaction in these new MOFs and give a good evidence that H_3BTC ligand coordinated to the metal center cation Pb(II) in the new compounds to display different coordination modes [194, 222], Figure 4.28, (All the FTIR patterns of other PbMOF compounds uploaded at Appendix A).

The presence of Lewis base (the O–H moiety) in these compounds are confirmed by Attenuated Total Reflectance Fourier-Transform Infrared (ATR FTIR) spectra from the observation of a peak around 3575 cm^{-1} indicating the existence of weakly hydrogen-bonded hydroxyl groups, Figure 4.29, confirming the observation in the crystal structure. Reduction of proton exchange due to relatively long hydrogen bonds leads to relatively sharp O-H stretch. A sharper peak, for a comparison, would be observed at 3600 cm^{-1} for a fully free O-H group of carboxylic acid in MOCP [240].

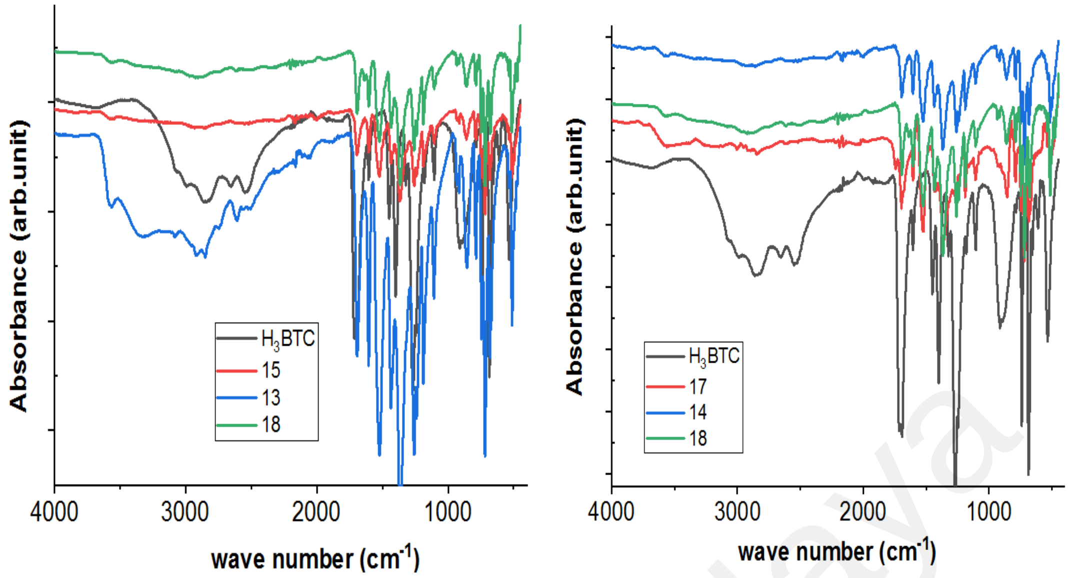

Figure 4.28: ATR FTIR spectra of: (left) 13, 15 and 18 comparing with the H$_3$BTC ligand, (right) 14, 17 and 18 comparing with the H$_3$BTC ligand showing spectral region extended 4000-400 cm^{-1}.

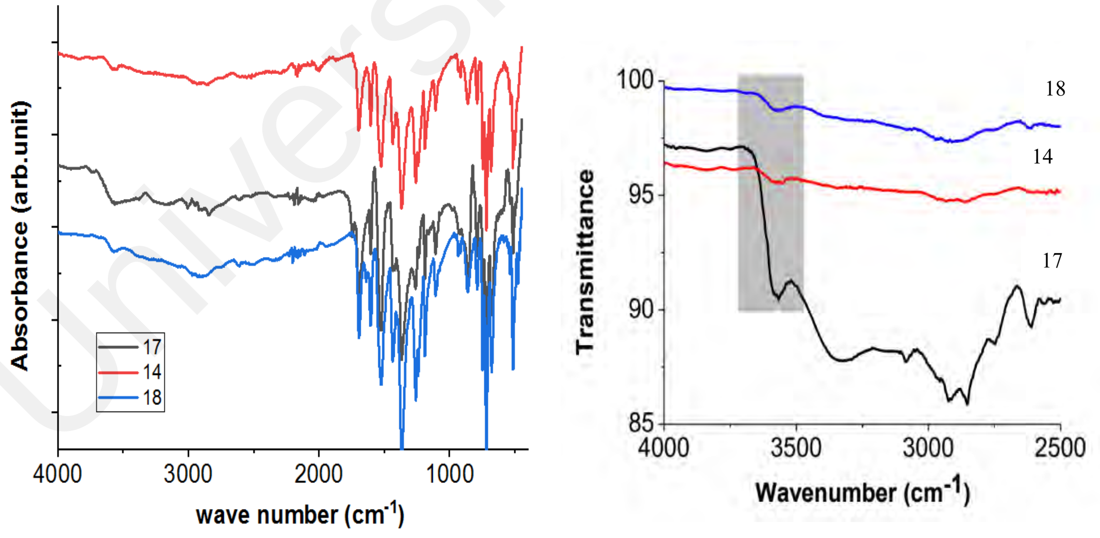

Figure 4.29: ATR FTIR spectra of 14, 17 and 18; (left) showing spectral region extended 4000-400 cm-1, (right): showing spectral region (shaded in grey) of weakly hydrogen-bonded O-H stretch.

4.3.3 SCXRD analysis: Structural Description

The single crystal structure refinements with their relevant crystallographic data for **14**, **17** and **18** are found in Table 4.7. Tables B-2 to B-4 in Appendix B show representative bond distances and angles of compounds **14**, **17** and **18**, respectively. Figure 4.30 (A) depicts the asymmetric unit of **14**, that consists one site of a lead atom ($Pb1^{iii}$) with one monoprotonated ligand ($HBTC^{-}$) at (O5) site, and a half molecule of uncoordinated 1,4-dioxane. The O atoms of $HBTC^{-}$ complete the coordination sphere around the lead cation, forming a distorted pentagonal bipyramid, PbO_7, Figure 4.30 (B).

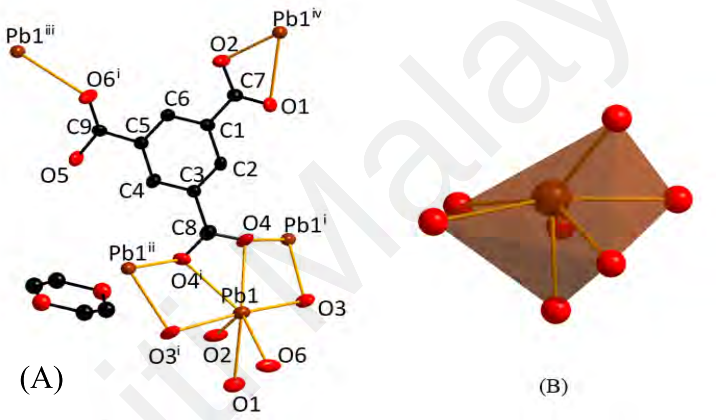

Figure 4.30: (A) Labeling scheme of compound 14. Displacement ellipsoids drawn at the 50% probability level. (B) The coordination environment around the lead atom in 14.

The asymmetric units of compounds **17** and **18**, also comprised of one lead cation, one $HBTC^{-}$, with additional five uncoordinated molecular water for **17** and one coordinated DMF for **18**. A distorted bicapped pentagonal bipyramid, PbO_9, was observed for both **17** and **18** with coordinated oxygen atoms are solely from the monoprotoned ligand ($HBTC^{-}$) for **17**, Figure 4.31, whereas, **18** has an additional coordinated oxygen from DMF (because the N atom in DMF structure connected to two methyl groups that push the electron density away from N atom and towards O atom, which has a higher electron negatively than N atom), Figure 4.32.

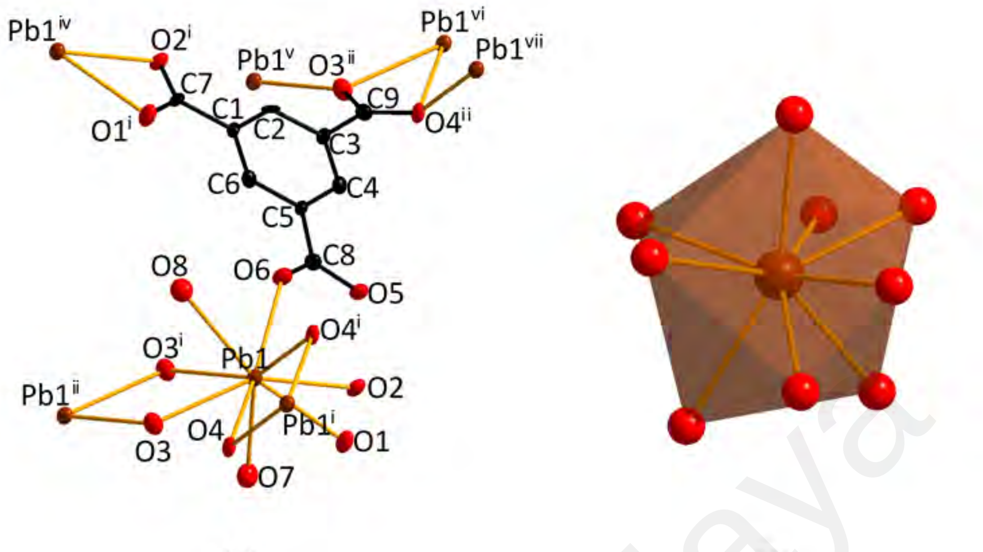

(A) (B)

Figure 4.31: (A) Labeling scheme of compound 17. Displacement ellipsoids drawn at the 50% probability level. (B) The coordination environment around the lead atom in 17.

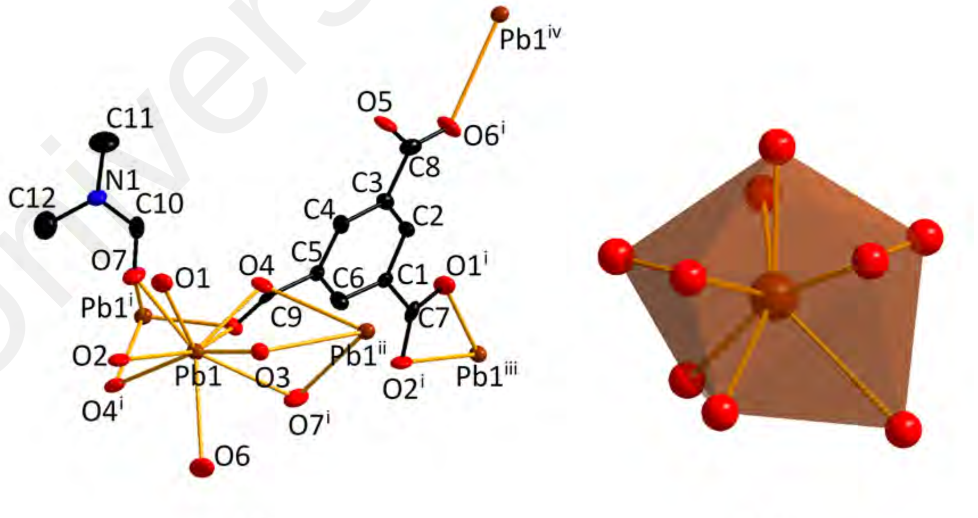

(A) (B)

Figure 4.32: (A) Labeling scheme of compound 18. Displacement ellipsoids drawn at the 50% probability level. (B) The coordination environment around the lead atom in 18.

Table 4.7: Crystal Data and Structure Refinement details for 14, 17 and 18.[a]

	Compound **14**	Compound **17**	Compound **18**
Empirical formula	$C_{13} H_{13} O_9 Pb$	$C_{18} H_8 O_{17} Pb_2$	$C_{12} H_{11} N O_7 Pb$
Formula weight	520.42	910.62	488.41
Temperature	293(2) K	203(2) K	296(2) K
Wavelength	0.71073 Å		
Crystal system	monoclinic	triclinic	monoclinic
Space group	*C*2/*c*	*P* -1	*P* 2_1/*n*
Unit cell dimensions	*a* = 17.239(2) Å, *α* = 90.00° *b* = 7.0225(8) Å, *β*= 104.735(10)° c = 19.911(2) Å, *γ* = 90.00°	*a* = 7.3989(4) Å, *α* = 94.336(4)° *b* = 8.2196(4) Å, *β* = 104.943(4)° *c* = 10.1437(5) Å, *γ* = 108.270(3)°	*a* = 10.5004(3) Å, *α* = 90° *b* = 7.1398(3) Å, *β* = 102.160(2)° *c* = 17.1285(5) Å, *γ* = 90°
Volume	2331.2(5) $Å^3$	557.70(5) $Å^3$	1255.32(7) $Å^3$
Z	6	1	4
Density (calculated)	2.224 g/cm^3	2.711 g/cm^3	2.584 g/cm^3
Absorption coefficient	10.900 mm^{-1}	15.163 mm^{-1}	13.476 mm^{-1}
F(000)	1470	416	912
Crystal size	0.12 × 0.032 × 0.024 mm^3	0.13 × 0.068 × 0.022 mm^3	0.127 × 0.032 × 0.026 mm^3
θ range for data collection	2.12 to 28.26°	2.648 to 28.35°	2.433 to 27.099°
Index ranges	-22<=h<=21, -9<=k<=9, -25<=l<=26	-8<=h<=9, -10<=k<=10, -13<=l<=13	-13<=h<=13, -9<=k<=9, -21<=l<=21
Reflections collected	14566	9327	10151
Independent reflections	2857 [R_{int} = 0.0910]	2752 [R_{int} = 0.0683]	2686 [R_{int} = 0.0719]
Completeness to θ = 27.56°	98.4%	99.5%	97.8%
Refinement method	Full-matrix least-squares on F^2		
Data / restraints / parameters	2857 / 0 / 174	2752 / 122 / 169	2686 / 0 / 190
Goodness-of-fit	1.000	1.006	1.029
Final *R* indices [I>2σ(I)]	R_{obs} = 0.0389, wR_{obs} = 0.0737	R_{obs} = 0.0471, wR_{obs} = 0.1125	R_{obs} = 0.0371, wR_{obs} = 0.0683
R indices [all data]	R_{all} = 0.0635, wR_{all} = 0.0819	R_{all} = 0.0616, wR_{all} = 0.1207	R_{all} = 0.0567, wR_{all} = 0.0767
Largest diff. peak and hole	1.523 and -1.321 e·$Å^{-3}$	3.343 and -2.571 e·$Å^{-3}$	1.384 and -1.087 e·$Å^{-3}$

$$^{a}R = \sum \| F_0 | - | F_C \| / \sum \| F_0 \| .wR_2 = \left\{ \sum \left[w\left(F_0^2 - F_C^2\right)^2 \right] / \sum \left[w\left(F_0^2\right)^2 \right] \right\}^{1/2}$$

Such distorted polyhedral was also observed in other lead-based coordination compounds, the Pb-O bond length fall into the range of 2.415(6) - 2.738(7) Å, typically observed in Pb-based coordination polymers [241- 246]. All coordination modes of $HBTC^{-}$ around Pb center for **14**, **17** and **18** show O, O-chelation, oxygen bridging, monodentate, as well as, uncoordinated oxygen atoms, which includes oxygen bridging from DMF in **18**, Figures 4.30 - 4.32.

The three compounds are built from slightly different 1D structures, in which PbO_x (x = 7 for **14**, and 9 for **17** and **18**) polyhedral are linked by oxygen bridging in zigzag manner to form 1D structures of $(Pb_2O_{12})_n$, $(Pb_2O_{16})_n$, and (Pb_2O_{15})n moieties for **14**, **17** and **18**, respectively, Figure 4.33. $(Pb_2O_{12})_n$ and $(Pb_2O_{15})_n$ moieties extend along the b-axis, whereas, $(Pb_2O_{16})_n$ stretches along the a-direction. Double oxygen bridges with zigzag pattern was observed for **14** (Figure 4.30) exhibiting nearly straight O-Pb-O angle (167.8 °), whereas, **17** and **18** exhibited slightly bent zigzag patterns (O-Pb-O angle of 150.8° for **17** and 136.8° for **18**), Figures 4.31, 4.32. Additional bridging oxygen from DMF was observed for **18**, Figure 4.33 (C). Unlike the 1D moieties of **14** and **17**, Figure 4.33 (A and B), that comprise of alternate polyhedral related by 2_1 screw axis, an inversion center relates the alternate polyhedral in **18** forming the 1D building block of the compound, Figure 4.33 (C).

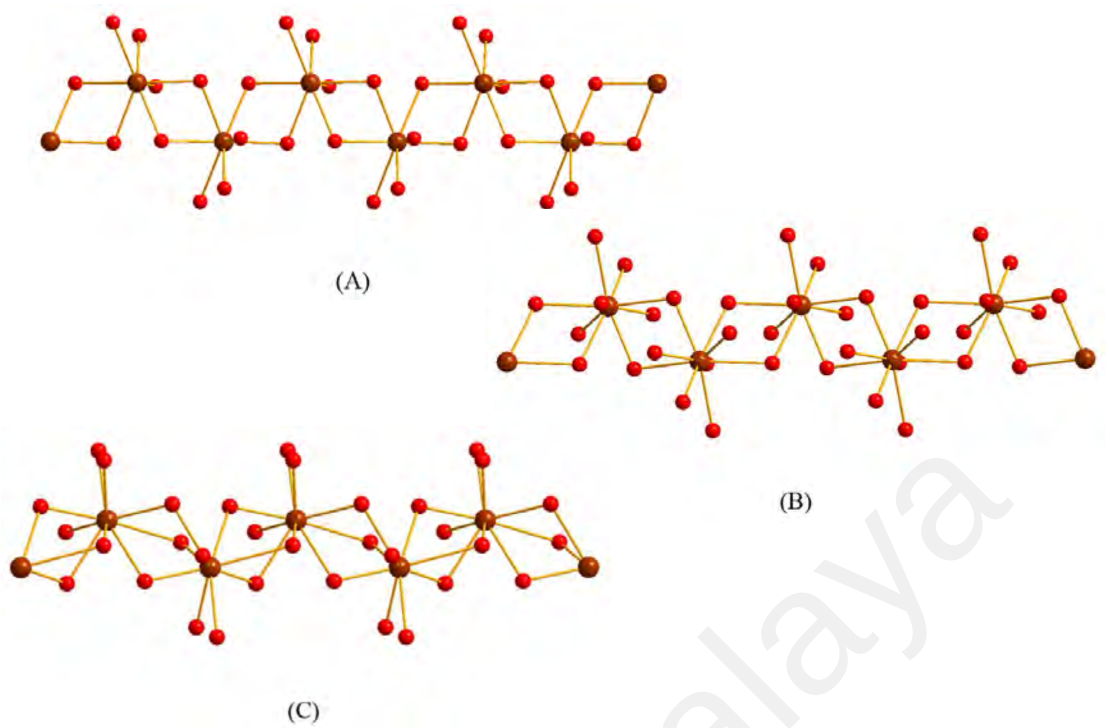

Figure 4.33: 1D building block of: (A) 14, (B) 17, and (C) 18, that builds into 3D MOF structures.

Such distinct 1D building blocks, templated by different solvent, determine their final 3D structures with slightly different frameworks, and pore sizes to accommodate their corresponding solvent in their infinite 1D channel, Scheme 4.1. In compound **14**, the HBTC$^-$ connect the 1D $(Pb_2O_{12})_n$ moieties in both *a*- and *c*-directions to form a porous 3D framework, in which each 1D moiety is related by a glide plane along the *c*-directions, Scheme 4.1 (A). The HBTC$^-$ also link the 1D $(Pb_2O_{16})_n$ in *b*- and *c*-directions forming a porous 3D framework of **17**, in which an *ac* mirror plane relates each $(Pb_2O_{16})_n$ moiety, Scheme 4.1 (B). The 1D $(Pb_2O_{15})_n$ moieties, related by a glide plane along the *c*-axis, are connected in *a*- and *c*-directions through HBTC$^-$ to construct a 3D framework of **18**, Scheme 4.1 (C). Compounds **14** and **17** have a rather similar pore size (~7.50 Å), and are bigger than that of compound **18** (~3.05 Å pore size). Summarizing results from the different approaches that used in the synthesizing of different batches of PbMOFs was explained in Scheme 4.1:

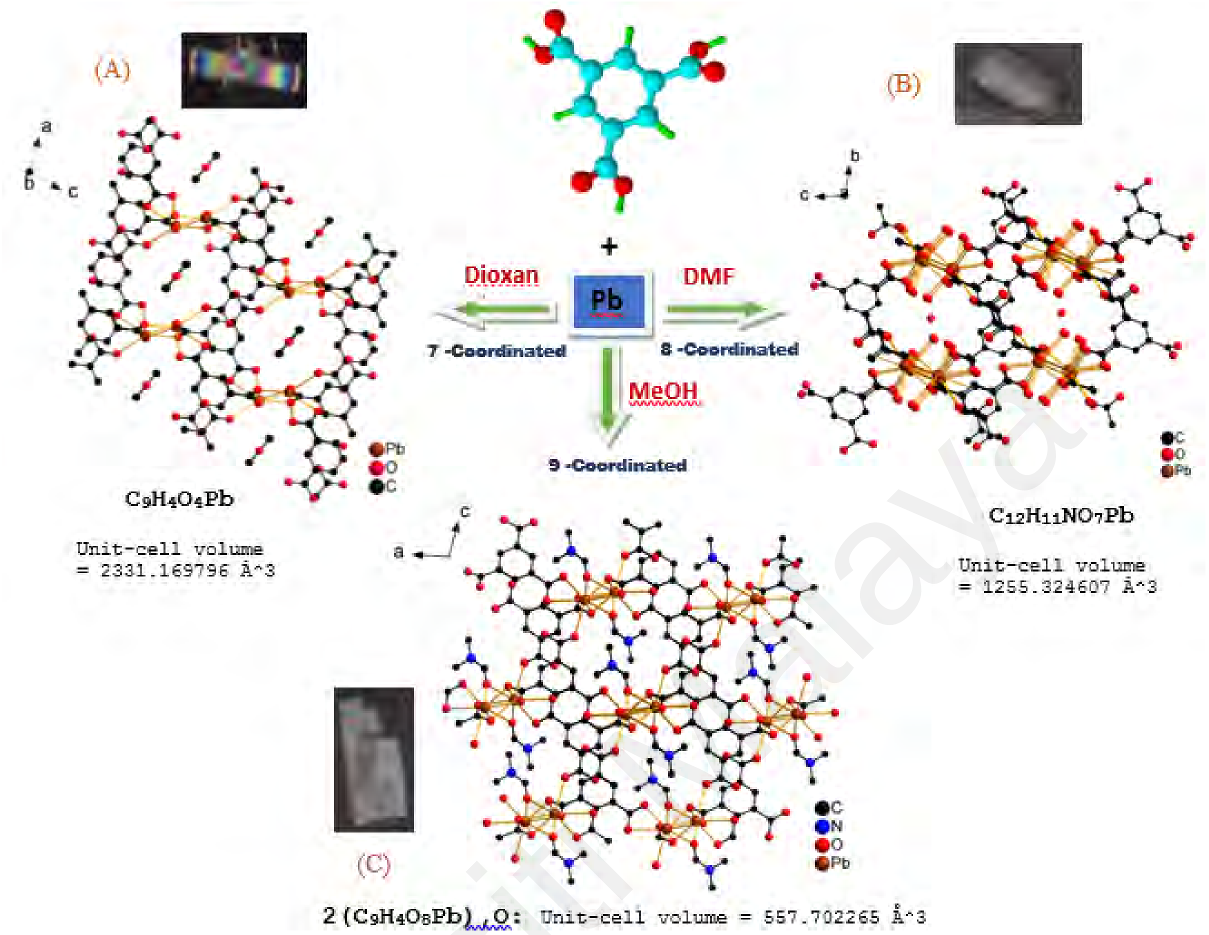

Scheme 4.1: 3D MOF structures of: (A) 14 viewed along the *b*-axis, (B) 17 viewed along the *a*-axis, (C) 18 viewed along *b*-axis; with insets show the corresponding optical microscopy image of each crystal.

Compounds (**13** and **14**) offered the same formula (based on PXRD measurements), [($C_{13}H_{13}O_9$)Pb]; Pb(HBTC)(1,4-dioxane)$_{0.5}$, (HBTC= $C_9H_6O_6$) and crystallize in the *C*2/*c* Monoclinic space group (a =17.239(2) Å, b =7.0225(8) Å, c =19.911(2) Å, β =104.74(1)°) with molecular mass of 520.46 gm.mol^{-1}; Compounds (**15** and **17**) display the same formula (based on PXRD measurements), [($C_{18}H_8O_{17}$)Pb_2]; Pb_2(HBTC)$_2$(H_2O)$_5$, and crystallize in the *P*-1 Triclinic space group (a = 7.3989(4) Å, b =8.2196(4) Å, c =10.1437(5) Å, α =94.336(4)°, β =104.943(4)°, γ =108.270(3)°) with molecular mass of 910.66 gm.mol^{-1}, while Compound **18** with the formula, [($C_{12}H_{11}NO_7$)Pb]; Pb(HBTC)(DMF), crystallizes in the $P2_1/n$ Monoclinic space group (a =10.5004(3) Å, b =7.1398(3) Å, c =17.1285(5) Å, β =102.160(2)°) with molecular mass of 488.44 gm.mol^{-1}

Another common feature of the three compounds (**14**, **17** and **18**), that may contribute to structural rigidity is the monoprotonated dicarboxylic acid, with Lewis base oxygen atoms (O(5) atoms of HBTC^{-}) located within the chains. There are weak hydrogen bonds, bond distances of 1.79 and 1.89Å, between O(2) atoms of HBTC^{-} and H(5) atoms of the mono-protonated dicarboxylic acid as shown in dashed blue bonds for **17** and **18**, respectively, Figure 4.34 (B and C). For compound **14**, Figure 4.34 (A), the weak hydrogen bond with bond length of 1.85Å, forms between O(1) atoms of HBTC^{-} ligand and H(5) atoms of the mono-protonated dicarboxylic acid.

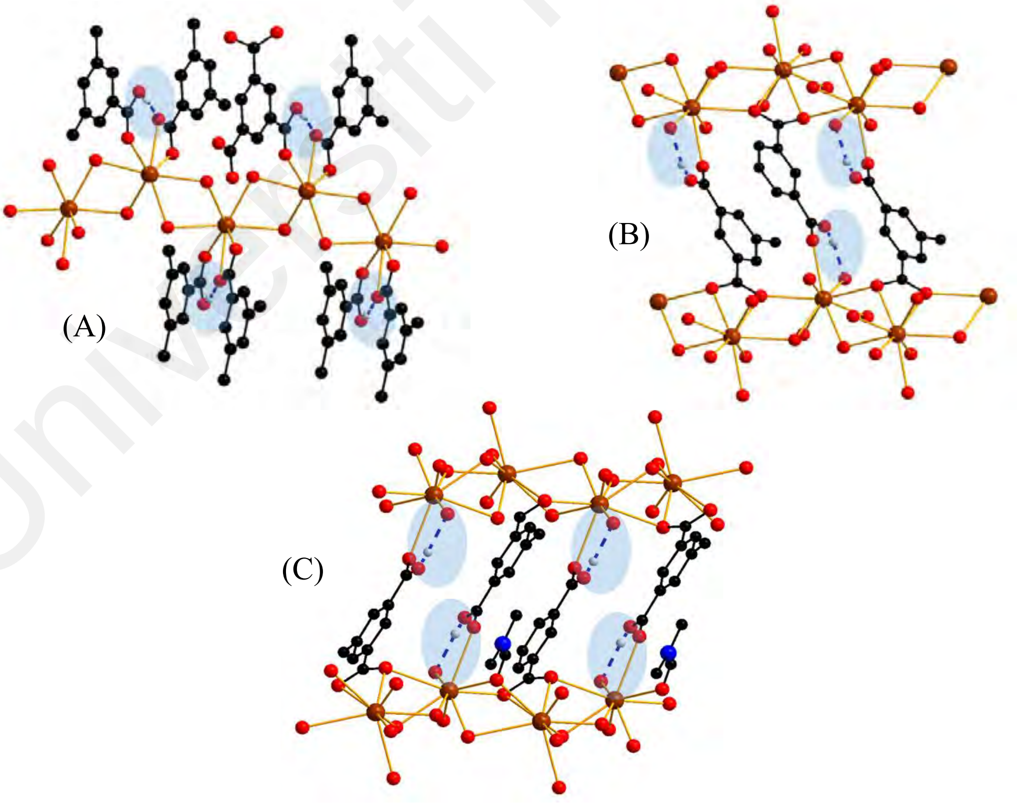

Figure 4.34: Hydrogen bonding images in: (A) 14, (B) 17, and (C) 18, common to all structures.

The topological analysis [247] of the three 3D structures reveal a 5-c uninodal net with topological symbol of $\{4^6.6^4\}$ for both **14** and **17**; whereas, a topological symbol of $\{4^6.5^2.6^2\}\{4^6.5^6.6^3\}$ simplified as a 5,6-c 2 nodal net is observed for compound **18**.

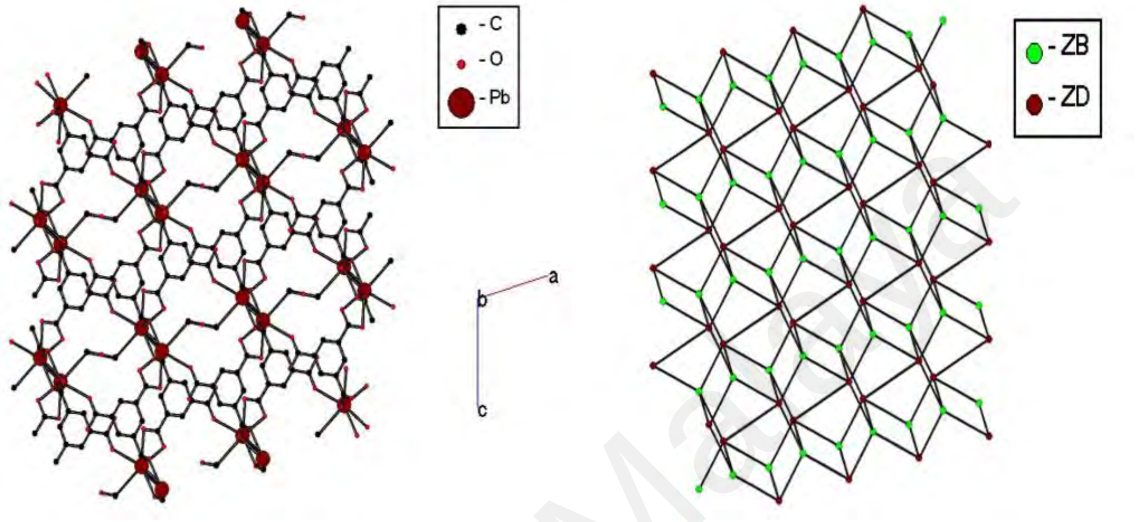

Figure 4.35: Normal and simplified underlying structure with 5,6-c net with stoichiometry (5-c)4(6-c)3; 2-nodal net Point symbol for net: $\{4^6.5^2.6^2\}\{4^6.5^6.6^3\}$, of compound 14, Topological type: NEW.

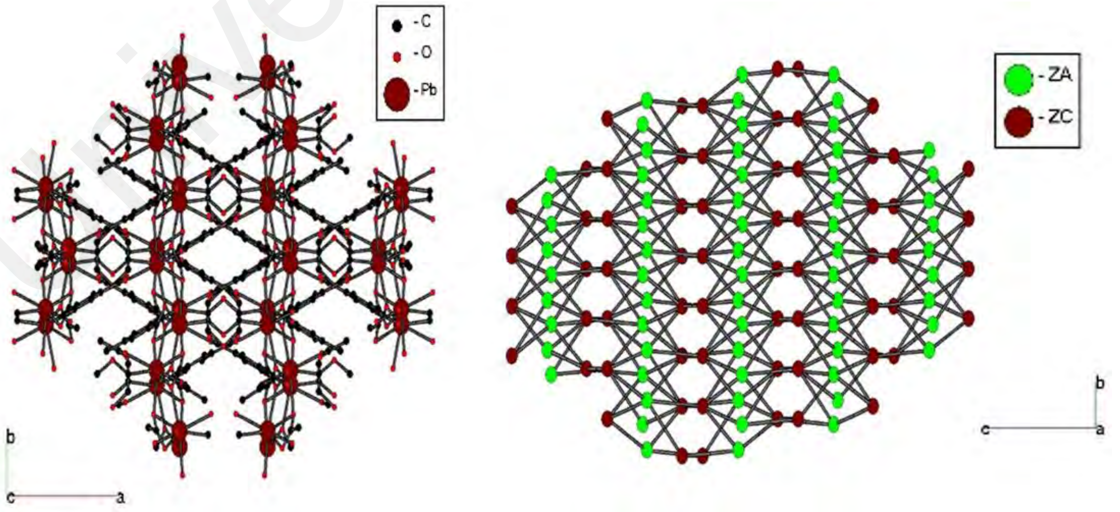

Figure 4.36: Projection along 100 plane of compound 14.

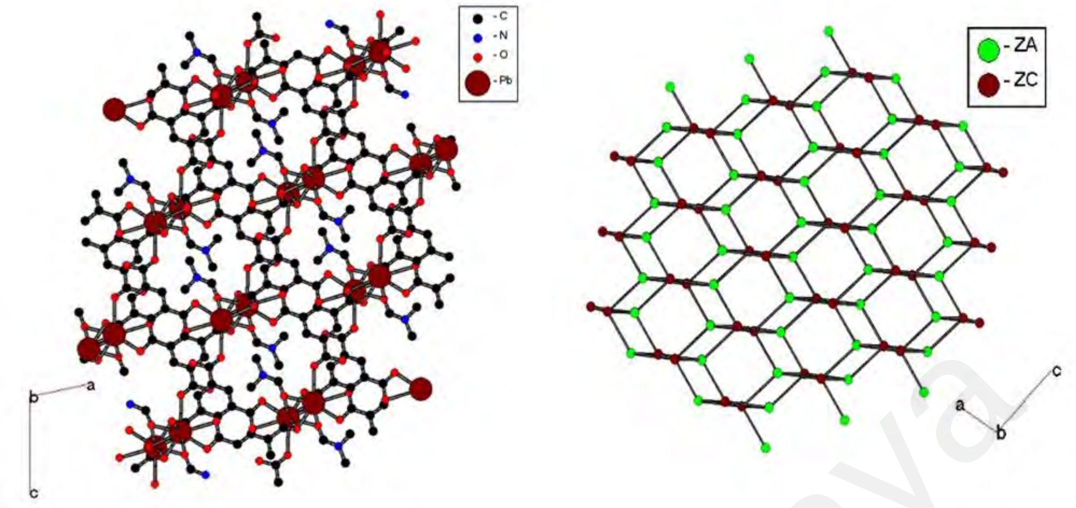

Figure 4.37: Normal and simplified underlying structure with 5-c net; uninodal net of compound 17 Point symbol for net: {$4^6.6^4$}.

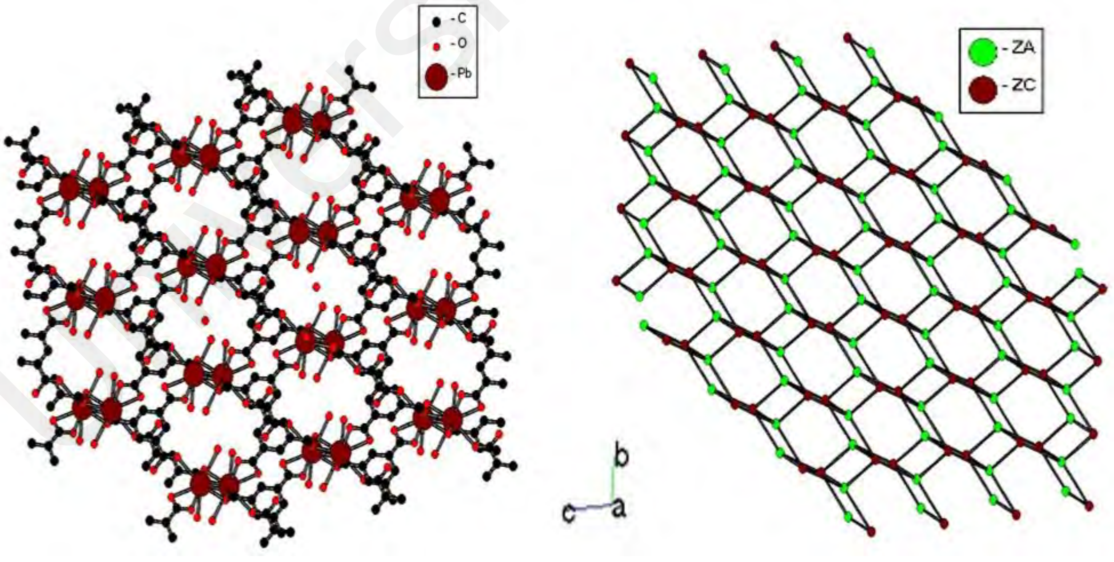

Figure 4.38: Normal and simplified underlying structure with 5,6-c net with stoichiometry (5-c)(6-c); 2-nodal net of compound 18, Point symbol for net: {$4^6.5^2.6^2$}{$4^6.5^6.6^3$}, Topological type: NEW.

4.3.4 Microscopic Features

The different batches (which produce from the same starting materials) of PbMOFs displayed different crystal shapes and morphologies with different crystal sizes observed under the electrical microscope, for instance, the stacks plate-like crystals, the ribbon-like crystals and the small thick block- like crystals. This feature can explain the key role of the varying of the solvent that use in the synthesizing procedure beside the use of a proper N-containing modulating agents to produce difference compounds from the same starting materials, Figure 4.39.

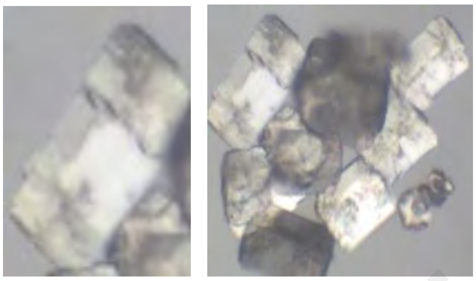

13: Pb(Dioxane)MOF

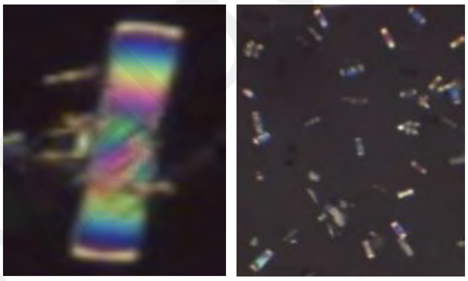

14: Pb(Dioxane+An)MOF

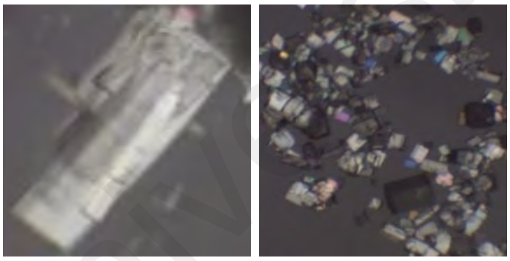

15: Pb(MeOH)MOF

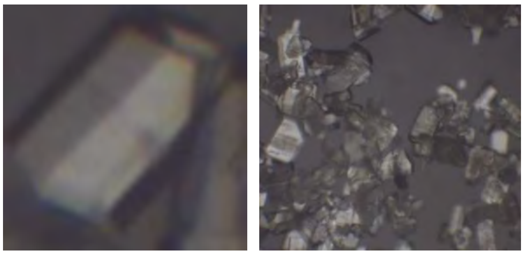

17: Pb(MeOH+Im)MOF

18: Pb(DMF)MOF

Figure 4.39: Optical-images from different batches of PbMOFs.

4.3.5 Photoluminescence (PL) Observation

The digital photo-images, that represented the PL observations under UV and visible light of different Pb-MOFs, Figure 4.40, shows that, compound **14** emits pale greenish yellow color because the absorption of the (An) molecules, while a “white” luminescent is emitted from compound **17** because the absorption of the (Im) molecules and a light yellow luminescent could be observed from compound **18** because the presence of the DMF molecules inside the pores of the framework.

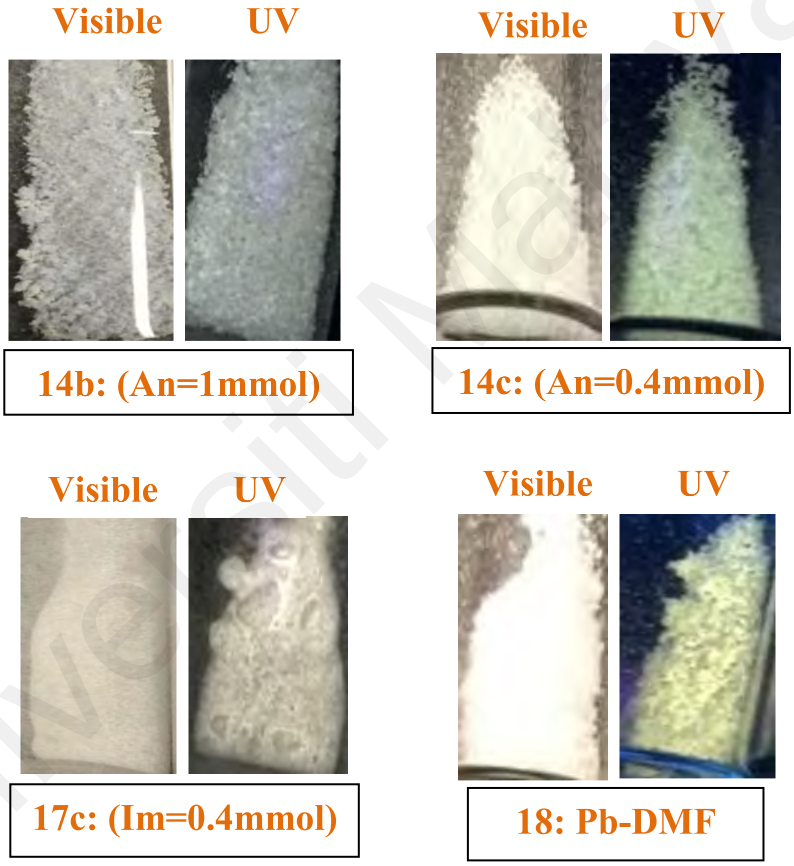

14b: (An=1mmol)

14c: (An=0.4mmol)

17c: (Im=0.4mmol)

18: Pb-DMF

Figure 4.40: Digital photo-images of PL of PbMOFs for different compounds.

4.3.5.1 Photoluminescence phenomena (PL)

The use of luminescing ligand in luminescing MOF is advantageous in two folds; increasing PL intensity and/or shifting emission maxima for tunable PL color. The latter phenomena have been reported to relate with white emission reported in several MOFs [37, 248, 249].

In recent years, there has been an immense interest in discovering white-light single phosphors from Pb-based compounds, due to its intrinsic broadband emission originated from self-trapping exaction and defects [233, 234]. Several white emitting Pb-based frameworks and coordination polymers (MOCP) have also been reported [37, 248, 249]. Enriching the library of single component, near white-emission Pb frameworks, herein the researcher report three new BTC-containing Pb frameworks, in which compound **17** displays near white-light emission. The compounds are made by using a facile dissolution-crystallization method, exploiting the use of hard-soft acid base (HSAB) principle to find a suitable modulator to yield a phase pure product.

The room temperature, solid state emission spectra of as received H_3BTC ligand, and compounds **14** and **17**, including their digital images representing their PL colors are shown in Figure 4.41. Compound **14**, when excited at 350 nm, emits pale greenish yellow color with broad peak covering 530-570 nm, Figure 4.41. Contrasting UV-Vis spectrum **14** to that of H_3BTC, both Intra Ligand (ILCT) and Ligand-to-Metal Charge Transfers (LMCT) might be responsible for the observed emission spectrum. ILCT is corroborated by a similar absorption band appears in both **14** and H_3BTC at maxima of 302nm. The disappearance of broad absorption shoulder of the ligand in **14** at 330nm, validates the LMCT, Figure 4.42.

A bluish white luminescent is observed for as received H_3BTC with broad emission spectrum covering almost entire visible range (420 to 620 nm) with several maxima at 490, 544, and 615nm when excited at 350 nm, Figure 4.41. Such emission is typically due to $n\rightarrow\pi^*$ and/or $\pi\rightarrow\pi^*$ transition [37, 248, 249]. A more pronounced “white” luminescent is emitted from compound **17** with a rather broad emission spectrum, covering also at 420 to 620 nm range, Figure 4.41. An additional feature of a shoulder band in yellow range (560-580 nm) was clearly observed for **17** compared to that of ligand, that could be partly ascribed to Metal-to-Ligand Charge Transfer, MLCT [37, 248, 249].

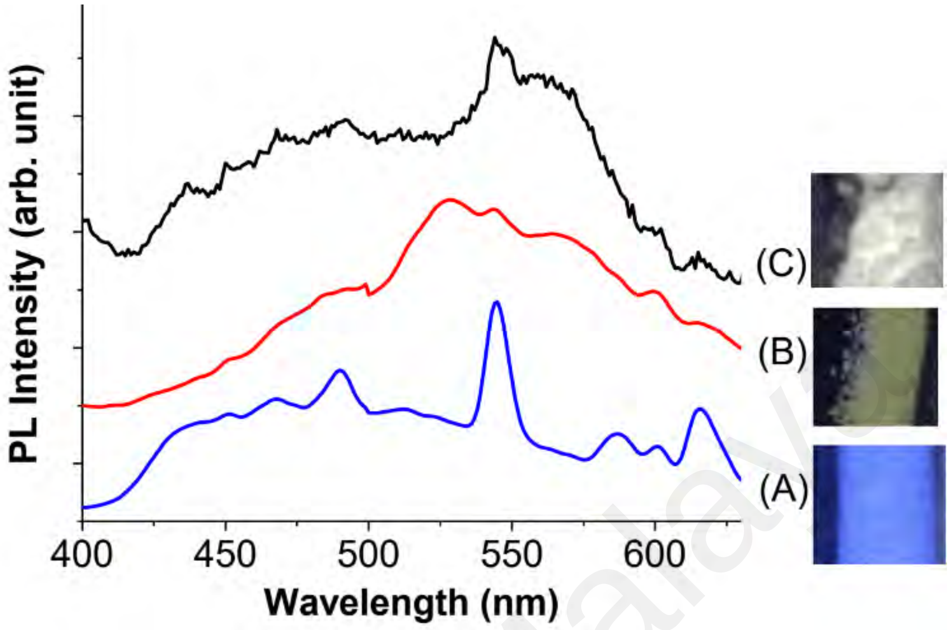

Figure 4.41: Solid state emission spectra and the corresponding PL color images of: (A) H_3BTC, (B)14, and (C) 17.

Overall, the observed near white light emission of **17** could be attributed to LMCT and/or MLCT, as well as, ligand-centered transitions (ILCT), which correspond well to UV-Vis spectra study, Figure 4.42. Comparing with spectrum of as received H_3BTC ligand, a disappearance of broad shoulder at 330nm in **17** might indicate the presence of LMCT, and the emergence of new maxima at 228 nm in **17** signals the existence of MLCT. Further, similar maxima at 302nm indicates ILCT also occurring in **17**. All of these transitions are represented by a broad emission spectrum, which leads to near white PL color emitted from **17**. Such a broad, white emission spectrum was not only observed in Pb-based MOF, but also is reported in other Pb-based compounds, such as Pb-based perovskite halides, in which such abroad emission spectrum signature might stem from excitation self-trapping [233, 234].

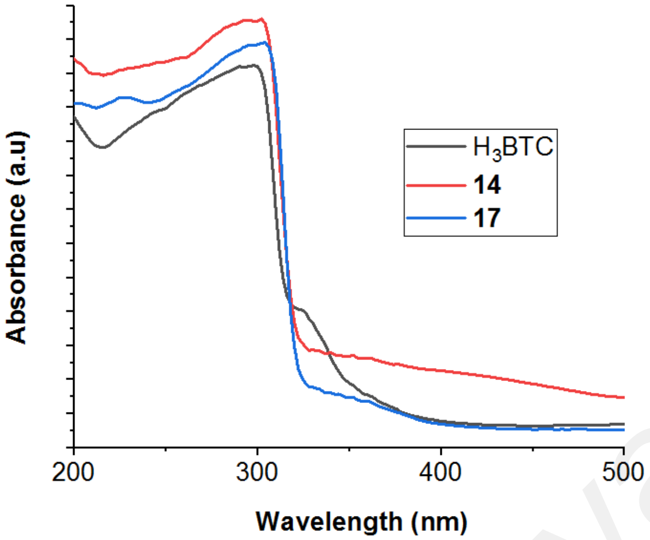

Figure 4.42: Solid state UV-Vis spectra of H_3BTC, compounds 14 and 17.

The quantified colors of the emissions of all compounds are plotted in the Commission International l'Eclairage (CIE) chromaticity diagram, Figure 4.43: The as received H_3BTC has CIE coordinates of (0.30,0.34), giving a white with blue tinge gamut, in accordance to the observed PL image, when excited at 350 nm. Compound **17** exhibits near white color gamut, when excited at 350 nm, with CIE coordinate of (0.33,0.36), showing potential for a single component white LED application. Several Pb-based MOFs were also reported, as a near white light single component phosphor with CIE coordinates very close to ideal (0.33, 0.33). The white light emission in these papers were likely due to combination of ILCT, LMCT and/or MLCT as well [37, 248, 249]. As expected, compound **14** gives greenish yellow CIE coordinate of (0.34, 0.44) under 350 nm excitation.

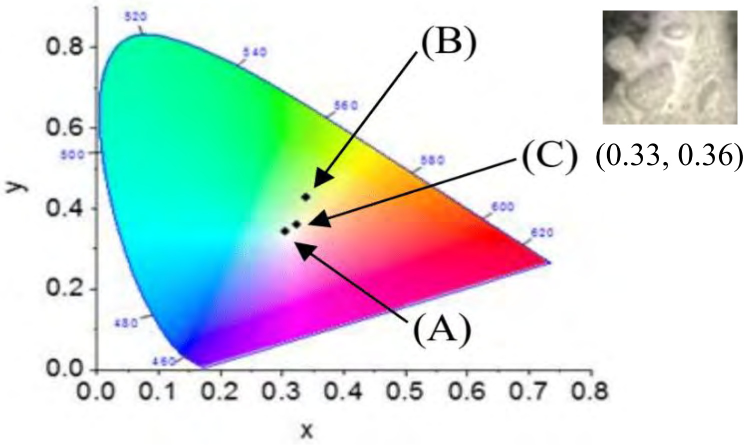

Figure 4.43: Corresponding CIE chromaticity diagram for: H_3BTC (A), 14 (B) and 17 (C).

4.3.6 Powder X-ray Diffraction (PXRD) analysis

The measured patterns were compared to the simulated diffraction patterns by using the respective single crystal data. Based on PXRD patterns, the researcher could confirm that, the synthesized Pb-MOFs (with all different solvents) show a high degree of crystallinity, with sharp and well-defined peaks comparing with the simulated patterns, that obtained from single crystal x-ray diffraction analysis (Crystallographic Information Framework, CIF file). PXRD was used to confirm the purity of the new compounds as it could provide phase purity information and also reveal the presence or absence of polymorphs.

After many trials to get a pure phase for the synthesized PbMOFs, it seems that, the addition of different appropriate modulator agent with exact molar ratio, to the PbMOFs helped in reducing the defects via giving a pure phase patterns and did a modulation on the framework structures of compounds **13,** Figure 4.44 (left), and **15**, Figure 4.46, which they had some unidentified peaks. The PXRD pattern of the products obtained after optimized synthetic conditions are showing the pure phase of **14**, Figure 4.44 (right) and **17,** Figure 4.47, which confirm that, no additional polymorph is present in the sample that was used for further PL study. For instance, the addition of (0.4mmol) aniline to **13** gave a pure phase PXRD pattren of compound **14**(c), Figure 4.44 (right), while the addition of (0.5mmol) of aniline to compound **13** gave a PXRD pattren which was not very matching with the simulated pattern, that was obtained from CIF, compound **14a**, Figure 4.45 (left). Furthormore, the addition of (1mmol) of aniline to compound **13** gave a different PXRD pattren which was not matching with the simulated pattern and showed many unidentified peaks, compound **14b**, Figure 4.45 (right).

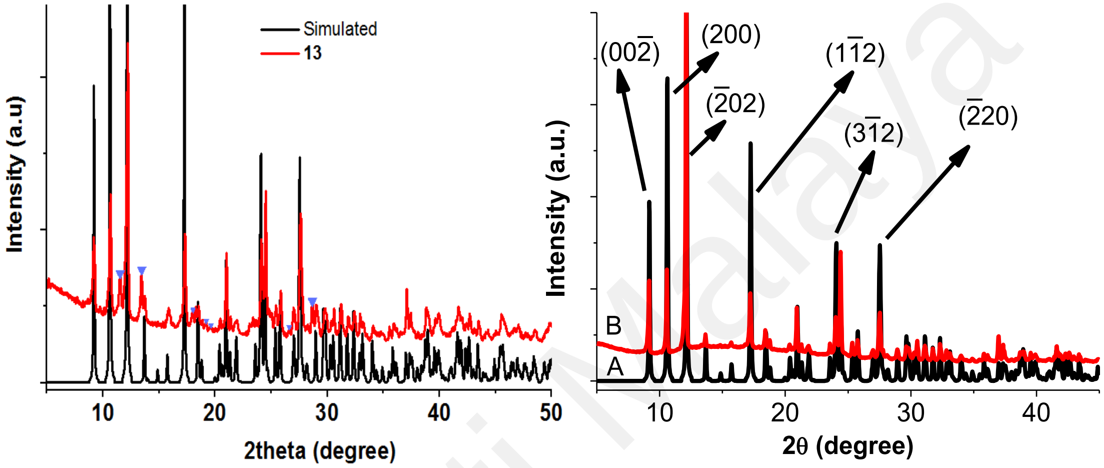

Figure 4.44: PXRD patterns of: (left) compound 13 (without N-donor) showing some unidentified peaks, (right) compound 14c (13 with An = 0.4mmol) shows simulated, A, and observed, B, patterns.

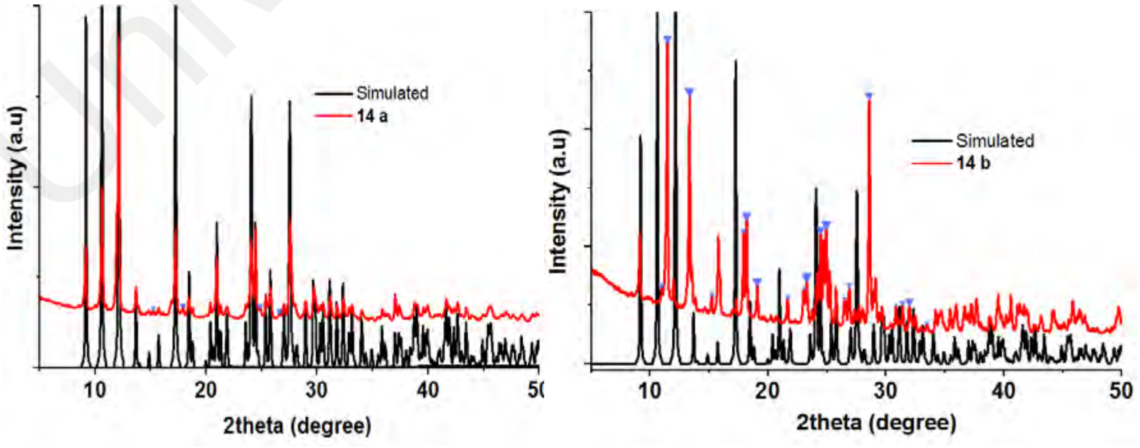

Figure 4.45: PXRD patterns of compounds: (left) 14a (with An=0.5mmole), (right) 14b (with An=1mmole).

On the other hand, and after trials to get a pure phase from either dry or mother liqour batch of **15**, Figure 4.46 (left or right), the researcher observed that, the addition of Im (0.4mmol) as a N-containing modulator agent to compound **15** gave a pure phase PXRD pattren of **17**, Figure 4.47. Whilst, the addition of aniline to compound **15** did not give a pure phase PXRD pattern comparing with the simulated one, that was obtained from CIF, Figure 4.48.

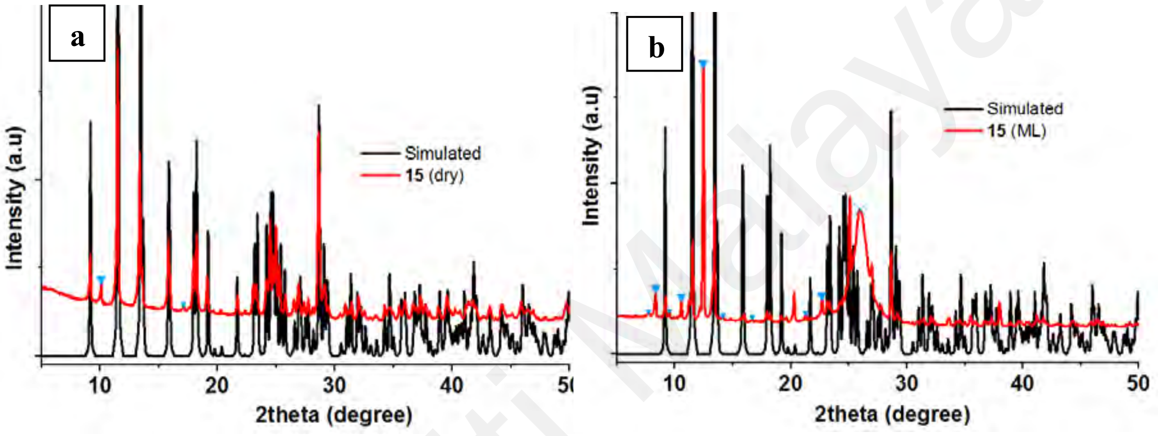

Figure 4.46: PXRD patterns of: (a) compound 15 in dry batch, (b) compound 15 in mother liquor batch.

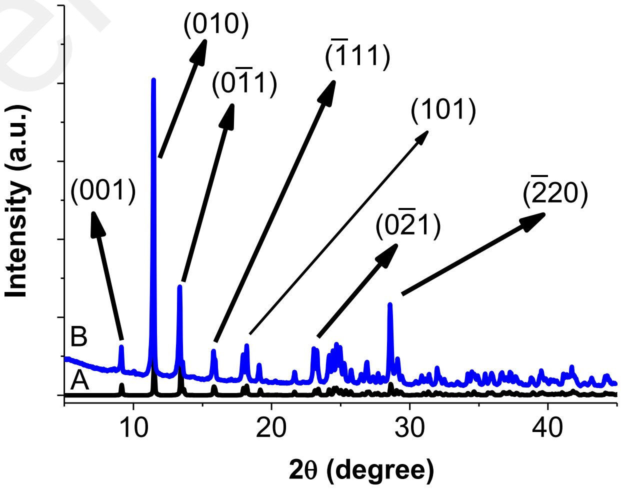

Figure 4.47: PXRD patterns of compound 17 shows the simulated, A, and observed, B, patterns.

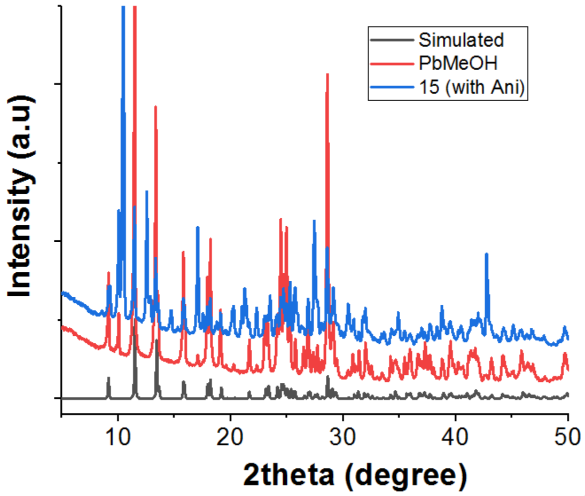

Figure 4.48: PXRD patterns of observed 15, red, comparing with the simulated black and its observed pattern after adding aniline, blue.

Besides that, the addition of (An) or (Im) or even Piperazine (Pip) to compound **18** did not give a pure phase PXRD pattern, Figure 4.50. While a washed and dried compound **18**, however, was found to coexist with unknown impurity, Figure 4.49, even after several optimization attempts; therefore, no further property was reported besides structural characterizations.

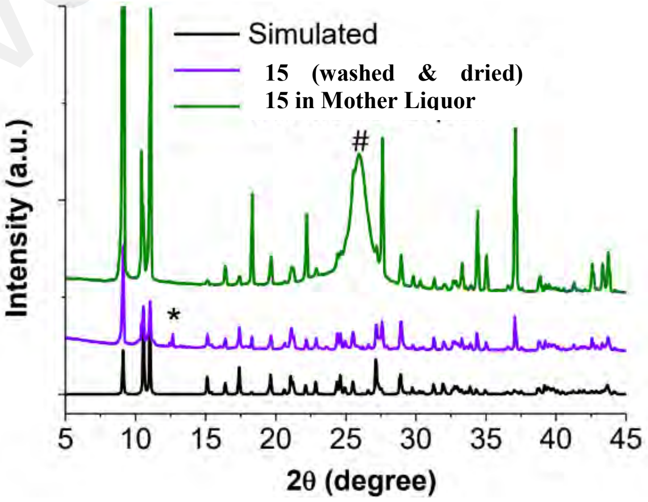

Figure 4.49: PXRD patterns of: simulated, observed (* shows unidentified peak in washed and dried), and observed (in mother liquor) patterns of compound 18 (# due to mylar film).

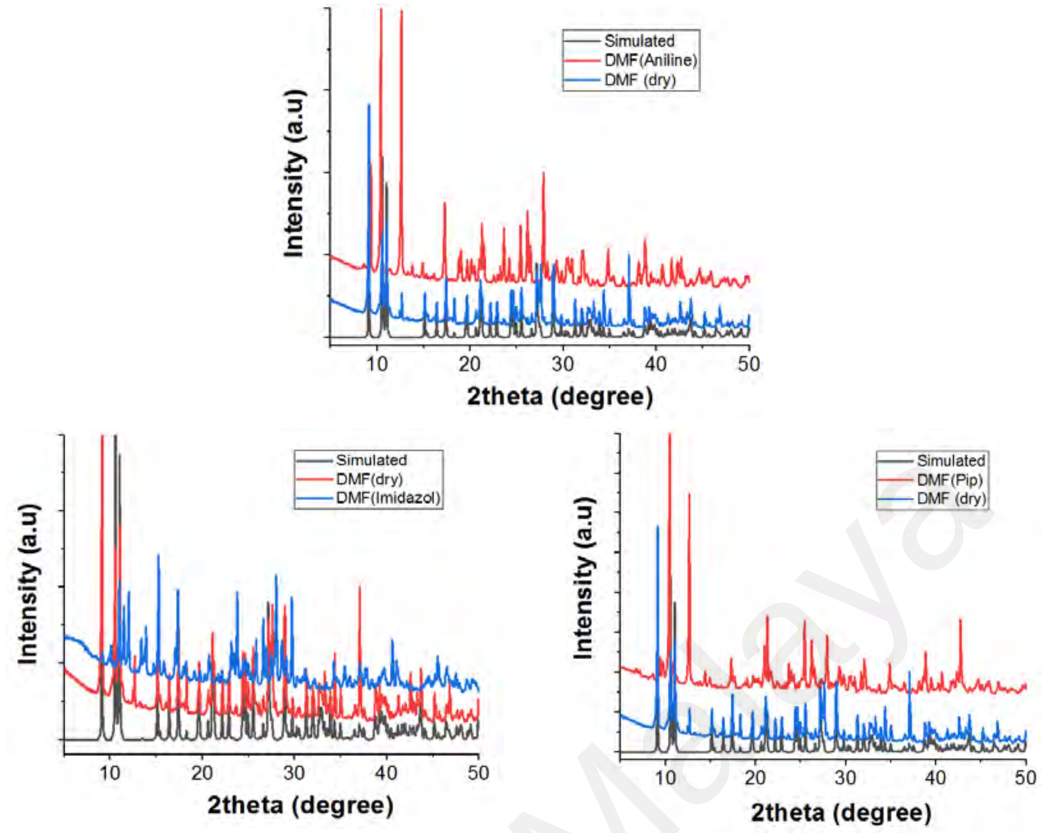

Figure 4.50: PXRD patterns of the dry batch of 18 comparing with its pattern after adding of (0.4mmol) of: (a) Aniline, (b) Imidazole (c) Piperazine as N-donor ligand.

4.3.7 TGA measurements

To determine the thermal stability of the studied lead compounds, a thermo-gravimetric analysis was performed. The studied compounds (**13-18**) were analyzed at TGA machine under 20 ml/min flowing nitrogen gas (N_2) with temperature ramping at a rate of 5 °C/min starting from RT to 900 °C, Figures 4.51 (a - e).

The bulk phase purity of **14** and **17** were further confirmed by TGA analysis in which, the observed weight losses of the corresponding solvent and the ligand are closely matched with the expected values that was calculated from formulas obtained from crystallographic refinements, Figure 4.51 (a) and (b). This may also support that, within the synthetic conditions, used in here, neither of the modulator is presented in the structure, in conjunction with crystallographic refinement results, as well as CHN analysis. The following TGA results, Figures 4.51 (a - e), confirmed that the materials which used in the synthesizing of PbMOFs are the same (the ligand H_3BTC and Lead cations) and the difference among the three different MOFs are only the used solvents.

The first mass loss for compound **14**, (100-89) %, started around 100 °C (near boiling point of dioxane) while the first weight loss for compound **17**, (100-91.5) %, started at 65 °C corresponding to the releasing of solvent molecules (H_2O or MeOH). The frameworks of **14** and **17** remained stable until the second weight loss occurred around (89-48) % at 390°C and around (89-44) % at 380 °C, respectively, when the organic ligand H_3BTC started to decomposed. The lead oxide started to precipitate at 540 °C and the lead metal started to precipitate at 500 °C from the frameworks of **14** and **17**, respectively, Figure 4.51 (a and b).

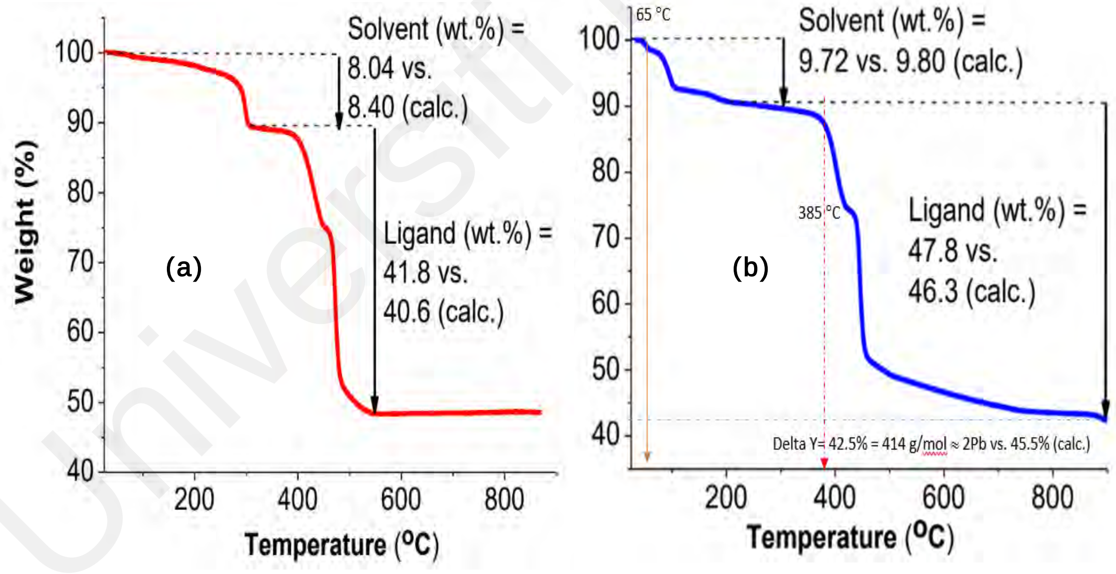

Figure 4.51: (a) TGA thermograms of 14, (b) TGA thermograms of 17, (c) TGA thermograms of 13, (d) TGA thermograms of 15, (e): TGA thermograms of 18.

4.3.7.1 Discussion of TGA measurements patterns for the other batches of PbMOF

The first mass loss for compound **13** and **15**, (100-92) %, started around 90 °C (near boiling point of dioxane) and 67 °C (boiling point of Methanol), respectively, corresponding to the releasing of solvent molecules, which exist inside the pores of the framework. The framework of **13** remained stable until 390 °C when the second mass loss occurred (91-57) % and the H_3BTC ligand started to decomposed, Figure 4.51 (c). Whilst, the framework of **15** remained stable until 400 °C when the organic ligand started to decomposed and the second weight loss occurred from (90-44) %, Figure 4.51 (d). The lead oxide started to precipitate around 540 °C from the framework of **13**, and around 510 °C from the framework of **15**.

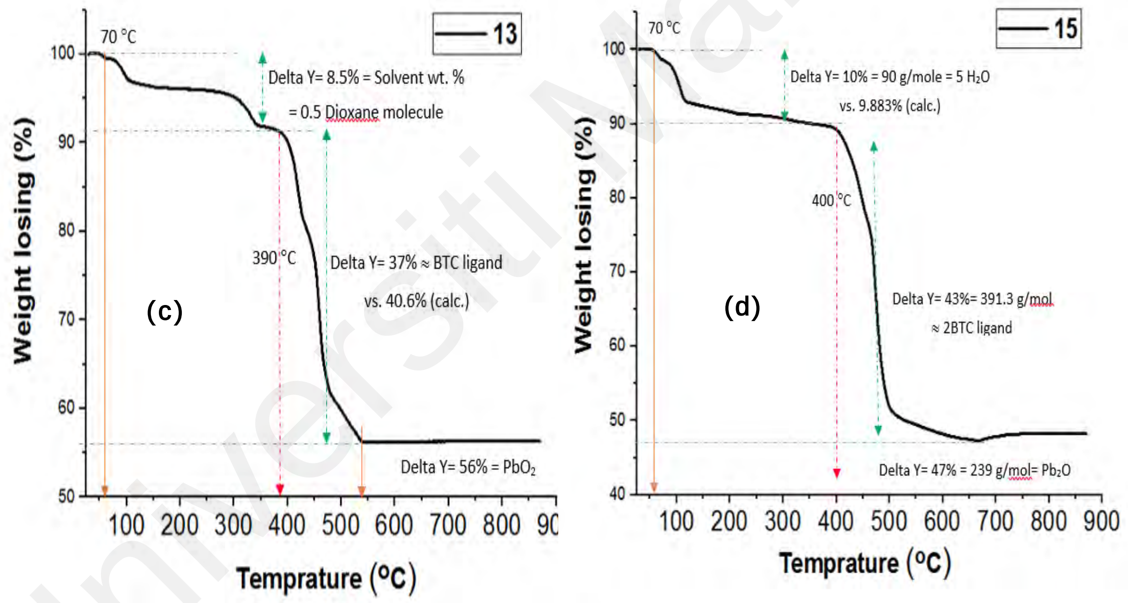

Figure 4.51: Continued.

The first mass loss for compound **18**, (100-90) % started around 100 °C corresponded to the releasing of solvent molecules (DMF), that exist inside the pores of the framework. The second weight loss of this compound occurred from (88-47) % and the framework remained stable until 400 °C when the H_3BTC started to decomposed, and around 510 °C the lead oxide started to precipitate, Figure 4.61 (e).

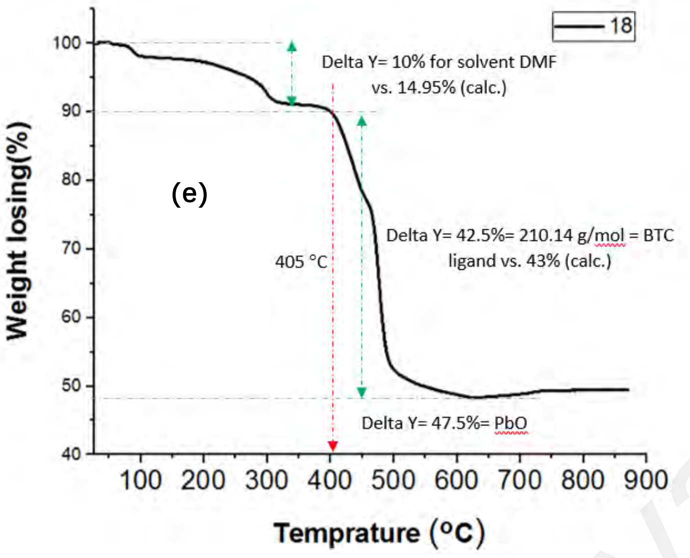

Figure 4.51: Continued.

Table 4.8: The summarized results of the TGA charts for different batches of PbMOF.

Comp. no.	first mass losing % = solvent formula weight (g/mole)	Temp. °C	No. of solvent molecules	Second mass losing % = ligand formula (g/mole)	Temp. °C
13	8.5% = 44.05 (g/mole)	75-100	0.5 $C_4H_8O_2$	37 ≈ H_3BTC	390
14	8.04% = 44 (g/mole)	85	0.5 $C_4H_8O_2$	41.8 ≈ H_3BTC	390
15	10% = 90 (g/mole)	70	≈3 MeOH	43 ≈ 2H_3BTC	395
17	9.72% = 89 (g/mole)	65	≈3 MeOH	47.8 ≈ 2H_3BTC	395
18	10% = 91.066 (g/mole)	100	1.25 DMF	42 ≈ 2H_3BTC	400

4.3.8 FESEM analysis

The bulk crystal morphologies show different corresponding stacks plate-like crystals for **14**, ribbon-like crystals for **17** and small thick block- like crystals for **18**, as shown in optical images, Figures 4.39, and SEM images, Figure 4.52. These results confirmed that by only changing of the solvents (1,4-dioxane, MeOH and DMF) which used in the synthesizing procedure it was able to get various structures with different morphologies from the same starting materials.

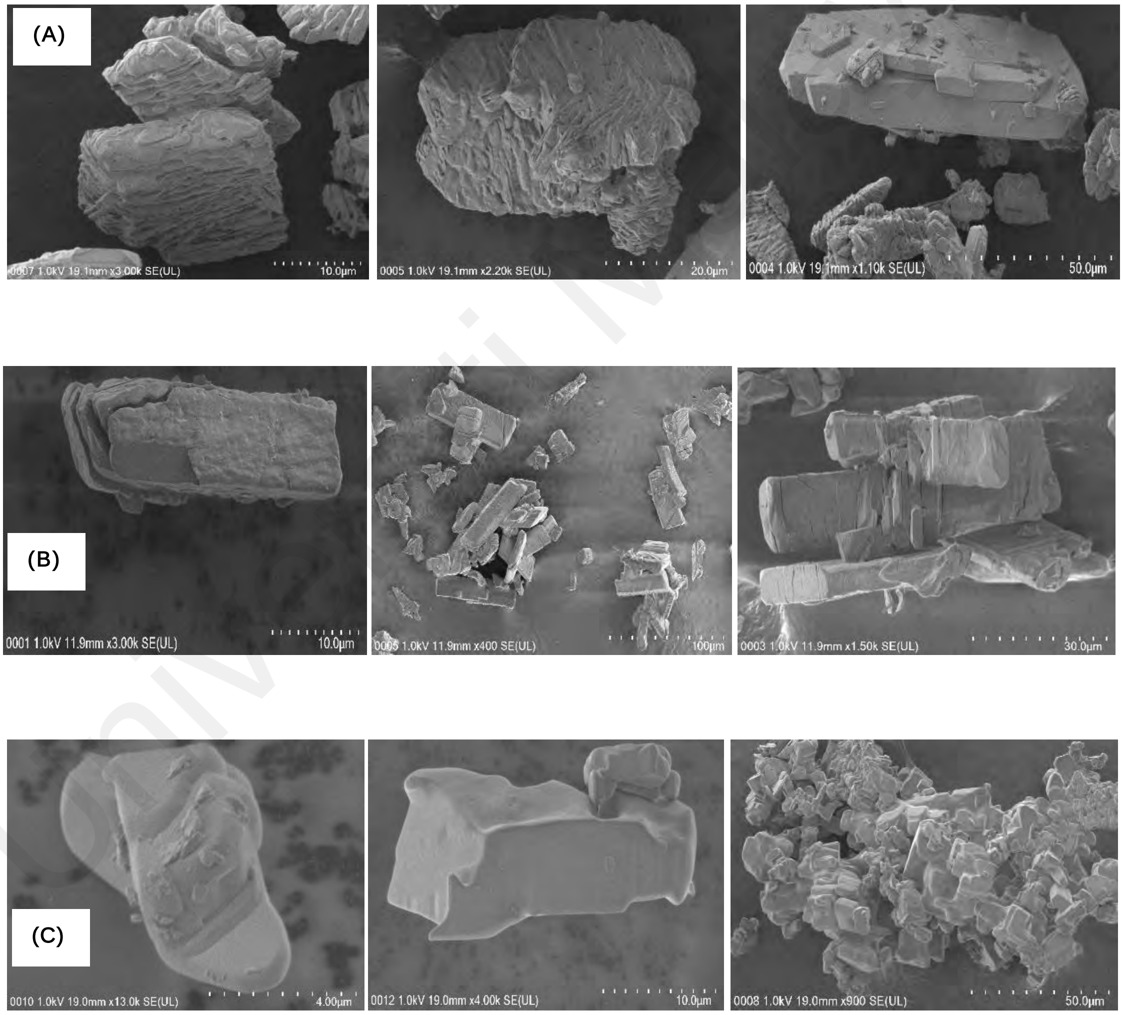

Figure 4.52: SEM images of: (A) plate stacks-like crystals of compound 14, (B) ribbon-like crystals of compound 17, (C) small thick block- like crystals for 18.

4.3.9 Dye adsorption study

Water pollution becomes worldwide threat, as we witness scarcity of clean water, due to global industrialization [250- 252]. Dyes, used in textiles, painting, paper, and plastic industries, contribute the most water pollutant. Close to 100,000 dyes are available with production rate of 10^5 tons/year, from which 2% effluents were discharged into surrounding aquatic system. Parts of the effluents might contain hazardous and toxic compounds, that are harmful to aquatic organisms that might eventually affecting human health [253]. The need for effective and efficient dye adsorbent is critical.

MOF, due to its versatile chemistry, is one of the most promising porous materials for dye adsorbent [254]. These new porous materials can absorb some guests such as water, solvents, organic molecules like dyes and aniline (An). The dyes Absorption behavior of some of the new synthesized compounds (**14** and **17**) were explored towards two organic dyes, methylene blue (MB; cationic dye) and methyl red (MR; neutral dye) through batch method and by using UV-vis spectrophotometer which confirm that **14** is more efficient than **17** in absorbing both MB and MR. The visual observations revealed that compound **13** can be employed as aniline sensor because it can produce new compounds with different colors depending on the concentration of the absorbed amount (An). These results suggested that **13** is not only a promising candidate as adsorbent for (An) removal but to be as (An) detector base on the PL emissions under UV and visible light. Having an infinite 1D pore with suitable size to capture dyes [255], compounds **14** and **17** were used to remove methylene blue (MB) and methyl red (MR) dyes from aqueous solution. Figure 4.53, 4.54, 4.55 and 4.56 showcase the quantification method of dye removal by using UV-Vis spectroscopy technique, along with the optical images of **14** and **17** soaked in MB and MR aqueous solution taken, during dye adsorption process. Attempts to activate **14** and **17**, starting from using rather harsh thermal activation to relatively milder supercritical CO_2, as well as, solvent exchange activations were unsuccessful. In spite of this, dyes adsorption of MB and MR onto both compounds, without activation (as synthesized) were successful. The amount of dyes left after 1 week of soaking was 1 ppm (~90% dye removal) for both compounds as quantified by UV-Vis spectra, for both MB and MR.

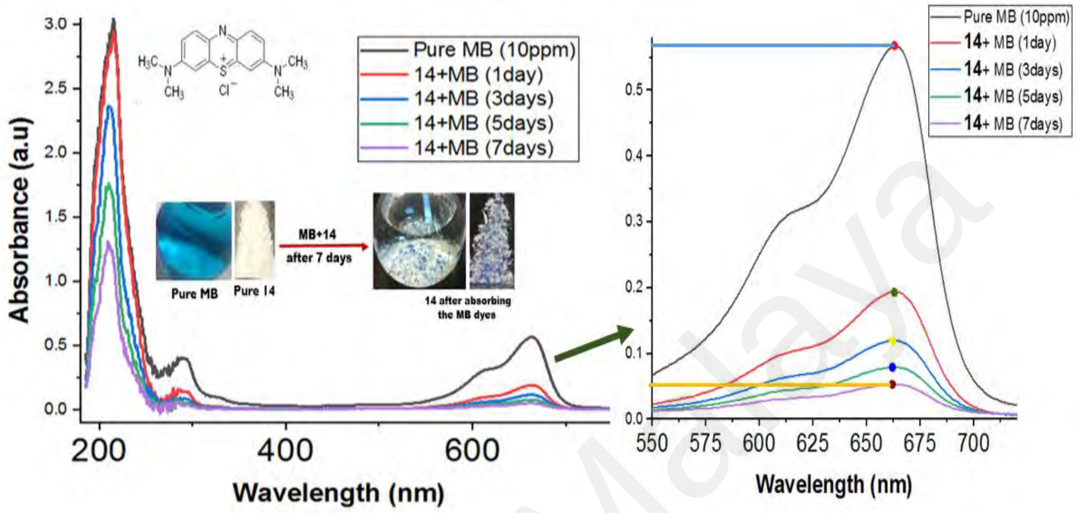

Figure 4.53: Quantification method of MB dye removal by compound 14 using UV-Vis spectroscopy technique.

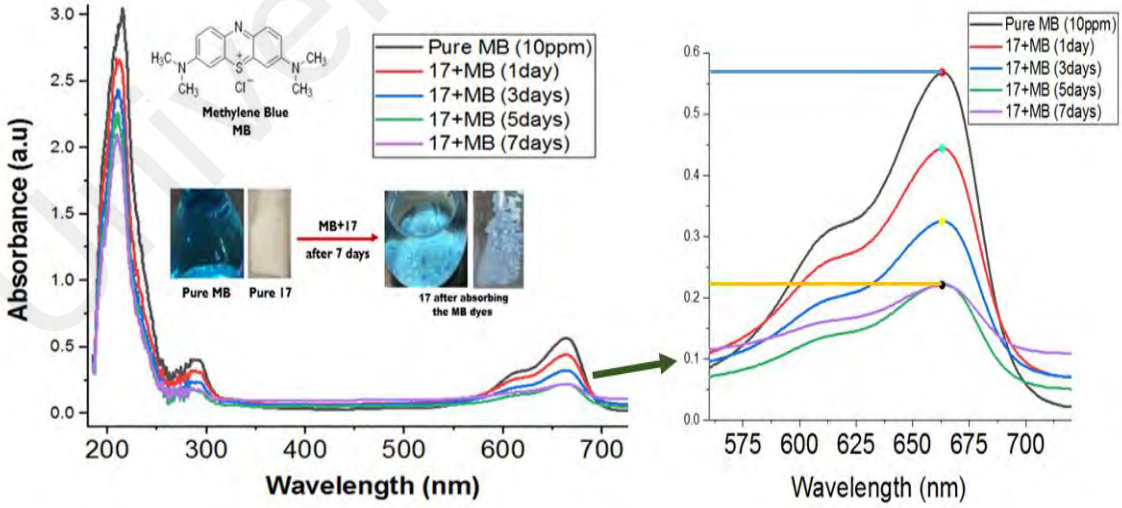

Figure 4.54: Quantification method of MB dye removal by compound 17 using UV-Vis spectroscopy technique.

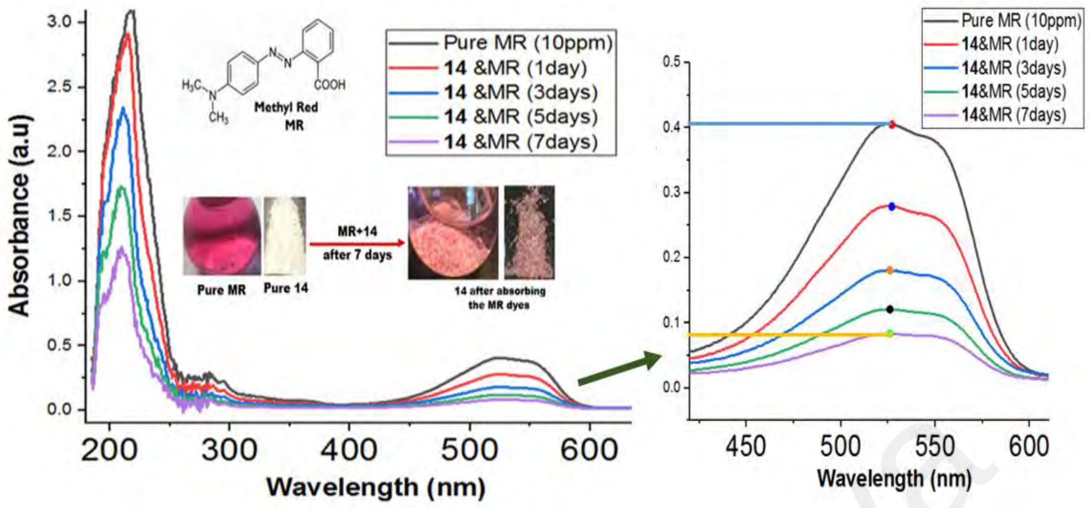

Figure 4.55: Quantification method of MR dye removal by compound 14 using UV-Vis spectroscopy technique.

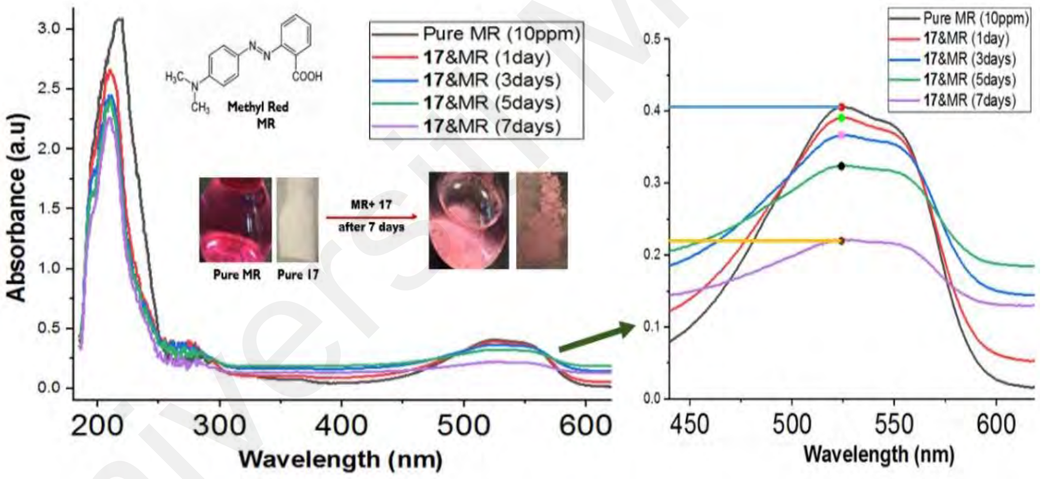

Figure 4.56: Quantification method of MR dye removal by compound 17 using UV-Vis spectroscopy technique.

Furthermore, compound **17** was found to maintain its structural integrity comparatively, better than **14** after dyes adsorption as shown in PXRD patterns, Figure 4.57. Since there are some new unidentified peak(s), observed after dyes adsorption in both **14** and **17**, also the fact that, they could not be activated, dyes desorption followed by re-adsorption of these compounds were not attempted.

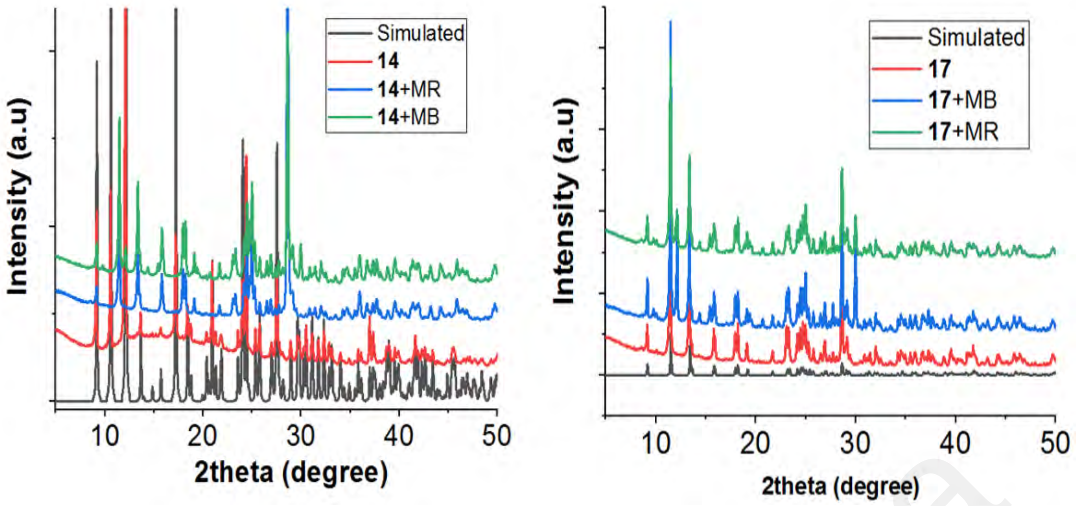

Figure 4.57: Powder X-ray diffraction patterns of: (left) compound 14 (after soaking with MR, MB dyes), (right) compound 17 (after soaking with MR, MB dyes) showing some unidentified peaks.

4.3.10 Brunauer-Emmett-Teller (BET) surface area analysis:

Stephen **B**runauer, Paul Hugh **E**mmett, and Edward **T**eller (**BET**) published an article about the BET theory at Journal of American Chemical Society in 1938. The BET theory gives an information about the physical properties and structure of solid porous and/or non-porous materials, because it was used to measure the surface areas of such materials and shows how the surface area of these materials affect and interact with the environment [256]. The BET theory principle is applicable for porous and non-porous materials, regardless of the shape and/or the size of particles because, it utilizes the gas adsorption data, so it is a useful instrument for manufacturing and investigating various solids [257].

Surface area analysis is a common method, that is widely used in the characterization of materials in order to manufacture and/or design of some solids. It is often correlated to some materials' properties, like moisture retention, dissolution rates, shelf life and catalytic activity [258].

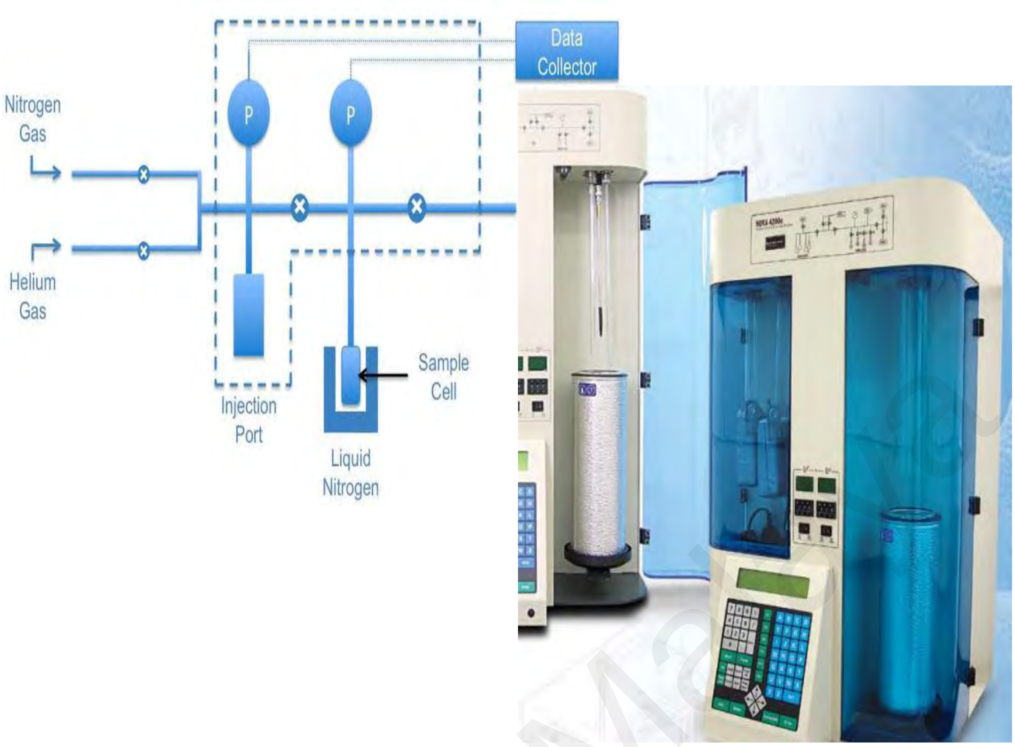

Figure 4.58: (Right): The BET instrument, (left): Schematic representation of the BET instrument showing the principle of measuring the surface areas and pore sizes process.

Multilayer adsorption systems are usually employed in BET to measure the surface areas of the materials by using probing gases as adsorbents. The most common adsorbent gas that is used in BET for surface area probing is nitrogen N_2 which has a boiling temperature about 77 K, that is why the standard BET analysis is usually conducted around this temperature [259]. There are some other gases that could be used as a probing adsorbent gas, such as carbon dioxide CO_2, argon Ar and even water to allow measuring of surface area with different measurement scales and different temperatures. The probing adsorbent gas in BET should not be chemically able to react with the material surface, this is called physisorption process, and it different from chemisorption clearly [260].

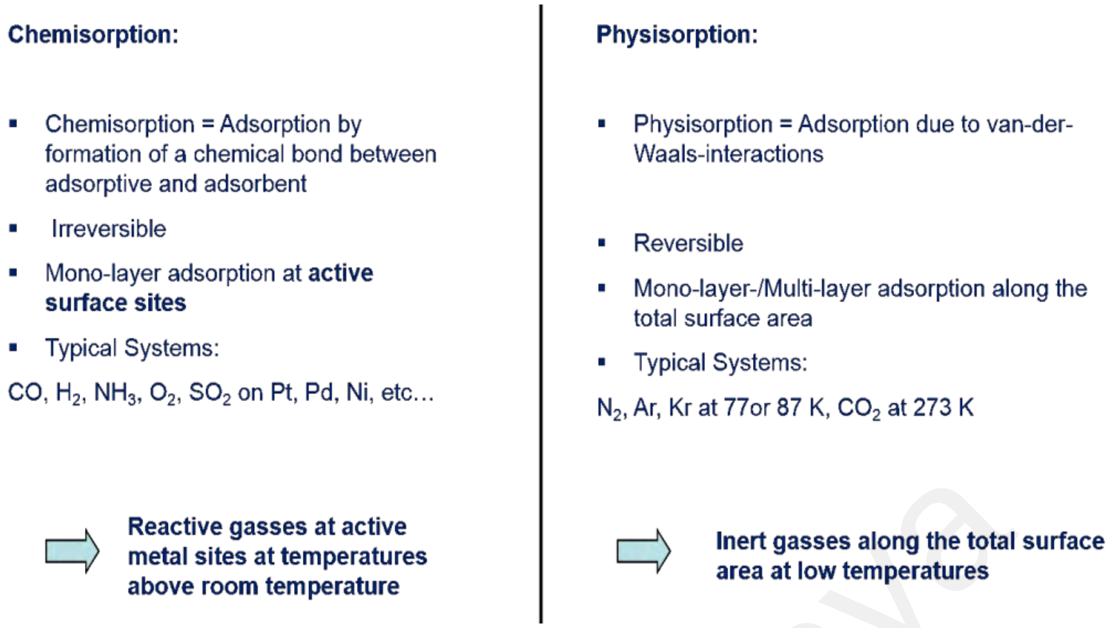

Chemisorption:

- Chemisorption = Adsorption by formation of a chemical bond between adsorptive and adsorbent
- Irreversible
- Mono-layer adsorption at **active surface sites**
- Typical Systems:

CO, H_2, NH_3, O_2, SO_2 on Pt, Pd, Ni, etc…

Reactive gasses at active metal sites at temperatures above room temperature

Physisorption:

- Physisorption = Adsorption due to van-der-Waals-interactions
- Reversible
- Mono-layer-/Multi-layer adsorption along the total surface area
- Typical Systems:

N_2, Ar, Kr at 77or 87 K, CO_2 at 273 K

Inert gasses along the total surface area at low temperatures

The quantities of specific surface area property which determined via BET theory is depended on the adsorption cross section of the adsorbent molecule, because, it is a scale-dependent property without definable single true value of specific surface area [261].

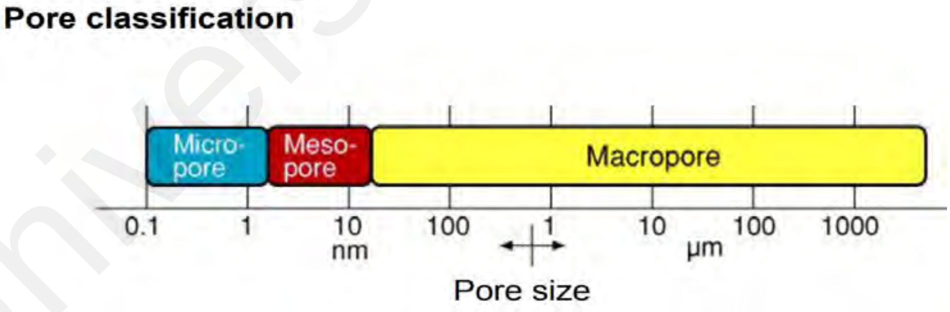

Table 4.9: Classification of the pores

Pore Name	Pore Size (Å)
Ultra-micropore	< 5
Micropore	5-20
Mesopore	20-500
Macropore	> 500

Note: Å= 10^{-10} m, nm= 10^{-9} m, µm= 10^{-6} m, so Å= 10^{-1} nm or 1nm= 10 Å

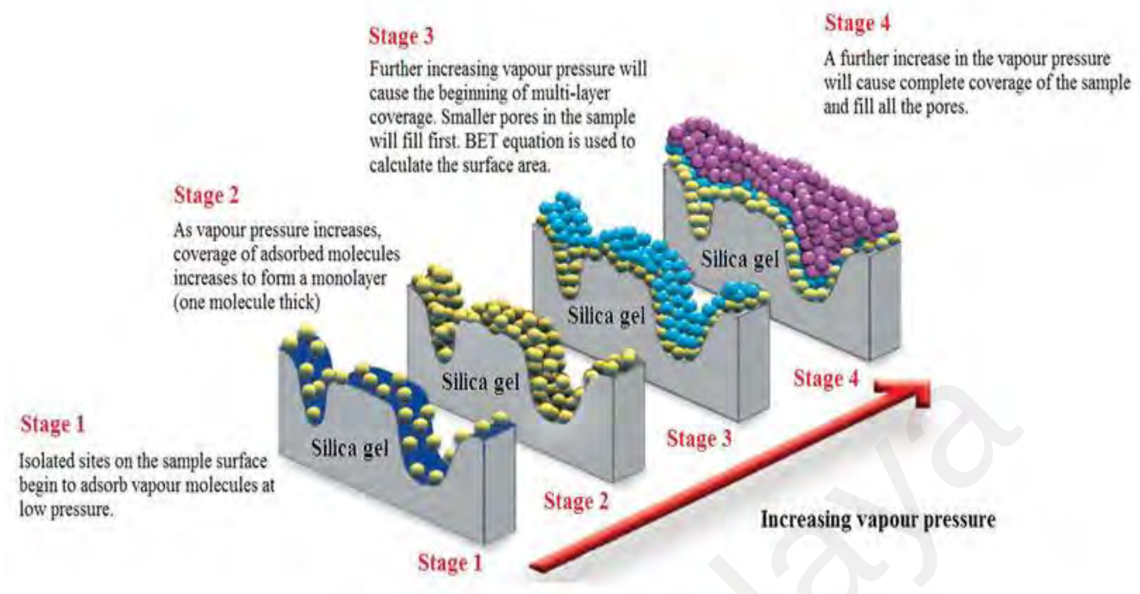

Scheme 4.2: Shows the different stages of gas adsorption process.

MOF is a coordination network with organic ligands containing potential voids, which means that, many systems are dynamic, and changes in structure and thus corresponding changes in potential porosity or solvent and/or guest filled voids might occur depending on temperature, pressure, or other external stimuli. For these reasons, it is also not required that, an MOF be crystalline. There were some attempts to get away for maintaining the porosity of the new synthesized MOFs and/or for getting rid of solvent in the pore by using activation conditions, such as, vacuum oven and/or solvents' exchanges but, unfortunately, failed all.

All industrial adsorbents, which are used as catalysts and supported materials in heterogeneous catalysis have large specific surface areas [262], e.g. silica gel has 300 - 350 m^2/g, γ-alumina has 200 - 500 m^2/g, zeolites have 500 - 1100 m^2/g. In addition, activated carbons have more than 300 - 2500 m^2/g of surface areas in a single gram. Therefore, they are highly porous or composed of very fine particles [260].

The physical adsorption isotherm charts can be classified as one of 6 types according to IUPAC classifications [263], Figure 4.59:

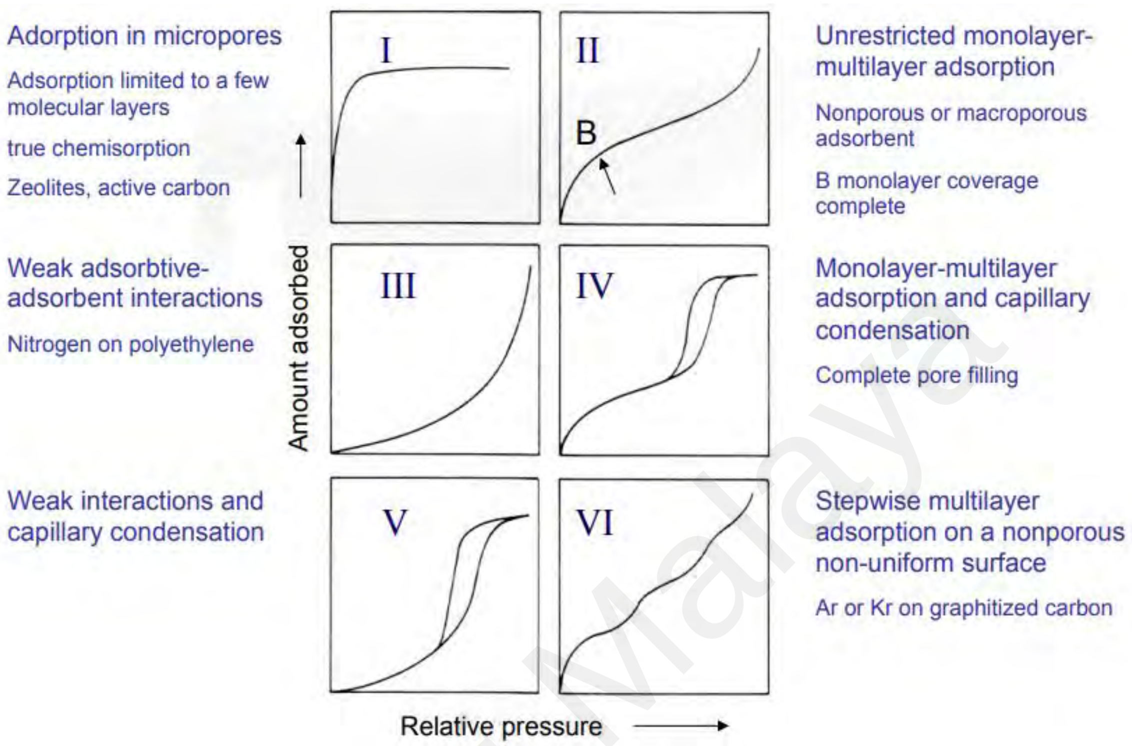

Figure 4.59: Different types of the physical adsorption isotherm charts.

The BET measurements of the new synthesized porous compounds which is summarized in Table 4.8, showed the lowest surface areas (0.6162, 1.6729) m^2/g for **1**, **18**, respectively, that **18** showed the largest pore sizes 979.12 Å. Compound **1** has lower pore size (141.73 Å) comparing with **18** but it has lower surface area, that is maybe attributed to the little number of pores within the selected surface area. Compound **13** showed 2.4632 m^2/g of surface area and large pore sizes 206.117 Å, while compound **14** (which was prepared by the addition of (An) as N-donor ligand to **13**) showed double of surface area (4.7061 m^2/g) and reduced pore sizes 59.212 Å comparing with **13**. Compound **15** has the highest surface areas (34.2916 m^2/g) and the lowest pore size (37.729 Å) among the new synthesized compounds.

It thus becomes obvious that, compounds **1**, **13**, **14** and **15** under this study show type IV isotherm chart of BET (Figure 4.60 and Figures 16-20 in Appendix C) with pore sizes of 14.17, 20.61, 5.92 and 3.8 nm, respectively, since their pore size greater than 20 Å and less than 500 Å according to BET surface area and BJH pore size distribution results. This occurs in mesoporous materials on porous adsorbents with pores sizes in a range of 2 – 50 nm showed hysterisis loop, capillary condensation and produce mono-multilayer adsorption. Whilst compound **18** shows type III with pore sizes of 97.9 nm which is usually be convex to P/P_o axis and characterized by heats of adsorption less than the adsorbate heat of liquification. Adsorption proceeds as the adsorbate interaction with an adsorbed layer, is greater than the interaction with adsorbent surface and have adsorbate-adsorbate interactions means unrestricted mono-multilayer adsorption occurs and indicates complete monolayer coverage for macro porous materials [264].

Therefore, the researcher could conclude that, the addition of (An) to compound **13** and producing of compound **14** did not only give a pure phase of PXRD for **13** but also increased the surface area and improve the adsorption isothermal pattern of this compound (The BET patterns of other synthesized MOFs uploaded at Appendix C).

Table 4.10: The surface areas and pore sizes of the new synthesized compounds.

Comp. Code	**S BET (m^2g^{-1})**	BET Adsorption pore size (Å)	**BJH Adsorption pore size (Å)**	Pore volume (cm^3g^{-1})
1	0.6162	129.966	141.730	0.001895
13	2.4632	213.007	206.117	0.012992
14	4.7061	26.7889	59.212	0.002777
15	34.2916	30.1488	37.729	0.020133
18	1.6729	235.9610	979.120	0.009313

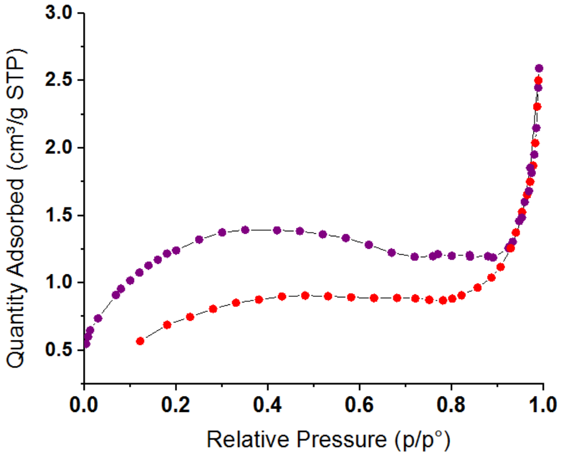

Figure 4.60: BET measurement of 14: shows the isotherm linear plot; red is adsorption curve, blue violate is desorption curve.

The vacuum oven activation of compound **14** did not affect on the crystallinity of the compound, but the structure was not still maintaining, hence, there was a shifting in some origin peaks and many new unidentified peaks, that showed up in the PXRD pattern after the activation process, Figure 4.74 (left). On the other hand, the BET activation of this compound did not affect its crystallinity and there was a little unidentified peak, that showed up in the PXRD pattern after the activation process, Figure 4.74 (right).

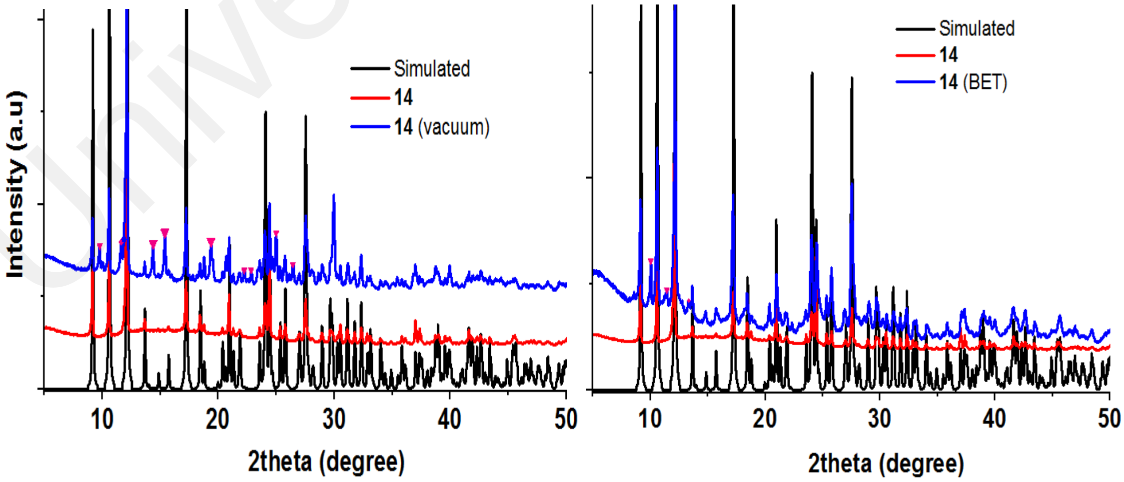

Figure 4.61: PXRD pattern of 14 after: (left) The vacuum oven activation, (right) the BET activation measurement.

CHAPTER 5: CONCLUSION AND FUTURE WORK

5.1 Conclusion

In summary, we have successfully synthesized a new, rare, and highly water stable Bi MOF by combining H_2pzdc ligand (which featuring O and N donor atoms) and Bi^{3+} cation using a simple slow evaporation method with an addition of imidazole required to obtain nearly quantitative yield. The resulting compound **1**, Bi(pzdc)(Hpzdc)·xH_2O (x= 0.5, 0.78, 0.9, 1.25, 1.9, and 6.0), consists of Bi dimer slabs that are connected into 3D coordination polymer via H_2pzdc linking ligands with hydrogen-bonded lattice water occupying the pore. The obtained publishable proton conductivity of 8.41×10^{-6} S·cm^{-1}, at 85 ºC and 95% RH is likely due to an extended hydrogen-bonded lattice water feature along the crystallographic *c*-direction reinforced by highly water stable structure of **1**.

We also have successfully synthesized three new lead MOFs based on H_3BTC ligand (which featuring only O donor atoms) using a simple dissolution-crystallization method. Although these compounds were unstable during storage, even under mother liquor, and utilizing HSAB principle, further, we successfully made air stable versions of **14** and **17** by adding a small amount of aniline and imidazole (as modulator agent), therefore they can be used for further bulk applications. In addition, the two compounds show different PL colors to that of BTC ligand, indicating a successful charge transfer. Compound **14** was found to luminesce pale greenish yellow under 350 nm excitation, while an interesting near white emission was observed for **17** when excited at 350 nm. The latter has potential for single phase, white-light emitting compound for solid-state lighting application.

Despite the fact that they cannot be activated, the researcher found that as synthesized **14** and **17** have the ability to remove MB and MR dyes up to 90% that they could be promising candidates as adsorbent for dyes removal from the water's environment.

Most of the synthesized compounds under this study **1**, **13**, **14** and **15** are mesoporous materials since, their pore size greater than 20 Å and less than 500 Å, while compound **18** with pore sizes of 97.9 nm is a macro porous material according to BET surface area and BJH pore size.

5.2 Future work

According to the results that obtained from the soaking of some different batches of BiMOFs in aqueous solution of sodium cation Na^+ and acetate CH_3COO^- or sulfate SO_4^{2-} anions to improve the proton conductivity of this MOF, our future work will be soaking these porous compounds in various cations and/or anions to check the ion- exchange ability of this kind of frameworks. Furthermore, there will be an attempt to explore the penetration of aniline and imidazole in the modulation process of the framework of PbMOFs (**13** and **15**) since these modulation agents did not incorporate in the structure of these compounds according to SCXRD measurements but only did an arrangement for the framework and gave very pure phase of PXRD pattern.

REFERENCES

1. Kickelbick, G. (2006). *Introduction to Hybrid Materials* (Ch.1, pp.1-48). Weinheim, Germany: Wiley-VCH Verlag GmbH & Co. KGaA.

2. Sebastian, Z., Pieremanuele, C., Kui, T., Yves, J. C., & Timo, T. (2014). Study of van der Waals bonding and interactions in metal organic framework materials. *Journal of Physics: Condensed Matter*, *26*(13), Article#133002.

3. Pedersen, C. J. (1967). Cyclic polyethers and their complexes with metal salts. *Journal of the American Chemical Society*, *89*, 7017-7036.

4. Morgan, A. B. (2008). Hybrid materials: Synthesis, characterization, and applications. Edited by Guido Kickelbick (Technische Universität Wien, Austria). *Journal of the American Chemical Society*, *130*(3), 1111-1112.

5. Hasegawa, T., Kasahara, Y., Yoshida, S., Kurashina, T., Aoki, S., Yoza, K., & Nomiya, K. (2007). Organic–inorganic hybrid material as zwitterion: Synthesis and structure of terminal ammonium ions-containing organosilyl species supported on mono-lacunary dawson polyoxometalate. *Inorganic Chemistry Communications*, *10*(12), 1416-1419.

6. Batten, S. R., Neville, S. M., Turner, D. R., & Fromm, K. M. (2009). Coordination polymers: Design, analysis and application. *A Journal of German Chemical Society*, *48*(27), 4890-4891.

7. Perry IV, J. J., Perman, J. A., & Zaworotko, M. J. (2009). Design and synthesis of metal–organic frameworks using metal–organic polyhedra as supermolecular building blocks. *Chemical Society Reviews*, *38*(5), 1400-1417.

8. Wang, G., Liu, Y., Huang, B., Qin, X., Zhang, X., & Dai, Y. (2015). A novel metal-organic framework based on Bismuth and trimesic acid: Synthesis, structure and properties. *Dalton Transactions*, *44*(37), 16238-16241.

9. Batten, S. R., Champness, N. R., Chen, X. M., Garcia, M. J., Kitagawa, S., O'Keeffe, M., … Reedijk, J. (2012). Coordination polymers, metal-organic frameworks and the need for terminology guidelines. *Crystal Engineering Communications*, *14*(9), 3001-3004.

10. Yaghi, O. M., Richardson, D. A., Davis, E., Li, G., & Groy, T. L. (1995). Open framework solid with diamond-like structures prepared from clusters and metal-organic building blocks. *Materials Research Society Symposium Proceedings*, *371*, 15-19.

11. Yaghi, O.M., & Li, H. (1995). Hydrothermal synthesis of a metal-organic framework containing large rectangular channels. *Journal of the American Chemical Society*. *117*(41), 10401-10402.

12. Shimomura, S., Horike, S., & Kitagawa, S. (2007). Chemistry and application of porous coordination polymers. *Studies in Surface Science and Catalysis*, *170B*, 1983-1990.

13. Noro, S. I., Ochi, R., Inubushi, Y., Kubo, K., & Nakamura, T. (2015). CH_4/CO_2 and CH_4/C_2H_6 gas separation using a flexible one-dimensional copper(II) porous coordination polymer. *Microporous and Mesoporous Materials*, *216*, 92-96.

14. Liu, D., Liu, T. F., Chen, Y. P., Zou, L., Feng, D., Wang, K., … Zhou, H. C. (2015). A Reversible crystallinity-preserving phase transition in metal-organic frameworks: Discovery, mechanistic studies, and potential applications. *Journal of American Chemical Society*, *137*(24), 7740-7746.

15. Weng, D. F., Wang, Z. M., & Gao, S. (2011). Framework-structured weak ferromagnets. *Chemical Society Reviews*, *40*(6), 3157-3181.

16. Wang, X. Y., Avendaño, C., & Dunbar, K. R. (2011). Molecular magnetic materials based on 4d and 5d transition metals. *Chemical Society Reviews*, *40*(6), 3213-3238.

17. Kuppler, R. J., Timmons, D. J., Fang, Q. R., Li, J. R., Makal, T. A., Young, M. D., … Zhou, H. C. (2009). Potential applications of metal-organic frameworks. *Coordination Chemical Reviews*, *253*, 3042–3066.

18. Heine, J., & Müller B. K. (2013). Engineering metal-based luminescence in coordination polymers and metal–organic frameworks. *Chemical Society Reviews*, *42*(24), 9232-9242.

19. Férey, G., Serre, C., Devic, T., Maurin, G., Jobic, H., Llewellyn, P. L., … Chang, J. S. (2011). Why hybrid porous solids capture greenhouse gases?. *Chemical Society Reviews*, *40*(2), 550-562.

20. Cui, Y., Yue, Y., Qian, G., & Chen, B. (2012). Luminescent functional MOF. *Chemistry Reviews*, *112*, 1126-1162.

21. Burtch, N. C., Jasuja, H., & Walton, K. S. (2014). Water stability and adsorption in metal-organic frameworks. *Chemistry Reviews*, *114*, 10575-10612.

22. Furukawa, H., Cordova, K. E., O'Keeffe, M., & Yaghi, O. M. (2013). The chemistry and applications of metal-organic frameworks. *Science*, *341*(6149), 974-986.

23. Han, Y., Li, J. R., Xie, Y., & Guo, G. (2014). Substitution reactions in metal-organic frameworks and metal-organic polyhedra. *Chemical Society Reviews*, *43*(16), 5952-5981.

24. Aamod, V. D., Biplab, M., Avishek, K., Amit, S., & Sujit, K. G. (2016). A water-stable cationic metal–organic framework as a dual adsorbent of oxoanion pollutants. *A Journal of German Chemical Society*, *55*(27), 7811-7815.

25. Karmakar, A., Desai, A. V., & Ghosh, S. K. (2016). Ionic metal-organic frameworks (iMOFs): Design principles and applications. *Coordination Chemistry Reviews*, *307*, 313-341.

26. O'Keeffe, M., Peskov, M. A., Ramsden, S. J., & Yaghi, O. M. (2008). The reticular chemistry structure resource (RCSR) database of, and symbols for, crystal nets. *Accounts of Chemical Research*, *41*(12), 1782-9.

27. Bureekaew, S., Shimomura, S., & Kitagawa, S. (2008). Chemistry and application of flexible porous coordination polymers. *Science and Technology of Advanced Materials*, *9*(1), Article#014108.

28. Morsali, A., & Hashemi, L. (2017). Main group metal coordination polymers: Structures and nanostructures. *A Journal of German Chemical Society*, *56*(45), 13938-13938.

29. Raut, R. K., & Majumdar, M. (2017). Direct coordination of a germanium(II) dicationic center to transition metals. *Chemical Communications*, *53*(9), 1467-1469.

30. (UBC), T.U.o.B.C., (2010). *Chemistry of element: the p-block elements and their compounds-I* (Ch.21, pp.42-61). Retrieved on 23 Novermber 2019 from https://nois.ac.in.

31. Miao, R. Q., Zhou, Q. Q., Wang, S. Q., Cheng, X. Y., Wang, D. F., & Huang, R. B. (2019). Solvent-induced Zn(II) coordination polymers with 1, 3, 5- benzene tricarboxylic acid. *Journal of Molecular Structure*, *1184*, 219-224.

32. Junkers, T., Vandenbergh, J., Adriaensens, P., Lutsen, L., & Vanderzande, D. (2012). Synthesis of poly(p-phenylene vinylene) materials via the precursor routes. *Polymer Chemistry*, *3*(2), 275-285.

33. Carter, K. P., Young, A. M., & Palmer, A. E. (2014). Fluorescent sensors for measuring metal ions in living systems. *Chemical Reviews*, *114*(8), 4564-4601.

34. Bansal, S., & Chiu, M. (2017). Atmospherically processed and stable Cs-pb based perovskite solar cells. *MRS Advances*, *2*(53), 3083-3090.

35. Elias, A. J. (2019). *The Chemistry of the p-Block Elements: Syntheses, Reactions and Applications* (1st ed.). India, Delhi: –Universities Press, Hyderabad 2018.

36. Mao, L. H., Morsali, A., & Aboutorabi, L. (2011). Lead(II) carboxylate supramolecular compounds: Coordination modes, structures and nano-structures aspects. *Coordination Chemistry Reviews*, *255*(23-24), 2821–2859.

37. Wibowo, A. C., Vaughn, S. A., Smith, M. D., & zur Loye, H. C. (2010). Novel bismuth and lead coordination polymers synthesized with pyridine-2,5-dicarboxylates: Two single component "white" light emitting phosphors. *Inorganic Chemistry*, *49*(23), 11001-11008.

38. Wibowo, A. C., Vaughn, S. A., Smith, M. D., & zur Loye, H. C. (2011). New 3D bismuth-oxo coordination polymers containing terephthalate-based ligands: Observation of Bi_2O_2-layer and Bi_4O_3-chain motifs. *Crystal Engineering Communications*, *13*(2), 426-429.

39. Wibowo, A. C., Smith, M. D., & zur Loye, H. C. (2011). Structural diversity of metal–organic materials containing bismuth(III) and pyridine-2,5-dicarboxylate. *Crystal Growth & Design*, *11*, 4449-4457.

40. Wibowo, A. C., Smith, M. D., Yeon, J., Halasyamani, P. S., & zur Loye, H. C., (2012). Novel 3D bismuth-based coordination polymers: Synthesis, structure, and second harmonic generation properties. *Journal of Solid State Chemistry*, *195*, 94-100.

41. Wardana, F. Y., Ng, S. W., & Wibowo, A. C. (2015). The lead coordination polymers containing pyrazine-2,3-dicarboxylic acid: Rapid structural transformations and cation exchange. *Crystal Growth & Design*, *15*(12), 5930-5938.

42. Thirumurugan, A., Tan, J. C., & Cheetham, A. K. (2010). Heterometallic inorganic−organic frameworks of sodium−bismuth benzenedicarboxylates. *Crystal Growth & Design*, *10*, 1736-1741.

43. Peedikakkal, A. M. P., & Vittal, J. J. (2011). Structural transformations of Pb(II)-trans-1,2-bis(4 '-pyridyl)ethene coordination polymers in solution. *Crystal Growth & Design*, *11*, 4697-4703.

44. Akhbari, K., & Morsali, A. (2013). Solid- and solution-state structural transformations in flexible lead(II) supramolecular polymers. *Crystal Engineering Communications*, *15*, 8915-8918.

45. Wibowo, A. C., Smith, M. D., & zur Loye, H. C. (2011). A new Kagomé lattice coordination polymer based on bismuth and pyridine-2,5-dicarboxylate: Structure and photoluminescent properties. *Chemical Communications*, *47*, 7371-7373.

46. Li, B., Zhang, H., Huynh, L., Diverchy, C., Hermans, S., Devillers, M., & Dikarev, E. V. (2009). Bismuth−palladium heterometallic carboxylate as a single-source precursor for the carbon-supported Pd−Bi/C catalysts. *Inorganic Chemistry*, *48*(13), 6152-6158.

47. Filatov, A. S., Napier, M., Vreshch, V. D., Sumner, N. J., Dikarev, E. V., & Petrukhina, M. A. (2012). From solid state to solution: Advancing chemistry of Bi–Bi and Bi–Rh paddlewheel carboxylates. *Inorganic Chemistry*, *51*, 566-571.

48. Dikarev, E. V., & Li, B. (2004). Rational syntheses, structure, and properties of the first bismuth(III) carboxylate. *Inorganic Chemistry*, *43*(11), 3461-3466.

49. Sukhov, B.G., Mukha, S. A., Antipova, I. A., Medvedeva, S. A., Larina, L. I., Chipanina, N. N., … Trofimov, B. A. (2008). Stereoactive lone pair of electrons on bismuth (III): Tris(3-hydroxy-2-methyl-4H-pyran-4-onato) bismuth (III). *Arkivoc*, *8*, 139-149.

50. Catalano, J., Murphy, A., Yao, Y., Yap, G. P. A., Zumbulyadis, N., Centeno, S. A., & Dybowski, C. (2015). Coordination geometry of lead carboxylates - spectroscopic and crystallographic evidence. *Dalton Transactions*, *44*(5), 2340-2347.

51. Persson, I., Lyczko, K., Lundberg, D., Eriksson, L., & Płaczek, A. (2011). Coordination chemistry study of hydrated and solvated lead(II) ions in solution and solid state. *Inorganic Chemistry*, *50*(3), 1058-1072.

52. Miao, M. S., Brgoch, J., Krishnapriyan, A., Goldman, A., Kurzman, J. A., & Seshadri, R. (2013). On the stereochemical inertness of the auride lone pair: Ab Initio studies of AAu (A = K, Rb, Cs). *Inorganic Chemistry*, *52*(14), 8183-8189.

53. Stoltzfus, M. W., Woodward, P. M., Seshadri, R., Klepeis, J. H., & Bursten, B. (2007). Structure and bonding in $SnWO_4$, $PbWO_4$, and $BiVO_4$: Lone pairs vs inert pairs. *Inorganic Chemistry*, *46*(10), 3839-3850.

54. Pearson, R. G. (1963). Hard and soft acids and bases. *Journal of the American Chemical Society*, *85*(22), 3533-3539.

55. Stavila, V., Davidovich, R. L., Gulea, A., & Whitmire, K. H. (2006). Bismuth(III) complexes with aminopolycarboxylate and polyaminopolycarboxylate ligands: Chemistry and structure. *Coordination Chemistry Reviews*, *250*(21), 2782-2810.

56. Gschwind, F., & Jansen, M. (2012). An unusual bismuth ethanedisulfonate network. *Crystals*, *2*(4), 1374-1381.

57. Whitmire, K. H. (2011). Bismuth: Inorganic chemistry, in encyclopedia of inorganic and bioinorganic chemistry. John Wiley & Sons, Ltd.

58. Hu, M. L., Morsali, A. & Aboutorabi, L. (2011). Lead(II) carboxylate supramolecular compounds: Coordination modes, structures and nano-structures aspects. *Coordination Chemistry Reviews*, *255*(23-24), 2821-2859.

59. Parr, J. (1997). Some recent coordination chemistry of lead(ll). *Polyhedron*, Elsevier Science Ltd, *16*(4), 551- 566.

60. Magyar, J. S., Weng, T. C., Stern, C. M., Dye, D. F., Rous, B. W., Payne, J. C., … Godwin, H. A. (2005). Reexamination of lead(II) coordination preferences in sulfur-rich sites: Implications for a critical mechanism of lead poisoning. *Journal of the American Chemical Society*, *127*(26), 9495-9505.

61. Seema, T., Tripathi, I. P., & Tiwari, H. L. (2013). Effects of lead on environment. *International Journal of Emerging Research in Management &Technology*, *2*(6), 1-5.

62. Zhai, Q. G. (2007). Coligand modulated six-, eight-, and ten-connected Zn/Cd-1,2,4-triazolate frameworks based on mono-, bi-, tri-, penta-, and heptanuclear cluster units. *Crystal Growth & Design*, *7*(11), 2332-2342.

63. Meng, L. (2017). Three 3D metal coordination polymers based on triazol-functionalized rigid ligand: Synthesis, topological structure and properties. *Journal of Solid State Chemistry*, *258*, 56-63.

64. Rosi, N. L., Kim, J., Eddaoudi, M., Chen, B., O'Keeffe, M., & Yaghi, O. M. (2005). Rod packings and metal-organic frameworks constructed from rod-shaped

secondary building units. *Journal of the American Chemical Society*, *127*(5), 1504-18.

65. Tranchemontagne, D. J., Mendoza, C. J. L., O'Keeffe, M., & Yaghi, O. M. (2009). Secondary building units, nets and bonding in the chemistry of metal-organic frameworks. *Chemical Society Reviews*, *38*(5), 1257-1283.

66. Eddaoudi, M., Moler, D. B., Li, H., Chen, B., Reineke, T. M., O'Keeffe, M., & Yaghi, O. M. (2001). Modular chemistry: Secondary building units as a basis for the design of highly porous and robust metal−organic carboxylate frameworks. *Accounts of Chemical Research*, *34*(4), 319-330.

67. Kalmutzki, M. J., Hanikel, N., & Yaghi, O.M. (2018). Secondary building units as the turning point in the development of the reticular chemistry of MOFs. *Science Advances*, *4*(10), Article#9180.

68. Brozek, C. K., & Dincă, M. (2012). Lattice-imposed geometry in metal–organic frameworks: lacunary Zn_4O clusters in MOF-5 serve as tripodal chelating ligands for Ni^{2+}. *Chemical Science*, *3*(6), 2110-2113.

69. Batten, S. R., Champness, N. R., Chen, X. M., Garcia, M. J., Kitagawa, S., Öhrström, L., … Reedijk, J. (2013). Terminology of metal–organic frameworks and coordination polymers. (IUPAC Recommendations 2013), *Pure and Applied Chemistry*, *85*(8), 1715–1724.

70. Moghadam, P. Z., Li, A., Wiggin, S. B., Tao, A., Maloney, A. G. P., Wood, P. A., … Fairen, J. D. (2017). Development of a cambridge structural database subset: A collection of metal–organic frameworks for past, present, and future. *Chemistry of Materials*, *29*(7), 2618-2625.

71. Papaefstathiou, G., & Macgillivray, L. (2003). Inverted metal-organic frameworks: Solid-state hosts with modular functionality. *Coordination Chemistry Reviews*, *246*, 169-184.

72. McNaught, A. D., & Wilkinson, A. (1994). International union of pure and applied chemistry : Glossary of terms used in physical organic chemistry. *Pure and Applied Chemistry*. *66*(5), 1077-1184.

73. McCleverty, J. A., & Ward, M. D. (1998). The role of bridging ligands in controlling electronic and magnetic properties in polynuclear complexes. *Accounts of Chemical Research*, *31*(12), 842-851.

74. Lestari, W., Winarni, I., & Rahmawati, F. (2017). Electrosynthesis of metal-organic frameworks (MOFs) based on nickel(II) and benzene 1,3,5-tri carboxylic acid (H_3BTC): An optimization reaction condition. *Materials Science and Engineering*, *172*, Article#012064.

75. Bosch, M., Zhang, M., & Zhou, H. C. (2014). Increasing the stability of metal-organic frameworks. *Advances in Chemistry*, *2014*, 1-8.

76. Xu, Z. X., Tan, Y. X., Fu, H. R., Kang, Y., & Zhang, J. (2015). Integration of rigid and flexible organic parts for the construction of homochiral metal-organic framework with high porosity. *Chemical Communications*, *51*, 2565-2568.

77. Gunasekaran, K., & Nussinov, R. (2007). How different are structurally flexible and rigid binding sites? Sequence and structural features discriminating proteins that do and do not undergo conformational change upon ligand binding. *Journal of Molecular Biology (JMB)*, *365*(1), 257-73.

78. He, H., Collins, D., Dai, F., Zhao, X., Zhang, G., Ma, H., & Sun, D. (2010). Construction of metal−organic frameworks with 1D chain, 2D grid, and 3D porous framework based on a flexible imidazole ligand and rigid benzenedicarboxylates. *Crystal Growth & Design*, *10*(2), 895-902.

79. Tan, Y. X., He, Y. P. & Zhang, J. (2012). Tuning MOF stability and porosity via adding rigid pillars. *Inorganic Chemistry*, *51*(18), 9649-9654.

80. He, Y., Shang, J., Gu, Q., Li, G., Li, J., Singh, R., … Webley, P. A. (2015). Converting 3D rigid metal–organic frameworks (MOFs) to 2D flexible networks via ligand exchange for enhanced CO_2/N_2 and CH_4/N_2 separation. *Chemical Communications*, *51*, Article#14716.

81. Lin, Z. J., Lu, J., Hong, M., & Cao, R. (2014). Metal-organic frameworks based on flexible ligands (FL-MOFs): Structures and applications. *Chemical Society Reviews*, *43*(16), 5867-5895.

82. Bučar, D. K., Papaefstathiou, G. S., Hamilton, T. D., Chu, Q. L., Georgiev, I. G., & MacGillivray, L. R. (2007). Template-controlled reactivity in the organic solid state by principles of coordination-driven self-assembly. *European Journal of Inorganic Chemistry*, *2007*(29), 4559-4568.

83. Shirani L. S., Ramli, Z., & Triwahyono, S. (2015). Effect of different templates on the synthesis of mesoporous sodalite. *Journal of Chemistry*, *2015*, 1-6.

84. Schmidt, J. E., Donglong, F., Deem, M. W., & Weckhuysen, B. M. (2016). Template–framework interactions in tetraethylammonium-directed zeolite synthesis. *A Journal of German Chemical Society*, 55(52), 16044-16048.

85. Yujia, S., & Hong, C. Z. (2015). Recent progress in the synthesis of metal–organic frameworks. *Science and Technology of Advanced Materials*, *16*(5), Article#054202.

86. Norbert, S., & Shyam, B. (2012). Synthesis of metal-organic frameworks (MOFs): Routes to various mof topologies, morphologies, and composites. *Chemical Reviews*, *112*(2), 933-969.

87. Nicholas, C. B., Himanshu, J., & Krista, S.W. (2014). Water stability and adsorption in metal–organic frameworks. *Chemical Reviews*, *114*(20), 10575-10612.

88. Elisa, B., Carmen, M., & Jorge A. R., (2014). Toxic gas removal – metal–organic frameworks for the capture and degradation of toxic gases and vapours. *Chemical Society Reviews*, *43*(16), 5419-5430.

89. Ryan, J. K., Daren J. T., Qian, R. F., Jian, R. L., Trevor A. M., Mark D. Y., … Cai, H. Z. (2009). Potential applications of metal-organic frameworks. *Coordination Chemistry Reviews*, *253*, 3042-3066.

90. Weng, D. F., Wang, Z. M., & Gao, S. (2011). Framework-structured weak ferromagnets. *Chemical Society Reviews*, *40*(6), 3157-3181.

91. Yuanjing, C., Yanfeng, Y., Guodong, Q., & Banglin, C. (2012). Luminescent functional metal–organic frameworks. *Chemical Reviews*, *112*(2), 1126-1162.

92. Rocha, J., Carlos, L. D., Almeida, P. F. A., & Duarte, A. (2011). Luminescent multifunctional lanthanides-based metal–organic frameworks. *Chemical Society Reviews*, *40*(2), 926-940.

93. Partha, M., Caroline, M. D., Partha, R., & Srinivasan, N. (2013). Solid state and solution mediated multistep sequential transformations in metal–organic coordination networks. *Crystal Growth & Design*, *13*(1), 155-168.

94. Wardana, F.Y., Ng, S. W., & Wibowo, A. C. (2015). The lead coordination polymers containing pyrazine-2,3-dicarboxylic acid: Rapid structural transformations and cation exchange. *Crystal Growth & Design*, *15*(12), 5930-5938.

95. Brozek, C. K., & Dincă, M. (2014). Cation exchange at the secondary building units of metal–organic frameworks. *Chemical Society Reviews*, *43*(16), 5456-5467.

96. Hamisu, A. M., Wardana, F. Y., Ariffin, A., Baig, I., Malliakas, C. D., & Wibowo, A. C. (2019). A new synthetic approach for substitutional solid solutions in a 3D coordination polymer: Cation vacancy, and tunable photoluminescence. *Journal of Solid State Chemistry*, *279*, Article#120948.

97. Chandan Dey, T. K., Bishnu P. Biswal, Mallick, A., & Banerjee, R. (2013). Crystalline metal-organic frameworks (MOFs): Synthesis, structure and function. *Acta Crystallographica Section B: Structural Science Crystal Engineering Materials*, *70*, 3-10.

98. Schoedel, A., Li, M., Li, D., O'Keeffe, M., & Yaghi, O. M. (2016). Structures of metal−organic frameworks with rod secondary building units. *Chemical Reviews*, *116*, 12466−12535.

99. Momma, K., & Izumi, F. (2011). MOFs from the fascination of crystals and symmetry. *Journal of Applied Crystallography*, *44*, 1272-1276.

100. Overview, I. R. A. (2018). The fascination of crystals and symmetry MOF nets: Correlation matrix of MOFs and their respective nets.

101. Zhou, Z., Xing, X., Tian, C., Wei, W., Li, D., Hu, F., & Du, S. (2018). A multifunctional nanocage-based MOF with tri- and tetranuclear zinc cluster secondary building units. *Scientific Reports*, *8*(1), Article#3117.

102. Almeida P. F. A., Klinowski, J., Vilela, S. M. F., Tomé, J. P. C., Cavaleiro, J. A. S., & Rocha, J. (2012). Ligand design for functional metal–organic frameworks. *Chemical Society Reviews*, *41*(3), 1088-1110.

103. Baumann, A. E., Burns, D. A., Liu, B., & Thoi, V. S. (2019). Metal-organic framework functionalization and design strategies for advanced electrochemical energy storage devices. *Communications Chemistry*, *2*(1), Article#86.

104. Seetharaj, R., Vandana, P. V., Arya, P., & Mathew, S. (2019). Dependence of solvents, pH, molar ratio and temperature in tuning metal organic framework architecture. *Arabian Journal of Chemistry*, *12*(3), 295-315.

105. ul Qadir, N., Said, S. A. M., & Bahaidarah, H. M. (2015). Structural stability of metal organic frameworks in aqueous media – Controlling factors and methods to improve hydrostability and hydrothermal cyclic stability. *Microporous and Mesoporous Materials*, *201*, 61-90.

106. Czaja, A. U., Trukhan, N., & Muller, U. (2009). Industrial applications of metal-organic frameworks. *Chemical Society Reviews*, *38*(5), 1284-1293.

107. Ogawa, T., Iyoki, K., & Fukushima, T. (2017). Landscape of research areas for zeolites and metal-organic frameworks using computational classification based on citation networks. *Materials* (Basel), *10*(12), Article#1428.

108. Farrusseng, D. (2011). Metal-organic frameworks: Applications from catalysis to gas storage. *A Jornal of German Chemical Society*, *51*(20), 4782-4783.

109. Sculley, J., Yuan, D., & Zhou, H. C. (2011). The current status of hydrogen storage in metal-organic frameworks-updated. *Energy & Environmental Science*, *4*(8), 2721-2735.

110. Ishaq, S., Tamime, R., Bilad, M. R., & Khan, A. L. (2019). Mixed matrix membranes comprising of polysulfone and microporous bio-MOF-1: Preparation and gas separation properties. *Separation and Purification Technology*, *210*, 442-451.

111. Keskin, S., & Kızılel, S. (2016). *Molecular simulations for adsorption-based CO_2 separation using metal organic frameworks* (Ch.4, pp.61-84). INTECH.

112. Gao, C. Y., Tian, H. R., Ai, J., Li, L. J., Dang, S., Lan, Y. Q., & Sun, Z. M. (2018). A microporous Cu-MOF with optimized open metal sites and pore spaces for high gas storage and active chemical fixation of CO_2. *Chemical Communications*, *54*(51), 7093-7094.

113. Camara, M., Daiguebonne, C., Guillou, O., Badiane, A. M., Badiane, I., Yague, S., & Le Dret, F. (2013). Synthesis and crystal structure of a new calcium-containing trimesate coordination polymer: $[Ca_3(BTC)_2(H_2O)_{12}]\infty$. J*ournal de la Société Ouest-Africaine de Chimie*, *35*, 57-63.

114. Jian-Rong, L., Julian, S., & Hong-Cai, Z. (2012). Metal–organic frameworks for separations. *Chemical Reviews*, *112*(2), 869-932.

115. Zheng, J. Y., Cui, X. L., Yang, Q. W., Ren, Q. L., Yang, Y. W., & Xing, H. B. (2018). Shaping of ultrahigh-loading MOF pellet with a strongly anti-tearing binder for gas separation and storage. *Chemical Engineering Journal*, *354*, 1075-1082.

116. Yangyang, L., Zhiyong U., W., & Hong-Cai, Z. (2012). Recent advances in carbon dioxide capture with metal-organic frameworks. *Greenhouse Gases: Science and Technology*, *2*(4), 239-259.

117. Ranocchiari, M., & van Bokhoven, J. A. (2011). Catalysis by metal-organic frameworks: Fundamentals and opportunities. *Physical Chemistry Chemical Physics*, *13*(14), 6388-6396.

118. Chen, L. J., Ding, X., Huo, J., El Hankari, S., & Bradshaw, D. (2019). Facile synthesis of magnetic macroporous polymer/MOF composites as separable catalysts. *Journal of Materials Science*, *54*(1), 370-382.

119. Zhu, W., Zhang, C. F., Li, Q., Xiong, L. K., Chen, R. X., Wan, X. B., … Peng, Y. (2018). Selective reduction of CO_2 by conductive MOF nanosheets as an efficient co-catalyst under visible light illumination. *Applied Catalysis B-Environmental*, *238*, 339-345.

120. Kreno, L. E., Leong, K., Farha, O. K., Allendorf, M., Van Duyne, R. P., & Hupp, J. T. (2012). Metal–organic framework materials as chemical sensors. *Chemical Reviews*, *112*(2), 1105-1125.

121. Yan, B. (2017). Lanthanide-functionalized metal–organic framework hybrid systems to create multiple luminescent centers for chemical sensing. *Accounts of Chemical Research*, *50*(11), 2789-2798.

122. Li, L. L., Feng, X. Q., Han, R. P., Zang, S. Q., & Yang, G. (2017). Cr(VI) removal via anion exchange on a silver-triazolate MOF. *Journal of Hazardous Materials*, *321*, 622-628.

123. Tian, B., Ning, Guo, H., Gao, Q., Tan, L. M., Tang, W., … Loh, K. P. (2016). Crystal engineering of naphthalenediimide-based metal–organic frameworks: Structure-dependent lithium storage. *ACS Applied Materials & Interfaces*, *8*(45), 31067-31075.

124. Wang, X. B., Zhu, H. J., Shi, X. Y., Qiu, X. Z., Lu, W. G., & Guo, H. S. (2019). Synthesis of MOF-199/CNTs nanocomposite for selective adsorption and determination of nonsteroidal anti-inflammatory drugs in human urine. *Journal of Nanoscience and Nanotechnology*, *19*(2), 627-633.

125. Zhang, L., Chen, Y., Shi, R., Rang, T. G., Pang, G. S., Wang, B. R., … Li, J. Y. (2018). Synthesis of hollow nanocages MOF-5 as drug delivery vehicle to solve the load-bearing problem of insoluble antitumor drug oleanolic acid (OA). *Inorganic Chemistry Communications*, *96*, 20-23.

126. Huxford, R. C., Rocca, J. D., & Lin, W. (2010). Metal-organic frameworks as potential drug carriers. *Current Opinion in Chemical Biology*, *14*(2), 262-268.

127. McKinlay, A. C., Morris, R. E., Horcajada, P., Férey, G., Gref, R., Couvreur, P., & Serre, C. (2010). BioMOFs: Metal–organic frameworks for biological and medical applications. *Journal of German Chemical Society*, *49*(36), 6260-6266.

128. Phan, A., Doonan, C. J., Uribe-Romo, F. J., Knobler, C. B., O'Keeffe, M., & Yaghi, O. M. (2010). Synthesis, structure, and carbon dioxide capture properties of zeolitic imidazolate frameworks. *Accounts of Chemical Research*, *43*(1), 58-67.

129. Murdock, C. R., Hughes, B. C., Lu, Z., & Jenkins, D. M. (2014). Approaches for synthesizing breathing MOFs by exploiting dimensional rigidity. *Coordination Chemistry Reviews*, *258-259*, 119-136.

130. Elsaidi, S. K., Mohamed, M. H., Banerjee, D., & Thallapally, P. K. (2018). Flexibility in metal–organic frameworks: A fundamental understanding. *Coordination Chemistry Reviews*, *358*, 125-152.

131. Taylor, J. M., Dawson, K. W., & Shimizu, G. K. H. (2013). A Water-stable Metal–organic framework with highly acidic pores for proton-conducting applications. *Journal of the American Chemical Society*, *135*(4), 1193-1196.

132. Tominaka, S., & Cheetham, A. K. (2014). Intrinsic and extrinsic proton conductivity in metal-organic frameworks. *RSC Advances*, *4*(97), 54382-54387.

133. Li, J., Yang, G., Hou, L., Cui, L., Li, Y., Wang, Y. Y., & Shi, Q. Z. (2013). Three new solvent-directed 3D lead(II)-MOFs displaying the unique properties of luminescence and selective CO_2 sorption. *Dalton Transactions*, *42*(37), 13590-13598.

134. Zhang, L., Li, Z. J., Lin, Q. P., Qin, Y. Y., Zhang, J., Yin, P. X., … Yao, Y. G. (2009). Synthesis, structure, and luminescent properties of hybrid inorganic-organic framework materials formed by lead aromatic carboxylates: Inorganic connectivity variation from 0D to 3D. *Inorganic Chemistry*, *48*, 6517-6525.

135. Abhinandan, R., Swapan, K. J., Madhusudan, B., Debdoot, H., Durga, S. C., Ennio, Z., & Sudipta, D. (2013). Two new metal-organic coordination polymers of lead with O-, N-donor ligands: Synthesis, characterization, luminescence and thermal behavior. *Journal of Solid State Chemistry*, *197*, 46-52.

136. Huggins, M. L. (1931). The role of hydrogen bonds in conduction by hydrogen and hydroxyl ions. *Journal of the American Chemical Society*, *53*(8), 3190-3191.

137. Biserka, K. P., & Kresimir, M. (2008). The nature of hydrogen bond: New insights into old theories. *Acta Chimica Slovenica*, *55*(4), 692–708.

138. Baikov, Y. M. (2009). Proton transfer in electrochemically active “solid hydroxide proton conductor-hydrogenated metal” heterostructures. *Russian Journal of Electrochemistry*, *45*(4), 364-373.

139. Takeo, M., & Marco, R. (2016). Grotthuss mechanisms: From proton transport in proton wires to bioprotonic devices. *Journal of Physics: Condensed Matter*, *28*(2), Article#023001.

140. von Grotthus, C. J. D. (1806). Pronton conductivity mechanism. *Annales de Chimie- Science des Matériaux (ACSM)*, *58*, 54-73.

141. Thomas, E. D. (2003). Voltage-gated proton channels and other proton transfer pathways. *Physiological Reviews*, *83*(2), 475-579.

142. Kreuer, K. D., Rabenau, A., & Weppner, W. (1982). Vehicle Mechanism: A New model for the interpretation of the conductivity of fast proton conductors. *A Journal of German Chemical Society*, *21*(3), 208–209.

143. Zhang, J., Bai, H. J., Ren, Q., Luo, H. B., Ren, X. M., Tian, Z.F., & Lu, S. (2018). Extra water- and acid-stable MOF-801 with high proton conductivity and its composite membrane for proton-exchange membrane. *ACS Applied Materials & Interfaces*, *10*(34), 28656-28663.

144. Wong, N. E., Ramaswamy, P., Lee, A. S., Gelfand, B. S., Bladek, K. J., Taylor, J. M., … Shimizu, G. K. H. (2017). Tuning intrinsic and extrinsic proton conduction in Metal–Organic Frameworks by the lanthanide contraction. *Journal of the American Chemical Society*, *139*(41), 14676-14683.

145. Loera, S. S., Oliver, T. M., De, M., López, N. L., Santana, C. A., Guzman, A., … Flores, J. (2012). Electrochemical behavior of [$Cu_3(BTC)_2$] metal–organic framework: The effect of the method of synthesis. *Journal of Alloys and Compounds*, *540*, 113-120.

146. Riccardi, D., König, P., Prat, R. X., Yu, H., Elstner, M., Frauenheim, T., & Cui, Q. (2006). "Proton Holes" in long-range proton transfer reactions in solution and enzymes: A theoretical analysis. *Journal of the American Chemical Society*, *128*(50), 16302-16311.

147. Joarder, B., Lin, J. B., Romero, Z., & Shimizu, G. K. H. (2017). Single crystal proton conduction study of a metal organic framework of modest water stability. *Journal of the American Chemical Society*, *139*(21), 7176-7179.

148. Wei, Y.S., Hu, X. P., Han, Z., Dong, X. Y., Zang, S. Q., & Mak, T. C. W. (2017). Unique proton dynamics in an efficient MOF-based proton conductor. *Journal of the American Chemical Society*, *139*(9), 3505-3512.

149. Zhang, F. M., Dong, L. Z., Qin, J. S., Guan, W., Liu, J., Li, S. L., … Zhou, H. C. (2017). Effect of imidazole arrangements on proton-conductivity in metal–organic frameworks. *Journal of the American Chemical Society*, *139*(17), 6183-6189.

150. Shao, Y. L., Cui, Y. H., Gu, J. Z., Wu, J., Wang, Y. W., & Kirillov, A. M. (2016). Exploring biphenyl-2,4,4′-tricarboxylic acid as a flexible building block for the hydrothermal self-assembly of diverse metal–organic and supramolecular networks. *Royal Society of Chemistry*, *18*(5), 765-778.

151. Liang, L., Liu, C., Jiang, F., Chen, Q., Zhang, L., Xue, H., … Hong, M. (2017). Carbon dioxide capture and conversion by an acid-base resistant metal-organic framework. *Nature Communications*, *8*, Article#1233.

152. Han, L., Qin, L., Yan, X. Z., Xu, L. P., Sun, J., Yu, L., … Zou, X. (2013). Two isomeric magnesium metal–organic frameworks with [24-MC-6] metallacrown cluster. *Crystal Growth & Design*, *13*(5), 1807-1811.

153. Cai, J. F., Rao, X. T., He, Y. B., Yu, J. C., Wu, C. D., Zhou, W., … Qian, G. D. (2014). A highly porous NbO type metal-organic framework constructed from an expanded tetracarboxylate. *Chemical Communications, 50*(13), 1552-1554.

154. Karra, J. R., & Walton, K. S. (2010). Molecular simulations and experimental studies of CO_2, CO, and N_2 adsorption in metal−organic frameworks. *The Journal of Physical Chemistry*, *114*(37), 15735-15740.

155. Ren, G. J., Liu, Y. Q., & Liu, S. J. (2015). Two novel metal-organic frameworks based on linear dicarboxylic acid and 5-(4-pyridyl)tetrazole. *Journal of Solid State Chemistry*, *232*, 79-82.

156. Masoomi, M. Y., Bagheri, M., & Morsali, A. (2015). Application of two cobalt-based metal–organic frameworks as oxidative desulfurization catalysts. *Inorganic Chemistry*, *54*(23), 11269-11275.

157. Zhu, J., Usov, P. M., Xu, W., Celis, S. P. J., Lin, S., Kessinger, M. C., … Morris, A. J. (2018). A New class of metal-cyclam-based zirconium metal–organic frameworks for CO_2 adsorption and chemical fixation. *Journal of the American Chemical Society*, *140*(3), 993-1003.

158. Maleki, A., Hayati, B., Naghizadeh, M., & Joo, S. W. (2015). Adsorption of hexavalent chromium by metal organic frameworks from aqueous solution. *Journal of Industrial and Engineering Chemistry*, *28*, 211-216.

159. Mahmoodi, N. M., & Abdi, J. (2019). Nanoporous metal-organic framework (MOF-199): Synthesis, characterization and photocatalytic degradation of Basic Blue 41. *Microchemical Journal*, *144*, 436-442.

160. Venkatesham, V., Madhu, G. M., Satyanarayana, S. V., & Preetham, H. S. (2013). Adsorption of lead on gel combustion derived nano ZnO. *Procedia Engineering*, *51*, 308-313.

161. Rao, C. N. R., & Venkataragh, R. (1964). Contribution to the infrared spectra of five-membered N- and N,S-heterocyclic compounds. *Canadian Journal of Chemistry*, *42*, 43-49.

162. Zhang, H., Hou, J., Hu, Y., Wang, P., Ou, R., Jiang, L., … Wang, H. (2018). Ultrafast selective transport of alkali metal ions in metal organic frameworks with subnanometer pores. *Science Advances*, *4*(2), eaaq0066. 1-8.

163. Peng, Y., Huang, H., Zhang, Y., Kang, C., Chen, S., Song, L., … Zhong, C. (2018). A versatile MOF-based trap for heavy metal ion capture and dispersion. *Nature Communications*, *9*(1), Article#187.

164. Sun, D.T., Peng, L., Reeder, W.S., Moosavi, S.M., Tiana, D., Britt, D.K., … Queen, W.L. (2018). Rapid, selective heavy metal removal from water by a metal–organic framework/polydopamine composite. *ACS Central Science*, *4*(3), 349-356.

165. Shi, Y., Wang, W. M., Tang, G. P., Zhang, Y.-X., Li, M., & Wu, Z. L. (2018). Robust lanthanide metal–organic frameworks with highly sensitive sensing of aniline and slow magnetization relaxation behaviors. *Polyhedron*, *153*, 122-127.

166. Hashemi, L., & Morsali, A. (2012). Reversible crystal-to-crystal transformation in nano-porous three-dimensional lead(II) MOFs; Study of solvent attendance on iodide adsorption affinity. *Crystal Engineering Communications*, *14*(24), 8349-8351.

167. Raquel, A. F. E., Augusto, R. de de O.G., & Palma, de de O.D. (2012). The impact of aromatic amines on the environment: Risks and damages. *Frontiers in Bioscience* (Elite edition), *4*, 914-923.

168. Jaros, S. W., Sokolnicki, J., Wołoszyn, A., Haukka, M., Kirillov, A. M., & Smoleński, P. (2018). A novel 2D coordination network built from hexacopper(I)-iodide clusters and cagelike aminophosphine blocks for reversible “turn-on” sensing of aniline. *Journal of Materials Chemistry C*, *6*(7), 1670-1678.

169. Shooto, N. D., Dikio, E. D., Wankasi, D., & Sikhwivhilu, L. (2017). Iron-based metal organic framework as an effective lead ions remover from aqueous solution: Thermodynamic and kinetic studies. *Chemical Industry Website*, *71*(3), 221-229.

170. Shooto, N. D., Dikio, E. D., Wankasi, D., & Sikhwivhilu, L. (2015). Synthesis, morphology and lead ion adsorption properties of metal organic frameworks of copper and cobalt. *Chemical Sciences Journal*, *6*(4), 1000113-1000121.

171. Meng, X. M., Zong, Z. A., Zhang, X. Y., Zhang, X., Jin, F., & Fan, Y. H. (2017). Syntheses, structural diversity and dye adsorption properties of various Co(II) coordination polymers based on rigid tris(imidazolyl) and dicarboxylate ligands. *Polyhedron*, *127*, 257-265.

172. Keskin, S., & Kızılel, S. (2011). Biomedical applications of metal organic frameworks. *Industrial & Engineering Chemistry Research*, *50*(4), 1799-1812.

173. Rojas, S., Devic, T., & Horcajada, P. (2017). Metal organic frameworks based on bioactive components. *Journal of Materials Chemistry B*, *5*(14), 2560-2573.

174. Hinks, N. J., McKinlay, A. C., Xiao, B., Wheatley, P. S., & Morris, R. E. (2010). Metal organic frameworks as NO delivery materials for biological applications. *Microporous and Mesoporous Materials*, *129*(3), 330-334.

175. Bowen, E. J. (1968). *Luminescence in chemistry, Van Nostrand series in physical chemistry* (1st ed.). London; Princeton: Van Nostrand.

176. Gao, X. S., Dai, H. J., Ding, M. J., Pei, W. B., & Ren, X. M. (2019). Stereochemically active and inactive lone pairs in two room-temperature

phosphorescence coordination polymers of Pb^{2+} with different tricarboxylic acids. *Inorganic Chemistry*, *58*(10), 6772–6780.

177. Allendorf, M.D., Bauer, C. A., Bhakta, R. K., & Houk, R. J. T. (2009). Luminescent metal-organic frameworks. *Chemical Society Reviews*, *38*(5), 1330-1352.

178. Braslavsky, S.E. (2006). Glossary of terms used in photochemistry, (3rd Ed.), (IUPAC Recommendations 2006), *Pure and Applied Chemistry*, *79*(3), 293−465.

179. Zhang, K. L., Liang, W., Chang, Y., Yuan, L. M., & Ng, S.W. (2009). Syntheses, characterization and luminescent properties of two lead(II) fumarate metal-organic frameworks. *Polyhedron*, *28*(4), 647-652.

180. Hu, R., Cai, H., & Luo, J. (2011). Synthesis, structure and luminescent property of a pillared-layer coordination polymer [Pb(Bpdc)] (BPDC=4,4′-biphenyldicarboxylate). *Inorganic Chemistry Communications*, *14*(2), 433-436.

181. Deibert, B. J., Velasco, E., Liu, W., Teat, S. J., Lustig, W. P., & Li, J. (2016). High-performance blue-excitable yellow phosphor obtained from an activated solvochromic bismuth-fluorophore metal–organic framework. *Crystal Growth & Design*, *16*(8), 4178-4182.

182. Lestari, W. W., Lonnecke, P., Sarosi, M. B., Streit, H. C., Adlung, M., Wickleder, C., … Hey, H. E. (2013). Syntheses, structures and luminescence properties of novel metal-organic frameworks based on zinc(II), cadmium(II) or lead(II) and a 2,2 [prime or minute]- dimethoxy- functionalised biphenyl linker. *Crystal Engineering Communications*, *15*(19), 3874-3884.

183. Wang, C., Volotskova, O., Lu, K., Ahmad, M., Sun, C., Xing, L., & Lin, W. (2014). Synergistic assembly of heavy metal clusters and luminescent organic bridging ligands in metal–organic frameworks for highly efficient x-ray scintillation. *Journal of the American Chemical Society*, *136*(17), 6171-6174.

184. Koppen, M., Beyer, O., Wuttke, S., Luning, U., & Stock, N. (2017). Synthesis, functionalisation and post-synthetic modification of Bismuth metal-organic frameworks. *Dalton Transactions*, *46*(26), 8658-8663.

185. Martinez, C. F. J., Canadillas, D. L., Cucinotta, F., Guerrero, M. A., Ramos, R. M., Marchese, L., … Jose, A. (2012). Luminescent lead(II) complexes: New three-dimensional mixed ligand MOFs. *Crystal Engineering Communications*, *14*(8), 2660-2668.

186. Li, Q., Wu, X., Huang, X., Deng, Y., Chen, N., Jiang, D., … Zhao, Y. (2018). Tailoring the fluorescence of AIE-active metal–organic frameworks for aqueous sensing of metal ions. *ACS Applied Materials & Interfaces*, *10*(4), 3801-3809.

187. Triguero, C., Coudert, F. X., Boutin, A., Fuchs, A. H., & Neimark, A. V. (2011). Mechanism of breathing transitions in metal-organic Frameworks. *Journal of Physical Chemistry Letters*, *2*(16), 2033-2037.

188. Coudert, F. X., Boutin, A., Fuchs, A. H., & Neimark, A. V. (2013). Adsorption deformation and structural transitions in metal-organic frameworks: From the unit cell to the crystal. *Journal of Physical Chemistry Letters*, *4*(19), 3198-3205.

189. Alhamami, M., Huu, D., & Chil, H. C. (2014). A Review on breathing behaviors of metal-organic-frameworks (MOFs) for Gas Adsorption. *Materials*, *7*(4), 3198-3250.

190. Lama, P., & Barbour, L. J. (2018). Distinctive three-step hysteretic sorption of ethane with in situ crystallographic visualization of the pore forms in a soft porous crystal. *Journal of the American Chemical Society*, *140*(6), 2145-2150.

191. Deria, P., Gómez, G., Diego, A., Bury, W., Schaef, H. T., Wang, T. C., … Farha, O. K. (2015). Ultraporous, water stable, and breathing zirconium-based metal–organic frameworks with ftw topology. *Journal of the American Chemical Society*, *137*(40), 13183-13190.

192. Zhang, S., Wei, Q., Xie, G., Yang, Q., & Chen, S. P. (2012). In situ hydrothermal syntheses, structures and photoluminescent properties of three coordination polymers based on 3-amidecarbonylpyrazine-2-carboxylic acid. *Inorganica Chimica Acta*, *387*, 52-57.

193. Che, T. L., Gao, Q. C., Zhang, W. P., Nan, Z. X., Li, H. X., Cai, Y. G., & Zhao, J. S. (2009). Two novel coordination polymers $[Sm_2(Pzdc)_3(H_2O)]x\cdot 2xH_2O$ and $[Nd_2(Pzdc)_3(H_2O)]x.2xH_2O$: Synthesis, structure, and photoluminescent properties. *Russian Journal of Coordination Chemistry*, *35*(10), 723-720.

194. Yeşilel, O. Z., Mutlu, A., & Büyükgüngör, O. (2008). A new coordination mode of pyrazine-2,3-dicarboxylic acid and its first monodentate complexes: Syntheses, spectral, thermal and structural characterization of $[Cu(pzdca)(H_2O)(en)_2]\cdot H_2O$ and $[Cu(pzdca)(H_2O)(dmpen)_2]$. *Polyhedron*, *27*(11), 2471-2477.

195. Yang, T. H., Silva, A., Fu, L., & Shi, F. N. (2017). Synthesis, crystal structure and catalytic property of porous 3d-4f heterometallic coordination polymers constructed from pyrazine-2,3-dicarboxylic acid. *Journal of Inorganic and General Chemistry*, *643*(22), 1801-1808.

196. Yin, H., & Liu, S. X. (2007). Syntheses, crystal structures and photoluminescence of Cd coordination polymers with 2,3-pyrazine dicarboxylic acid. *Polyhedron*, 26, 3103-3111.

197. Günay, G., Yeşilel, O. Z., Soylu, M. S., Keskin, S., & Dal, H. (2011). Two novel 2D and 3D coordination polymers constructed from pyrazine-2,3-dicarboxylic acid and chloride bridged secondary building units. *Synthetic Metals*, *161*(21), 2471-2480.

198. Hernandez, M. J., Rodinson, R., Arrieta, P., Jos , N., Primera, P., & Exley, J. (2015). Structure of a porous $Cu_2(pzdc)_2(bpp)$ (pzdc: pyrazine-2,3-dicarboxylate, bpp: 1,3-Bis(4-pyridyl)propane) coordination polymer and flexibility upon concomitant hysteretic CO_2 adsorption. *Crystal Growth & Design*, *15*(8), 4123–4131.

199. Arzehgara, Z., Sajjadifara, S., & Arandiyanb, H. (2019). HKUST-1 as an efficient and reusable heterogeneous catalyst for synthesis of 1,4-dihydropyridine at room temperature. *Asian Journal of Green Chemistry*, *3*(1), 43-52.

200. Hongmei, W., Tao, Y., Xin, T., Zhang, H., Peng, L., Huimin, L., … Jinhua, Y. (2016). Enhanced photocatalytic oxidation of isopropanol by HKUST-1@TiO_2 core–shell structure with ultrathin anatase porous shell: toxic intermediate control. *Industrial & Engineering Chemistry Research*, *55*(29), 8096–8103.

201. Fenqiang, L., Yaolin, L., Liyan, Z., Xiaomei, L., & Yuwu, C. (2015). Encapsulation of Hemin in metal–organic frameworks for catalyzing the chemiluminescence reaction of the H_2O_2–Luminol system and detecting glucose in the neutral condition. *ACS Applied Materials & Interfaces*, *7*(21), 11322-11329.

202. Schneider, C., Ukaj, D., Koerver, R., Talin, A. A., Kieslich, G., Pujari, S. P., … Fischer, R. A. (2018). High electrical conductivity and high porosity in a Guest@MOF material: Evidence of TCNQ ordering within Cu_3BTC_2 micropores. *Chemical Science*, *9*(37), 7405–7412.

203. Sel, K., Demirci, S., Öztürk, Ö., Aktas, N., & Sahiner, N. (2015). NH_3 gas sensing applications of metal organic frameworks. *Microelectronic Engineering*, *136*, 71-76.

204. Guang, B. C., Jing, C., Xiang, C. W., Chun, B., Chun, J. W., Shen, T. W., & Yong, S. Y. (2011). A novel pillared double-layered Pb(II) coordination polymer based on 1,3,5-benzenetricarboxylic acid and dipyrido[3,2-a:2′,3′-c]-phenazine-2-carboxylic acid. *Inorganic Chemistry Communications*, *14*(7), 1086-1088.

205. Song, J. L., Jiang, G. M., Yan, Q. S. & Clearfield, A. (2003). Novel hybrid porous 3D networks of Lead(II) diphosphonate and triphosphonate containing 1,3,5 benzenetricarboxylate. *European Journal of Inorganic Chemistry*, *2003*(32), 4218-4226.

206. Jie, P. Z., Pei, Q. L., Hao, L. Z., Rui, B. L., & Xiao, M. C. (2014). Single-crystal X-ray diffraction studies on structural transformations of porous coordination polymers. *Chemical Society Reviews*, *43*(16), 5789-5814.

207. Shuai, D. Z., Zheng, Y. Z., Jun, G., Ling, H. L., Hui, H., Long, L. G., ...Yun, W. L. (2018). Structure modulation from unstable to stable MOFs by regulating secondary N-donor ligands. *Dalton Transactions*, *47*(39), 14025-14032.

208. Tse-Lok, H. (1975). Hard soft acids bases (HSAB) principle and organic chemistry. *Chemical Reviews*, *75*(1), 1-20.

209. Sun, Y. Q., Ge, S. Z., Liu, Q., Zhong, J. C., & Chen, Y. P. (2013). A novel 3-D chiral bismuth–organic framework with mixed carboxylate, pyridine and thiolate donors exhibiting a semiconductive property. *Crystal Engineering Communications*, *15*, 10188-1019.

210. Wang, G., Sun, Q., Liu, Y., Huang, B., Dai, Y., Zhang, X., & Qin, X. (2014). A bismuth-based metal-organic framework as an efficient visible-light-driven

photocatalyst. *Chemistry* (Weinheim an der Bergstrasse, Germany), *21*(6), 2364-2367.

211. Savage, M., Yang, S., Suyetin, M., Bichoutskaia, E., Lewis, W., Blake, A. J., ... Schröder, M. (2014). A Novel bismuth-based metal–organic framework for high volumetric methane and carbon dioxide adsorption. *Chemistry—A European Journal*, *20*, 8024-8029.

212. Feyand, M., Mugnaioli, E., Vermoortele, F., Bueken, B., Dieterich, J. M., Reimer, T., ... Stock, N. (2012). Automated diffraction tomography for the structure elucidation of twinned, sub-micrometer crystals of a highly porous, catalytically active Bismuth metal–organic framework. *A Journal of the German Chemical Society*, *51*, 10373-10376.

213. Hu, Z., Castano, I., Wang, S., Wang, Y., Peng, Y., Qian, Y., ... Zhao, D. (2016). Modulator effects on the water-based synthesis of Zr/Hf metal–organic frameworks: Quantitative relationship studies between modulator, synthetic condition, and performance. *Crystal Growth & Design*, *16*(4), 2295-2301.

214. Vermoortele, F., Bueken, B., Le Bars, G., Van de Voorde, B., Vandichel, M., Houthoofd, K., … De Vos, D. E. (2013). Synthesis modulation as a tool to increase the catalytic activity of metal–organic frameworks: The unique case of UiO-66(Zr). *Journal of the American Chemical Society*, *135*(31), 11465–11468.

215. Webber, T. E., Liu, W. G., Desai, S. P., Lu, C. C., Truhlar, D. G., & Penn, R. L. (2017). Role of a modulator in the synthesis of phase-pure NU-1000. *ACS Applied Materials & Interfaces*, *9*(45), 39342-39346.

216. Zahn, G., Zerner, P., Lippke, J., Kempf, F., Lilienthal, S., Schröder, C., ... Behrens, P. (2014). Insight into the mechanism of modulated syntheses: In situ synchrotron diffraction studies on the formation of Zr-fumarate MOF. *Crystal Engeneering Communications*, *16*(39), 9198-9207.

217. Spek, A. L. (2009). PLATON, A Multipurpose crystallographic tool, Utrecht University, Utrecht, The Netherlands. *Acta Crystallographica Section D*, *65*, 148-155.

218. Guilin, C., Jin, Z., Hui, F., Feifei, F., Pengfei, X., Saifei, P., … Zhaosheng, Q. (2019). A simple and efficient phosphorescent probe for iodide-specific detection based on crystallization-induced phosphorescence of organic ionic crystals. *Journal of Materials Chemistry C*, *7*(1), 43-47.

219. Max, J. J., & Chapados, C. (2004). Infrared spectroscopy of aqueous carboxylic acids: comparison between different acids and their salts. *The Journal of Physical Chemistry A*, *108*(16), 3324-3337.

220. Palacios, B., E., Juárez, L., G., & Monhemius, J. (2004). Infrared spectroscopy of metal carboxylates: Analysis of Fe(III), Ni and Zn carboxylate solutions. *Hydrometallurgy*, *72*, 139–148.

221. Krishnakumar, V., & Prabhavathi, N. (2009). Scaled quantum chemical calculations and FTIR, FT-Raman spectral analysis of 2-Methylpyrazine.

Spectrochimica Acta: Part A, Molecular and biomolecular spectroscopy, *72*(4), 743-747.

222. Nakamoto, K. (1997). *Infrared and raman spectra of inorganic and coordination compounds* (5th ed.). New York: Wiley Interscience.

223. Katritzky, A. R., & Jones, R. A. (1961). Infra-red absorption of heteroaromatic and benzenoid six-membered monocyclic nuclei—XI: Pyr-4-ones and pyr-4-thiones. *Spectrochimica Acta*, *17*(1), 64-67.

224. Wibowo, A. C., Smith, M. D., & zur Loye, H. C. (2011). A new Kagomé lattice coordination polymer based on bismuth and pyridine-2,5-dicarboxylate: structure and photoluminescent properties. *Chemical Communications*, *47*(26), 7371-7373.

225. Dikarev, E. V., Gray, T. G., & Li, B. (2005). Heterobimetallic main-group-transition-metal paddle-wheel carboxylates. *A Journal of the German Chemical Society*, *44*(11), 1721-1724.

226. van der Velde, J. H. M. (2016). A simple and versatile design concept for fluorophore derivatives with intramolecular photostabilization. *Nature Communications*, *7*(1), Article#10144.

227. Ramaswamy, P., Wong, N. E., & Shimizu, G. K. H. (2014). MOFs as proton conductors - challenges and opportunities. *Chemical Society Reviews*, *43*(16), 5913-5932.

228. Satoshi, H., Daiki, U., & Susumu, K. (2013). Ion Conductivity and transport by porous coordination polymers and metal–organic frameworks. *Accounts of Chemical Research*, *46*(11), 2376-2384.

229. Wong, N. E., Ramaswamy, P., Lee, A. S., Gelfand, B. S., Bladek, K. J., Taylor, J. M., … Shimizu, G.K.H. (2017). Tuning intrinsic and extrinsic proton conduction in metal–organic frameworks by the lanthanide contraction. *Journal of the American Chemical Society*, *139*, 14676–14683.

230. Yong-Sheng, W., Xiao-Peng, H., Zhen, H., Xi-Yan, D., Shuang-Quan, Z., & Thomas C. W. M. (2017). Unique proton dynamics in an efficient MOF-based proton conductor. *Journal of the American Chemical Society*, *139*(9), 3505-3512.

231. Laurita, G., Fabini, D. H., Stoumpos, C. C., Kanatzidis, M. G., & Seshadri, R. (2017). Chemical tuning of dynamic cation off-centering in the cubic phases of hybrid tin and lead halide perovskites. *Chemical Science*, *8*(8), 5628-5635.

232. Fabini, D. H., Labram, J. G., Lehner, A. J., Bechtel, J. S., Evans, H. A., Van der Ven, A., … Seshadri, R. (2017). Main-group halide semiconductors derived from perovskite: Distinguishing chemical, structural, and electronic aspects. *Inorganic Chemistry*, *56*(1), 11-25.

233. Smith, M. D., Connor, B. A., & Karunadasa, H. I. (2019). Tuning the luminescence of layered halide perovskites. *Chemical Reviews*, *119*(5), 3104-3139.

234. Smith, M. D., & Karunadasa, H. I. (2018). White-light emission from layered halide perovskites. *Journal of the American Chemical Society*, *51*(3), 619-627.

235. Osama, S. (2010). Layer-by-layer method for the synthesis and growth of surface mounted Metal-Organic Frameworks (SURMOFs). *Materials* (Basel), *3*(2), 1302–1315.

236. Xinghua, L., Jianjian, W., Xin, L., Lingmei, L., Dongkyu, C., Xinliang, Z., … Yu, H. (2019). Direct imaging of tunable crystal surface structures of MOF MIL101 using high-resolution electron microscopy. *Journal of the American Chemical Society*, *141*(30), 12021–12028.

237. Briand, G. G., & Burford, N. E. (2000). Coordination complexes of bismuth(III) involving organic ligands with pnictogen or chalcogen donors. *Advances in Inorganic Chemistry*, *50*, 285-357

238. Pearson, R. G. (1963). Hard and soft acids and bases. *Journal of the American Chemical Society*, *85*(22), 3533-3539.

239. Setareh, H., & Sedighe, Z. (2016). Design and fabrication of capacitive nanosensor based on MOF nanoparticles as sensing layer for VOCs detection. *Sensors and Actuators B: Chemical*, *237*(C), 776-786.

240. Karagiaridi, O., Vermeulen, N. A., Klet, R. C., Wang, T. C., Moghadam, P. Z., Al-Juaid, S. S., … Farha, O. K. (2015). Functionalized defects through solvent-assisted linker exchange: Synthesis, characterization, and partial postsynthesis elaboration of a Metal–Organic Framework containing free carboxylic acid moieties. *Inorganic Chemistry*, *54*, 1785-1790.

241. Davidovich, R. L., Stavila, V., Marinin, D. V., Voit, E. I., & Whitmire, K. H. (2009). Stereochemistry of lead(II) complexes with oxygen donor ligands. *Coordination Chemistry Reviews*, *253*(9), 1316-1352.

242. Li, Q. Y., Yang, G. W., Ma, Y. S., Li, M. J., & Zhou, Y. (2008). Synthesis and structural characterization of two novel 2D coordination polymers $[\text{PbCl(atza)}]_n$ and $[\text{PbCl(a4-ptz)}]_n$. *Inorganic Chemistry Communications*, *11*, 795-798.

243. Wang, X. W., Han, L., Tie, J. C., Zheng, Y. Q., Chen, J. Z., & Deng, Q. (2007). A Novel chiral doubly folded interpenetrating 3D metal-organic framework based on the flexible zwitterionic ligand. *Crystal Growth & Design*, *7*(6), 1027-1030.

244. Yu, X. Y., Xin, R., Gao, W. P., Wang, N., Zhang, X., Yang, Y. Y., & Qu, X. S. (2013). Three Pb-II coordination polymers based on 2-(pyridin-2-yl)-1. H-imidazole-4,5-dicarboxylic acid: syntheses, crystal structures, and fluorescent properties. *Journal of Solid State Chemistry*, *204*, 314-320.

245. Zhang, K. L., Pan, Z. C., Chang, Y., Liu, W. L., & Ng, S. W. (2009). Synthesis and characterization of an energetic three-dimensional metal-organic framework with blue photoluminescence. *Material Letters*, *63*, 2136-2138.

246. Jingjing, Z., Linke, L., Changhong, W., Wenju, L., Ruina, W., Xiaofang, Z., & Hongwei, H. (2012). Unusual 3D pillared-layer Pb(II) complex supported by

mercapto-triazole ligand: synthesis, structure and luminescent property. *Inorganic Chemistry Communications*, *20*, 205–208.

247. Blatov, V. A. (2006). Multipurpose crystallochemical analysis with the program package TOPOS. *Newsletter-International Union of Crystallography: Computing Commission*, *7*, 4-38.

248. Peedikakkal, A. M. P., Quah, H. S., Chia, S., Jalilov, A. S., Shaikh, Abdul R., Al-Mohsin, H. A., … Vittal, J. J. (2018). Near-white light emission from lead(II) metal–organic frameworks. *Inorganic Chemistry*, *57*(18), 11341-11348.

249. Hai-X., Q., Hongil, J., & Kang, M., O. (2018). Pb[$NC_5H_3(CO_2)_2$]: A white light emitting single component coordination polymer revealing high quantum efficiency and thermal stability. *Inorganic Chemistry Frontiers*, *5*(6), 1273-1276.

250. Adejumoke, A. I., Babatunde, O. A., Abimbola P. O., Tabitha, A. A., Adewumi, O. D., & Toyin, A. O. (2018). *Water pollution: Effects, prevention, and climatic impact* (Ch.3, pp.35-53). Environmental Science, INTECH.

251. Bian, Y., Xiong, N., & Zhu, G. (2018). Technology for the remediation of water pollution: a review on the fabrication of metal organic frameworks. *Processes*, *6*(8), Article#122.

252. Mon, M., Bruno, R., Ferrando, S., J., Armentano, D., & Pardo, E. (2018). Metal–organic framework technologies for water remediation: Towards a sustainable ecosystem. *Journal of Materials Chemistry A*, *6*(12), 4912-4947.

253. Adhikari, B., Palui, G., & Banerjee, A. (2009). Self-assembling tripeptide based hydrogels and their use in removal of dyes from waste-water. *Soft Matter*, *5*(18), 3452-3460.

254. Drout, R. J., Robison, L., Chen, Z., Islamoglu, T., & Farha, O. K. (2019). Zirconium metal–organic frameworks for organic pollutant adsorption. *Trends in Chemistry*, *1*(3), 304-317.

255. Arora, C. S. S., Sahu, S., Mittal, J., Kumar, P., & Bajpai, P. K. (2019). Iron based metal organic framework for efficient removal of methylene blue dye from industrial waste. *Journal of Molecular Liquids*, *284*, 343-352.

256. Brunauer, S., Emmett, P. H., & Teller, E. (1938). Adsorption of gases in multimolecular layers. *Journal of the American Chemical Society*, *60*(2), 309-319.

257. Lowell, S., Shields, J. E., Thomas, M. A., & Thommes, M. (2004). *Characterization of porous solids and powders: Surface area, pore size, and density*. Particle Technology Series (Vol.16). Dordrecht: Kluwer Academic Publishers.

258. Thommes, M. Kaneko, K., Neimark, A. V., Olivier, J. P., Reinoso, F. R-., Rouquerol, J. & Sing, K. S. W. (2016). Physisorption of gases, with special reference to the evaluation of surface area and pore size distribution (IUPAC Technical Report), *Pure and Applied Chemistry*, *87*(9-10), 1-19.

259. Ambroz, F., Macdonald, T. J., Martis, V., & Parkin, I. P. (2018). Evaluation of the BET theory for the characterization of meso and microporous MOFs. *Small Methods*, *2*(11), Article#1800173.

260. Rouquerol, F., Rouquerol, J., & Sing, K. (1999). *Adsorption by powders and porous solids: Principles, methodology and applications* (1st Ed., pp.1-26). Academic Press: London.

261. Hanaor, D. A. H., Ghadiri, M., Chrzanowski, W., & Gan, Y. (2014). Scalable surface area characterization by electrokinetic analysis of complex anion adsorption. *Langmuir*, *30*(50), 15143-15152.

262. Dillon, E. C., Wilton, J. H., Barlow, J. C., & Watson, W. A. (1989). Large surface area activated charcoal and the inhibition of aspirin absorption. *Annals of Emergency Medicine*, *18*(5), 547–552.

263. Sing, K. S. W., Everett, D. H., Haul, R. A. W., Moscou, L., Pierotti, R. A., Rouquerol, J. & Siemieniewska, T. (1985). Reporting physisorption data for gas/solid systems with special reference to the determination of surface area and porosity, (Recommendations 1984). *Pure and Applied Chemistry*, *57*(4), 603-619.

264. Dollimore, D., Spooner, P., & Turner, A. (1976). The BET method of analysis of gas adsorption data and its relevance to the calculation of surface areas. *Surface Technology*, *4*(2), 121-160.

LIST OF PUBLICATIONS AND PAPERS PRESENTED

List of Publications

1. **Mesoun A. A.,** Aliyu, M. H., Ariffin, A., Zhang, J., Shimizu, G. K. H., Hongil J., … Wibowo, A. C. (2021). A new bismuth coordination polymer with proton conductivity and orange-red photoluminescence, *Journal of Coordination Chemistry,* https://doi.org/10.1080/00958972.2021.1921167.

2. **Mesoun A. A.,** Aliyu, M. H., Wardana, F. Y., Ariffin, A., Hongil J., & Wibowo, A. C. (2019). Lead−organic frameworks containing trimesic acid: Facile dissolution−crystallization and near-white light emission, *Crystal Growth Design*, ***19***, 6274−6282.

Poster Presented

1. **Mesoun A. A. Al-Nubi,** Azhar Ariffin, & Arief C. Wibowo (2017). Synthesis of novel bismuth metal–organic frameworks: Poster presented at the 4th International Conference on Science, Computing, Chemistry and Management 2017 (ICSCCM 2017). Langkawi, Malaysia.